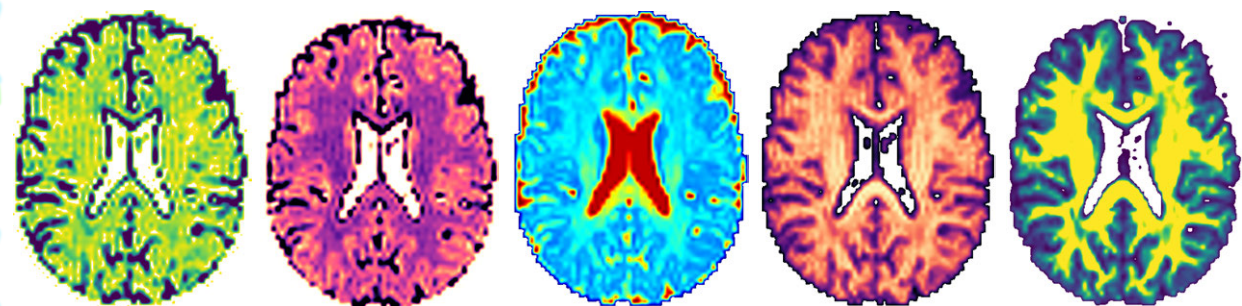


Diffusion MRI

with generalised gradient waveforms: methods, models, and neuroimaging applications

Deneb Boito



Linköping Studies in Science and Technology
Dissertations, No. 2362

Diffusion MRI with generalised gradient waveforms: methods, models, and neuroimaging applications

Deneb Boito



Linköping University
Department of Biomedical Engineering
SE-581 83 Linköping, Sweden

Linköping 2023



This work is licensed under a Creative Commons Attribution-NonCommercial 4.0 International License.

<https://creativecommons.org/licenses/by-nc/4.0/>

Edition 1.0

© Deneb Boito, 2023

ISBN 978-91-8075-442-2 (print)

ISBN 978-91-8075-443-9 (PDF)

ISSN 0345-7524

URL <https://doi.org/10.3384/9789180754439>

Published articles have been reprinted with permission from the respective copyright holder.

Typeset using \LaTeX

Printed by LiU-Tryck, Linköping 2023

POPULÄRVETENSKAPLIG SAMMANFATTNING

Studier av biologisk vävnad såsom den mänskliga hjärnan är centrala för vår förståelse av hur dess anatomi och fysiologi påverkas av sjukdomar, och för vår förmåga att finna den bästa behandlingen mot dessa. Magnetisk resonansavbildning (MRI) är en teknik som tillåter icke-invasiva studier av levande vävnad genom listigt utformade magnetfält. Tack vare sin stora känslighet för ett stort antal olika vävnadsegenskaper är MRI idag ett av de mest utnyttjade verktygen när det gäller att undersöka hjärnan kliniskt. En speciell tillämpning av MRI, kallad diffusions-MRI, utnyttjar vattenmolekylernas rörelse inom och mellan cellerna som bygger upp vävnaden. Egenskaper som är relaterade till olika aspekter av cellernas utformning samt deras sammansatta struktur, och vilka är osynliga för andra bildalstrande metoder, kan via dessa molekylrörelser mätas och göras tillgängliga med diffusions-MRI.

Trots den anmärkningsvärda känsligheten för mikroskopiska vävnadsegenskaper, är det en utmaning att tolka mätdata som man har fått via diffusions-MRI. Traditionella mätningar har svårt att särskilja specifika uppmätta egenskaper i den komplicerade blandning av celler som vävnaden utgör. För att lösa det problemet har forskare utvecklat innovativa mätscheman för att urskilja det önskade bidraget från övriga mät-signaler. Arbetet i denna avhandling presenterar nya sätt analysera och modellera data från diffusions-MRI, med målet att dessa ska kunna användas i klinisk praktik.

De två första arbetena i avnhandlingen presenterar scheman för en mer pålitlig skattning av parametrar ur data från diffusions-MRI, samtidigt som mätningarna kan göras snabbare, vilket underlättar för patienten. I det tredje arbetet används dessa mätscheman för att undersöka hjärnorna hos patienter som tidigare har varit inlagda för COVID-19, och som fortfarande lider av neurologiska besvär månader efter genomgången infektion. Resultaten visar utbredda förändringar i patienternas hjärnor, och kan vara till hjälp för att förstå de bakomliggande orsakerna till de kvarvarande symptomen. I det fjärde arbetet undersöks ett alternativt sätt att modellera diffusionen som finns i varje del av den undersökta vävnaden, och det påvisas att detta ger en bättre representation jämfört med den vanligtvis använda tekniken.

ABSTRACT

The incessant, random motion of water molecules within biological tissues reveals unique information about the tissues' structural and functional characteristics. Diffusion magnetic resonance imaging is sensitive to this random motion, and since the mid-1990s it has been extensively employed for studying the human brain. Most notably, measurements of water diffusion allow for the early detection of ischaemic stroke and for the unveiling of the brain's wiring via reconstruction of the neuronal connections. Ultimately, the goal is to employ this imaging technique to perform non-invasive, *in vivo* virtual histology to directly characterise both healthy and diseased tissue.

Recent developments in the field have introduced new ways to measure the diffusion process in clinically feasible settings. These new measurements, performed by employing generalised magnetic field gradient waveforms, grant access to specific features of the cellular composition and structural organisation of the tissue. Methods based on them have already proven beneficial for the assessment of different brain diseases, sparking interest in translating such techniques into clinical practice. This thesis focuses on improving the methods currently employed for the analysis of such diffusion MRI data, with the aim of facilitating their clinical adoption.

The first two publications introduce constrained frameworks for the estimation of parameters from diffusion MRI data acquired with generalised gradient waveforms. The constraints are dictated by mathematical and physical properties of a multi-compartment model used to represent the brain tissue, and can be efficiently enforced by employing a relatively new optimisation scheme called semidefinite programming. The developed routines are demonstrated to improve robustness to noise and imperfect data collection. Moreover, constraining the fit is shown to relax the requirements on the number of points needed for the estimation, thus allowing for faster data acquisition.

In the third paper, the developed frameworks are employed to study the brain's white matter in patients previously hospitalised for COVID-19 and who still suffer from neurological symptoms months after discharge. The results show widespread alterations to the structural integrity of their brain, with the metrics available through the advanced diffusion measurements providing new insights into the damage to the white matter.

The fourth paper revisits the modelling paradigm currently adopted for the analysis of diffusion MRI data acquired with generalised gradient waveforms. Hitherto, the assumption of free diffusion has been employed to represent each domain in a multi-compartmental picture of the brain tissue. In this work, a model for restricted diffusion is considered instead to alleviate the paradoxical assumption of free but compartmentalised diffusion. The model is shown to perfectly capture restricted diffusion as measured with the generalised diffusion gradient waveforms, thus endorsing its use for representing each domain in the multi-compartmental model of the tissue.

Acknowledgments

I still find it hard to believe that five years have passed. Looking back, it has been an eventful time, both professionally and privately. Certainly, this achievement would have not been possible without the work and support from many.

My thanks go first and foremost to my mentors, for guiding me through this adventure and for sharing their wisdom and knowledge. Working with you has been an absolute privilege. To **Evren Özarslan**, for giving me this opportunity and supporting me along the way. I deeply value the trust and freedom you have granted me from the beginning, as well as your humanity and all the greatly executed barbecues. I like to think that we both have learned and have developed throughout this experience. To **Magnus Herberthson**, for his infinite patience in answering all my maths related questions, and the never ending anecdotes. To **Anders Eklund**, for his direct and incisive comments. To **Ida Blystad**, for introducing me to the clinical world and its challenges. Many thanks also to **Tom Dela Haije**, for a wonderful collaboration and for being an unofficial supervisor.

This thesis would have also not been possible without the help and work of **Cem Yolcu**, **Anders Tisell**, **Richard Levi**, **Aasa Feragen**, and **C-F Westin**. Moreover, the contributions of all personnel at IMT and CMIV cannot be overlooked, and to all of you goes my gratitude. In particular, thanks to all the fellow PhD students, because only those who share our struggles can make us feel understood.

A big shout out to **Cem Yolcu**: Life at IMT has not been the same since you left. To **Nayereh Ghazi**, for the long conversations about anything and everything. A special note of appreciation to **Alfredo Ordinola**, **Chiara Trenti**, **David Abramian**, and **Iulian Tampu**: above all for your friendship, the fikas, and the adventures shared during the conferences expeditions, but also for helping with this book.

Finally, to the wonderful people who are close to me and with whom I share the joyful and adverse moments in life. To my friends: the Linköping gang, the brother-from-another-mother in Stockholm, and the Italian crew. No matter where I am, you make me feel at home. To my family, to whom I don't dedicate nearly enough time. To my sisters, for the fights, the laughs, and all the little things that bind us. To my father, for teaching me many things often without speaking a word, and having supported me in all my life choices. *Un grazie speciale alla mia mamma, per tutto il suo amore, la sua generosità, e la forza con cui è sempre riuscita a rialzarsi.*

To all of you who have in any way contributed and dedicated some of your time goes my heartfelt appreciation.

Contents

Abstract	iii
Acknowledgments	vi
Contents	vii
List of Papers	ix
List of Abbreviations	xi
List of Figures	xiii
1 Introduction	1
1.1 Aim	2
1.2 Thesis outline	2
1.3 Data and Ethics	3
1.4 Funding	3
2 Mathematical notation and tools	5
2.1 Tensors	5
2.2 Positive (semi-)definite matrices	8
3 Magnetic Resonance Imaging	11
3.1 The MR scanner	11
3.2 Spins, precession, and magnetisation	12
3.3 Excitation, resonance, and relaxation	14
3.4 Pulse sequences, spin-echo, and contrast	16
3.5 Gradients, spatial localisation, and imaging	18
4 Diffusion Magnetic Resonance Imaging	21
4.1 Diffusion	21
4.2 Diffusion and MR	24
4.3 Measuring diffusion with MR	26
4.4 Diffusion within confined pores	32
5 Mapping heterogeneity with generalised diffusion gradients	37

5.1	Tensor-valued diffusion encoding	37
5.2	Tensor distributions as a proxy to intravoxel heterogeneity	40
5.3	Q-space trajectory imaging	43
5.4	Distributions of confinement tensors	47
6	Parameter estimation	51
6.1	Optimisation problems	51
6.2	Numerical inversion of the Laplace transform	53
6.3	Estimation routines for q-space trajectory imaging	55
6.4	A machine learning approach	57
7	Review of papers & conclusions	65
7.1	Papers I & II	65
7.2	Paper III	66
7.3	Paper IV	67
7.4	Conclusions	68
	Bibliography	71
	Paper I	87
	Paper II	109
	Paper III	121
	Paper IV	137

List of Papers

This thesis is based on the following publications, referred to in the text with their roman numeral:

I Q-space trajectory imaging with positivity constraints (QTI+).

Magnus Herberthson, Deneb Boito, Tom Dela Haije, Aasa Feragen, Carl-Fredrik Westin, Evren Özarslan.

Neuroimage 2021, 238, 118198.

DOI: <https://doi.org/10.1016/j.neuroimage.2021.118198>

Published under CC-BY-NC-ND license.

II Diffusivity-limited q-space trajectory imaging.

Deneb Boito, Magnus Herberthson, Tom Dela Haije, Ida Blystad, Evren Özarslan.

Magnetic Resonance Letters 2023, 3, 187-196 .

DOI: <https://doi.org/10.1016/j.mrl.2022.12.003>

Published under CC-BY-NC-ND license.

III MRI with generalized diffusion encoding reveals damaged white matter in patients previously hospitalized for COVID-19 and with persisting symptoms at follow-up.

Deneb Boito, Anders Eklund, Anders Tisell, Richard Levi, Evren Özarslan, Ida Blystad.

Brain Communication 2023, 5.

DOI: <https://doi.org/10.1093/braincomms/fcad284>

Published under CC-BY license.

IV Multidimensional diffusion MRI methods with confined subdomains.

Deneb Boito, Cem Yolcu, Evren Özarslan.

Frontiers in Physics 2022, 10, 830274.

DOI: <https://doi.org/10.3389/fphy.2022.830274>

Published under CC-BY license.

Publications and conference abstracts not included in the thesis

Publications

Applying positivity constraints to q-space trajectory imaging: the QTI+ implementation.

Deneb Boito, Magnus Herberthson, Tom Dela Haije, Evren Özarslan.

SoftwareX 2022, 18, 101030.

DOI: 10.1016/j.softx.2022.101030

Diffusion within pores fully revealed by magnetic resonance.

Evren Özarslan, Cem Yolcu, Alfredo Ordinola, Deneb Boito, Tom Dela Haije, Mathias Højgaard Jensen, Magnus Herberthson.

The Journal of Chemical Physics 2023, 158, 161102.

DOI: 10.1063/5.0146304

Conference abstracts

Compartment-specific diffusivity: A new dimension in multidimensional diffusion MRI?

Deneb Boito, Cem Yolcu, Evren Özarslan.

Poster presentation at ISMRM 2020 Virtual Conference. Selected for the highlights of diffusion MRI.

Enforcing positivity constraints in Q-space Trajectory Imaging (QTI) allows for reduced scan time.

Deneb Boito, Magnus Herberthson, Tom Dela Haije, Evren Özarslan.

Oral presentation at ISMRM 2021 Virtual Conference. Magna cum Laude Merit Award winner.

Diffusivity-limited q-space trajectory imaging.

Deneb Boito, Magnus Herberthson, Evren Özarslan.

Poster presentation at the 30th ISMRM annual meeting, London, United Kingdom, 2022.

Detecting White-Matter changes due to severe Covid-19 infection with tensor-encoded diffusion MRI: a pilot study.

Deneb Boito, Ida Blystad, Anders Eklund, Evren Özarslan.

Poster presentation at the ISMRM diffusion workshop, Amsterdam, Netherlands, 2022.

Q-space trajectory imaging with positivity constraints: a machine learning approach.

Deneb Boito and Evren Özarslan.

Poster presentation at the 31st ISMRM annual meeting, Toronto, Canada, 2023

Abbreviations

ADC	apparent diffusion coefficient
AD	axial diffusivity
C_c	orientation coherence
C_{MD}	variance in size
COM	centre of mass
DDE	double diffusion encoding
DEC-FA	direction-encoded fractional anisotropy
DKI	diffusional kurtosis imaging
dMRI	diffusion magnetic resonance imaging
DTD	diffusion tensor distribution
DTI	diffusion tensor imaging
DWIs	diffusion-weighted images
EAP	ensemble-averaged propagator
ELU	exponential linear unit
EPI	echo-planar imaging
FA	fractional anisotropy
GPA	Gaussian phase approximation
IFT	inverse Fourier transform
IP	interior point
LTE	linear tensor encoding
MA	macroscopic anisotropy
μA	microscopic anisotropy
MD	mean diffusivity
μFA	microscopic fractional anisotropy
ML	machine learning
MR	magnetic resonance
MRI	magnetic resonance imaging

NLLS	non-linear least squares
NN	neural network
NNLS	non-negative least squares
ON	orthonormal
OP	order parameter
PD	proton density
PGSE	pulsed-gradient spin-echo
PSD	positive semi-definite
PTE	planar tensor encoding
QTI	q-space trajectory imaging
RD	radial diffusivity
RF	radio frequency
SE	spin-echo
SDP	semidefinite programming
SNR	signal-to-noise ratio
STE	spherical tensor encoding
TBSS	tract-based spatial statistics
T_E	time of echo
T_R	repetition time
V_{bulk}	bulk variance
V_{iso}	isotropic variance
V_{shear}	shear variance

List of Figures

2.1	Shapes of axisymmetric tensors	8
3.1	Spins	13
3.3	Spin-Echo pulse sequence	17
3.4	Proton-density, T_1 , and T_2 weighted MR images of a brain	18
4.1	One-dimensional Gaussian distributions of particles displacements for different diffusion times and different diffusion coefficients	23
4.2	Diffusion tensor ellipsoids	24
4.3	Diffusion-weighted images for increasing b-value	25
4.4	Stejskal-Tanner pulse sequence diagram	27
4.5	Scalar invariants from the diffusion tensor	29
4.6	Free, hindered, and restricted diffusion time dependence.	30
4.7	Signal decay implied by the diffusional kurtosis model.	31
4.8	Scalar invariants from the confinement tensor model	33
4.9	Scalar invariants from the confinement tensor model for a brain tumour	34
4.10	MR signal for restricted diffusion and confinement tensor model for different diffusion times	34
5.1	Linear, planar, and spherical tensor encoding waveforms and q-space trajectories	39
5.2	Linear and spherical tensor encoding signals for heterogeneous voxels	41
5.3	Diffusional variances from the covariance tensor	45
5.4	Examples of q-space trajectory imaging indices for 8 different voxel compositions	46
5.5	Scalar invariants from the covariance tensor	47
5.6	Statistical descriptors for joint distributions of confinement tensors - effective diffusivities	49
5.7	Examples of confinement tensor distributions	50
6.1	Neural network architecture for regression analysis	58

6.2	QTI+ and machine learning fit comparison on synthetic data . . .	60
6.3	QTI+ and machine learning fit comparison on experimental data	61
6.4	Tract-based spatial statistics results obtained from QTI \pm and machine learning fits	61
6.5	QTI+ and machine learning fit comparison on brain tumor data .	62
6.6	Diffusion tensor distributions estimation with a conventional algorithm and machine learning	63

1

Introduction

Since its introduction in the mid 1980s [1], [2], diffusion Magnetic Resonance Imaging (dMRI) has established itself as one of the main research and clinical tools for the study and diagnosis of the *in vivo* brain. At its foundations, dMRI leverages the ever-present random motion of water molecules to infer characteristics of the environment where these molecules reside. Barriers and physiological processes influence this random movement, thus imprinting their presence into the dMRI data. Successful applications of dMRI demonstrating the exquisite sensitivity of this technique to the tissue microstructure are found in the early detection of ischaemic stroke [3] — not otherwise visible with other MR imaging modalities until hours after the onset of the event — and the study of the brain connectivity, where the highly anisotropic nature of diffusion within the neural tissue is exploited to reconstruct the pathways between different areas of the brain [4]–[8].

Beyond these successful applications, the long-standing goal of dMRI is to perform non-invasive histology, allowing structures on the microscopic scale to be seen from images acquired with millimetre resolution. However, this objective has largely been hampered by the limited information obtainable from conventional diffusion MRI data. The workhorse of diffusion MRI experiments remains an MR sequence introduced in 1965 by Stejskal and Tanner, where water self-diffusion is measured by applying two rectangular magnetic field gradient pulses with opposite polarity [9]. While this experiment is sensitive to many features of the cells making up the tissue, it also produces a signal where all these properties conflate and cannot be disentangled. Widely employed clinical neuroimaging methods developed on top of this sequence, such as diffusion tensor imaging (DTI) [10] and apparent diffusion coefficient (ADC) mapping [2], thus provide only a glimpse towards the many tissue properties available through the random diffusive motion of water molecules.

Much work in the dMRI field has been devoted towards developing new ways of measuring the diffusion process, aiming at specifically targeting different aspects of the cellular tissue composition [11]–[16]. In this thesis, the focus is on a particular class of measurements in which the Stejskal-Tanner experiment is extended to encompass general time-varying magnetic field gradients that efficiently probe water diffusion in multiple directions simultaneously. When analysed under the assumption of free diffusion, these data are commonly referred to as tensor-encoded or tensor-valued diffusion MRI data [17]–[19], since all the experimental parameters collapse into a single descriptor called the B-tensor. The higher specificity to different tis-

sue characteristics accessed with tensor-valued dMRI compared to Stejskal-Tanner measurements allows the computation of markers of intravoxel tissue heterogeneity which have already been instrumental in better characterising the healthy and diseased brain [17], [18], [20], [21]. This demonstrated the relevance for such diffusion measurements and methods to reach routine clinical practice.

The overarching goal of this work is to facilitate this transition by improving on the technologies currently employed for the analysis of diffusion MRI data encoded with generalised gradient waveforms. The methods have so far been based on a picture of the brain microstructure as being composed of many pores each represented by a diffusion tensor [6], [22]. As such, the goal is to either estimate the distribution of diffusion tensors making up the tissue [23], or access its statistical properties [17], [24]. Two avenues have been explored through the work presented here. The first concerns producing reliable parameter estimates for the q-space trajectory framework employed to access the mean and covariance of the diffusion tensor distribution [17]. These estimates are in turn used to compute descriptors of the brain cellular composition and organisation, with the ultimate goal of using them for characterising diseased tissue. Therefore, it is imperative to ensure that these descriptors are robustly estimated from the data before endorsing their use in clinical practice. The second avenue deals instead with the modelling of the diffusion MRI data given a compartmentalised picture of the intravoxel brain microstructure. The current models employ the assumption of free diffusion occurring in separated compartments. Besides being rather paradoxical, this representation ignores the distinctive features imprinted on the MR signal by restricted diffusion, since the data are analysed via the B-tensor only [25]. Therefore, a more suitable model for describing the diffusion process in each pore making up the tissue should be considered.

1.1 Aim

The aim of this thesis can be summarised in the following three objectives, listed according to the publications in which they are addressed:

papers I & II Develop methods for producing reliable estimates for the parameters attainable via tensor-valued diffusion MRI.

paper III Investigate patients' brain microstructure using diffusion MRI with generalised gradient waveforms.

paper IV Extend the analysis of diffusion MRI with generalised gradient waveforms beyond the free diffusion assumption.

1.2 Thesis outline

Including this introduction, the thesis is divided into 7 chapters. Chapter 2 introduces the mathematical notation and several definitions useful for reading the content presented in this book and in the publications. Chapters 3 and 4 present funda-

mental concepts of Magnetic Resonance Imaging and diffusion Magnetic Resonance Imaging, respectively. Chapter 5 then introduces the diffusion MRI measurements performed with generalised gradient waveforms, and how these can be exploited to characterise tissue heterogeneity via representations of the diffusion signal. Chapter 6 deals with the estimation of model parameters from performed measurements, and contains largely unpublished material on a machine learning approach for performing model fitting. Finally, Chapter 7 presents an overview of the papers included in the thesis.

1.3 Data and Ethics

In papers I, II, and IV publicly available data have been employed [26]. These were also used to generate the images displayed in this book, unless otherwise stated in the figures' caption. In paper II, additional diffusion MRI data from healthy volunteers were acquired with ethical approval from the Swedish ethical review authority, Dnr 2019-06123. These were also used in Figure 3.4. In paper III, data from both healthy subjects and patients were collected with ethical approval from the Swedish ethical review authority, Dnr 2020-03029 and 2015/13-31. These data were also used to generate Figure 6.4. In Figures 4.9 and 6.5 data from brain tumor patients collected with ethical approval EPM 2020-01404 are shown.

1.4 Funding

This work was financially supported by Linköping University (LiU) Center for Industrial Information Technology (CENIIT), LiU Cancer, VINNOVA/ITEA3 IMPACT and ASSIST, Analytic Imaging Diagnostic Arena (AIDA), the Swedish Foundation for International Cooperation in Research and Higher Education (STINT), the Swedish Foundation for Strategic Research (RMX18-0056), and the Swedish Research Council 2016-04482.

2

Mathematical notation and tools

This chapter introduces the notation employed throughout this thesis, and several mathematical concepts used in later chapters.

2.1 Tensors

When working in vector spaces V equipped with a scalar product and hence an orthonormal (ON) basis, a (cartesian) tensor T of order m is a multilinear map:

$$T = V^m \rightarrow \mathbb{R}. \quad (2.1)$$

The order m of the tensor indicates the number of indices necessary to identify one of its elements. For example, elements of second-order tensors, for which $m = 2$, are identified by 2 indices.

Throughout the thesis, zeroth-order tensors, i.e. scalars, are indicated by non-bold characters. First-order tensors, represented by vectors, are indicated by lower-case bold characters. Second-order tensors, represented by matrices, are indicated with upper-case bold characters. Fourth-order tensors, represented by 4-dimensional arrays, are indicated with blackboard characters. For example, a is a scalar/zeroth-order tensor, \mathbf{a} is a vector/first-order tensor, \mathbf{A} is a matrix/second-order tensor, and \mathbb{A} is a 4-dimensional array/fourth-order tensor.

Symmetric tensors

The second and fourth-order tensors encountered in this thesis present symmetries. A symmetric second-order tensor \mathbf{A} is such that $A_{ij} = A_{ji}$, where A_{ij} and A_{ji} are i -th and j -th elements of tensor \mathbf{A} , respectively. Fourth-order tensors are said to have *major* symmetry if $A_{ijkl} = A_{klij}$, *minor* symmetry if $A_{ijkl} = A_{jikl} = A_{ijlk}$, and *total* symmetry if $A_{ijkl} = A_{\sigma(ijkl)}$, where $\sigma(ijkl)$ indicates any possible permutation of the indices.

Inner and outer products

Inner products between first-order tensors, i.e. scalar products, are indicated either by “ \cdot ” or by transposing the first tensor. For example, given an ON basis, the inner product between $\mathbf{a} = (a_1 \ a_2 \ a_3)^\top$, $\mathbf{b} = (b_1 \ b_2 \ b_3)^\top \in \mathbb{R}^3$ is:

$$v = \mathbf{a} \cdot \mathbf{b} = \mathbf{a}^\top \mathbf{b} = a_1 b_1 + a_2 b_2 + a_3 b_3 = \sum_i a_i b_i. \quad (2.2)$$

The inner product extends the concept of scalar product to tensors of order higher than 1. Inner products are indicated with “ $:$ ”, and the resultant is the scalar c obtained by adding the point-wise multiplied elements of the tensors. For example, for two second-order tensors \mathbf{A} and \mathbf{B} :

$$c = \mathbf{A} : \mathbf{B} = \sum_i \sum_j A_{ij} B_{ij}. \quad (2.3)$$

When the tensors can be expressed via matrices, the inner product can also be computed as:

$$c = \text{Tr}(\mathbf{A}^\top \mathbf{B}), \quad (2.4)$$

where the operator $\text{Tr}(\cdot)$ denotes the trace of a square matrix, which is the sum of its diagonal elements.

The outer product, or tensor product, between two tensors is indicated with “ \otimes ”. Given two tensors of order m and n , their outer product is a tensor of order $m + n$ constructed by multiplying each element of the two tensors. For example, the outer product between two vectors \mathbf{a} and $\mathbf{b} \in \mathbb{R}^3$ is the second-order tensor \mathbf{C} :

$$\mathbf{C} = \mathbf{a} \otimes \mathbf{b} = \begin{pmatrix} a_1 b_1 & a_1 b_2 & a_1 b_3 \\ a_2 b_1 & a_2 b_2 & a_2 b_3 \\ a_3 b_1 & a_3 b_2 & a_3 b_3 \end{pmatrix}. \quad (2.5)$$

The disposition of the elements in the constructed tensor is seen via index notation. For example, the ij -th element in \mathbf{C} is $C_{ij} = a_i b_j$. For a fourth-order tensor $\mathbf{C} = \mathbf{A} \otimes \mathbf{B}$, the $ijkl$ -th element is $C_{ijkl} = A_{ij} B_{kl}$.

For first-order tensors/vectors, the outer product can also be indicate by transposing the second vector: $\mathbf{C} = \mathbf{a} \mathbf{b}^\top$.

The outer product of a tensor with itself is indicated with:

$$\mathbf{A}^{\otimes 2} = \mathbf{A} \otimes \mathbf{A}. \quad (2.6)$$

Parameterisation of 3x3 axisymmetric tensors

There exist several ways to parameterise an axisymmetric 3×3 tensor \mathbf{A} when it is expressed in a basis such that its matrix representation is diagonal. Here the "Haerben convention" [27]–[29] is considered as it is instrumental for later expressing the relation between tensor-encoding shapes and probed diffusion patterns:

$$\mathbf{\Lambda} = \begin{pmatrix} \lambda_{xx} & 0 & 0 \\ 0 & \lambda_{yy} & 0 \\ 0 & 0 & \lambda_{zz} \end{pmatrix} \quad \text{with} \quad |\lambda_{zz} - \lambda_{\text{iso}}| \geq |\lambda_{xx} - \lambda_{\text{iso}}| \geq |\lambda_{yy} - \lambda_{\text{iso}}|, \quad (2.7)$$

where

$$\lambda_{\text{iso}} = \frac{\lambda_{xx} + \lambda_{yy} + \lambda_{zz}}{3} = \frac{\text{Tr}(\mathbf{\Lambda})}{3} \quad (2.8)$$

represents the isotropic average of the tensor, and it relates to its *size*.

The *shape* of the tensor can be identified by the unitless parameter κ_λ :

$$\kappa_\lambda = \frac{1}{3\lambda_{\text{iso}}} \left(\lambda_{zz} - \frac{\lambda_{xx} + \lambda_{yy}}{2} \right). \quad (2.9)$$

κ_λ takes value in the range $[-0.5, 1]$, where $\kappa_\lambda = -0.5$ corresponds to "pancake" tensors, $\kappa_\lambda = 0$ corresponds to spherical tensors, and $\kappa_\lambda = 1$ corresponds to "stick" tensors, see Figure 2.1.

Axisymmetric tensors, for which $\lambda_{xx} = \lambda_{yy} = \lambda_\perp$ and $\lambda_{zz} = \lambda_\parallel$, can be represented in terms of λ_{iso} and κ_λ only as:

$$\mathbf{\Lambda} = \lambda_{\text{iso}} \left\{ \begin{pmatrix} 1 & 0 & 0 \\ 0 & 1 & 0 \\ 0 & 0 & 1 \end{pmatrix} + \kappa_\lambda \begin{pmatrix} -1 & 0 & 0 \\ 0 & -1 & 0 \\ 0 & 0 & 2 \end{pmatrix} \right\}, \quad (2.10)$$

where

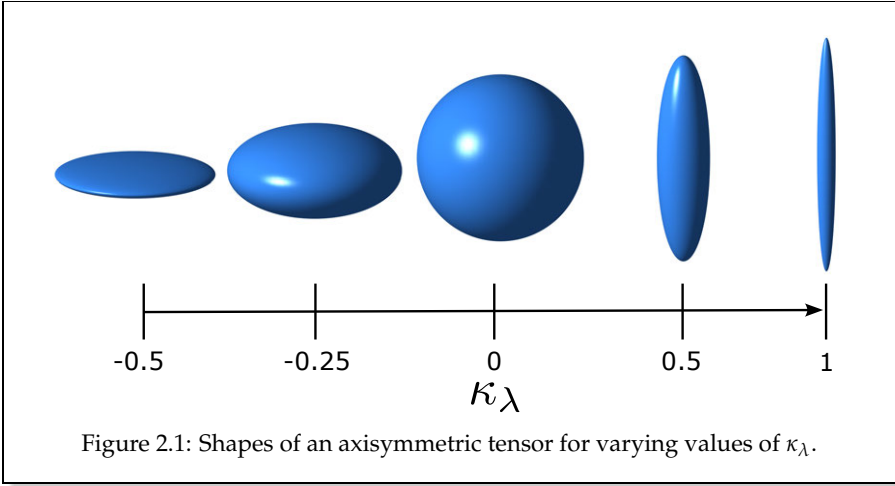
$$\lambda_{\text{iso}} = \frac{\lambda_\parallel + 2\lambda_\perp}{3} \quad \text{and} \quad \kappa_\lambda = \frac{\lambda_\parallel - \lambda_\perp}{3\lambda_{\text{iso}}}. \quad (2.11)$$

The diagonalised tensor $\mathbf{\Lambda}$ can then be oriented in space by means of successive rotations, resulting in a non-diagonal tensor $\mathbf{\Lambda}_{\text{rot}} = \mathbf{R}_z(\phi) \mathbf{R}_y(\theta) \mathbf{\Lambda} \mathbf{R}_y^\top(\theta) \mathbf{R}_z^\top(\phi)$, where θ and ϕ are the *polar* and *azimuthal* angles defining the target direction of the axis of symmetry, respectively, and \mathbf{R}_y and \mathbf{R}_z are the matrices expressing the rotations around the y and z axes, respectively [28]. The effect of the rotation on the parameterised tensor is seen via a matrix \mathbf{L} :

$$\mathbf{L} = \frac{1}{2} \begin{pmatrix} 3l_x^2 - 1 & 3l_x l_y & 3l_x l_z \\ 3l_x l_y & 3l_y^2 - 1 & 3l_y l_z \\ 3l_x l_z & 3l_y l_z & 3l_z^2 - 1 \end{pmatrix} \quad \text{with} \quad \begin{aligned} l_x &= \sin \theta \cos \phi \\ l_y &= \sin \theta \sin \phi \\ l_z &= \cos \theta \end{aligned} \quad (2.12)$$

so that

$$\mathbf{\Lambda}_{\text{rot}} = \lambda_{\text{iso}} (\mathbf{I} + 2\kappa_\lambda \mathbf{L}). \quad (2.13)$$



2.2 Positive (semi-)definite matrices

An $n \times n$ real symmetric matrix \mathbf{M} is positive semi-definite (PSD) if, for all vectors $\mathbf{v} \in \mathbb{R}^n$, $\mathbf{v}^T \mathbf{M} \mathbf{v} \geq 0$. If, for all non-zero vectors $\mathbf{v} \in \mathbb{R}^n$, $\mathbf{v}^T \mathbf{M} \mathbf{v} > 0$, then \mathbf{M} is positive definite. Equivalently, a matrix is positive semi-definite if all its eigenvalues are non-negative (if the eigenvalues are all strictly positive, then the matrix is positive definite), or if there exists a real matrix \mathbf{B} such that $\mathbf{M} = \mathbf{B}^T \mathbf{B}$. The positive semi-definiteness and positive definiteness of a matrix are denoted with the symbols “ ≥ 0 ” and “ > 0 ”, respectively.

Cholesky decomposition

The Cholesky decomposition is the factorization of a real symmetric positive (semi-)definite matrix into the product of a lower triangular matrix with its transpose:

$$\mathbf{M} \geq 0, \quad \mathbf{M} = \mathbf{L} \mathbf{L}^T \quad (2.14)$$

where \mathbf{L} is of the form:

$$\begin{pmatrix} L_{11} & 0 & \cdots & 0 \\ L_{21} & L_{22} & \ddots & \vdots \\ \vdots & & \ddots & 0 \\ L_{n1} & \cdots & \cdots & L_{nn} \end{pmatrix}. \quad (2.15)$$

If \mathbf{M} is positive-definite, the matrix \mathbf{L} has positive entries on its main diagonal, and it is uniquely determined by \mathbf{M} . If \mathbf{M} is positive semi-definite, a matrix \mathbf{L} having non-negative entries on its main diagonal exists, but it is not necessarily unique.

Block matrices

The positive semidefiniteness of block matrices can be established via the *Schur complements* [30]. For a symmetric block matrix \mathbf{M} ,

$$\mathbf{M} = \begin{pmatrix} \mathbf{A} & \mathbf{B} \\ \mathbf{B}^\top & \mathbf{C} \end{pmatrix}, \quad (2.16)$$

where \mathbf{A} , \mathbf{B} , and \mathbf{C} are matrices (with \mathbf{A} and \mathbf{C} being square matrices), the following conditions establish whether \mathbf{M} is PSD:

- if $\mathbf{A} \succ 0$, then $\mathbf{M} \succeq 0 \iff \mathbf{M}/\mathbf{A} = \mathbf{C} - \mathbf{B}^\top \mathbf{A}^{-1} \mathbf{B} \succeq 0$
- if $\mathbf{C} \succ 0$, then $\mathbf{M} \succeq 0 \iff \mathbf{M}/\mathbf{C} = \mathbf{A} - \mathbf{B} \mathbf{C}^{-1} \mathbf{B}^\top \succeq 0$

where \mathbf{M}/\mathbf{A} and \mathbf{M}/\mathbf{C} are the Schur complements of the \mathbf{A} and \mathbf{C} blocks, respectively.

If \mathbf{M} is block diagonal, i.e.

$$\mathbf{M} = \begin{pmatrix} \mathbf{A} & \mathbf{0} \\ \mathbf{0} & \mathbf{C} \end{pmatrix}, \quad (2.17)$$

then $\mathbf{M} \succeq 0 \iff \mathbf{A} \succeq 0$ and $\mathbf{C} \succeq 0$.

3

Magnetic Resonance Imaging

Magnetic Resonance Imaging (MRI) is nowadays ubiquitous in medical practice due to its unique ability to produce high-resolution 3-dimensional images and time series of soft tissues' structure, metabolism, and physiology; all of it in a non-invasive and safe manner! These different types of contrast are based on the manipulation of a quantum property of atomic nuclei called *spin*. Most of the imaging is based on hydrogen spins, as hydrogen is abundant in most biological systems, and this abundance is required in order to create a detectable signal.

This chapter introduces the foundations necessary for generating this detectable signal: starting from the hardware, going through the fundamental physical concepts, and ending with how images are created by manipulations of magnetic field gradients.

3.1 The MR scanner

An MR scanner is fundamentally composed of three parts: the main magnet, a system of three orthogonal gradient coils, and a radio frequency (RF) coil system. The main magnet and the gradients coils are wrapped around the scanner opening, called *bore*, where the object to be scanned is placed.

The main magnet, referred to as b_0 , is responsible for generating the strong uniform magnetic field in which the object to be scanned is placed. Conventionally, the orientation of this field determines the z-axis of the reference system, and aligns with the scanner's bore. Typical clinical MR scanners generate b_0 fields of 1.5 – 3.0 Tesla [T], with recent developments both in the direction of lower (0.064 T) and higher (7 T) field strengths. For comparison, Earth's magnetic field is approximately 40 μ T, about 70000 times weaker than that generated by a 3 T system.

The system of orthogonal gradient coils is used to generate time-varying magnetic fields, resulting in linearly changing magnetic field strengths along arbitrary orientations. These are necessary for imaging purposes, in order to achieve spatial localisation of the MR signal within the object, but also for measuring diffusion, as discussed in the next chapter. Maximum gradient strengths on clinical and research scanners, measured in [mT/m], are in the range of 40 – 80 mT/m .

Finally, the RF system comprises two antennas, often combined into a single coil, used for the transmission and detection of rotating magnetic fields. These coils can take various shapes and forms depending on the object to be scanned; this is done in order to maximise the signal-to-noise ratio (SNR) at reception, and to transmit a field as homogeneous as possible. As elaborated in Section 3.3, the transmitted RF field, referred to as b_1 , is responsible for the selective excitation of spins precessing at a specific frequency, thus fulfilling the *resonance condition* which gives the name to this imaging technique.

3.2 Spins, precession, and magnetisation

Atomic nuclei with an odd number of protons and/or neutrons possess an intrinsic angular momentum \mathbf{j} called *spin*. The spin is a quantised property, meaning that it can only take on a discrete set of values. The number of possible values is given by $2j+1$, where j is the spin quantum number which is related to the magnitude of the (spin) angular momentum via

$$||\mathbf{j}||^2 = \hbar^2 j(j+1), \quad \text{with } j = 0, \frac{1}{2}, 1, \frac{3}{2}, \dots \quad (3.1)$$

where \hbar is Planck's constant divided by 2π [31]. For hydrogen atoms (protons), to which we restrict the theory, $j = 1/2$, indicating that when measured along a certain orientation they can only be pointing in either of 2 directions [32].

In classical mechanics, the spin can be interpreted as a rotation of the nucleus around its axis. Like any other charged spinning object, this will result in the creation of a (microscopic) magnetic field around the nucleus, which effectively acts like a tiny magnet, see Figure 3.1 panel A. The magnetic moment $\boldsymbol{\mu}$ of this magnet is directly proportional to the spin via a constant γ called gyromagnetic ratio:

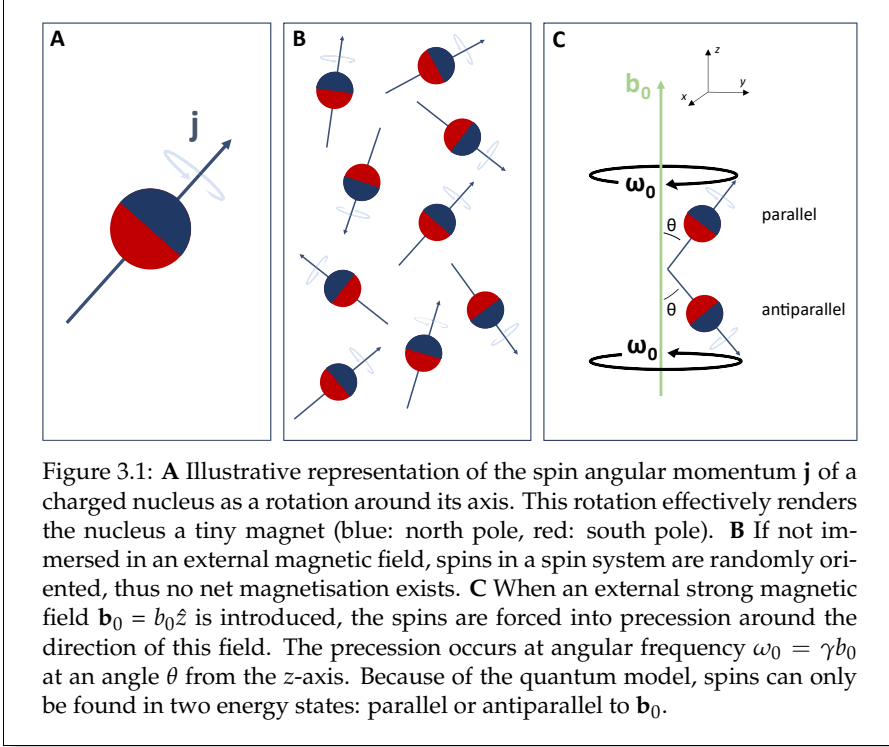
$$\boldsymbol{\mu} = \gamma \mathbf{j}. \quad (3.2)$$

For hydrogen, $\gamma = 2\pi \times 42.58 \frac{\text{rad} \cdot \text{MHz}}{\text{T}}$.

At equilibrium, the orientation of the spin's magnetic moment is completely random. This means that for a nuclear spin system, i.e. a collection of spins of the same type, no net magnetisation exists when an external magnetic field is not applied (see Figure 3.1 panel B). If the spins instead experience a strong magnetic field $\mathbf{b}_0 = b_0 \hat{z}$, they will be subject to a torque $\boldsymbol{\mu} \times \mathbf{b}_0$ which will make them precess around the direction of the field. A spin system immersed in a strong magnetic field is said to be magnetised. The angular velocity ω_0 at which the spins precess around \mathbf{b}_0 is known as the *Larmor frequency*, and, as it will be apparent later, is perhaps the single most important concept in MR:

$$\omega_0 = \gamma b_0. \quad (3.3)$$

Given the quantisation, each spin can only be found either pointing in a direction parallel (spin-up) or anti-parallel (spin-down) to \mathbf{b}_0 , at an angle $\theta = 54.44^\circ$ with respect to the external field orientation, see Figure 3.1 panel C.



According to quantum theory, the energy of interaction with the magnetic field, $E = -\boldsymbol{\mu} \cdot \mathbf{b}_0$, depends on the orientation of the spins. For spin-up, $E_\uparrow = -\frac{1}{2}\gamma\hbar b_0$, while for spin-down $E_\downarrow = \frac{1}{2}\gamma\hbar b_0$. It follows that spin-up is the lower energy state. The non-zero energy difference between the two states, $\Delta E = \gamma\hbar b_0$, is known as the *Zeeman splitting* phenomenon [32]. The number of spins in either state is related to this energy difference:

$$\frac{N_\uparrow}{N_\downarrow} = \exp\left(\frac{\Delta E}{k_B T_s}\right), \quad (3.4)$$

where k_B is the Boltzmann's constant, T_s is the absolute temperature of the spin system, and N_\uparrow and N_\downarrow indicate the total number of spins in the up and down states, respectively. To first approximation, the excess number of protons found in the spin-up state is:

$$N_\uparrow - N_\downarrow \approx \frac{\Delta E}{2k_B T_s} N, \quad (3.5)$$

where N is the total number of spins in the system. This difference is typically very small: for an experiment at $T_s = 310$ K in an MR system with $b_0 = 3$ T, there are only

20 excess spins per million protons. Nevertheless, a typical spin system in MR imaging comprises a number of protons in the order of 10^{20} , thus producing a detectable magnetisation \mathbf{m} :

$$\mathbf{m} = \sum_{n=1}^N \boldsymbol{\mu}_n = m_x \hat{x} + m_y \hat{y} + m_z \hat{z}. \quad (3.6)$$

The z-component of this magnetisation vector, m_z , is referred to as the *longitudinal magnetisation* as it lies in the direction of \mathbf{b}_0 , whereas the xy-component, m_{xy} , is referred to as the *transverse magnetisation*, as it lies on the plane orthogonal to the \mathbf{b}_0 field. At equilibrium (indicated with the superscript 0), \mathbf{m} is aligned in the direction of \mathbf{b}_0 : $\mathbf{m}^0 = m_z^0 \hat{z} = \|\mathbf{m}\| = (\gamma^2 \hbar^2 b_0 N) / (4k_B T_s)$, while $m_{xy}^0 = 0$ since the magnetic moments in the transverse plane have random orientations. Note how the magnetisation strength is directly proportional to the strength of the \mathbf{b}_0 field.

3.3 Excitation, resonance, and relaxation

To obtain a measurable response, the net magnetisation needs to be perturbed from its equilibrium state. This perturbation comes in the form of energy deposition into the spin system by means of an oscillating magnetic field, $\mathbf{b}_1(t)$, perpendicular to \mathbf{b}_0 . The energy carried by an electromagnetic wave of frequency ω_{rf} is $E_{rf} = \hbar \omega_{rf}$. According to the quantum model, to induce a spin system to change from one state to another, the deposited energy must match the difference in energy between the adjacent spin states. This is what is known as the *resonance condition*. From the previous section, $\Delta E = \gamma \hbar b_0$, and therefore, for the resonance condition to be satisfied, $\omega_{rf} = \gamma b_0 = \omega_0$. To summarise, the oscillation frequency of $\mathbf{b}_1(t)$ needs to match the Larmor frequency of the spin system in order for the net magnetisation to be perturbed. Given that for $b_0 \approx 1$ T the Larmor frequency for hydrogen spins is in the radio frequency range, and that the oscillating field is turned on for short periods of time, \mathbf{b}_1 is referred to as an RF pulse.

Under the resonance condition, and for the time τ during which the RF pulse is applied, the spin system will be forced into precession around the direction of \mathbf{b}_1 with precession frequency $\omega_1(t) = \gamma b_1(t)$. On a coordinate system rotating at Larmor frequency around the z-axis, this appears as a tilt of the magnetisation towards the xy-plane, see Figure 3.2 panel A. The angle of this tilt is called *flip angle* and is given by

$$\alpha = \int_0^\tau \omega_1(t) dt = \int_0^\tau \gamma b_1(t) dt. \quad (3.7)$$

An RF pulse is characterised in terms of the flip angle it produces and the direction along which it is applied. For example, a 90_x° RF pulse produces a flip angle of 90° and is applied along the x axis. In the remainder of the thesis, when stating the direction of application is not necessary, RF pulses will only be referred to by the flip angle they generate.

When the RF pulse is turned off, the spin system starts to return to its equilibrium state in a process called relaxation. The relaxation process is described by the phenomenological Bloch equations [33], and it differs for the longitudinal and the trans-

verse components of the magnetisation. In the $x'y'z'$ reference system rotating at the Larmor frequency:

$$\begin{cases} \frac{dm_{z'}}{dt} = -\frac{m_{z'} - m_z^0}{T_1}, \\ \frac{dm_{x'y'}}{dt} = -\frac{m_{x'y'}}{T_2}. \end{cases} \quad (3.8)$$

T_1 and T_2 are the characteristic relaxation times for the longitudinal and transverse magnetisations, respectively. Solution to 3.8 gives:

$$\begin{cases} m_{z'}(t) = m_z^0(1 - e^{-t/T_1}) + m_{z'}(0)e^{-t/T_1}, \\ m_{x'y'}(t) = m_{x'y'}(0)e^{-t/T_2}, \end{cases} \quad (3.9)$$

where $m_{z'}(0)$ and $m_{x'y'}(0)$ are the longitudinal and transverse magnetisation right after the application of the RF pulse.

The longitudinal relaxation describes the regrowth of the longitudinal magnetisation to its equilibrium state, and it is also known as *spin-lattice* relaxation since it mostly concerns the energy exchange between the spins and their surrounding. The transverse relaxation describes instead the loss of spin precession coherence, and thus the vanishing of the transverse magnetisation. It is also known as *spin-spin* relaxation, as the loss of phase coherence is due to changes in precessional frequencies caused by neighbouring nuclei. These two processes occur at two different scales, with $T_1 \geq T_2$. A basic source of contrast in MR images relies on selectively making the experiment more sensitive to either of these relaxation processes. Section 3.4 explains how these different sensitisations can be achieved.

The MR signal

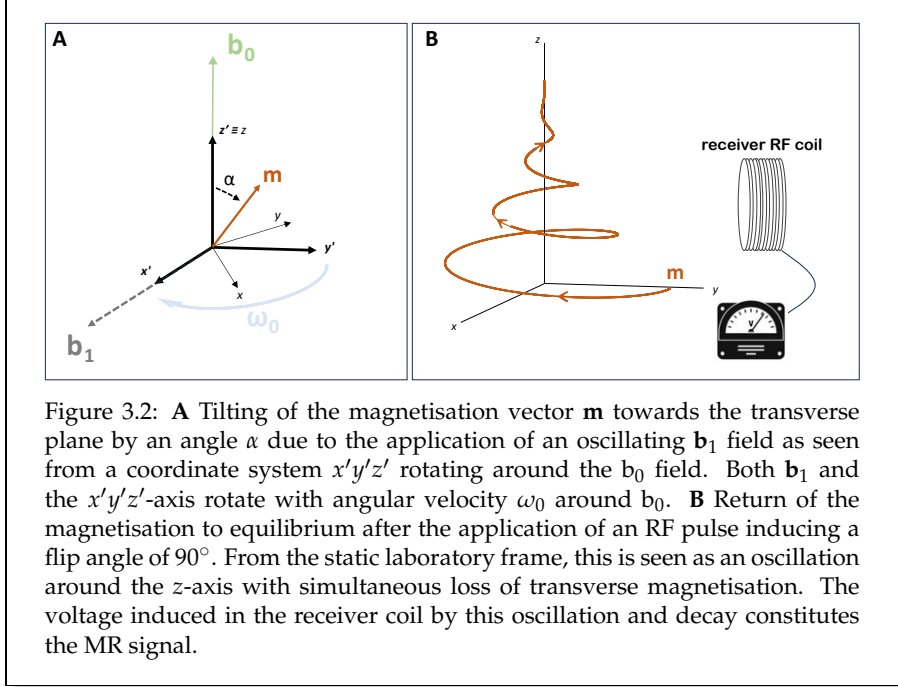
If viewed from the static reference system, the time evolution of the transverse magnetisation $m_{xy}(t) = m_{xy}(0)e^{-t/T_2}e^{-i\omega_0 t}$ combines the effects of the free precession around b_0 , and the transverse (T_2) relaxation, see Figure 3.2 panel **B**. This is what constitutes the detected MR signal. By Faraday's law of induction, the varying magnetic flux produced by the rotating and vanishing magnetisation will induce a voltage in the (receiving) RF coil. This voltage is proportional to the rate at which the magnetisation is decaying, which is determined by T_2 relaxation. Note that due to field inhomogeneities, the decay of the transverse magnetisation is typically faster than that implied by T_2 relaxation only. This is discussed in the next section.

For an object placed in the MR scanner, the detected signal comprises the contributions of all spins:

$$S(t) \propto \int_{\text{object}} m_{xy}(\mathbf{r}, 0) e^{-t/T_2(\mathbf{r})} e^{-i\omega(\mathbf{r})t} d\mathbf{r}, \quad (3.10)$$

where $\omega(\mathbf{r})$ is the free precession frequency accounting for spatial changes in the b_0 field, and the spatial dependence of T_2 is also taken into consideration. A signal obtained by recording the return to equilibrium of the magnetisation after the application of an RF pulse is called *free induction decay* (FID), and it constitutes the archetypal

MR signal. The quantity $m_{xy}(\mathbf{r}, 0)$ gives a measure of proton density of the scanned object.



3.4 Pulse sequences, spin-echo, and contrast

Due to field inhomogeneities, the observed magnetisation decay in an FID experiment occurs at a T_2^* rate which is typically faster than T_2 relaxation only. The effect of these macroscopic inhomogeneities on the MR signal can be compensated by clever sequences of RF pulses. In a phenomenon already discovered by Erwin Hahn in the 1950s [34], spins dephasing due to macroscopic field inhomogeneities can be brought back to coherence by means of refocusing RF pulses. This regain of phase coherence results in echoes. Echoes can be produced both by RF pulse sequences, or by employing magnetic field gradients. We will focus on the first case. At least two pulses are needed to generate RF-echoes, and the most common form of echo, the *spin-echo* (SE), is generated with only two RF excitations.

Before explaining how a SE is created, let us define the phase of a precessing spin. In the rotating coordinate system, a spin precessing with angular velocity $\omega(t')$ around the z -axis travels a distance $\phi(t) = \phi_0 + \int_{t_0}^{t_0+t} \omega(t') dt'$ during a time t , for some initial position ϕ_0 . $\phi(t)$ defines the phase of the spin. This quantity is ubiquitous in MRI as the effect of different processes acting on the magnetisation can be understood by considering the phase distribution evolution of the spin system.

Figure 3.3 shows how a spin-echo is obtained. The first RF pulse excites the magnetisation onto the transverse plane. As spins experience different local magnetic fields, they will begin to precess at different frequencies, thus progressively getting out of phase. After a time τ , the spin system is excited again with a second RF pulse. The second pulse is designed to achieve a flip angle of 180° , which effectively flips the precessing spins onto the other side of the transverse plane. Assuming that the spins will continue their precessions with the same angular frequency and orientation as before the application of the second pulse, they will start to regain phase coherence thus regrowing the transverse magnetisation. After another time interval τ , the regaining of phase coherence results in the echo. Differently from the FID, this signal carries only the effects of T_2 relaxation: since the same macroscopic inhomogeneities that brought the spins out of phase also made them regain coherence, their effect on the magnetisation has been nulled. The time at which the echo occurs, $T = 2\tau$, takes the name of *time of echo* or *echo time*, T_E . This is a parameter that can be controlled by the MR scanner operator.

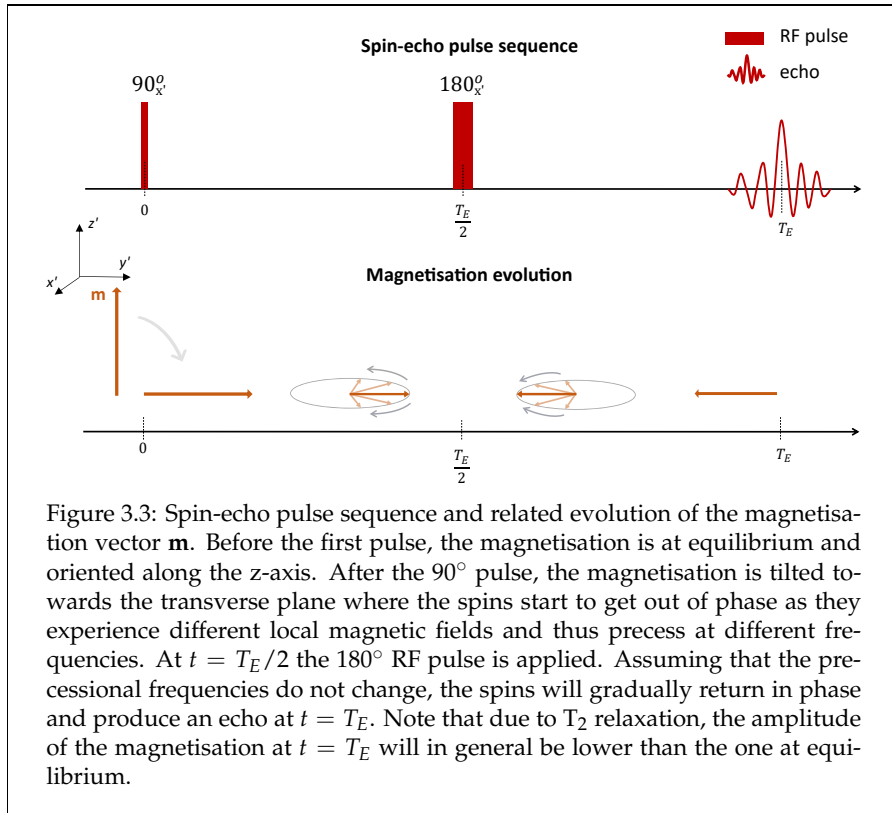


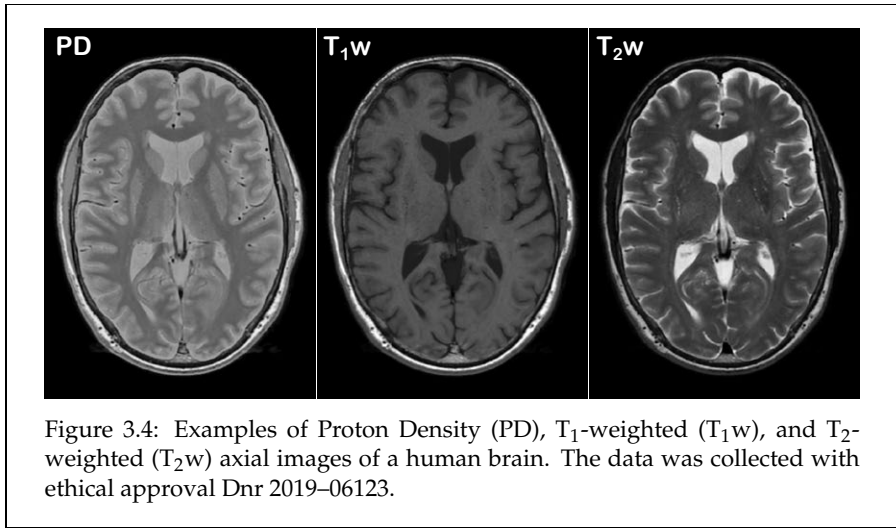
Figure 3.3: Spin-echo pulse sequence and related evolution of the magnetisation vector \mathbf{m} . Before the first pulse, the magnetisation is at equilibrium and oriented along the z -axis. After the 90° pulse, the magnetisation is tilted towards the transverse plane where the spins start to get out of phase as they experience different local magnetic fields and thus precess at different frequencies. At $t = T_E/2$ the 180° RF pulse is applied. Assuming that the precessional frequencies do not change, the spins will gradually return in phase and produce an echo at $t = T_E$. Note that due to T_2 relaxation, the amplitude of the magnetisation at $t = T_E$ will in general be lower than the one at equilibrium.

The spin-echo experiment is typically repeated several times to, for example, allow for a complete acquisition of an image, boost the SNR with averaged acquisitions, or allow the magnetisation to reach steady state before acquiring the data. The time separation between experiments is called *repetition time* T_R , and it is also a parameter that

can be controlled. The dependence of the longitudinal and transverse magnetisations on T_E and T_R at steady state is given by:

$$\begin{cases} m_z = m_z^0(1 - e^{-T_R/T_1}), \\ m_{x'y'} = m_z^0(1 - e^{-T_R/T_1})e^{-T_E/T_2}. \end{cases} \quad (3.11)$$

It follows that T_E is connected to the T_2 decay, while T_R is related to T_1 relaxation. Although the MR signal will always carry contributions from both relaxation processes, by tuning T_E and T_R the experiment can be made more sensitive to either. In MR imaging, there are three primary contrast mechanisms: proton density (PD), T_1 -weighting (T_1w), and T_2 -weighting (T_2w). In PD experiments, both relaxation effects are minimised. This is achieved by employing short T_E and long T_R . In T_1w experiments, the effect of longitudinal relaxation is enhanced; this is obtained by minimising the echo time, and thus the contribution of T_2 relaxation. Conversely, in T_2w experiments the contrast introduced by T_1 relaxation is minimised by employing a long T_R . In practice, PD is rarely used as it provides little contrasts between different tissues. T_1w and T_2w images are instead widely employed to detect and characterise different diseases. Examples of PD, T_1w , and T_2w brain images are shown in Figure 3.4.



3.5 Gradients, spatial localisation, and imaging

The MR signal presented in the previous section encompasses contributions from all the spins in the scanned object irrespective of their location, and can therefore not be used to create an image. Imaging a 3-dimensional object with MR is typically done by acquiring a series of 2-dimensional images. Each image is obtained from a certain slice of the object. A technique called *slice selection* is employed to select

the slice. The spins' positions in the other two dimensions can then be determined via *spatial encoding*, typically combining *phase-encoding* and *frequency-encoding*. All these methods rely on the use of time-varying magnetic fields generated by gradient coils. These coils are designed to produce linearly varying magnetic fields in space, $b(\mathbf{r}, t) = \mathbf{r} \cdot \mathbf{g}(t)$, where $\mathbf{g}(t)$ is the magnetic field gradient. Their purpose is to make the Larmor frequency of the spins space-dependent:

$$\omega(\mathbf{r}) = \gamma(b_0 + \mathbf{g}(t) \cdot \mathbf{r}), \quad (3.12)$$

so that the position can be encoded in the collected MR signal.

In *slice selection*, a gradient is applied simultaneously to an RF pulse to selectively excite only a slab of spins precessing at a specific frequency.

In *frequency encoding*, a gradient is applied during the read-out of the signal to make the precession frequency linearly dependent along a certain direction \mathbf{r}_{fe} . Let's call this gradient \mathbf{g}_{fe} . Omitting the factor e^{-t/T_2} and denoting the spin density $\rho(\mathbf{r}) = m_{xy}(\mathbf{r}, 0)$ in 3.10, the recorded signal from all spins in the excited slab can be written as:

$$\begin{aligned} S(t) &\propto \int_{\text{slab}} \rho(\mathbf{r}) e^{-i\omega(\mathbf{r})t} d\mathbf{r} = \int_{\text{slab}} \rho(\mathbf{r}) e^{-i\gamma(b_0 + \mathbf{g}_{fe} \cdot \mathbf{r})t} d\mathbf{r} \\ &= e^{-i\omega_0 t} \int_{\text{slab}} \rho(\mathbf{r}) e^{-i\gamma \mathbf{g}_{fe} \cdot \mathbf{r} t} d\mathbf{r}. \end{aligned} \quad (3.13)$$

In *phase encoding*, a gradient \mathbf{g}_{pe} is applied for a certain time T_{pe} prior signal read-out to impart different phase shifts to the spins depending on their location. A spin located at position \mathbf{r} will accumulate a phase $\phi(\mathbf{r}) = \gamma(b_0 + \mathbf{g}_{pe} \cdot \mathbf{r})T_{pe}$ during the time the gradient is applied. The resulting signal will be

$$S(\mathbf{g}_{pe}) \propto e^{-i\omega_0 t} \int_{\text{slab}} \rho(\mathbf{r}) e^{-i\gamma \mathbf{g}_{pe} \cdot \mathbf{r} T_{pe}} d\mathbf{r}, \quad (3.14)$$

which can be interpreted as a non-encoded signal with an initial position-dependent phase angle. In both 3.13 and 3.14, the carrier frequency $e^{-i\omega_0 t}$ will be removed by demodulating the signal. Note that while in the *frequency encoding* direction the signal is sampled as a function of time, to resolve the spins' positions along the *phase encoding* direction the measurement needs to be repeated by varying the strength of \mathbf{g}_{pe} .

By applying each encoding along two orthogonal axes on the slab, we obtain a signal from which the image of the spin density can be recovered via 2D inverse Fourier Transform. This is better seen via the so-called k-space formalism.

k-space

By introducing the variable

$$\mathbf{k}(t) = \frac{\gamma}{2\pi} \int_0^t \mathbf{g}(t') dt', \quad (3.15)$$

3. MAGNETIC RESONANCE IMAGING

the evolution of a spin's phase under the influence of a time-varying magnetic field can be written as:

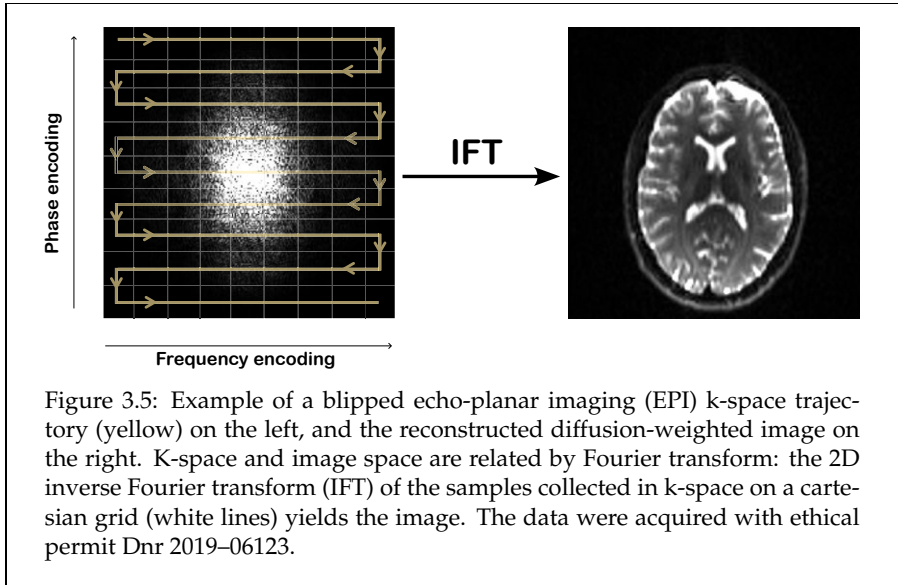
$$\phi(\mathbf{r}, t) = \gamma \int_0^t \mathbf{g}(t') \cdot \mathbf{r} dt' = 2\pi \mathbf{k}(t) \cdot \mathbf{r}. \quad (3.16)$$

The MR signal can in general then be written as

$$S(\mathbf{k}) \propto \int_{\text{slab}} \rho(\mathbf{r}) e^{-i2\pi \mathbf{k}(t) \cdot \mathbf{r}} d\mathbf{r}, \quad (3.17)$$

which shows that the registered MR signal is proportional to the Fourier transform of the spin density. The MR signal is thus sampled at discrete points in the space of spatial frequencies, called in MRI *k-space*. These points are collected along trajectories achieved by spatial encoding. Figure 3.5 shows an example trajectory widely used in diffusion MRI called Echo-Planar Imaging (EPI), and the corresponding reconstructed image. In phase encoding, the *k*-space coordinate is set by the time of acquisition: $k_{pe} = \gamma g_{pe} T_{pe}$; traversing of *k*-space along the *pe*-direction corresponds to jumps defined by g_{pe} and T_{pe} . In frequency encoding, *k*-space is traversed during read-out along a linear trajectory described by Equation 3.15.

The 3-dimensional image is thus obtained via a 2-dimensional inverse Fourier transform of the sampled *k*-space for each slice. The reconstructed image is composed of voxels, the 3-dimensional equivalent of a pixel in 2D images. Typical voxel sizes for T_1w and T_2w images are in the order of $0.5 \times 0.5 \times 0.5 \text{ mm}^3$, while diffusion-weighted images (DWIs) tends to have larger voxels in the order of $2 \times 2 \times 2 \text{ mm}^3$.



4

Diffusion Magnetic Resonance Imaging

Diffusion MRI (dMRI) is a powerful probe of the tissue microstructure; It relies on the random motion of water molecules to probe structural and physiological tissue features at scales not otherwise accessible via direct MR imaging. In this chapter, the basics of diffusion and diffusion MRI are introduced as well as relevant representations for the diffusion-weighted MR signal.

4.1 Diffusion

Diffusion relates to mass transport occurring in the absence of bulk motion [35]. When considering ensembles of particles, diffusion arises due to gradients in particle concentration thus inducing a flux from high concentration to low concentration areas. This flux is described by Fick's first law:

$$\mathbf{j} = -D\nabla C(\mathbf{r}, t), \quad (4.1)$$

where \mathbf{j} is the flux, C is the particle concentration, and D is the diffusion coefficient. D is an intrinsic property of the medium depending on its temperature T , viscosity η , and size. For a spherical particle of radius R ,

$$D = \frac{k_B T}{6\pi\eta R}. \quad (4.2)$$

Fick's second law, also known as the *diffusion equation*, stems from the law of mass conservation. This requires that a change in concentration is accompanied by a change in flux: $\partial C(\mathbf{r}, t) / \partial t + \nabla \cdot \mathbf{j} = 0$, leading to

$$\frac{\partial C(\mathbf{r}, t)}{\partial t} = D\nabla^2 C(\mathbf{r}, t). \quad (4.3)$$

At the molecular level, diffusive processes arise instead due to particle collisions and mechanical motion which are attributed to thermal energy only, without requiring

any gradient in concentration. This is what is referred to as Brownian motion since this phenomenon was first observed by botanist Robert Brown. In 1905, Albert Einstein described diffusive processes in terms of the probability of particle displacement [36], by introducing the conditional probability of a particle to move from a position \mathbf{r}_0 to a position \mathbf{r}_1 during a time Δ , $\mathcal{P}(\mathbf{r}_1, \Delta | \mathbf{r}_0)$. This quantity, known as the *diffusion propagator*, allows the treatment of Brownian motions as stochastic processes [37].

The diffusion propagator obeys Fick's laws, which can therefore describe changes in concentration in terms of this conditional probability:

$$\frac{\partial}{\partial t} \mathcal{P}(\mathbf{r}_1, \Delta | \mathbf{r}_0) = D \nabla^2 \mathcal{P}(\mathbf{r}_1, \Delta | \mathbf{r}_0). \quad (4.4)$$

For $\Delta \rightarrow \infty$, the solution to this differential equation for free and homogeneous diffusion with initial condition $\mathcal{P}(\mathbf{r}_1, 0 | \mathbf{r}_0) = \delta(\mathbf{r}_1 - \mathbf{r}_0)$ is the Gaussian

$$\mathcal{P}(\mathbf{r}_1, \Delta | \mathbf{r}_0) = \frac{1}{(4\pi D \Delta)^{3/2}} \exp\left(-\frac{(\mathbf{r}_1 - \mathbf{r}_0)^2}{4D\Delta}\right). \quad (4.5)$$

The mean squared displacement $\langle (\mathbf{r}_1 - \mathbf{r}_0)^2 \rangle$, which tells on average how far particles have moved from their initial position during a certain time (here taken to be Δ), is computed from 4.5 as:

$$\langle (\mathbf{r}_1 - \mathbf{r}_0)^2 \rangle = \int_{\mathcal{R}^3} (\mathbf{r}_1 - \mathbf{r}_0)^2 \mathcal{P}(\mathbf{r}_1, \Delta | \mathbf{r}_0) d\mathbf{r}_1 = 6D\Delta. \quad (4.6)$$

Equation 4.6 is known as Einstein's equation for diffusion, and highlights that (for unbounded homogeneous motion) the squared distance between the initial and "final" positions of the particles grows linearly with time via the diffusion coefficient.

For particles diffusing in one dimension, $\langle (r_1 - r_0)^2 \rangle = 2D\Delta$, and the diffusion coefficient can be defined as

$$D = \frac{1}{2} \frac{\langle (r_1 - r_0)^2 \rangle}{\Delta}. \quad (4.7)$$

Figure 4.1 shows particles' displacement distributions for different diffusion times and different diffusion coefficients for 1-dimensional free diffusion.

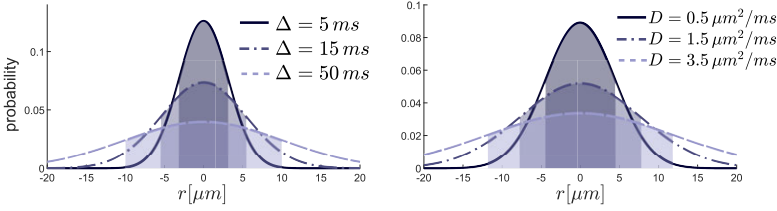


Figure 4.1: One-dimensional Gaussian distributions of particles displacement for increasing diffusion time and fixed diffusion coefficient $D = 1 \mu\text{m}^2/\text{ms}$ (left), and different diffusion coefficients and fixed diffusion time $\Delta = 20 \text{ ms}$ (right). The distributions are given by equation 4.5. The shaded area under each curve represents the portion of the distribution bounded within $[-\sqrt{2D\Delta}, +\sqrt{2D\Delta}]$, i.e. between the negative and positive standard deviation of the stochastic variable representing the net displacement. Note how for longer diffusion times, the particles move further from their initial position. The same occurs for increasing values of the diffusion coefficient.

The diffusion tensor

The results presented so far can be generalised to the case of free anisotropic diffusion, when the motion of water particles cannot be accurately described by a single scalar value D . In this case, the particles flux in any direction can be represented by a symmetric second-order tensor known as the diffusion tensor \mathbf{D} . This tensor represents the covariance matrix of the 3-dimensional (Gaussian) distribution of particles' displacement. Defining x, y , and z as the particles' displacement along three orthogonal directions, the diffusion tensor is [38]:

$$\mathbf{D} = \frac{1}{2\Delta} \begin{pmatrix} \langle x^2 \rangle & \langle xy \rangle & \langle xz \rangle \\ \langle yx \rangle & \langle y^2 \rangle & \langle yz \rangle \\ \langle zx \rangle & \langle zy \rangle & \langle z^2 \rangle \end{pmatrix}, \quad (4.8)$$

where each element is

$$D_{ij} = \frac{1}{2} \frac{\langle (r_1 - r_0)_i (r_1 - r_0)_j \rangle}{\Delta}. \quad (4.9)$$

Since it represents a covariance, the diffusion tensor is positive semi-definite. The symmetry implies that $D_{ij} = D_{ji}$, so only six elements of the tensor are unique. The symmetry and positive semi-definiteness also imply that the matrix \mathbf{D} representing the tensor can be diagonalised, and that the diagonal entries are non-negative: $\mathbf{D} = \mathbf{T}^\top \mathbf{\Lambda} \mathbf{T}$, where the matrix \mathbf{T} contains the eigenvectors on the columns, $\mathbf{T} = [\mathbf{e}_1 | \mathbf{e}_2 | \mathbf{e}_3]$,

and the diagonal matrix $\mathbf{\Lambda}$ contains the eigenvalues, $\mathbf{\Lambda} = \begin{pmatrix} \lambda_1 & 0 & 0 \\ 0 & \lambda_2 & 0 \\ 0 & 0 & \lambda_3 \end{pmatrix}$, with $\lambda_i \geq 0$.

0. With this representation, the diffusion tensor is often displayed as an ellipsoid with semi-axes equal to the square root of the eigenvalues, and with the orientation given by the associated eigenvectors. Figure 4.2 panel A shows a general diffusion

tensor ellipsoid, while panel **B** shows particles' displacements and the corresponding diffusion tensor ellipsoid for isotropic and anisotropic diffusion.

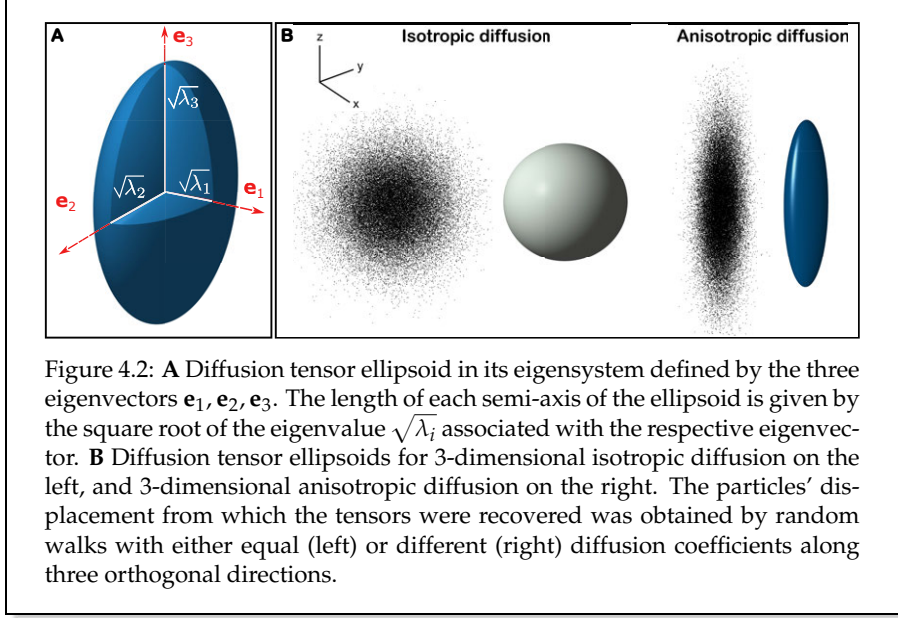


Figure 4.2: **A** Diffusion tensor ellipsoid in its eigensystem defined by the three eigenvectors \mathbf{e}_1 , \mathbf{e}_2 , \mathbf{e}_3 . The length of each semi-axis of the ellipsoid is given by the square root of the eigenvalue $\sqrt{\lambda_i}$ associated with the respective eigenvector. **B** Diffusion tensor ellipsoids for 3-dimensional isotropic diffusion on the left, and 3-dimensional anisotropic diffusion on the right. The particles' displacement from which the tensors were recovered was obtained by random walks with either equal (left) or different (right) diffusion coefficients along three orthogonal directions.

4.2 Diffusion and MR

The Bloch-Torrey equation

The mathematical framework describing the evolution of the magnetisation for an MR experiment under relaxation and isotropic diffusion processes is given by the Bloch-Torrey equations [39]. For the transverse local magnetisation $m_{xy}(\mathbf{r}, t)$:

$$\frac{\partial m_{xy}(\mathbf{r}, t)}{\partial t} = \left[\nabla \cdot D \nabla - i\omega(\mathbf{r}, t) - \frac{1}{T_2} \right] m_{xy}(\mathbf{r}, t), \quad (4.10)$$

where ω is the space and time-dependent Larmor frequency for spins in an inhomogeneous magnetic field oriented along the direction of \mathbf{b}_0 , $b_0 \hat{\mathbf{z}} = b_0 + \mathbf{g}(t) \cdot \mathbf{r}$. The gradient $\mathbf{g}(t)$ can take any form, though it is assumed that for experiments involving some sort of echo signal, $\int_0^{T_E} \mathbf{g}(t') dt' = 0$. This requirement is known as the *refocusing* or *rephasing condition*.

Solving 4.10 with appropriate boundary and initial conditions would give the measured MR signal for a voxel:

$$S(t) = \int m_{xy}(\mathbf{r}, t) d\mathbf{r}. \quad (4.11)$$

The only available analytical solution to the Bloch-Torrey equation in the case of general $\mathbf{g}(t)$ exists for the case of free and homogeneous diffusion, for which (discarding

the free precession phase component):

$$S = S_0 e^{-bD}, \quad (4.12)$$

where S_0 is the macroscopic signal obtained without an applied $\mathbf{g}(t)$, i.e. due to relaxation processes only, and the exponential term captures the decay introduced by the diffusion process. Generalisation to anisotropic multidimensional diffusion leads to

$$S = S_0 e^{-\mathbf{B}:\mathbf{D}}. \quad (4.13)$$

b is commonly referred to as the *b-value*, and it is given by

$$b = \text{Tr}(\mathbf{B}) \quad \text{with} \quad \mathbf{B} = \int_0^{T_E} \mathbf{q}(t) \mathbf{q}^T(t) dt, \quad (4.14)$$

where \mathbf{B} is the measurement B-tensor and $\mathbf{q}(t) = -\gamma \int_0^t \mathbf{g}(t') dt'$ is the *dephasing vector*. In a diffusion MR experiment, the b-value controls the level of sensitivity to the diffusion process. For increasing values of b and a fixed diffusion coefficient, the MR signal will be more diffusion-attenuated. Examples of diffusion-weighted MR images acquired with different b-values are shown in Figure 4.3.

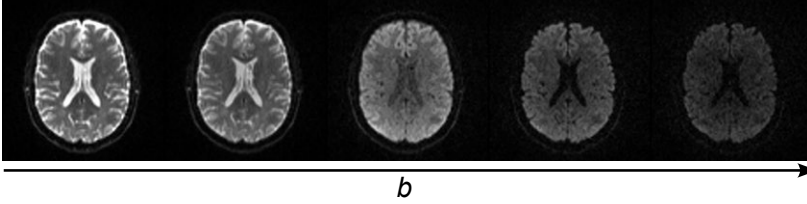


Figure 4.3: Diffusion-weighted MR images for increasing diffusion weighting as quantified by the b-value. As b increases, more of the signal is attenuated, as a manifestation of the magnetisation decay induced by the diffusion process. This attenuation naturally results in a lower signal-to-noise ratio as b increases.

The probabilistic interpretation

An alternative way of looking at the MR signal for diffusing particles without resorting to the Bloch-Torrey equation is by considering the effects of the gradient $\mathbf{g}(t)$ on the spins' phase [40]. Omitting the contribution of free precession, the phase of a spin following a trajectory $\mathbf{r}(t)$ is:

$$\phi(\mathbf{r}, T) = \gamma \int_0^T \mathbf{g}(t) \cdot \mathbf{r}(t) dt. \quad (4.15)$$

The accrued phase at time T will depend on the initial position and the random trajectory followed by the spin up to that point. For the local magnetisation $m_{xy}(\mathbf{r}, t)$,

the decay induced by the diffusion process would be given by the average phase dispersion for all the trajectories ending at position \mathbf{r} at time T :

$$m_{xy}(\mathbf{r}, t) = \rho(\mathbf{r}) \left\langle e^{-i\gamma \int_0^T \mathbf{g}(t) \cdot \mathbf{r}(t) dt} \right\rangle = \rho(\mathbf{r}) \left\langle e^{-i\phi(\mathbf{r}, T)} \right\rangle. \quad (4.16)$$

In the absence of local T_1 and T_2 relaxations, the macroscopic signal would then depend on the macroscopic T_2 relaxation, and on the average over the phases accrued by all spins in the voxel:

$$S(t) = e^{-t/T_2} \int m_{xy}(\mathbf{r}, t) d\mathbf{r} = S_0 \left\langle e^{-i\phi(T)} \right\rangle. \quad (4.17)$$

Dropping the dependence on \mathbf{r} and T , this expression can also be written in terms of the spins' phase distribution function $\mathcal{P}(\phi)$ [41]:

$$S(t) = S_0 \int_{-\infty}^{\infty} \mathcal{P}(\phi) e^{-i\phi} d\phi. \quad (4.18)$$

If diffusion is free and homogeneous, $\mathcal{P}(\phi)$ is Gaussian, and Equation 4.18 reduces to:

$$S(t) = S_0 \exp\left(-\frac{1}{2} \langle \phi^2(T) \rangle\right), \quad (4.19)$$

from which one recovers 4.12 [41]. Expressions like 4.17 and 4.18 are ubiquitous in diffusion MRI, and will appear again later on in this and the next chapter.

4.3 Measuring diffusion with MR

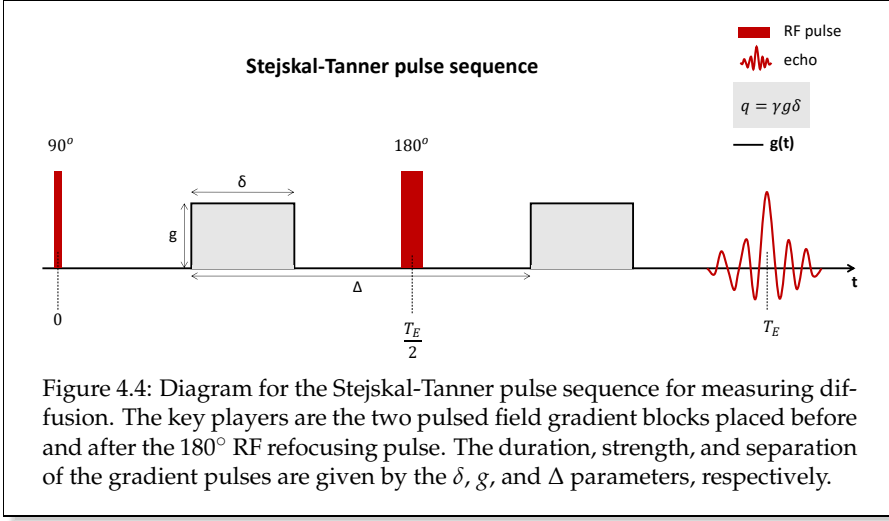
Diffusion MR experiments are performed by controlling the gradient $\mathbf{g}(t)$ strength temporal profile. By doing so, the MR signal can be sensitised to different aspects of the diffusion process. The material presented in this section deals with one particular pulsed-gradient spin-echo (PGSE) experiment which is still the most employed method for measuring diffusion. In the next chapter, the focus is placed instead on diffusion measurements performed with general time-varying magnetic fields.

The Stejskal-Tanner experiment

Although introduced almost 60 years ago, the Stejskal-Tanner spin-echo experiment is still the workhorse for most diffusion MRI experiments. A variation of the PGSE sequence is depicted in Figure 4.4. It involves two rectangular gradient pulses of duration δ before and after the 180° refocusing pulse, separated by a time $\Delta - \delta$. This separation is referred to as the *diffusion time*. The b-value for this sequence is obtained by inserting the gradient profile into 4.14, which gives:

$$b = \gamma^2 g^2 \delta^2 (\Delta - \delta/3), \quad (4.20)$$

where $g = \|\mathbf{g}\|$.



The narrow-pulse approximation and q-space

The success of the Stejskal-Tanner sequence is due to the fact that when δ is very short, diffusion during the application of the gradient pulses can be neglected. This is known as the *narrow-pulse approximation*. The idea is that the first gradient pulse will impart a phase shift on each spin depending on their position which will be reverted by the second gradient pulse if the spin does not move during the diffusion time. Conversely, if the spin changes location in between the gradient pulses, it will accumulate a net phase shift based only on the magnetic field experienced at its initial and final positions.

Even though the narrow pulse condition is rarely realised in practice, it offers a theoretical framework under which the solution to the Bloch-Torrey equation can be found for diffusion processes other than the free and homogeneous case. The MR signal attenuation due to diffusion processes only, $E(\mathbf{q})$, is given by [9]:

$$E(\mathbf{q}) = \int \rho(\mathbf{r}_0) \int \mathcal{P}(\mathbf{r}_1, \Delta | \mathbf{r}_0) e^{-i\mathbf{q} \cdot (\mathbf{r}_1 - \mathbf{r}_0)} d\mathbf{r}_1 d\mathbf{r}_0, \quad (4.21)$$

where $\rho(\mathbf{r}_0)$ is the spin density at \mathbf{r}_0 , and $\mathbf{q} = \gamma \mathbf{g} \delta$. By introducing the ensemble averaged propagator (EAP) $\mathcal{P}(\mathbf{r}, \Delta) = \int \rho(\mathbf{r}_0) \mathcal{P}(\mathbf{r}_0 + \mathbf{r}, \Delta | \mathbf{r}_0) d\mathbf{r}_0$, where $\mathbf{r} = \mathbf{r}_1 - \mathbf{r}_0$ is the net displacement variable, equation 4.21 can be rewritten as

$$E(\mathbf{q}) = \int \mathcal{P}(\mathbf{r}, \Delta) e^{-i\mathbf{q} \cdot \mathbf{r}} d\mathbf{r}. \quad (4.22)$$

Equation 4.22 relates the MR signal to the EAP via Fourier transform. Similarly to what is done for MR imaging, where the signal is sampled in k-space, the MR signal decay due to diffusion is sampled in q-space [42]. In the small q regime, only the bulk content of the diffusion process is accessed, whereas the high q regime contains the fine details. Recovering the EAP by inverse Fourier transform of $E(\mathbf{q})$, and thus

obtaining an image of displacements, is called *q-space MRI* [43], [44]. However, due to the high number of samples required for the inversion, this technique is almost never feasible in practice.

Long pulses: centre of mass propagator

As the duration δ of the gradients in the Stejskal-Tanner sequence is prolonged, the narrow-pulse approximation becomes invalid. Mitra and Halperin [45] showed that for finite-pulse widths, the diffusion MR signal is described by a centre-of-mass propagator rather than a diffusion propagator [46]. This propagator describes the probability that a trajectory having a certain centre of mass during the first gradient pulse ends up having a trajectory with another centre of mass during the second gradient pulse. By inserting the $\mathbf{g}(t)$ for the Stejskal-Tanner sequence into Equation 4.15 one obtains:

$$\begin{aligned}\phi(\mathbf{r}, \Delta + \delta) &= \gamma \mathbf{g} \cdot \left(\int_0^\delta \mathbf{r}(t) dt - \int_\Delta^{\Delta+\delta} \mathbf{r}(t) dt \right) \\ &= \mathbf{q} \cdot \left(\frac{1}{\delta} \int_0^\delta \mathbf{r}(t) dt - \frac{1}{\delta} \int_\Delta^{\Delta+\delta} \mathbf{r}(t) dt \right),\end{aligned}\tag{4.23}$$

where $\mathbf{q} = \gamma \mathbf{g} \delta$. The quantity $\mathbf{r}_{\text{COM}}^\delta(\tau) = \frac{1}{\delta} \int_\tau^{\tau+\delta} \mathbf{r}(t) dt$ is the centre-of-mass (COM) for a trajectory of duration δ . The MR signal decay due to diffusion is then given by:

$$E(\mathbf{q}) = \left\langle e^{-i\mathbf{q} \cdot [\mathbf{r}_{\text{COM}}^\delta(0) - \mathbf{r}_{\text{COM}}^\delta(\Delta)]} \right\rangle,\tag{4.24}$$

where the average is taken over all the spins' trajectories.

Diffusion Tensor Imaging

If diffusion is free and homogeneous, the diffusion propagator is Gaussian, and the signal measured with the Stejskal-Tanner pulse sequence reduces to

$$S = S_0 e^{-b \mathbf{n}^\top \mathbf{D} \mathbf{n}},\tag{4.25}$$

where b is the b-value given in Equation 4.20 and \mathbf{n} is the vector giving the direction of the diffusion measuring gradient $\mathbf{g} = \|\mathbf{g}\| \mathbf{n}$. The diffusion tensor \mathbf{D} and the non-diffusion-weighted signal S_0 can be estimated by collecting data with diffusion-sensitive gradients applied along at least six non-collinear directions and one measurement without diffusion weighting [10]. From the estimated diffusion tensor, rotational invariants can be obtained from the eigenvalues of \mathbf{D} . These quantities do not depend on the orientation of the laboratory frame in which the tensor is measured. Commonly employed ones are the mean diffusivity (MD), axial diffusivity (AD), radial diffusivity (RD), and fractional anisotropy (FA):

$$\text{MD} = (\lambda_1 + \lambda_2 + \lambda_3)/3\tag{4.26}$$

$$\text{AD} = \lambda_3\tag{4.27}$$

$$\text{RD} = (\lambda_1 + \lambda_2)/2\tag{4.28}$$

$$\text{FA} = \frac{\sqrt{(\lambda_1 - \lambda_2)^2 + (\lambda_1 - \lambda_3)^2 + (\lambda_2 - \lambda_3)^2}}{\sqrt{2(\lambda_1^2 + \lambda_2^2 + \lambda_3^2)}}, \quad (4.29)$$

where it is assumed that $\lambda_3 \geq \lambda_2 \geq \lambda_1$. Maps of fractional anisotropy can be color-coded using a red-green-blue (RGB) scheme according to the direction given by the eigenvector associated with the main eigenvalue, \mathbf{e}_3 . These images are referred to as direction-encoded fractional anisotropy (DEC-FA) maps. In brain imaging, blue encodes for the superior-inferior direction, green for the anterior-posterior direction, and red for the left-right direction. Example maps of MD, AD, RD, FA, and DEC-FA for a human brain are shown in Figure 4.5.

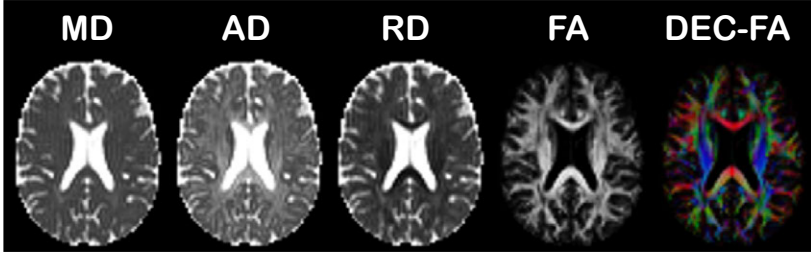


Figure 4.5: Example of scalar invariants obtained from the diffusion tensor: mean diffusivity (MD), axial diffusivity (AD), radial diffusivity (RD), fractional anisotropy (FA), and direction-encoded fractional anisotropy (DEC-FA). MD gives an average measure of diffusivity, whereas AD and RD quantify the diffusivity along the main tensor axis and the directions orthogonal to it, respectively. FA quantifies the variance between the tensor's eigenvalues which expresses its anisotropy. With respect to brain imaging, this quantity is often high along the main neural tracts connecting different areas of the brain, with the orientation of the tracts given by the DEC-FA (blue for the superior-inferior direction, green for the anterior-posterior direction, and red for the left-right direction).

The apparent diffusion coefficient and apparent diffusion tensor

When diffusion is not free, the spins' phase distribution considered in 4.18 is in general not of Gaussian form, and the diffusion process cannot be accurately described via the diffusion coefficient or the diffusion tensor [47]. This happens, for example, when particles encounter barriers such as cell membranes, or are diffusing in a tortuous intra-cellular space, see Figure 4.6. For small diffusion weighting gradients, diffusion can still be considered Gaussian though slowed down. This slowdown is often represented with an *apparent diffusion coefficient* (ADC) or *apparent diffusion tensor* (\mathbf{D}_{app}).

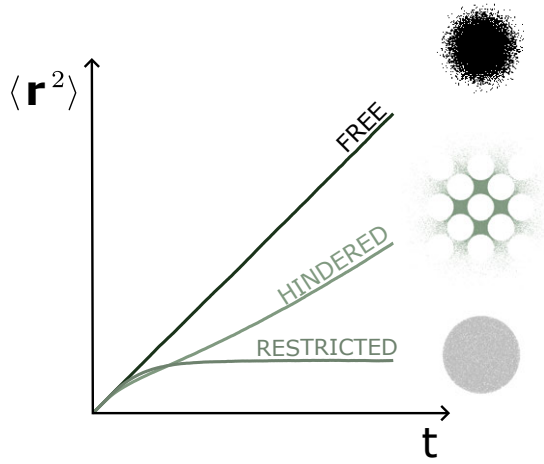


Figure 4.6: Mean squared displacement $\langle \mathbf{r}^2 \rangle$ for free, hindered, and restricted diffusion as a function of time. For free diffusion, the slope of the curve corresponds to the diffusion coefficient, and it is time-independent. For hindered and restricted diffusion, the slope is also a straight line for short diffusion times (before the particles can experience hindrances/restrictions), and then deviates from this behaviour. For hindered diffusion, the dependence appears linear at long times though with a reduced diffusion coefficient. For restricted diffusion, the mean squared displacement reaches a plateau given by the restriction size, and the diffusion coefficient appears to be 0.

A formal explanation can be given by considering the cumulant expansion of the exponential factor in equation 4.17 up to the fourth order:

$$\ln(S(t)/S_0) \approx -\frac{1}{2}c_2 + \frac{1}{24}c_4, \quad (4.30)$$

where the odd terms vanish due to the refocusing condition [48]. The coefficients for the two cumulants are

$$c_2 = \langle \phi(T)^2 \rangle \quad (4.31)$$

and

$$c_4 = \langle \phi(T)^4 \rangle - 3\langle \phi(T)^2 \rangle^2, \quad (4.32)$$

respectively [48], [49]. For $g \rightarrow 0$, the quadratic term dominates the series. This regime is what is referred to as the *Gaussian Phase Approximation* (GPA). Under the GPA, all terms higher than the quadratic one are neglected, and the signal is given by:

$$S(t) \approx S_0 \exp\left(-\frac{1}{2}\langle \phi^2(T) \rangle\right). \quad (4.33)$$

This Gaussian distribution of the spins' phase can be captured by an apparent diffusion coefficient:

$$S(t) = S_0 e^{-b \text{ADC}}. \quad (4.34)$$

Note that contrary to the diffusion coefficient D , the ADC is influenced by the geometry of the medium and by the parameters of the experiment (such as the orientation of the diffusion measurement and the diffusion time). It is thus not an intrinsic property of the tissue.

For free diffusion, the phase distribution is Gaussian, and the terms higher than the quadratic one disappear, so that the relation in 4.34 is correct (and analogous to Equation 4.19). To simplify the notation, in the remainder of this thesis the distinction between ADC and D (and between \mathbf{D} and \mathbf{D}_{app}) is neglected.

Diffusional Kurtosis

As the gradient strength increases, the contribution of the higher order terms in 4.30 cannot be neglected when diffusion is not free; this is typically seen as a deviation from a straight line when plotting $\ln(S(t)/S_0)$ as a function of b , see Figure 4.7.

Inclusion of the fourth order cumulant in the signal expression gives the *kurtosis* model [47], [50]:

$$S(t) = S_0 \exp\left(-bD + \frac{1}{6}b^2D^2K\right), \quad (4.35)$$

where $K = c_4/c_2^2$ is the diffusional kurtosis. This parameter quantifies the degree of non-Gaussian diffusion, without however being specific to the underlying cause [50], [51].

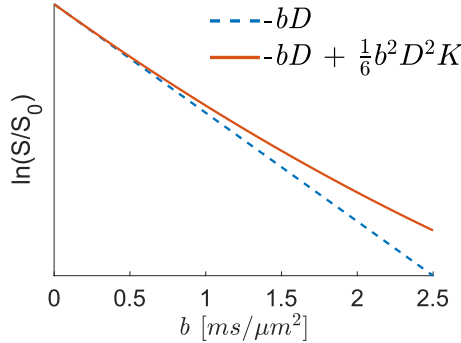


Figure 4.7: Logarithmic MR signal decay as a function of b for the free diffusion (dashed-blue line) and kurtosis (orange line) models. At low b -values, both signals decay in a straight fashion. As b increases, the effect of the kurtosis is no longer negligible and the signal deviates from the straight line.

Similarly to the case of anisotropic diffusion, the directional dependence of the kurtosis can be captured with a tensorial object. The kurtosis tensor \mathbb{W}_{ijkl} is a fully symmetric fourth-order tensor; of its 81 elements, only 15 are unique due to the complete interchangeability of the indexes. Estimation of \mathbb{W} is achieved in Diffusional Kurtosis Imaging (DKI) [50].

4.4 Diffusion within confined pores

The strong time-dependence of the diffusion process as shown in Figure 4.6 is a hallmark of restricted diffusion [52], [53]. In the narrow-pulse regime for a Stejskal-Tanner experiment, the size of the restricting geometry can be recovered thanks to the so-called diffusion-diffraction phenomena at high q -values [54], [55] provided that $\delta \ll a^2/D$, where a is the characteristic size of the restriction, and that Δ is long enough so that the particles can explore the pore space many times. Different methods and formalisms have been developed to study the problem of restricted diffusion when these conditions are not met, and when general gradient waveforms are employed [56]–[59]. While there are expressions for computing the MR signal for particles diffusing in simple symmetric geometries (slab, cylinder, sphere), the analysis of more general 3-dimensional pore shapes is difficult.

The confinement tensor

The alternative that was considered in this thesis (paper IV) consists of picturing diffusion as occurring in a potential landscape, where the confining potential takes the parabolic form [60]:

$$V(r) = \frac{1}{2}k r^2, \quad (4.36)$$

where k is the stiffness of a spring. The diffusing spins thus experience an external (Hookean) restoring force that prohibits them from escaping to infinity (as instead implied in free diffusion). This is seen in the (1-dimensional) mean squared displacement which takes the form:

$$\langle (r_1 - r_0)^2 \rangle = \frac{2}{C}(1 - e^{-DCt}). \quad (4.37)$$

In the limit of $t \rightarrow \infty$, this mean squared displacement approaches the constant value of $2/C$, where C is a measure of confinement, $C = \frac{k}{k_B T}$, having units of inverse squared length.

The resulting model for the 3-dimensional anisotropic diffusion process consists of a tensorial quantity, the confinement tensor, which captures the geometrical features of the restricting pore, and an effective diffusivity which can be expressed either through a tensorial (akin to the diffusion tensor) or scalar quantity. The MR signal decay for the confinement tensor model is given by [60]:

$$E = \exp \left(-D_{\text{eff}} \int_0^{t_f} |\mathbf{u}(t)|^2 dt \right) \exp \left(-\frac{D_{\text{eff}}}{2} \mathbf{u}^T(0) \mathbf{\Omega}^{-1} \mathbf{u}(0) \right) \quad (4.38)$$

with

$$\mathbf{u}(t) = \gamma \int_t^{t_f} e^{-\Omega(t'-t)} \mathbf{g}(t') dt' \quad (4.39)$$

and

$$\Omega = D_{\text{eff}} \mathbf{C}_{\text{eff}}, \quad (4.40)$$

where D_{eff} is the effective (isotropic) diffusivity, and \mathbf{C}_{eff} is the (effective) confinement tensor. Note that conversely to the apparent diffusion tensor, where the geometry of the medium slowing down the diffusion becomes entangled with the diffusivity property, in this model the two are separated. Figure 4.8 shows examples of "mean confinement" ($\text{Tr}(\mathbf{C}_{\text{eff}})$) and D_{eff} maps for an axial slice of a healthy brain [26]. Figure 4.9 shows axial slices of mean confinement and effective diffusivity for a brain tumour. Both results were obtained from non-linear fittings of the confinement tensor model to diffusion MRI data acquired with generalised gradient waveforms.

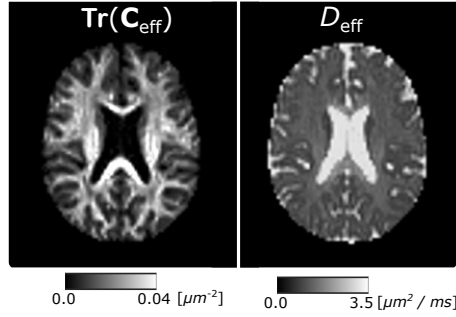


Figure 4.8: Confinement tensor trace (left) and effective diffusivity (right) maps for a healthy brain. The trace gives a measure of mean confinement; It is high in white matter where water experiences the tight restriction of the axons' membranes, and low in the ventricles where water diffuses freely. The effective diffusivity is akin to the axial diffusivity in Figure 4.5. This is expected since with the confinement model the diffusivity is decoupled from the geometry of the pore, thus it reflects a "free" diffusivity (as it is along fibers in DTI) rather than a mean diffusivity.

For the Stejskal-Tanner sequence, the signal given by the confinement tensor model can be computed analytically [60]:

$$E = e^{-\mathbf{g}^T \mathcal{A} \mathbf{g}}, \quad (4.41)$$

with \mathcal{A} being the real symmetric matrix:

$$\mathcal{A} = D_{\text{eff}} \gamma^2 \Omega^{-3} \left[(\mathbf{1} - e^{-\Omega \Delta}) (\mathbf{1} - e^{-\Omega \delta})^2 e^{\Omega \delta} - (\mathbf{1} - e^{-2\Omega \delta}) e^{\Omega \delta} + 2\Omega \delta \right]. \quad (4.42)$$

Both 4.38 and 4.41 highlight the different time-dependence of the model on the sequence parameters, compared to the free diffusion scenario (see Equation 4.12) where everything condenses into b . Figure 4.10 shows that this time dependence is consistent with that of restricted diffusion.

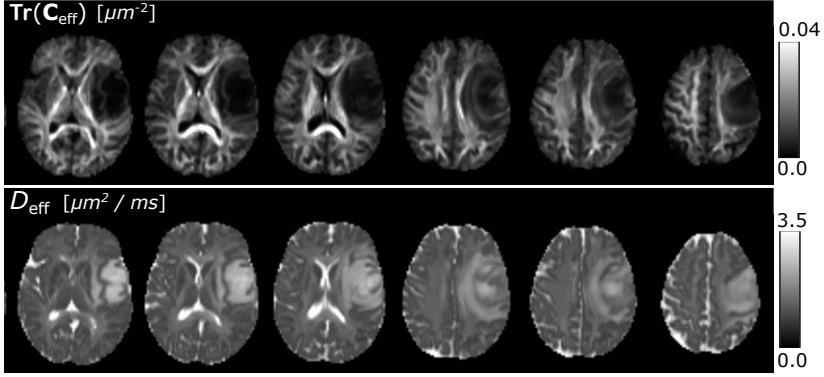


Figure 4.9: Invariants from the confinement tensor model for axial slices of a brain tumour identified by pathology as a grade 4 glioblastoma. The trace of the confinement tensor suggests low restriction around the tumoral zone, with the elevated diffusivity shown in the D_{eff} map possibly indicating peritumoral oedema. Data were acquired with ethical permission EPM 2020 – 01404.

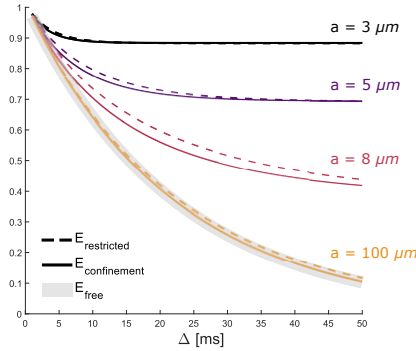


Figure 4.10: Dashed lines: MR signal for particles diffusing between two parallel plates separated by a distance $2a$, as a function of the diffusion time Δ . The signal $E_{\text{restricted}}$ is computed according to equation 32 in [61], and it is used here as ground truth. The solid lines ($E_{\text{confinement}}$) correspond to the signal predicted using equations 4.41 and 4.42 for the confinement tensor model with $C = 12/(2a)^2$. The gradients' pulse width and strength were set to $\delta = 10 \text{ ms}$ and $g = 80 \text{ mT/m}$, while the diffusion coefficient was set to $D = 1 \mu\text{m}^2/\text{ms}$. The plot highlights that the confinement model possesses a time dependency similar to that of restricted diffusion. The plot also shows that the confinement model accommodates free diffusion (E_{free}) when the restrictions are not felt by the diffusing particles.

Effective potential for restricted diffusion

The propagator for diffusion taking place in a confining potential is also of Gaussian form [62], [63], and the quadratic dependence on the magnetic field gradient's strength seen in 4.41 highlights that the confinement tensor model is based on the Gaussian phase approximation. Therefore, the contributions of higher order terms are neglected. Nevertheless, there are relevant experimental scenarios, often realised in clinical settings, for which the confinement tensor becomes the effective model for restricted diffusion.

The simple case concerns the use of small gradient strengths; as discussed in the previous section, for $g \rightarrow 0$ the spin phase distribution is approximately Gaussian, and therefore the confinement model would perfectly represent the data. Especially for experiments considering diffusion time-dependence, the parabolic potential would provide a superior representation of the diffusion process compared to a slowed free diffusion [64].

The second relevant scenario concerns measurements performed using long pulses. In this case, as exemplified in Equations 4.23 and 4.24, the signal becomes sensitive to the centre of mass of the trajectories rather than to the instantaneous positions. For particles trapped in a pore, the distribution of the centre of masses of the trajectories approaches a Gaussian as $\delta \rightarrow \infty$ [40], [65], [66], which renders the MR signal insensitive to all the fine features of the restricting geometry. The only surviving property is the force that does not allow the particles to escape, which is perfectly captured by a Hookean force [65]. In paper IV, we showed that currently employed diffusion measurements with general time-varying magnetic field gradients fall in this long pulse category, thus endorsing the use of the confinement tensor for analysing such data.

5

Mapping heterogeneity with generalised diffusion gradients

A powerful aspect of diffusion MRI is that resolution is primarily determined by the distance traveled by the water molecules during the experiment, rather than by the voxel-size of the reconstructed image. Typical diffusion MRI measurements performed in clinical settings probe the random motion of water molecules over hundreds of milliseconds. Considering a representative diffusion coefficient of $10^{-9} \text{ m}^2/\text{s}$ for brain tissue, the mean squared displacement given by 4.6 would approximately be $\langle r^2 \rangle \approx 10^{-10} \text{ m}^2$, resulting on an average particle displacement in the order of $10 \mu\text{m}$. This happens to coincide with the typical cell size, entailing that the MR signal resulting from this molecular motion is sensitive to cellular structures.

However, all the spins residing within the approximately $2 \times 2 \times 2 \text{ mm}^3$ voxel will contribute to the averaged signal. In DTI, this averaged signal is used to obtain a global measure of diffusion anisotropy. In DKI, the signal is used to estimate a deviation from Gaussianity, though without being specific to the underlying cause. This chapter introduces diffusion measurements by means of generalised gradient waveforms which efficiently sample diffusion along different directions simultaneously, allowing the contributions to the MR signal of different sources of intravoxel heterogeneity to be separated. Under the assumption of free diffusion, these generalised waveforms are typically designed to achieve specific shapes of the measurement B-tensor. Thus, one often refers to them as tensor-valued diffusion encoding.

5.1 Tensor-valued diffusion encoding

As seen in the previous chapter, diffusion MRI is performed by sampling q -space. The dephasing vector $\mathbf{q}(t)$ encompasses the q -space trajectory determined by the time-varying magnetic field gradient $\mathbf{g}(t)$ employed to measure diffusion:

$$\mathbf{q}(t) = \gamma \int_0^t \mathbf{g}(t') dt'. \quad (5.1)$$

5. MAPPING HETEROGENEITY WITH GENERALISED DIFFUSION GRADIENTS

For free diffusion, all the experimental parameters condense into the measurement B-tensor \mathbf{B} defined in Equation 4.14 [67]:

$$\mathbf{B} = \int_0^{T_E} \mathbf{q}(t) \otimes \mathbf{q}(t) dt. \quad (5.2)$$

Similarly to the diffusion tensor, the B-tensor is a symmetric positive semi-definite tensor. For Stejskal-Tanner measurement, this tensor is of rank-1, meaning that only one of the eigenvalues is non-zero. In tensor-valued dMRI, the gradient waveforms $\mathbf{g}(t)$ are designed to yield measurement tensors of rank 1, 2, and 3 [68].

Typically, measurement tensors of rank 1 are referred to as linear tensor encoding (LTE), axisymmetric measurement tensors of rank 2 as planar tensor encoding (PTE), and rank 3 isotropic measurement tensors as spherical tensor encoding (STE). The nomenclature is based on the respective shapes of the B-tensor ellipsoid. Figure 5.1 shows the magnetic field gradient waveforms, q-space trajectories, and resulting B-tensors for the Stejskal-Tanner experiment and tensor-valued diffusion pulse sequences.

Note that different shapes of the B-tensor can also be achieved by sequential repetitions of the pulse gradients used in the Stejskal-Tanner experiment. For example, by adding another pair of pulses, one can achieve planar B-tensors [11], and by adding a third pair of pulses one achieves spherical tensor encoding [69]. Especially the use of two pairs of pulses, in the so-called double diffusion encoding (DDE) experiments, has found large employment since it provides information not achievable with a single pair of pulsed gradients [14], [15], [70]–[73]. The advantage of adopting the generalised gradient waveforms presented here is that they allow for measurements more easily realisable in clinical settings, where the limited strength of the gradient system would not allow for achieving significant b-values in short echo times when repeating the pulsed gradients multiple times.

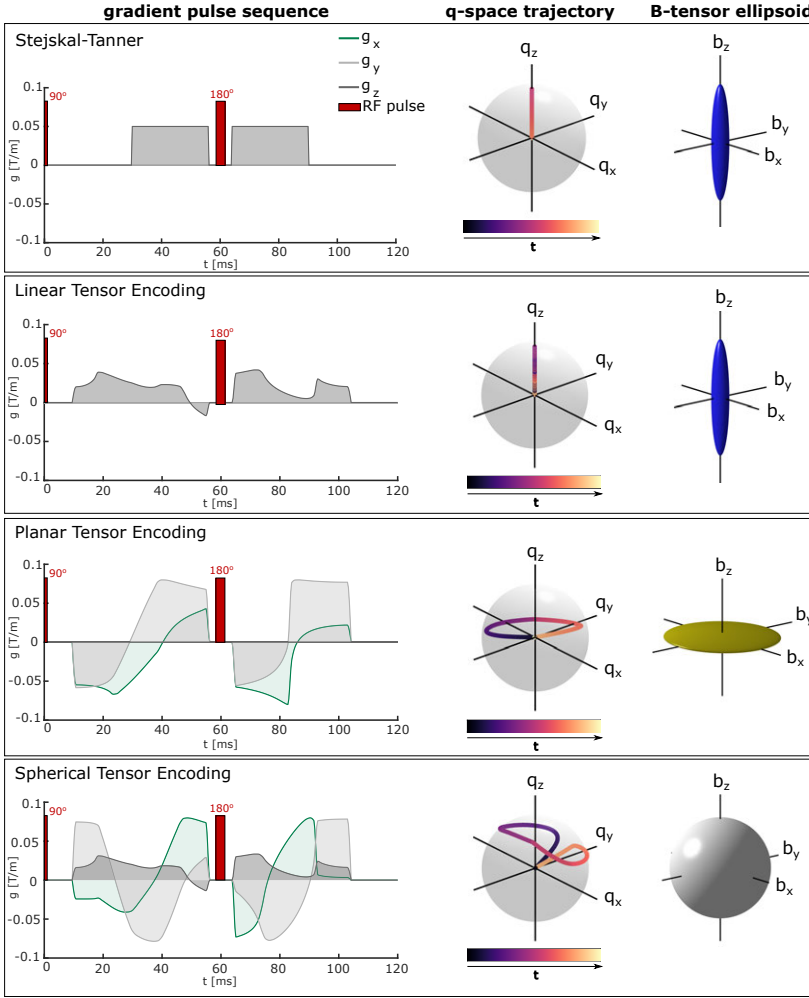


Figure 5.1: Magnetic field gradient waveforms, q-space trajectory, and measurement B-tensor ellipsoids for Stejskal-Tanner pulse sequence, linear tensor encoding, planar tensor encoding, and spherical tensor encoding. The q-space trajectories were obtained from the gradient waveforms according to Equation 5.1, and were color-coded to show the time evolution. Due to the refocusing condition, all trajectories start and end at 0. The B-tensors were obtained from the q-trajectories according to 5.2. For Stejskal-Tanner and LTE, only one eigenvalue of the B-tensor is non-zero, and the shape is thus a stick (for visualization purposes, the 0 eigenvalues were replaced with a non-zero value). For PTE, two eigenvalues are non-zero, thus the B-tensor is a disc/pancake. For STE, all the eigenvalues are equal and non-zero thus the B-tensor ellipsoid is a sphere.

Connection between measurement tensors and diffusion patterns

A simple intuition behind the link between the shape of the measurement tensor and the probed diffusion pattern is based on the tensor parameterisations expressed via Equations 2.10 and 2.13 which were presented in Chapter 2. Recall that the MR signal depends on the product between the measurement B-tensor and the diffusion tensor:

$$S = S_0 e^{-\mathbf{B}:\mathbf{D}}. \quad (5.3)$$

Given an axisymmetric measurement tensor \mathbf{B} and an axisymmetric diffusion tensor \mathbf{D} , by expressing the diffusion tensor in the eigenbasis of the measurement tensor, their product becomes [28]:

$$\mathbf{B}:\mathbf{D} = bD_{\text{iso}} \left(1 + \kappa_b \kappa_D [3\cos^2(\theta) - 1] \right), \quad (5.4)$$

where D_{iso} is the isotropic component of \mathbf{D} , $D_{\text{iso}} = \text{Tr}(\mathbf{D})/3$, κ_b and κ_D are defined as in Expression 2.9, and θ is the angle between the major axis of symmetry of the two tensors. From Equation 5.4 one can see that spherical encoding ($\kappa_b = 0$) selectively probes the isotropic component of \mathbf{D} , while other shapes of the encoding tensor ($\kappa_b \neq 0$, $\kappa_b = 1$ for LTE and $\kappa_b = -0.5$ for PTE) conflate information regarding the size, shape, and orientation of \mathbf{D} . Overall, the idea is that by using different shapes of the measurement tensor, different parts of the diffusion tensor can be probed, thus probing specific patterns.

5.2 Tensor distributions as a proxy to intravoxel heterogeneity

The mismatch between the millimeter-scale voxel size and the micrometer-scale sensitivity of the diffusion measurements can be bridged by representing diffusion in each pore within the voxel with a tensorial quantity. As such, the voxel-level signal is assumed to be the sum of the contributions from spin-packets residing in different non-communicating environments [74], [75]. Under the GPA, each environment can be represented with a diffusion tensor, and the resulting signal arising from a distribution of diffusion tensors (DTD) reads as [22]:

$$S(\mathbf{B}) = S_0 \int_{\mathbf{D}} \mathcal{P}(\mathbf{D}) e^{-\mathbf{B}:\mathbf{D}} d\mathbf{D}, \quad (5.5)$$

where $\mathcal{P}(\mathbf{D})$ is the distribution function for the stochastic variable \mathbf{D} . This function essentially weights the contribution of each diffusion tensor in the distribution towards the voxel-level signal. Note that if there is no heterogeneity in the voxel, meaning that the diffusion process can be captured by a global diffusion tensor, $\mathcal{P}(\mathbf{D})$ is a delta function, and Equation 5.5 reduces to 5.3.

Equation 5.5 relates the MR signal to the Laplace transform of $\mathcal{P}(\mathbf{D})$, implying that the DTD can in principle be recovered by inverse transformation of the MR signal

acquired with a family of measurement tensors \mathbf{B}_n , $n = 1, \dots, N$. Once at hand, statistical descriptors of the DTD, such as means, variances, and covariances, can be used to characterise the intravoxel heterogeneity [23], [76], [77]. However, the numerical inversion of the Laplace transform from a discrete sampling of the signal is known for being an ill-posed problem [78]–[80]. For the problem at hand, this results in the following undesirable properties: in general, the obtained solution is not unique, meaning that many different DTDs will represent the signal from the employed measurement tensors equally well; Subtle variations in the input signal, for example due to noise, will correspond to a largely different solution. Schemes for the numerical inversion of the Laplace transform are discussed in the next chapter.

To stabilise the inversion of Equation 5.5, enough information needs to be encoded into $S(\mathbf{B})$ to promote differentiation between different heterogeneities in the voxel. Figure 5.2 shows that this cannot be achieved with diffusion measurements performed with the Stejskal-Tanner sequence only. The example depicts two different voxels which would yield identical signals if measured with linear tensor encoding only, and one would therefore measure the same kurtosis in both cases despite the different underlying sources. For this reason, the diffusion signal produced with Stejskal-Tanner type of measurements has sometimes been referred to as ‘remarkably unremarkable’ [75], [81], and a plethora of different measurements schemes have been proposed to achieve higher specificity to different diffusion features [11]–[16], [72], [82]. For example, the two voxels can be torn apart when measurements with spherical tensor encoding are added. In paper IV, we argued that adding measurements performed by varying the frequency content of the magnetic field gradient waveforms could also aid in differentiating between different voxel compositions when considering distributions of confinement tensors, which are presented later in the Chapter [60], [83], [84].

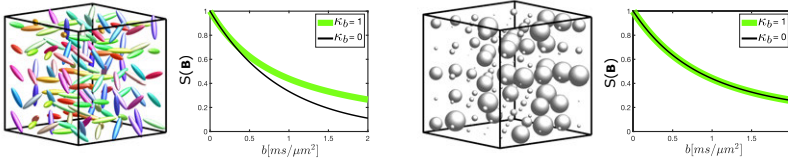


Figure 5.2: Example of two voxels for which the LTE signal is identical despite the different sources of heterogeneity. On the left, the system is microscopically anisotropic, but macroscopically isotropic due to the orientation dispersion. On the right, the system is both locally and globally isotropic, with dispersion in mean diffusivity. The two collections of tensors were designed to yield the same mean diffusion tensor. As shown in the plots, the LTE signal ($\kappa_b = 1$) is the same in the two cases, whereas the STE signal ($\kappa_b = 0$) differs. As detailed in Section 5.3, this extra information can be used to tell the two cases apart by resolving the sources of intravoxel heterogeneity.

Wishart-distributed diffusion tensors

Even when employing diffusion measurements covering different shapes, sizes, and orientations of the B-tensors (and possibly employing gradient waveforms with varied frequency content), the inversion of the Laplace transform in Expression 5.5 remains a remarkably difficult problem. One way of getting around this problem is to impose a known form for the probability distribution function $\mathcal{P}(\mathbf{D})$ for which the Laplace transform can be computed analytically. For example, a natural choice is to set $\mathcal{P}(\mathbf{D})$ to follow the Wishart distribution [85], since it is a family of distributions for symmetric positive semi-definite random matrices, which can represent covariance matrices like the diffusion tensor [86]. Indeed, using this distribution as an extension to DTI was considered in [22] for measurements performed with the Stejskal-Tanner pulse sequences. For diffusion measurements performed with tensor encoding, the Gamma distribution (which the Wishart distribution generalises) has also been employed to characterise tissue heterogeneity in the healthy and diseased human brain [20], [24], [87].

A symmetric $d \times d$ positive semi-definite random matrix \mathbf{D} is said to follow the central Wishart distribution $\mathcal{W}_d(p, \mathbf{\Sigma})$ if its probability density function is given by:

$$p(\mathbf{D}) = \frac{|\mathbf{D}|^{(d-p-1)/2}}{|\mathbf{\Sigma}|^{p/2} 2^{dp/2} \Gamma_d(\frac{p}{2})} e^{-\frac{1}{2}\text{Tr}(\mathbf{\Sigma}^{-1}\mathbf{D})}, \quad (5.6)$$

where the scale matrix $\mathbf{\Sigma}$ belongs to the manifold of $d \times d$ positive semi-definite matrices, the scale parameter p represents the degrees of freedom of the distribution, and Γ_d is the multivariate gamma function. d gives the dimensionality of the problem; for diffusion in three dimensions, $d = 3$. A sample random matrix drawn from the Wishart distribution $\mathcal{W}_d(p, \mathbf{\Sigma})$ is such that:

$$\mathbf{D} = \sum_{i=1}^p x_i x_i^T, \quad x_i \sim \mathcal{N}_d(0, \mathbf{\Sigma}), \quad i = 1, \dots, p \quad (5.7)$$

where $\mathcal{N}_d(0, \mathbf{\Sigma})$ is the d-variate normal distribution defined by the covariance matrix $\mathbf{\Sigma}$. The mean of the Wishart distribution is directly proportional to this covariance matrix:

$$\langle \mathbf{D} \rangle = p\mathbf{\Sigma}. \quad (5.8)$$

The diffusion-weighted MR signal for Wishart-distributed diffusion tensors can be obtained by inserting 5.6 into 5.5, which yields [40]:

$$S(\mathbf{B}) = |\mathbf{I} + 2\mathbf{B}\mathbf{\Sigma}|^{-p/2}, \quad (5.9)$$

where $|\cdot|$ indicates the determinant. In paper I, this expression generalised to the case of non-central Wishart distributed diffusion tensors [88], [89] was used to simulate the diffusion-weighted MR signals for given measurement tensors \mathbf{B} and scale matrices $\mathbf{\Sigma}$. These signals were then employed to test the performance of a developed

framework for the estimation of the mean and covariance of the DTD from diffusion data acquired with general time-varying magnetic field gradients [17], [89], [90].

5.3 Q-space trajectory imaging

Another way of getting around the problem of numerically inverting the Laplace transform in 5.5 was presented by Westin et al. in [17]. It was shown that by considering the cumulant expansion of Equation 5.5, one could estimate the mean and covariance of the DTD from diffusion measurements performed with different tensor encoding shapes. The technique was named q-space trajectory imaging (QTI).

Equation 5.5 can be interpreted in terms of the expected value of the function of the stochastic variable \mathbf{D} :

$$S(\mathbf{B})/S_0 = \langle e^{-\mathbf{B}:\mathbf{D}} \rangle. \quad (5.10)$$

The term on the right side of the equation reads as the moment-generating function of \mathbf{D} . The terms of the cumulant expansion are given by the Taylor expansion of the logarithm of this function for $\mathbf{B}:\mathbf{D} \rightarrow 0$. The Taylor expansion of $\langle e^{-\mathbf{B}:\mathbf{D}} \rangle$ gives

$$\langle e^{-\mathbf{B}:\mathbf{D}} \rangle \approx \left\langle 1 - \mathbf{B}:\mathbf{D} + \frac{1}{2}\mathbf{B}^{\otimes 2}:\mathbf{D}^{\otimes 2} \right\rangle = 1 - \mathbf{B}:\langle \mathbf{D} \rangle + \frac{1}{2}\mathbf{B}^{\otimes 2}:\langle \mathbf{D}^{\otimes 2} \rangle. \quad (5.11)$$

By taking the logarithm of the expression above and using $\ln(1+x) \approx x - \frac{1}{2}x^2$, the expansion, limited to the second order terms, is found to be:

$$\ln \left(\langle e^{-\mathbf{B}:\mathbf{D}} \rangle \right) \approx -\mathbf{B}:\langle \mathbf{D} \rangle + \frac{1}{2}\mathbf{B}^{\otimes 2}:\langle \mathbf{D}^{\otimes 2} \rangle - \frac{1}{2}\mathbf{B}^{\otimes 2}:\langle \mathbf{D} \rangle^{\otimes 2}. \quad (5.12)$$

Therefore,

$$\ln(S(\mathbf{B})) \approx \ln(S_0) - \mathbf{B}:\langle \mathbf{D} \rangle + \frac{1}{2}\mathbf{B}^{\otimes 2}:\left(\langle \mathbf{D}^{\otimes 2} \rangle - \langle \mathbf{D} \rangle^{\otimes 2}\right). \quad (5.13)$$

One recognises that the first cumulant corresponds to the mean of the distribution, $\langle \mathbf{D} \rangle = \hat{\mathbf{D}}$, while the second cumulant corresponds to the 4-th order covariance tensor $\mathbf{C} = \langle (\mathbf{D} - \hat{\mathbf{D}}) \otimes (\mathbf{D} - \hat{\mathbf{D}}) \rangle$. The \mathbf{C} tensor can be seen to have major and minor symmetries, thus 21 of its elements are independent. Therefore, \mathbf{C} can be represented by a 6×6 symmetric matrix \mathbf{C} . The covariance tensor can also be expressed in terms of the second moment tensor $\mathbf{M} = \langle \mathbf{D} \otimes \mathbf{D} \rangle = \langle \mathbf{D}^{\otimes 2} \rangle$:

$$\mathbf{C} = \mathbf{M} - \langle \mathbf{D} \rangle \otimes \langle \mathbf{D} \rangle = \mathbf{M} - \langle \mathbf{D} \rangle^{\otimes 2}. \quad (5.14)$$

Ignoring the higher order cumulants corresponds to considering the diffusion tensor distribution to be Gaussian, and the MR signal in 5.10 can be written as:

$$S(\mathbf{B}) = S_0 e^{-\mathbf{B}:\mathbf{D} + \frac{1}{2}\mathbf{B}:\mathbf{C}}, \quad (5.15)$$

5. MAPPING HETEROGENEITY WITH GENERALISED DIFFUSION GRADIENTS

where $\mathbb{B} = \mathbf{B}^{\otimes 2}$. Clearly, relying only on the first two terms of the expansion to represent the signal may bias the results, when the higher-order cumulants are not null. For this approximation to hold, only measurements performed at low b values should be considered.

Similarly to what is done in DTI, scalar invariants relating to features of the microstructure can be obtained from $\hat{\mathbf{D}}$ and \mathbf{C} . From $\hat{\mathbf{D}}$ the same invariants as from the diffusion tensor can be obtained. These were presented in Section 4.3 and depicted in Figure 4.5. Scalar invariants from the covariance tensor can be computed by inner products between \mathbf{C} and 4-th order tensors borrowed from the field of mechanics [91].

Scalar invariants from the covariance tensor

By analogy with the 4-th order elasticity tensor [91]–[93], the isotropic, shear, and bulk variances can be obtained from the covariance tensor \mathbf{C} by inner products with three fourth-order tensors (which have the same symmetries as \mathbf{C}) [17]:

$$\mathbb{E}^{\text{iso}}, \text{ where only the } E_{ijij} \text{ elements have non zero value, } E_{ijij} = \begin{cases} \frac{1}{3} & \text{if } i = j, \\ \frac{1}{6} & \text{if } i \neq j \end{cases} \quad (5.16)$$

$$\mathbb{E}^{\text{bulk}} = \mathbb{E}^{\text{iso}} \otimes \mathbb{E}^{\text{iso}}, \quad \text{with} \quad \mathbb{E}^{\text{iso}} = \frac{1}{3} \mathbf{I} \quad (5.17)$$

$$\mathbb{E}^{\text{shear}} = \mathbb{E}^{\text{iso}} - \mathbb{E}^{\text{bulk}} \quad (5.18)$$

The isotropic, bulk, and shear variances in diffusivity can be obtained from the covariance tensor as:

$$V_{\text{bulk}} = \mathbf{C} : \mathbb{E}^{\text{bulk}} \quad (5.19)$$

$$V_{\text{shear}} = \mathbf{C} : \mathbb{E}^{\text{shear}} \quad (5.20)$$

$$V_{\text{iso}} = V_{\text{bulk}} + V_{\text{shear}} = \mathbf{C} : \mathbb{E}^{\text{iso}} \quad (5.21)$$

Note that, as alluded to in Figure 5.2, the bulk and shear components cannot be obtained when only LTE measurements are employed. Disentangling these two variances' contribution to the total isotropic variance requires measuring diffusion with at least LTE and STE. The bulk part of the variance relates to the spread in size or mean diffusivity between different environments. If each tensor's mean diffusivity is equal this variance would be zero, while its value would grow as the dispersion between each domain's size increases. The shear variance is instead sensitive to differences in shapes and orientations between the different environments. Returning to the example presented in Figure 5.2, the V_{iso} for the voxel on the left would entirely be determined by V_{shear} , as there is no variation in compartment size, while for the voxel on the right, it would be fully determined by V_{bulk} , since there is no anisotropy nor orientation dispersion. An example of how these variances look for a healthy brain is shown in Figure 5.3.

Note that V_{shear} is a composite variance determined by a microscopic and a macroscopic component [17]:

$$V_{\text{shear}} = \mathbf{C} : \mathbb{E}^{\text{shear}} = \langle \mathbf{D}^{\otimes 2} : \mathbb{E}^{\text{shear}} \rangle - \langle \mathbf{D} \rangle^{\otimes 2} : \mathbb{E}^{\text{shear}} = V_{\mu A} - V_{MA}. \quad (5.22)$$

The microscopic shear variance $V_{\mu A}$ refers to a measure of microscopic anisotropy unconfounded by the orientation of each pore, while the anisotropy measured by macroscopic shear variance V_{MA} reflects the degree of orientation coherence of the microenvironments.

These variances can be reconducted to more intuitive parameters of the microstructure, all taking value in the range $[0, 1]$. Here the focus is posed in particular on the microscopic fractional anisotropy μFA [11], [24], [94]–[97], orientation coherence C_c , and variance in mean diffusivity C_{MD} , since they were employed (together with the metrics from $\hat{\mathbf{D}}$) in papers I, II, and III:

$$\mu FA^2 = \frac{3}{2} \frac{\mathbf{M} : \mathbb{E}^{\text{shear}}}{\mathbf{M} : \mathbb{E}^{\text{iso}}} \quad (5.23)$$

$$C_c = \frac{(\hat{\mathbf{D}}^{\otimes 2} : \mathbb{E}^{\text{shear}}) (\mathbf{M} : \mathbb{E}^{\text{iso}})}{(\hat{\mathbf{D}}^{\otimes 2} : \mathbb{E}^{\text{iso}}) (\mathbf{M} : \mathbb{E}^{\text{shear}})} = \frac{FA^2}{\mu FA^2} \quad (5.24)$$

$$C_{MD} = \frac{\mathbf{C} : \mathbb{E}^{\text{bulk}}}{\mathbf{M} : \mathbb{E}^{\text{bulk}}} \quad (5.25)$$

In words, μFA is a measure of local anisotropy unconfounded by dispersion in orientation, meaning that it would yield a high value when the local diffusion tensors are anisotropic, irrespectively of their relative orientation. C_c gives a measure of global alignment of anisotropic tensors: it is 1 when the anisotropic compartments are coherently aligned, and 0 when they are instead randomly oriented. The definition in 5.24 establishes the relation between the local (μFA) and global (FA) anisotropy. When the compartments in the voxel share a common orientation, $C_c = 1$, and these two measures coincide. Conversely, when anisotropic compartments are out of alignment, μFA will retain a high value while FA decreases due to a reduction in C_c . Lastly, C_{MD} is simply the normalised bulk variance that was previously described. A picto-

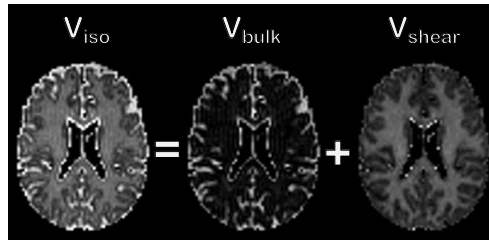
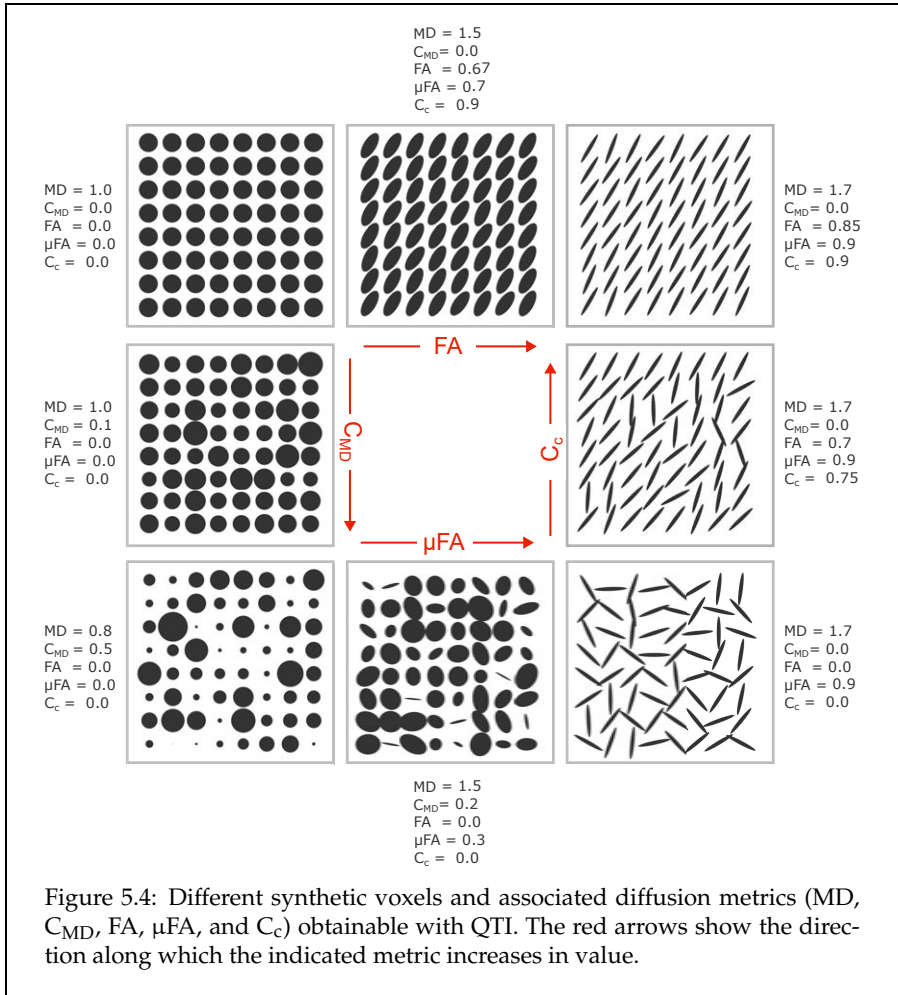


Figure 5.3: Example maps of variances obtained from the covariance tensor \mathbf{C} for a healthy brain. The total isotropic variance, V_{iso} , shows non-zero values everywhere in the brain except in the ventricles, where no heterogeneity is expected. Most of the variance in mean diffusivity V_{bulk} is found at the interface between different tissue types, whereas the shear variance V_{shear} is predominant in white matter, where anisotropy and orientation effects dominate the MR signal.

5. MAPPING HETEROGENEITY WITH GENERALISED DIFFUSION GRADIENTS



rial representation how these and the parameters from \hat{D} change for different tissue compositions is presented in Figure 5.4. Figure 5.5 shows instead example brain images of μFA , C_c , and C_{MD} . The accuracy and precision of these metrics as recovered via QTI were recently discussed. It was reported that in voxels presenting large variations in compartment size and/or high degree of orientation dispersion these metrics tend to be inaccurate, possibly because of the contributions of the higher order cumulants [98]–[100]. However, these situations should not be commonly encountered when studying the brain white matter.

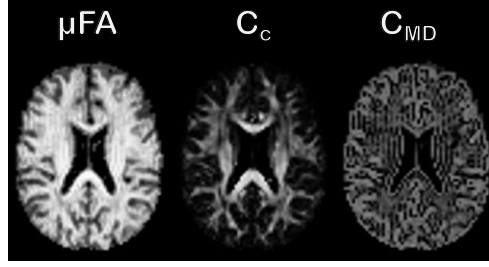


Figure 5.5: Example of scalar invariants obtained from the covariance tensor \mathbf{C} for a healthy brain. μFA has elevated values in essentially all the brain parenchyma, while high values in orientation coherence C_c are found in white matter where axons fibre bundles are coherently aligned. C_{MD} is the normalised variance in mean diffusivity.

5.4 Distributions of confinement tensors

In paper IV we argued that it is quite paradoxical to consider a compartmentalised picture of the tissue microstructure when diffusion is modelled as free (i.e. with a diffusion tensor) in each compartment. Further, it was shown via simulations that for current clinical tensor-valued diffusion measurements [26], the employed gradient waveforms are effectively long pulsed gradients [84]. Thus, indeed the net displacement of particles within each environment is well captured by a Gaussian distribution, but this Gaussian is the one implied by the confinement tensor model and not by the diffusion tensor. This was particularly evident for STE measurements, where the modulation imparted on the MR signal by the restricting geometry for different orientations of $\mathbf{g}(t)$ cannot be captured by a diffusion tensor, since the spherical B-tensor will be identical irrespective of the rotation of the waveform. Conversely, the modulation is perfectly described by the confinement tensor, which we thus suggested as a better candidate to represent each pore in a compartmentalised picture of the microstructure.

For a joint distribution of confinement tensors and effective diffusivities with probability density $\mathcal{P}(\mathbf{C}, D)$, the signal is given by:

$$S(\mathbf{g}(t)) = S_0 \int E(\mathbf{g}(t), \mathbf{C}, D) \mathcal{P}(\mathbf{C}, D) d\mathbf{C} dD, \quad (5.26)$$

where $E(\mathbf{g}(t), \mathbf{C}, D)$ is the signal implied by the confinement tensor model given by Equations 4.38, 4.39, and 4.40. For brevity, the subscripts for the effective confinement tensor and effective diffusivity are hereby dropped.

Using the algorithm described in the next chapter, discrete joint distributions of axisymmetric confinement tensors and effective diffusivities can be estimated from the data by numerically inverting the Laplace transform in Equation 5.26. According to the definitions given in Section 2.1, axisymmetric confinement tensors are parameterised by a parallel C_{\parallel} and a perpendicular C_{\perp} component, and two angles θ and ϕ

5. MAPPING HETEROGENEITY WITH GENERALISED DIFFUSION GRADIENTS

defining the orientation of the main axis of symmetry. From the distributions, various means $\mathbf{E}[\cdot]$, variances $\mathbf{V}[\cdot]$, and covariances $\mathbf{Cov}[\cdot, \cdot]$ can be computed in terms of the tensors' shape κ_C , size C_{iso} , and diffusivity D . κ_C and C_{iso} are defined as in 2.11. Figure 5.6 shows examples of such statistical descriptors.

Additionally, the space defined by C_{\parallel} and C_{\perp} can be divided into different zones so that each tensor in the distribution gets mapped to a geometrical shape [23]. The mapping presented here (and in paper IV) is done so that each pair of C_{\parallel} and C_{\perp} connects to the represented *pore* shape rather than to the confinement tensor's shape. For example, for $C_{\perp} \gg C_{\parallel}$ the confinement tensor would have a pancake shape, meaning that diffusion is strongly confined in two directions but not along the main axis of symmetry. This would correspond to a stick-like pore. Figure 5.7 shows examples of confinement tensor-effective diffusivity distributions for voxels from the white matter, gray matter, and ventricles. In the same figure the different zones in the C_{\parallel} and C_{\perp} and the geometry they map to are displayed. Assigning each confinement tensor in the distribution to a pore shape allows computing the relative fraction of each geometry found in the voxel. Further, it is possible to compute and display the average effective diffusivity for each pore shape. Examples of the relative fractions and per-shape average effective diffusivity are shown in Figure 5.7. According to the space division considered in the figure, stick-like pores are found in the white matter, while spheres are mostly located in the gray matter. Free water is found in the ventricles and spaces surrounding the brain parenchyma, as well as in gray matter. Note that the free-water condition is determined by simultaneously low C_{\parallel} and C_{\perp} values, rather than by high diffusivity. By comparing the two panels in the bottom part of Figure 5.7, the results suggest that geometrically unconfined water can diffuse at a speed lower than that of free water (which is $D_0 \approx 3.0 \mu\text{m}^2/\text{ms}$ for water at 37° [101]). This is perhaps reflecting unbounded water diffusing in the tortuous extracellular environment. Otherwise, as expected, truly free fast diffusing water is found in the ventricles and outside the brain parenchyma, with average diffusivity matching the expected D_0 value. Diffusivities inside stick-like pores are found instead to be around $2.0 \mu\text{m}^2/\text{ms}$.

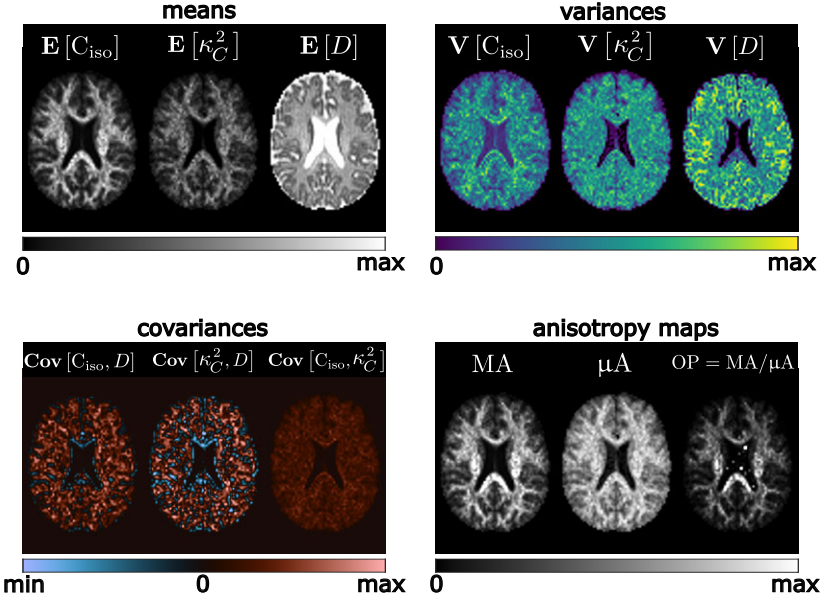


Figure 5.6: Statistical descriptors for joint distributions of confinement tensors-effective diffusivities. Means, variances, and covariances are computed in terms of the isotropic component of the confinement tensor C_{iso} , its squared anisotropy κ_C^2 , and effective diffusivity D . The maps $E[C_{\text{iso}}]$ and $E[D]$ should correspond to those presented in Figure 4.8 ($\text{Trace}(C_{\text{eff}})$ and D_{eff} , respectively). The variance in effective diffusivity $V[D]$ is similar in spirit to V_{bulk} from QTI. However, since geometry and diffusivity are not entangled in the confinement model, this variance reflects purely a spread in diffusivity, rather than an indirect variance in size as observed through a change in diffusivity as measured by V_{bulk} . The variance in pore size is instead captured by $V[C_{\text{iso}}]$. The separation between geometry and diffusivity can also be observed in the covariance maps. Interestingly, an increase in C_{iso} , i.e. a reduction in pore size, is in most cases accompanied by an increase in diffusivity.

The anisotropy maps are instead computed from the eigenvalues of the confinement tensors, which in the case of axisymmetry are C_{\parallel} and C_{\perp} . The macroscopic anisotropy (MA) is obtained by computing the variance of the eigenvalues of the mean confinement tensor of the distribution, while the microscopic anisotropy (μA) is the average of the eigenvalue variance computed for each confinement tensor in the distribution. MA is reminiscent of FA, while μA is the un-normalized version of μFA . The order parameter (OP) is the ratio between these two, and expresses orientation coherence between the tensors in the distribution similarly to C_c in QTI.

5. MAPPING HETEROGENEITY WITH GENERALISED DIFFUSION GRADIENTS

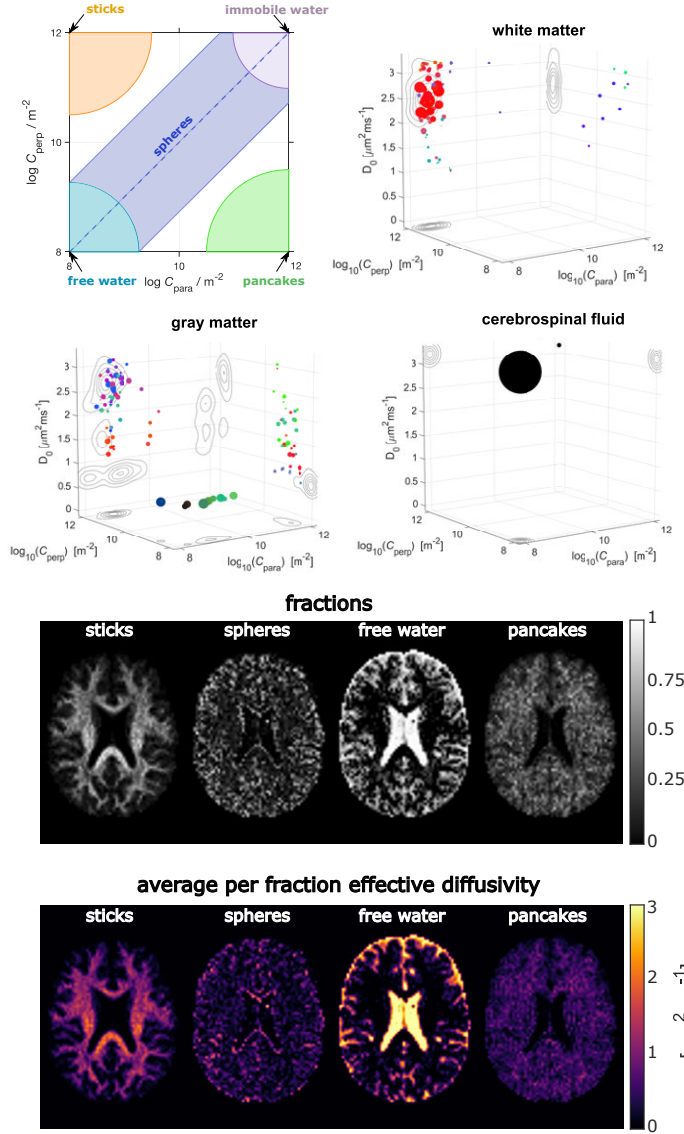


Figure 5.7: On top: examples of joint confinement tensor-effective diffusivity distributions for different tissue types, and birds' eye view on the C_{\parallel} - C_{\perp} plane where regions are defined to assign each confinement tensors to a different shape. In the C_{\parallel} - C_{\perp} - D plots, each dot represents a confinement tensor-effective diffusivity, with the size indicating the weight in the distribution and the colour denoting the tensor orientation (red for left-right, green for anterior-posterior, blue for superior-inferior). The projections of the points on the three axes are delineated by the contours. On the bottom: fractions of each pore shape per voxel determined using the C_{\parallel} - C_{\perp} space division presented on top, and average per-fraction effective diffusivity.

6

Parameter estimation

The content of this final chapter deals with the estimation of model parameters from data. In particular, the focus is on the problem introduced in Section 5.2 regarding the inversion of the Laplace transform, and on the estimation of the q-space trajectory imaging parameters. In the last section, a machine learning approach for solving both problems is presented along with results on data from brain tumor patients and COVID-19 survivors.

6.1 Optimisation problems

Estimating model parameters given some data is a form of optimisation where the goal is to find the set of values for the variables that best describes the observations. This often involves limiting the search space for the parameters to regions where these take meaningful values for the problem. A general optimisation problem can take the form:

$$\begin{aligned} & \underset{\mathbf{x}}{\text{minimise}} && f(\mathbf{x}) \\ & \text{subject to} && g_i(\mathbf{x}) \leq b_i, \quad i = 1, \dots, m \end{aligned} \tag{6.1}$$

where $\mathbf{x} \in \mathbf{R}^k$ is the vector containing the variables of the model, $f : \mathbf{R}^k \rightarrow \mathbf{R}$ is the objective function, $g_i : \mathbf{R}^k \rightarrow \mathbf{R}$ are the constraint functions, and the constants b_i are the bounds for the constraints. The problem is said to be linear if both the objective and the constraint functions are linear. Solving the problem in 6.1 consists of finding a vector \mathbf{x}^* that yields the minimum value of $f(\mathbf{x})$ while satisfying the constraints. If a vector \mathbf{x}^* is found, then $\mathbf{x}^* = \text{argmin}(f(\mathbf{x}))$. Different classes of optimisation problems are defined with respect to the type of objective function and constraint inequalities. The next two sections present two classes of convex optimisation problems relevant to this thesis.

Least squares

Least squares problems are frequently encountered in data fitting. The goal is to find the combination of parameters that minimises the quadratic norm of the vector

containing the differences between N observed data points and their prediction based on the model. The unconstrained problem takes the form:

$$\underset{\mathbf{x}}{\text{minimise}} \quad \|\boldsymbol{\eta}\|_2^2 = \|\mathbf{Ax} - \mathbf{y}\|_2^2 = \sum_{n=1}^N (\mathbf{a}_n \cdot \mathbf{x} - y_n)^2, \quad (6.2)$$

where $\|\cdot\|_2$ indicates the Euclidian norm, the matrix \mathbf{A} is the design matrix containing the experimental parameters, and \mathbf{a}_n is the n -th row of \mathbf{A} . The elements of the vector $\boldsymbol{\eta}$ are called the residuals. The solution to this problem can be found analytically (knowing that stationary points for this problems correspond to minimising points) by expanding the objective function and evaluating its derivative to find the minimum value:

$$\begin{aligned} f(\mathbf{x}) &= \mathbf{x}^T \mathbf{A}^T \mathbf{Ax} - 2\mathbf{y}^T \mathbf{Ax} + \mathbf{y}^T \mathbf{y} \\ \nabla f(\mathbf{x}) &= 2\mathbf{A}^T \mathbf{Ax} - 2\mathbf{A}^T \mathbf{y} = 0 \\ \mathbf{A}^T \mathbf{Ax} &= \mathbf{A}^T \mathbf{y} \\ \mathbf{x} &= (\mathbf{A}^T \mathbf{A})^{-1} \mathbf{A}^T \mathbf{y}, \end{aligned}$$

where the inverse of $\mathbf{A}^T \mathbf{A}$ exists if \mathbf{A} has full rank. The least squares problem can be interpreted in the statistical sense as the maximum likelihood estimation of the vector \mathbf{x} from measurements corrupted by Gaussian noise. When the noise is of unequal variance for the different measurements, weights are introduced in the problem formulation to restore homoskedasticity.

Semidefinite programming

Semidefinite programming (SDP) are constrained linear convex problems of the form [102]:

$$\begin{aligned} \underset{\mathbf{x}}{\text{minimise}} \quad & \mathbf{c}^T \mathbf{x} \\ \text{subject to} \quad & \mathbf{F}(\mathbf{x}) \succeq 0 \end{aligned} \quad (6.3)$$

with

$$\mathbf{F}(\mathbf{x}) = \mathbf{F}_0 + \sum_{i=1}^m x_i \mathbf{F}_i, \quad (6.4)$$

where \mathbf{c} is the vector containing the observations, $\mathbf{F}_0, \dots, \mathbf{F}_m$ are symmetric $k \times k$ matrices, and the matrix $\mathbf{F}(\mathbf{x})$ is positive semi-definite. Contrary to linear least squares, there is no analytical solution for SDP problems. However, interior-point (IP) methods can solve them very efficiently in a few iterations [102]. Moreover, convexity guarantees that, if found, the vector \mathbf{x}^* minimising the objective function is the global minimum.

Linear convex (constrained) problems can often be reformulated as SDP, thus exploiting IP algorithms to find the solution. The standard tricks for converting optimisation problems into SDP consist of introducing auxiliary variables and employing *Schur complements* [30]. For example, the least squares problem presented above can

be reformulated as:

$$\begin{aligned} & \underset{\{t, \mathbf{x}\}}{\text{minimise}} \quad t \\ & \text{subject to} \quad t - \mathbf{x}^T \mathbf{A}^T \mathbf{A} \mathbf{x} + 2\mathbf{y}^T \mathbf{A} \mathbf{x} \geq 0, \end{aligned} \quad (6.5)$$

where the variable t serves as an upper bound to the objective function, entailing that by minimising t we also find the minimum to the objective function. Note that the term $\mathbf{y}^T \mathbf{y}$ was dropped as it is a constant. The product $\mathbf{A}^T \mathbf{A} = \mathbf{Q}$ is positive-semidefinite, and thus $\mathbf{Q} = \mathbf{P}^T \mathbf{P}$ for some square matrix \mathbf{P} . By substituting $\mathbf{c} = -2\mathbf{A}^T \mathbf{y}$, the constraint becomes $t - \mathbf{x}^T \mathbf{P}^T \mathbf{P} \mathbf{x} - \mathbf{c}^T \mathbf{x} \geq 0$. Requiring this is equivalent to requiring

$$\mathbf{F}(\mathbf{x}) = \begin{pmatrix} \mathbf{I} & \mathbf{P}\mathbf{x} \\ \mathbf{x}^T \mathbf{P}^T & t - \mathbf{c}^T \mathbf{x} \end{pmatrix} \geq 0, \quad (6.6)$$

where \mathbf{I} is the identity matrix with same size as \mathbf{Q} . The equivalency is seen via the properties of the Schur complements listed in Section 2.2. Since \mathbf{I} is positive definite, then $\mathbf{F}(\mathbf{x}) \geq 0$ if and only if $t - \mathbf{x}^T \mathbf{P}^T \mathbf{P} \mathbf{x} - \mathbf{c}^T \mathbf{x} \geq 0$. This shows that the least squares problem can be recast as an SDP, with the benefit that constraints can be included in the optimisation problem via linear matrix inequalities.

6.2 Numerical inversion of the Laplace transform

As shown in the previous chapter, in the absence of exchange the MR signal is the average of the contributions from spins residing in different environments within the voxel. Independently of the chosen representation for these environments, the signal reads as the Laplace transform of the compartments' probability density distribution function. Here, the signal for a joint distribution of confinement tensors and effective diffusivities with probability density $\mathcal{P}(\mathbf{C}, D)$ is considered:

$$S(\mathbf{g}(t)) = S_0 \int E(\mathbf{g}(t), \mathbf{C}, D) \mathcal{P}(\mathbf{C}, D) d\mathbf{C} dD. \quad (6.7)$$

To numerically invert the Laplace transform and obtain $\mathcal{P}(\mathbf{C}, D)$ without assuming any parametric form for the distribution (as was instead presented for the DTD in the previous chapter, Section 5.2), one needs to consider a discrete distribution of h tensors. In this case, the probability density function is given by a sum of h delta functions:

$$\mathcal{P}(\mathbf{C}, D) = \sum_{i=1}^h w_i \delta_{\mathbf{C}_i}(\mathbf{C}) \delta_{D_i}(D), \quad (6.8)$$

and the signal is given by:

$$S(\mathbf{g}(t)) = \sum_{i=1}^h w_i (\mathbf{C}_i, D_i) E(\mathbf{g}(t), \mathbf{C}_i, D_i). \quad (6.9)$$

For N diffusion measurements performed by varying the gradient waveform $\mathbf{g}(t)$, the above expression can be cast into a vector-matrix product:

$$\underbrace{\mathbf{S}}_{N \times 1} = \underbrace{\mathbf{E}}_{N \times h} \underbrace{\mathbf{w}}_{h \times 1} \quad (6.10)$$

where \mathbf{S} is the vector containing the diffusion measurements obtained with N different $\mathbf{g}(t)$, \mathbf{E} is the matrix (sometimes referred to as dictionary) where each column contains the signal produced by a confinement tensor and effective diffusivity (or a diffusion tensor when considering a DTD instead) for the given measurements, and \mathbf{w} is the vector of probabilities associated with each item in the joint distribution.

The elements in vector \mathbf{w} can be obtained by solving the constrained least square problem:

$$\begin{aligned} & \underset{\mathbf{w}}{\text{minimise}} \quad \|\mathbf{S} - \mathbf{E} \mathbf{w}\|_2^2 \\ & \text{subject to} \quad w_i \geq 0, \end{aligned} \tag{6.11}$$

where the constraint requiring the positivity of the elements in \mathbf{w} follows from the interpretation of the w_i as probability densities. The problem in 6.11 can be solved by non-negative linear least-squares programs (NNLS), for example, the *lsqnonneg* Matlab (The MathWorks, Natick) function which implements the active-set algorithm described in [103]. Though the solution to 6.11 is unique, the ill-conditioned nature of the problem will manifest itself in that this solution will strongly depend on the noise [104]. It can indeed be shown that different noise realisations within the same noise statistics would lead to vastly different solutions [105]. In the following subsections two different strategies aiming at mitigating this problem are presented.

Adding a regularisation term

One strategy to reduce the noise-dependency of the solution is to include a regularisation term in 6.11 [103], [105]–[107]:

$$\begin{aligned} & \underset{\mathbf{w}}{\text{minimise}} \quad \|\mathbf{S} - \mathbf{E} \mathbf{w}\|_2^2 + \lambda \Phi(\mathbf{w}) \\ & \text{subject to} \quad w_i \geq 0, \end{aligned} \tag{6.12}$$

where $\lambda \geq 0$ determines the balance between the data consistency and the regularisation. The regularisation term can be selected in many ways, for example to promote sparsity [108]–[110] or smoothness [106], [111] in the solution. Even though the addition of a regularisation term reduces the ill-conditioning of the problem, the solution then shows features arising from the regularisation. Moreover, as the weight of the regularisation term increases, the solution becomes less consistent with the data.

Monte Carlo sampling

A different strategy consists of finding a set of plausible vectors \mathbf{w} for which the associated distributions fit the data equally well according to 6.11 [105]. An algorithm implementing this approach was proposed in [112], [113]. Briefly, one instance of the plausible solutions is found by iteratively constructing the dictionary \mathbf{E} by randomly sampling the parameter space; only the tensors for which the elements of \mathbf{w} , as found with an NNLS algorithm [103], are non-zero, are saved. After several iterations, only the n tensors with the highest w are retained. This process is then repeated a number of times, to collect a set of tensor distributions each describing equally well the MR signal. This approach was the one employed in paper IV and to obtain the results

presented in Figures 5.6 and 5.7 in the previous chapter. Since several solutions to the same problem are considered, this approach, referred to as Monte Carlo, allows the study of the uncertainty around the retrieved distributions based on statistical descriptors [105], [112], [113].

6.3 Estimation routines for q-space trajectory imaging

The MR signal considered in q-space trajectory imaging is determined by the non-diffusion weighted signal S_0 , the distribution average diffusion tensor $\hat{\mathbf{D}}$, and the covariance tensor \mathbf{C} :

$$S(\mathbf{B}) = S_0 e^{-\mathbf{B} : \hat{\mathbf{D}} + \frac{1}{2} \mathbf{B} : \mathbf{C}}. \quad (6.13)$$

These three are the quantities that we want to estimate from N diffusion measurements obtained by employing different b-values and shapes of the measurement B-tensor \mathbf{B} , $S(\mathbf{B}_n)$, $n = 1, \dots, N$. The problem can be formulated as a least squares, though the objective function is in this case non-linear:

$$\begin{aligned} \underset{\{S_0, \hat{\mathbf{D}}, \mathbf{C}\}}{\text{minimise}} \quad & \|\boldsymbol{\eta}\|_2^2 = \sum_{n=1}^N \eta_n^2 \\ \text{with } \eta_n = & S_0 e^{-\mathbf{B}_n : \hat{\mathbf{D}} + \frac{1}{2} \mathbf{B}_n : \mathbf{C}} - S(\mathbf{B}_n). \end{aligned} \quad (6.14)$$

Non-linear least squares

The problem in 6.14 can be readily solved using non-linear least squares (NLLS) routines, for example employing the Levenberg-Marquardt algorithm [114]–[116]. The downside of non-linear estimation is that there is no guarantee that the *global* minimum of the objective function will be reached, and the retrieved minimum will typically depend on the initial guess for the solution. Additionally, the iterative nature of the solvers generally results in lengthy computational times.

Weighted linear least squares

To avoid solving the non-linear problem, Equation 6.14 can be linearised by taking the logarithm. To correct for the heteroskedasticity introduced by the logarithmic operation, each error term η_n needs to be weighted. To first approximation, the weights can be determined by rearranging the equation on the right in 6.14 and taking the logarithm:

$$\ln(\eta_n + S(\mathbf{B}_n)) = \ln(S_0) - \mathbf{B}_n : \hat{\mathbf{D}} + \frac{1}{2} \mathbf{B}_n : \mathbf{C}. \quad (6.15)$$

For small η_n , the left side of the equation can be rewritten as:

$$\begin{aligned} \ln \left(S(\mathbf{B}_n) \left(1 + \frac{\eta_n}{S(\mathbf{B}_n)} \right) \right) &= \ln(S(\mathbf{B}_n)) + \ln \left(1 + \frac{\eta_n}{S(\mathbf{B}_n)} \right) \\ &\approx \ln(S(\mathbf{B}_n)) + \frac{\eta_n}{S(\mathbf{B}_n)}. \end{aligned} \quad (6.16)$$

This shows that for the log-linearised problem, the error terms need to be multiplied by the measured signal values:

$$\eta_n = S(\mathbf{B}_n) \left(\ln(S_0) - \mathbf{B}_n : \hat{\mathbf{D}} + \frac{1}{2} \mathbf{B}_n : \mathbf{C} - \ln(S(\mathbf{B}_n)) \right). \quad (6.17)$$

Adopting the measured signals as weights is typical for the estimation of DTI parameters [10], [117]. However, to obtain the best linear unbiased estimator, the weighting should be done with the noise-free signal values [118]. Since these are in practice not available, iterative re-weighting strategies, where the weights are updated with the noise-free model prediction of the signal, can be employed [119].

The log-linearised problem can then be cast into matrix form:

$$\underbrace{\boldsymbol{\eta}}_{N \times 1} = \underbrace{\mathbf{A}}_{N \times 28} \underbrace{\mathbf{x}}_{28 \times 1} - \underbrace{\mathbf{y}}_{N \times 1} \quad (6.18)$$

where \mathbf{A} is the design matrix containing the experimental parameters multiplied by the signal values, \mathbf{x} is the vector of unknown parameters to be estimated (S_0 , the 6 six unique elements of $\hat{\mathbf{D}}$, and the 21 unique elements of \mathbf{C}), and \mathbf{y} is the vector containing the log of the measured signals multiplied by the signal values. The objective is to minimise the squared norm of $\boldsymbol{\eta}$, which can be achieved via conventional linear least squares routines. As this essentially involves inverting a matrix, the solution to the linearised problem can be obtained very quickly compared to its non-linear counterpart. Moreover, if the solution exists, it is guaranteed to be the global minimum, and there is no need for an initial guess for the solution.

Semidefinite programming

The log-linearised least squares problem can also be reformulated as a semidefinite programming as explained in Section 6.1. The advantage of employing this formulation rather than the least squares one is that it naturally allows for constraints expressed via positive semidefinite matrices to be included in the problem. For example, since both the average diffusion tensor $\hat{\mathbf{D}}$ and the covariance tensor \mathbf{C} represent a covariance matrix, their estimates should be positive semidefinite [89]. This can be strictly required in the SDP formulation by expanding the constraint matrix $\mathbf{F}(\mathbf{x})$ in 6.6 to be:

$$\mathbf{F}(\mathbf{x}) = \begin{pmatrix} \mathbf{I} & \mathbf{P}\mathbf{x} & 0 & 0 \\ \mathbf{x}^T \mathbf{P}^T & t - \mathbf{c}^T \mathbf{x} & 0 & 0 \\ 0 & 0 & \hat{\mathbf{D}} & 0 \\ 0 & 0 & 0 & \mathbf{C} \end{pmatrix} \geq 0, \quad (6.19)$$

where \mathbf{C} is the 6×6 representation of \mathbf{C} .

QTI+ and QTI±

In papers I and II we developed two constrained frameworks, named QTI+ and QTI±, for estimating the QTI parameters under observance of several physical and

mathematical conditions dictated by the model itself. These involve the positivity of the $\hat{\mathbf{D}}$, \mathbf{C} , and \mathbf{M} tensors, which was considered in QTI+, and observance of the “speed limit” for the diffusivities which cannot exceed the value of free water, which was instead added in QTI \pm . As imposing these conditions often involves requiring matrices to be positive semi-definite, the SDP formulation is the natural choice for solving the constrained problem. Moreover, since the estimation of model parameters for each voxel is independent, fitting over N voxels can be computed at once by having as objective function the sum of all the objective functions, and having all the constraints included in the diagonal of the matrix $\mathbf{F}(\mathbf{x})$. With this formulation, the SDP solver is called only once instead of N times, resulting in a tremendous reduction in computational time.

The frameworks are implemented in Matlab (The MathWorks, Natick), and QTI+ was made freely available¹. Both SDP and non-linear least squares are used to obtain robust estimates for S_0 , $\hat{\mathbf{D}}$, and \mathbf{C} . A description of the software was published but is not included in this thesis [90]. We also made a Python implementation of QTI+ available through the `dipy` library [120].

6.4 A machine learning approach

Estimation of model parameters from data is increasingly being attained using artificial intelligence. In the dMRI field, machine learning (ML) has, for example, been investigated for avoiding lengthy computations due to non-linear objective functions [121]–[123], overcome the degeneracy problem where more than one solution can fit the data [121], [124], [125], and perform model parameters estimation using minimal, clinical-friendly dMRI protocols [126], [127]. In this section, a simple but powerful neural network (NN) architecture for performing model fitting is described. Results are presented for QTI and DTD applied to data from healthy subjects, brain tumor patients, and COVID-19 survivors.

Neural network architecture

The employed NN for the estimation of QTI and DTD parameters, named QTI_{ML}+ and DTD_{ML} respectively, are shown in Figure 6.1. Both are based on an encoder/decoder architecture, where the encoder consists of three fully connected hidden layers with exponential linear unit (ELU) activation [128], and the decoder implements the functional form of the considered model for the dMRI data. In DTD_{ML}, dropout [129] is used on the last hidden layer to implement the Monte Carlo Dropout technique [130], detailed later. The output of the encoder is thus interpreted as being the QTI and DTD model parameters that are to be estimated.

The NN is trained in a self-supervised voxel-wise fashion, where the loss objective is to minimise the error between the measured dMRI data (input) and predicted dMRI signal (output) for a voxel, thus essentially performing regression. A typical dMRI brain dataset comprising ≈ 50000 voxels is sufficient to train the NN for the estimation of the QTI model parameter. In the case of the DTD estimation, it becomes

¹<https://github.com/DenebBoito/qtiplus>

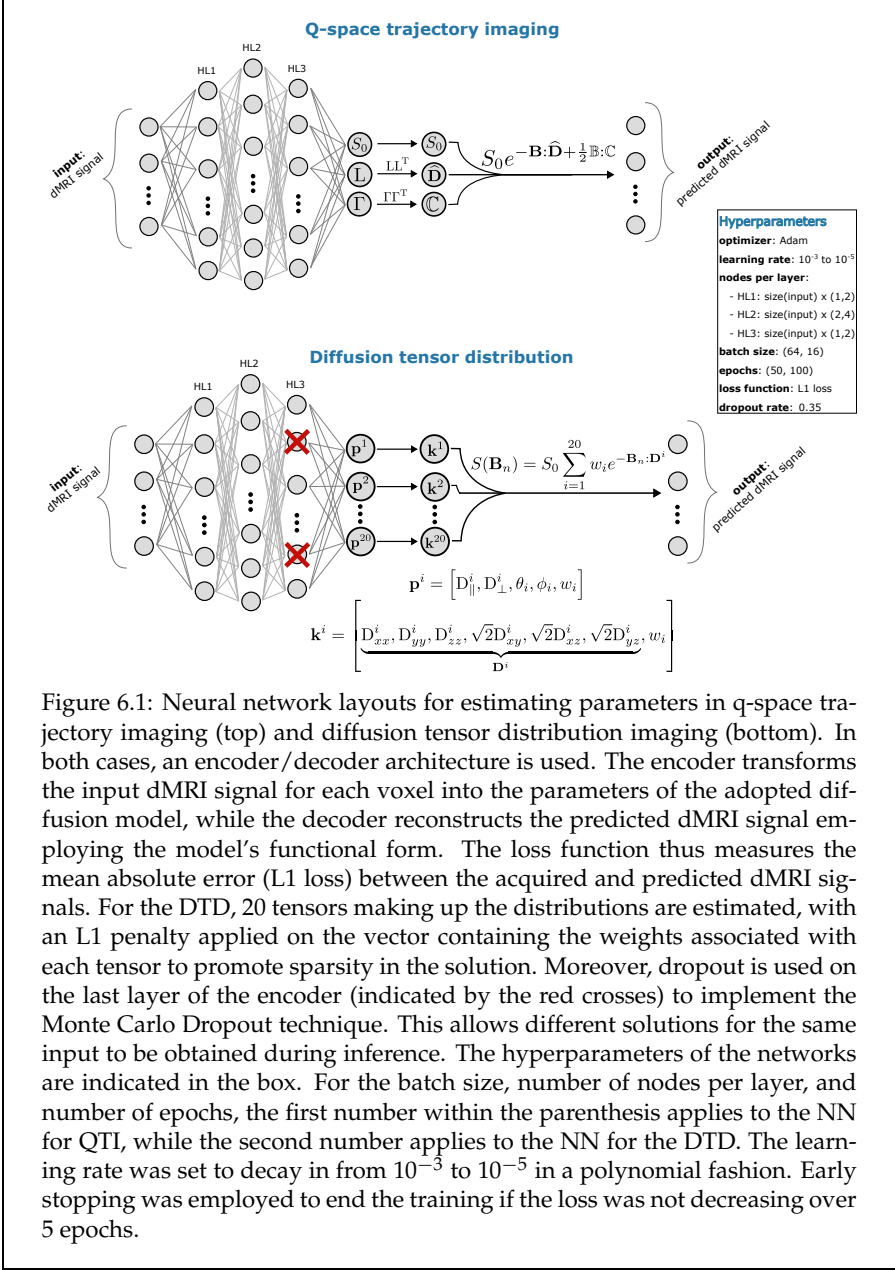


Figure 6.1: Neural network layouts for estimating parameters in q-space trajectory imaging (top) and diffusion tensor distribution imaging (bottom). In both cases, an encoder/decoder architecture is used. The encoder transforms the input dMRI signal for each voxel into the parameters of the adopted diffusion model, while the decoder reconstructs the predicted dMRI signal employing the model's functional form. The loss function thus measures the mean absolute error (L1 loss) between the acquired and predicted dMRI signals. For the DTD, 20 tensors making up the distributions are estimated, with an L1 penalty applied on the vector containing the weights associated with each tensor to promote sparsity in the solution. Moreover, dropout is used on the last layer of the encoder (indicated by the red crosses) to implement the Monte Carlo Dropout technique. This allows different solutions for the same input to be obtained during inference. The hyperparameters of the networks are indicated in the box. For the batch size, number of nodes per layer, and number of epochs, the first number within the parenthesis applies to the NN for QTI, while the second number applies to the NN for the DTD. The learning rate was set to decay in from 10^{-3} to 10^{-5} in a polynomial fashion. Early stopping was employed to end the training if the loss was not decreasing over 5 epochs.

instead necessary to increase the number of training examples, for example by generating synthetic data. In our experiments, we pre-train the network on synthetic data (≈ 2 million voxels) before fine-tuning it or applying it on experimental data.

Q-space trajectory imaging

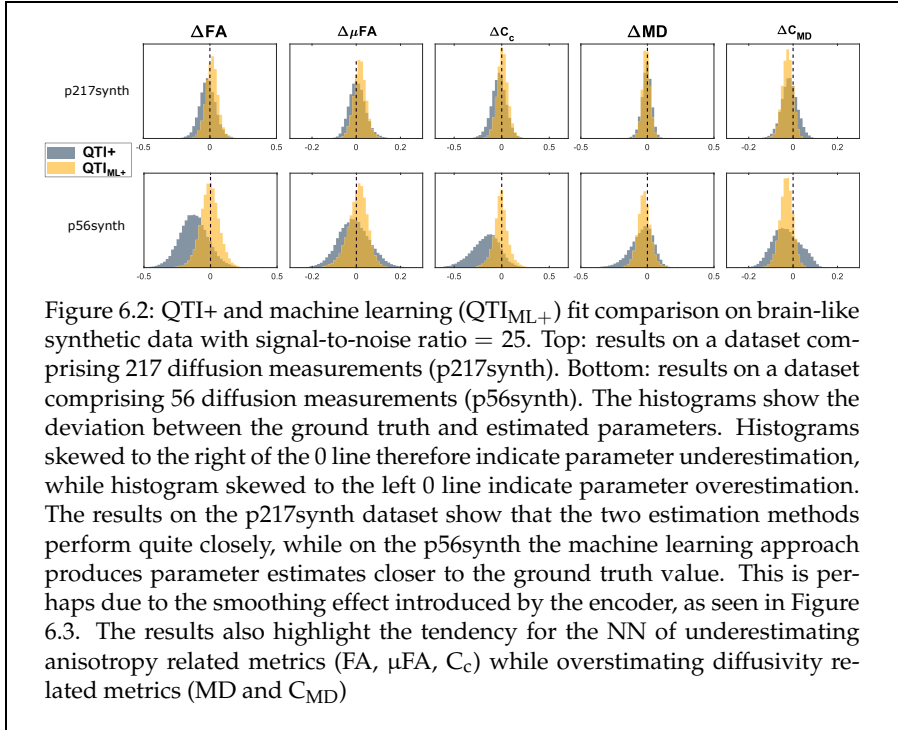
The top panel in Figure 6.1 shows that positivity constraints acting on the $\hat{\mathbf{D}}$ and \mathbf{C} tensors in QTI can be strictly imposed within the network. The \mathbf{L} and $\mathbf{\Gamma}$ matrices in the encoder output represent the lower triangular matrices in the Cholesky factorisation of the average diffusion and covariance tensors, respectively, such that

$$\hat{\mathbf{D}} = \mathbf{L}\mathbf{L}^T \quad \text{and} \quad \mathbf{C} = \mathbf{\Gamma}\mathbf{\Gamma}^T, \quad (6.20)$$

where \mathbf{C} is the 6×6 representation of \mathbf{C} . Having the constraints strictly imposed within the NN is a great advantage compared to relying on the network to learn the conditions from the training examples.

Figure 6.2 shows a comparison between the invariants obtained from the $\hat{\mathbf{D}}$ and \mathbf{C} tensors as estimated using QTI+ and the machine learning approach. The comparison is drawn based on two brain-like synthetic datasets that were generated by computing the QTI signal from parameters obtained by employing QTI+ on a publicly available dataset and its subsampled versions [26], [89]. The experimental datasets are hereafter referred to as p217 and p56 according to the number of diffusion measurements included in the respective sets. Noise from the Rician distribution was added to the synthetic data generated as described above, obtaining the p217synth and p56synth datasets with a signal-to-noise ratio of 25. The QTI+ and QTI_{ML+} performances were assessed by computing the difference between the ground truth invariants and those obtained with the two methods. The results show that the ML approach performs similarly to QTI+ on the larger dataset, while providing closer-to-ground truth parameters when fewer data points are employed for the estimation. This is possibly due to the inherent denoising resulting from the data compression carried out by the encoder segment of the NN. The denoising and smoothing attained with the ML approach are clearly seen in Figure 6.3, where the invariants obtained with QTI+ and QTI_{ML+} from the experimental p217 and p56 datasets are displayed.

Figure 6.4 shows tract-based spatial statistics (TBSS) [131] results obtained by comparing the brain white matter of patients previously hospitalised for COVID-19 and healthy controls using fits produced with QTI \pm and QTI_{ML+}. The results obtained with QTI \pm were used in paper III, where a detailed description of the clinical study is given. Here the focus is only on comparing the two fitting approaches. The QTI_{ML+} fits were obtained by training separate networks on each subject. QTI \pm and QTI_{ML+} produced rather consistent results, highlighting that the relevant patterns in the various QTI maps are preserved despite the smoothing introduced by the neural network's encoder. Note that the “speed limit” conditions considered in QTI \pm can also be enforced with the ML approach, albeit in a soft manner. This corresponds to adding penalties to the cost function whenever the conditions are violated. However, training such NN is more complicated and typically requires lengthier computations, without guaranteeing clear improvements to the results already attainable with QTI_{ML+}. Figure 6.5 shows results obtained from a brain tumor dataset for QTI+, QTI_{ML+}, and QTI_{ML+}^{*}. The difference between QTI_{ML+} and QTI_{ML+}^{*} is that while the first is trained by fitting the tumor data directly, the second is trained on data from a healthy volunteer and then applied on the tumor data. While the fit residuals are clearly lower for QTI_{ML+}, the difference between the invariants computed with both ML methods and QTI+ is similar, suggesting that training on the “healthy voxels” al-



ready spans the entire parameter space of the diffusion model, and results on unseen “disease voxels” can be obtained by mere interpolation. This result is of relevance for two reasons. First, trained neural networks do not require expensive and high-end machines to run inferences on new data. As such, they are a more portable technology compared to that typically needed for estimating parameters using non-linear objective functions. Second, the time gain. For the rather simple neural network architectures considered here (with in general less than 250000 trainable parameters), inference can be achieved for an entire brain dataset in less than a second. As a reference, the computational times for the three routines employed in Figure 6.5, timed on the CPU of the same high-end desktop computer, were ≈ 15 minutes for QTI+, ≈ 5 minutes for QTI_{ML+}, and ≤ 1 second for QTI_{ML+}^{*} (after ≈ 5 minutes for pre-training on the data from the healthy subject). Note that the SDP solver employed in QTI+ (Mosek, MOSEK ApS, Denmark) is a commercial product and it is free to use only for academic research. Other open-source SDP solvers, like SDPT3 [132], are typically 2 – 3 times slower. Therefore, whenever time is of concern, the machine learning approach is a truly viable option.

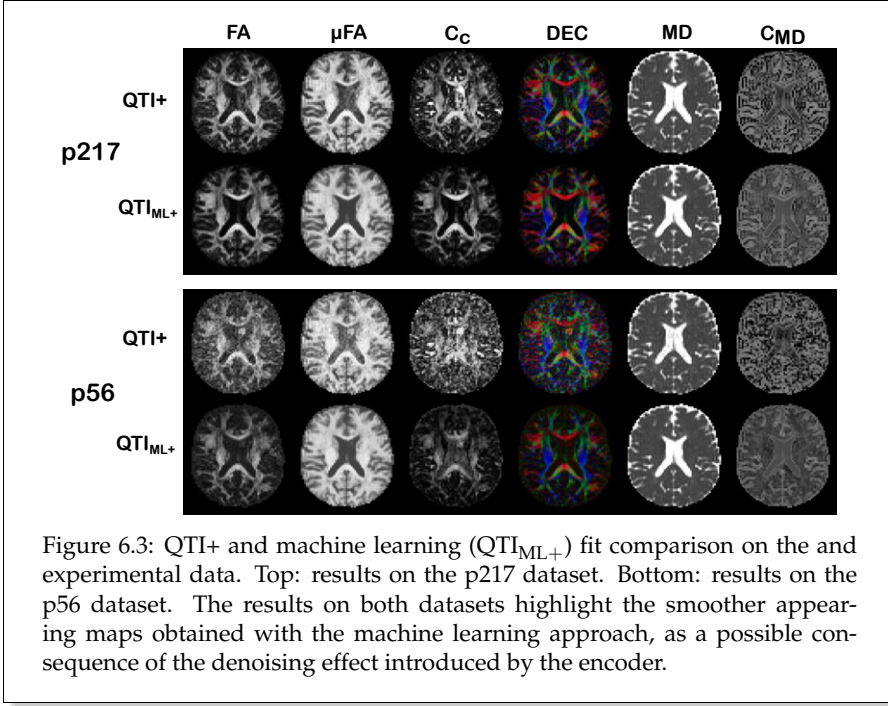


Figure 6.3: QTI+ and machine learning (QTI_{ML+}) fit comparison on the and experimental data. Top: results on the p217 dataset. Bottom: results on the p56 dataset. The results on both datasets highlight the smoother appearing maps obtained with the machine learning approach, as a possible consequence of the denoising effect introduced by the encoder.

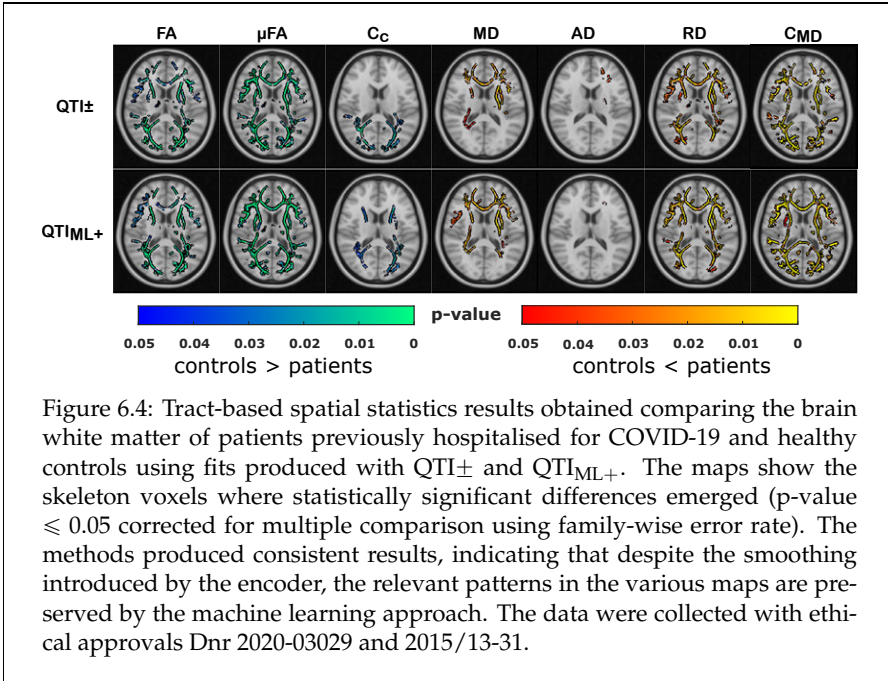
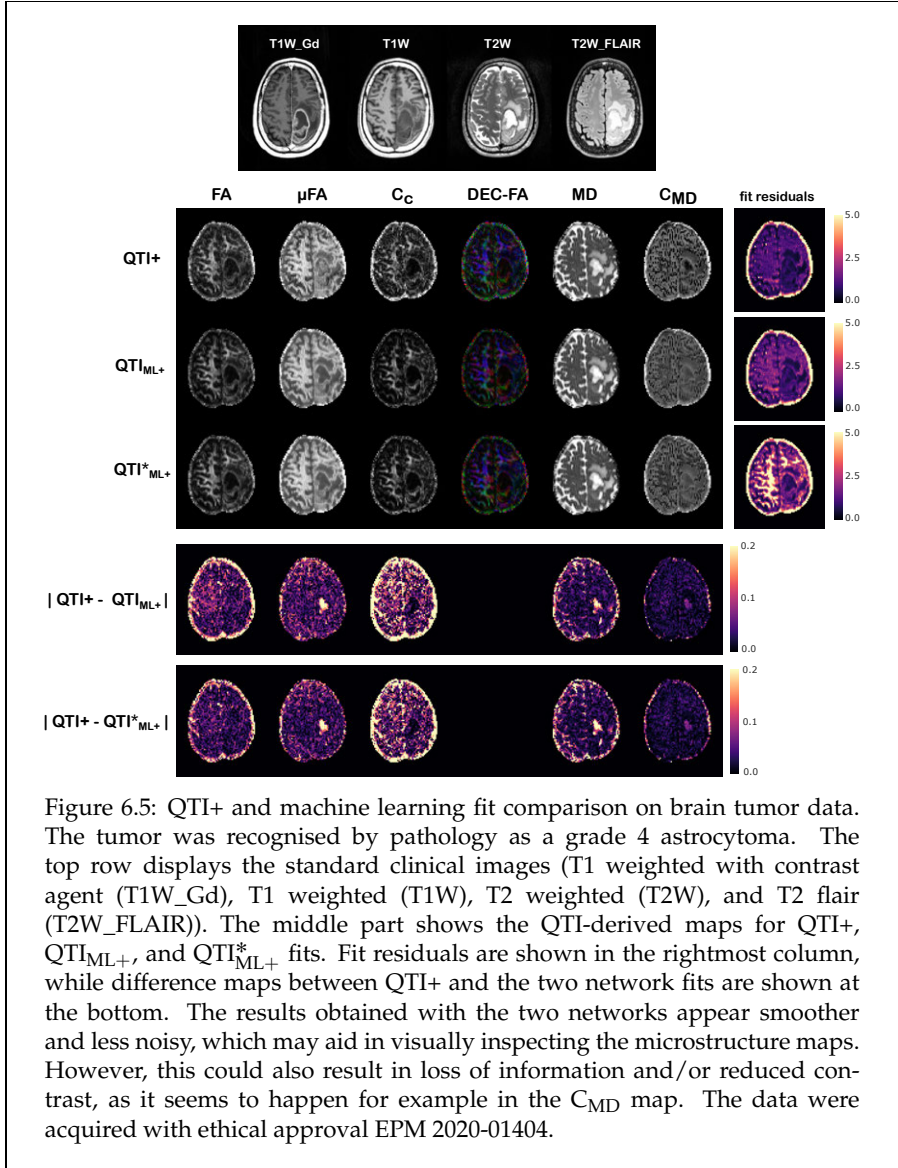


Figure 6.4: Tract-based spatial statistics results obtained comparing the brain white matter of patients previously hospitalised for COVID-19 and healthy controls using fits produced with QTI± and QTI_{ML+}. The maps show the skeleton voxels where statistically significant differences emerged (p-value ≤ 0.05 corrected for multiple comparison using family-wise error rate). The methods produced consistent results, indicating that despite the smoothing introduced by the encoder, the relevant patterns in the various maps are preserved by the machine learning approach. The data were collected with ethical approvals Dnr 2020-03029 and 2015/13-31.



Diffusion tensor distribution

The bottom panel of Figure 6.1 shows the NN architecture for the estimation of axisymmetric diffusion tensors distributions. Each node \mathbf{p}^i in the encoder's output is, in this case, interpreted as the $D_{\parallel}^i, D_{\perp}^i, \theta_i$ and ϕ_i components, and associated w_i weight of the i -th diffusion tensor in the distribution. From these components, the 6 elements of the diffusion tensors are obtained and fed into the decoder to compute the predicted dMRI signal.

The last hidden layer of the decoder is followed by a dropout layer, indicated by the red crosses in Figure 6.1. Although dropout is used as a regularisation when training neural networks [129], here it is primarily employed to implement the Monte Carlo Dropout technique [130]. Contrary to the standard use of dropout layers, which are turned off at inference time, in Monte Carlo Dropout these are maintained active so that different solutions can be obtained for the same input. In this way, the NN can be used to mimic the Monte Carlo sampling method for the inversion of the Laplace transform which was described in Section 6.2, thus computing several solutions that fit the input signal. The major advantage of the machine learning approach is then found in the time it takes to produce these multiple solutions. While the Monte Carlo sampling may take days to complete [113], the trained neural network can produce hundreds of different solutions in a matter of seconds. Figure 6.6 shows example results of statistical descriptors for DTDs estimated with the Monte Carlo sampling strategy (DTD_{NNLS}) and the machine learning (DTD_{ML}) approach on the p217 dataset. Similar to what was discussed for QTI, the DTD_{ML} tends to produce smoother maps compared to DTD_{NNLS} .

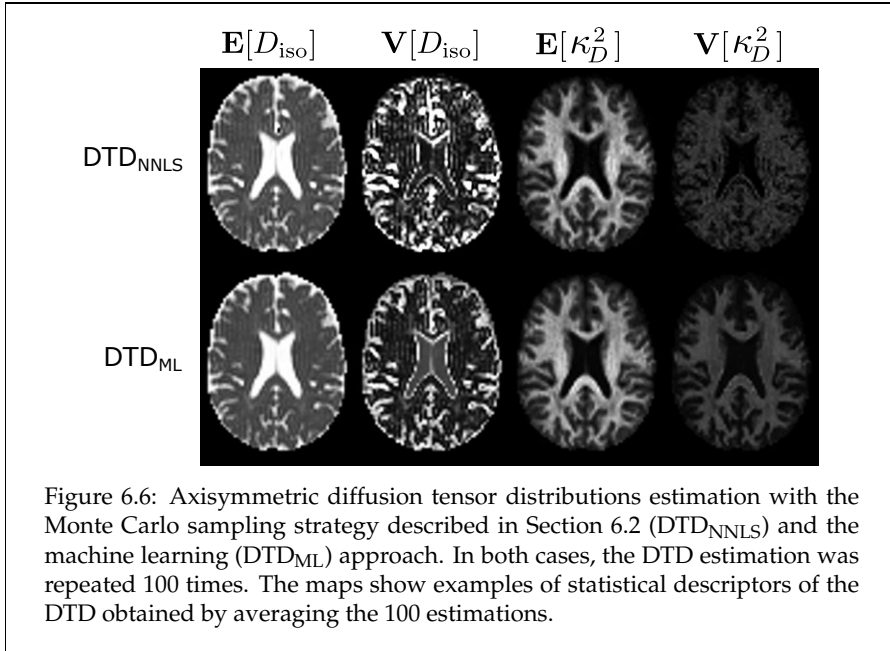


Figure 6.6: Axisymmetric diffusion tensor distributions estimation with the Monte Carlo sampling strategy described in Section 6.2 (DTD_{NNLS}) and the machine learning (DTD_{ML}) approach. In both cases, the DTD estimation was repeated 100 times. The maps show examples of statistical descriptors of the DTD obtained by averaging the 100 estimations.

7

Review of papers & conclusions

The overarching goal of this thesis was promote the clinical adoption of diffusion MRI measurements performed with generalised gradient waveforms. In particular, the focus was directed towards improving the methods currently employed for the analysis of the data. This translated into creating algorithms for robust estimation of q-space trajectory imaging (QTI) parameters (papers I and II, Section 6.4), employing the developed methods for assessing the brain microstructure of COVID-19 survivors (paper III), and suggesting an alternative to the diffusion tensor distribution (DTD) for modelling the collection of compartments making up the intravoxel tissue composition (paper IV). This last chapter presents an overview of the papers and discuss their main contributions in relation to the aims set forth in Chapter 1.

7.1 Papers I & II

Aim: Develop methods for producing reliable estimates for the parameters attainable via tensor-valued diffusion MRI

Investigative studies employing q-space trajectory imaging have demonstrated that the diffusion metrics accessed by employing this technique can be extremely instrumental in better characterising several neurological diseases compared to more widely adopted diffusion methods [17], [18], [20], [21], [133]. The first two papers thus focused on developing optimisation schemes for robustly estimating the diffusion and covariance tensors accessed via QTI. Several mathematical and physical properties of the diffusion $\hat{\mathbf{D}}$, covariance \mathbf{C} , and second moment \mathbf{M} tensors estimated in QTI were identified, and included in two constrained frameworks which enforce them during model fitting. In paper I, the focus was directed towards ensuring the positivity of the \mathbf{D} , \mathbf{C} , and \mathbf{M} tensors, while in paper II the focus was on “speed limit” conditions aiming at prohibiting diffusion faster than that of free water. Since these conditions are expressed via positive semidefinite matrices, they can be efficiently imposed using semidefinite programming. The developed routines were called QTI+ and QTI±, respectively, for nomenclature consistency with other methods employed to enforce positivity conditions in diffusion MRI [134].

Through simulations and experimental data, the results obtained in paper I showed how the constrained estimation improved the reliability of the estimated quantities with respect to noise, especially when compared to those achieved with unconstrained methods. Moreover, it was clearly shown on a public dataset [26] that when the \mathbf{D} , \mathbf{C} , and \mathbf{M} tensors are estimated with the (currently employed) unconstrained methods, there are violations of the positivity conditions in almost every voxel. This means that the obtained estimates are not mathematically or physically meaningful, thus justifying the need for the constrained routines. The speed limit conditions considered in paper II were then shown to further improve the results attainable with QTI+, especially in brain regions where voxels present partial voluming with free water pools.

Additionally, we found that even though each voxel is fitted independently, the constrained estimation yields smoother-appearing maps. A third important outcome of these works was learning that constrained optimisation can obviate imperfections in the data sampling schemes, and requires fewer datapoints for the estimation. These results are particularly relevant for the clinical translation of q-space trajectory imaging. Indeed, to aid patients' comfort we should strive to keep the scan time as short as possible, which requires our estimation routines to perform robustly even on sub-optimally sampled data. The creation of robust estimation routines thus complements the efforts towards designing parsimonious data acquisition protocols for QTI [135]. Moreover, we envision that similar results regarding the possibility of faster acquisitions would be found for other diffusion MRI techniques for which mathematical and physical constraints are available [134], [136].

The time gain on the acquisition side can be complemented by the fast parameter estimation attainable with the machine learning approach presented in Section 6.4. Indeed, the constrained estimation achieved via semidefinite programming tends to be much slower compared to the unconstrained least square fit, and typically requires high-end machinery not often available in clinical settings. While for the offline estimation of QTI parameters this does not constitute an obstacle, in cases where a rapid initial assessment of the microstructure is necessary, faster methods are required. The machine learning approach nicely fits these requirements by being extremely lightweight and computationally quick. Moreover, the considered architecture allows the two most influential positivity constraints [89] to be strictly imposed within the network, thus ensuring that the estimated parameters fall within a mathematically and physically meaningful range.

7.2 Paper III

Aim: Investigate patients' brain microstructure using diffusion MRI with generalised gradient waveforms

Increased evidence for the long-term effects of COVID-19 on the central nervous system is being reported [137]–[143]. These typically involve fatigue, cognitive impairment, stress, and anxiety. In this work we employed the QTI± scheme developed in paper II to investigate the brain white matter microstructure of patients previously hospitalised for COVID-19, and who still suffer from neurological symptoms months

after hospital discharge. While conventional MR images did not reveal typical patterns that could be linked to the experienced symptomatology [144], the results obtained in this work showed widespread alterations to the patients' white matter microstructure.

The results were the outcome of a group comparison between 16 healthy controls (11 males) and 16 male patients. The comparison was based on the several diffusion metrics attainable with QTI (MD, AD, RD, C_{MD} , FA, μ FA, C_c), and was performed using the tract-based spatial statistic (TBSS) method [131]. The statistical analysis revealed widespread reductions in FA and μ FA, while reductions in C_c were mostly located in the parietal lobe. These changes could be indicative of oedema, axonal damage, and loss of fibre orientation coherence, respectively. Importantly, having access to μ FA and C_c , thus disentangling the contributions of local anisotropy and structural organisation to the macroscopic anisotropy, allowed more specific insights into the possible pathogenesis. In particular, it showed that the majority of the observed changes in anisotropy are due to local rather than structural alterations, with only certain regions of the brain being affected by both mechanisms. Moreover, as μ FA was found to vary more frequently than FA, certain changes could have gone undetected if this metric was not available. Widespread changes were also found for MD, RD, and C_{MD} , with their values being higher in the patient population. An increase in RD is typically associated with demyelination [145], while increased C_{MD} could indicate cellular membrane disruption, cell swelling, and cellular atrophy [20].

Overall, the results once more demonstrated the sensitivity of diffusion MRI to microstructural alterations otherwise not visible with other MR imaging sequences, with the information provided by the QTI-accessible metrics allowing a more in-depth characterisation of the detected changes.

7.3 Paper IV

Aim: Extend the analysis of diffusion MRI with generalised gradient waveforms beyond the free diffusion assumption

The analysis of tensor-valued dMRI data remains largely based on the assumption of the signal rising from a collection of compartments each exhibiting free diffusion, i.e. a distribution of diffusion tensors. As explained in Chapter 5, one then wishes to recover either the diffusion tensor distribution making up the tissue [23], or estimate the parameters of some predefined functional form for it [17], [22], [24]. In either case, statistical descriptors of the intravoxel tissue compositions can be obtained.

In this paper we propose instead to represent each compartment in the tissue with a model for restricted diffusion, namely the confinement tensor [60]. Such representation overcomes the assumption of free diffusion in a compartmentalised medium. Moreover, unlike for the diffusion tensor, the MR signal implied by the confinement tensor model is inextricably linked to the temporal dependence of the diffusion gradient waveform, rather than simply depending on the B-tensor. Through simulations we highlighted that, especially for spherical tensor encoding, where the measurement is assumed to be rotationally invariant with respect to the direction of the diffusion gradient, the signal modulation due to restricting boundaries cannot possibly

be captured via the B-tensor only. Ignoring the diffusion time-dependence effects on isotropic diffusion measurements was shown to result in errors and biases in the metrics derived from the diffusion tensor distribution [25], [51], [83], [146]. In particular, the excess kurtosis arising from compartmental restrictions would erroneously contribute to the bulk and shear variances accessed via the diffusion tensor distribution, thus introducing biases which could confound the assessment of the microstructure [25], [147]–[149].

Even though time-dependent diffusion has been observed in brain white-matter in clinical acquisitions [149]–[151], these biases would ultimately depend on the parameters of the experiment [152]. As the duration of the diffusion gradient pulses is prolonged, the compartmental kurtosis would disappear, eventually leading to a Gaussian spin phase distribution [65], [153], [154]. As explained in Section 4.4, under this condition the confinement tensor becomes the effective model of restricted diffusion. In the paper we demonstrated via simulations that the generalised diffusion gradients employed to achieve current clinical tensor-valued protocols are effectively long-pulsed gradients, and the signal modulation due to restricted diffusion is in this case perfectly described by the confinement tensor model. Therefore, the diffusion metrics obtained from the distribution of confinement tensors should not exhibit any bias from the compartmental kurtosis due to confined diffusion. As such, the confinement tensor model constitutes the natural choice for representing each isolated domain in a multi-compartment picture of the tissue microstructure.

Expressions for computing distributions of confinement tensors and performing q-space trajectory imaging with confined subdomains were given. Examples of confinement tensor distributions for different brain tissue types as recovered via the numerical inversion of the Laplace transform [23], [112] described in Section 6.2 were shown. Finally, it was demonstrated through simulations that by adding diffusion measurements with varied frequency content, it is possible to increase the precision of the estimated compartmental diffusivity.

7.4 Conclusions

MRI measurements of water diffusion beyond the Stejskal-Tanner experiment permits targeting specific microscopic properties of biological tissues, thus allowing for a better in-vivo characterisation of these complex media. This thesis has dealt with a particular class of measurements based on generalised gradient waveforms which, by relying on the assumption of the tissue being composed of several non-exchanging compartments, disentangles different sources of intravoxel heterogeneity.

As it was shown in paper III as well as in other works [18], [20], [21], [155], measures of intravoxel heterogeneity improve the assessment of microstructural changes in the presence of diseases. Moreover, they may disentangle competing intravoxel effects which lead to opposite directional changes in voxel-level metrics such as fractional anisotropy [133], [156], [157]. Given the clinical feasibility of tensor-valued diffusion measurements [135], [158], [159], and the robust and fast analysis methods developed within this thesis (papers I and II) [89], [160], investigations of the tissue microstructure via intravoxel diffusion metrics could become routine clinical practice.

The work performed in paper IV further contributed to this endeavour by proposing a better model for each isolated compartment in the tensor distribution representing the tissue microstructure. Differently from the diffusion tensor, the confinement tensor model was shown to perfectly capture the diffusion time-dependence due to restrictions in data acquired with the clinically available tensor-valued diffusion MRI protocols. Therefore, future studies should consider employing such model for investigations of intravoxel heterogeneity.

Bibliography

- [1] D. Le Bihan and E. Breton, "Imagerie de diffusion in vivo par résonance magnétique nucléaire," *Comptes rendus de l'Académie des sciences. Série 2, Mécanique, Physique, Chimie, Sciences de l'univers, Sciences de la Terre*, vol. 301, no. 15, pp. 1109–1112, 1985, ISSN: 0764-4450.
- [2] D. Le Bihan, E. Breton, D.ALLEMAND, P. Grenier, E. Cabanis, and M. Laval-Jeantet, "MR imaging of intravoxel incoherent motions: Application to diffusion and perfusion in neurologic disorders.," en, *Radiology*, vol. 161, no. 2, pp. 401–407, Nov. 1986, ISSN: 0033-8419, 1527-1315. DOI: 10 . 1148 / radiology.161.2.3763909.
- [3] M. E. Moseley, Y. Cohen, J. Kucharczyk, J. Mintorovitch, H. S. Asgari, M. F. Wendland, J. Tsuruda, and D. Norman, "Diffusion-weighted MR imaging of anisotropic water diffusion in cat central nervous system.," en, *Radiology*, vol. 176, no. 2, pp. 439–445, Aug. 1990, ISSN: 0033-8419, 1527-1315. DOI: 10 . 1148/radiology.176.2.2367658.
- [4] M. E. Moseley, J. Kucharczyk, H. S. Asgari, and D. Norman, "Anisotropy in diffusion-weighted MRI," en, *Magnetic Resonance in Medicine*, vol. 19, no. 2, pp. 321–326, Jun. 1991, ISSN: 07403194, 15222594. DOI: 10 . 1002 / mrm . 1910190222.
- [5] C. Beaulieu, "The basis of anisotropic water diffusion in the nervous system - a technical review," en, *NMR in Biomedicine*, vol. 15, no. 7-8, pp. 435–455, Nov. 2002, ISSN: 0952-3480, 1099-1492. DOI: 10 . 1002 / nbm . 782.
- [6] P. Basser, J. Mattiello, and D. LeBihan, "MR diffusion tensor spectroscopy and imaging," en, *Biophysical Journal*, vol. 66, no. 1, pp. 259–267, Jan. 1994, ISSN: 00063495. DOI: 10 . 1016/S0006-3495(94)80775-1.
- [7] S. Mori, B. J. Crain, V. P. Chacko, and P. C. M. Van Zijl, "Three-dimensional tracking of axonal projections in the brain by magnetic resonance imaging," en, *Annals of Neurology*, vol. 45, no. 2, pp. 265–269, Feb. 1999, ISSN: 0364-5134, 1531-8249. DOI: 10 . 1002/1531-8249(199902)45:2<265::AID-ANA21>3.0.CO;2-3.
- [8] P. J. Basser, S. Pajevic, C. Pierpaoli, J. Duda, and A. Aldroubi, "In vivo fiber tractography using DT-MRI data," en, *Magnetic Resonance in Medicine*, vol. 44, no. 4, pp. 625–632, Oct. 2000, ISSN: 0740-3194, 1522-2594. DOI: 10 . 1002/1522-2594(200010)44:4<625::AID-MRM17>3.0.CO;2-O.
- [9] E. O. Stejskal and J. E. Tanner, "Spin Diffusion Measurements: Spin Echoes in the Presence of a Time-Dependent Field Gradient," en, *The Journal of Chemical Physics*, vol. 42, no. 1, pp. 288–292, Jan. 1965, ISSN: 0021-9606, 1089-7690. DOI: 10.1063/1.1695690.

- [10] P. J. Basser, Mattiello, J., and LeBihan, D., "Estimation of the effective self-diffusion tensor from the NMR spin echo," vol. 103, pp. 247–254, 1994.
- [11] D. G. Cory, A. N. Garroway, and J. B. Miller, "Applications of Spin Transport as a Probe of Local Geometry," *Polymer Preprints*, vol. 31, pp. 149–150, 1990.
- [12] P. P. Mitra, "Multiple wave-vector extensions of the NMR pulsed-field-gradient spin-echo diffusion measurement," en, *Physical Review B*, vol. 51, no. 21, pp. 15 074–15 078, Jun. 1995, ISSN: 0163-1829, 1095-3795. DOI: 10 . 1103/PhysRevB.51.15074.
- [13] N. Shemesh, E. Özarslan, T. Adiri, P. J. Basser, and Y. Cohen, "Noninvasive bipolar double-pulsed-field-gradient NMR reveals signatures for pore size and shape in polydisperse, randomly oriented, inhomogeneous porous media," en, *The Journal of Chemical Physics*, vol. 133, no. 4, p. 044 705, Jul. 2010, ISSN: 0021-9606, 1089-7690. DOI: 10 . 1063/1 . 3454131.
- [14] P. T. Callaghan and M. E. Komlosh, "Locally anisotropic motion in a macroscopically isotropic system: Displacement correlations measured using double pulsed gradient spin-echo NMR," en, *Magnetic Resonance in Chemistry*, vol. 40, no. 13, S15–S19, Dec. 2002, ISSN: 0749-1581, 1097-458X. DOI: 10 . 1002/mrc . 1122.
- [15] E. Özarslan and P. J. Basser, "Microscopic anisotropy revealed by NMR double pulsed field gradient experiments with arbitrary timing parameters," en, *The Journal of Chemical Physics*, vol. 128, no. 15, p. 154 511, Apr. 2008, ISSN: 0021-9606, 1089-7690. DOI: 10 . 1063/1 . 2905765.
- [16] M. Schachter, M. Does, A. Anderson, and J. Gore, "Measurements of Restricted Diffusion Using an Oscillating Gradient Spin-Echo Sequence," en, *Journal of Magnetic Resonance*, vol. 147, no. 2, pp. 232–237, Dec. 2000, ISSN: 10907807. DOI: 10 . 1006/jmre . 2000 . 2203.
- [17] C.-F. Westin, H. Knutsson, O. Pasternak, F. Szczepankiewicz, E. Özarslan, D. van Westen, C. Mattisson, M. Bogren, L. J. O'Donnell, M. Kubicki, D. Topgaard, and M. Nilsson, "Q-space trajectory imaging for multidimensional diffusion MRI of the human brain," en, *NeuroImage*, vol. 135, pp. 345–362, Jul. 2016, ISSN: 10538119. DOI: 10 . 1016/j . neuroimage . 2016 . 02 . 039.
- [18] B. Lampinen, A. Zampeli, I. M. Björkman-Burtscher, F. Szczepankiewicz, K. Källén, M. Compagno Strandberg, and M. Nilsson, "Tensor-valued diffusion MRI differentiates cortex and white matter in malformations of cortical development associated with epilepsy," en, *Epilepsia*, vol. 61, no. 8, pp. 1701–1713, Aug. 2020, ISSN: 0013-9580, 1528-1167. DOI: 10 . 1111/epi . 16605.
- [19] F. Szczepankiewicz, C.-F. Westin, and M. Nilsson, "Gradient waveform design for tensor-valued encoding in diffusion MRI," en, *Journal of Neuroscience Methods*, vol. 348, p. 109 007, Jan. 2021, ISSN: 01650270. DOI: 10 . 1016/j . jneumeth . 2020 . 109007.

- [20] F. Szczepankiewicz, D. Van Westen, E. Englund, C.-F. Westin, F. Ståhlberg, J. Lätt, P. C. Sundgren, and M. Nilsson, "The link between diffusion MRI and tumor heterogeneity: Mapping cell eccentricity and density by diffusional variance decomposition (DIVIDE)," en, *NeuroImage*, vol. 142, pp. 522–532, Nov. 2016, ISSN: 10538119. DOI: 10.1016/j.neuroimage.2016.07.038.
- [21] K. W. Andersen, S. Lasič, H. Lundell, M. Nilsson, D. Topgaard, F. Sellebjerg, F. Szczepankiewicz, H. R. Siebner, M. Blinkenberg, and T. B. Dyrby, "Disentangling white-matter damage from physiological fibre orientation dispersion in multiple sclerosis," en, *Brain Communications*, vol. 2, no. 2, fcaa077, Jul. 2020, ISSN: 2632-1297. DOI: 10.1093/braincomms/fcaa077.
- [22] B. Jian, B. C. Vemuri, E. Özarslan, P. R. Carney, and T. H. Mareci, "A novel tensor distribution model for the diffusion-weighted MR signal," en, *NeuroImage*, vol. 37, no. 1, pp. 164–176, Aug. 2007, ISSN: 10538119. DOI: 10.1016/j.neuroimage.2007.03.074.
- [23] D. Topgaard, "Diffusion tensor distribution imaging," en, *NMR in Biomedicine*, vol. 32, no. 5, e4066, May 2019, ISSN: 0952-3480, 1099-1492. DOI: 10.1002/nbm.4066.
- [24] S. Lasič, F. Szczepankiewicz, S. Eriksson, M. Nilsson, and D. Topgaard, "Microanisotropy imaging: Quantification of microscopic diffusion anisotropy and orientational order parameter by diffusion MRI with magic-angle spinning of the q-vector," *Frontiers in Physics*, vol. 2, 2014, ISSN: 2296-424X. DOI: 10.3389/fphys.2014.00011.
- [25] S. N. Jespersen, J. L. Olesen, A. Ianuş, and N. Shemesh, "Effects of non-gaussian diffusion on "isotropic diffusion" measurements: An ex-vivo microimaging and simulation study," en, *Journal of Magnetic Resonance*, vol. 300, pp. 84–94, Mar. 2019, ISSN: 10907807. DOI: 10.1016/j.jmr.2019.01.007.
- [26] F. Szczepankiewicz, S. Hoge, and C.-F. Westin, "Linear, planar and spherical tensor-valued diffusion MRI data by free waveform encoding in healthy brain, water, oil and liquid crystals," en, *Data in Brief*, vol. 25, p. 104208, Aug. 2019, ISSN: 23523409. DOI: 10.1016/j.dib.2019.104208.
- [27] U. Haeberlen, *High Resolution NMR in Solids Selective Averaging: Supplement 1 Advances in Magnetic Resonance*, eng. Saint Louis: Elsevier Science, 2014, OCLC: 1058445294, ISBN: 978-0-323-16025-4.
- [28] D. Topgaard, "Multidimensional diffusion MRI," en, *Journal of Magnetic Resonance*, vol. 275, pp. 98–113, Feb. 2017, ISSN: 10907807. DOI: 10.1016/j.jmr.2016.12.007.
- [29] A. Reymbaut and M. Descoteaux, "Advanced encoding methods in diffusion MRI," 2019, Publisher: arXiv Version Number: 3. DOI: 10.48550/ARXIV.1908.04177.
- [30] F. Zhang, Ed., *The Schur Complement and Its Applications* (Numerical Methods and Algorithms), en. New York: Springer-Verlag, 2005, vol. 4, ISBN: 978-0-387-24271-2. DOI: 10.1007/b105056.

- [31] R. W. Brown, Y.-C. N. Cheng, E. M. Haacke, M. R. Thompson, and R. Venkatesan, *Magnetic Resonance Imaging: Physical Principles and Sequence Design*, en, 1st ed. Wiley, Apr. 2014, ISBN: 978-0-471-72085-0 978-1-118-63395-3. DOI: 10.1002/9781118633953.
- [32] Z.-P. Liang and P. C. Lauterbur, *Principles of magnetic resonance imaging: a signal processing perspective* (IEEE Press series in biomedical engineering). Bellingham, Wash. : New York: SPIE Optical Engineering Press ; IEEE Press, 2000, ISBN: 978-0-7803-4723-6.
- [33] F. Bloch, "Nuclear Induction," en, *Physical Review*, vol. 70, no. 7-8, pp. 460–474, Oct. 1946, ISSN: 0031-899X. DOI: 10.1103/PhysRev.70.460.
- [34] E. L. Hahn, "Spin Echoes," en, *Physical Review*, vol. 80, no. 4, pp. 580–594, Nov. 1950, ISSN: 0031-899X. DOI: 10.1103/PhysRev.80.580.
- [35] P. J. Basser and E. Özarslan, "Introduction to Diffusion MR," en, in *Diffusion MRI*, Elsevier, 2014, pp. 3–9, ISBN: 978-0-12-396460-1. DOI: 10.1016/B978-0-12-396460-1.00001-9.
- [36] A. Einstein, "Über die von der molekularkinetischen Theorie der Wärme geforderte Bewegung von in ruhenden Flüssigkeiten suspendierten Teilchen," de, *Annalen der Physik*, vol. 322, no. 8, pp. 549–560, 1905, ISSN: 00033804, 15213889. DOI: 10.1002/andp.19053220806.
- [37] P. T. Callaghan, *Translational Dynamics and Magnetic Resonance: Principles of Pulsed Gradient Spin Echo NMR*. Oxford University Press, Sep. 2011, ISBN: 978-0-19-955698-4. DOI: 10.1093/acprof:oso/9780199556984.001.0001.
- [38] P. J. Basser, "Relationships between diffusion tensor and q-space MRI," en, *Magnetic Resonance in Medicine*, vol. 47, no. 2, pp. 392–397, Feb. 2002, ISSN: 0740-3194, 1522-2594. DOI: 10.1002/mrm.10052.
- [39] H. C. Torrey, "Bloch Equations with Diffusion Terms," en, *Physical Review*, vol. 104, no. 3, pp. 563–565, Nov. 1956, ISSN: 0031-899X. DOI: 10.1103/PhysRev.104.563.
- [40] C. Liu and E. Özarslan, "Multimodal integration of diffusion MRI for better characterization of tissue biology," en, *NMR in Biomedicine*, vol. 32, no. 4, e3939, Apr. 2019, ISSN: 0952-3480, 1099-1492. DOI: 10.1002/nbm.3939.
- [41] D. C. Douglass and D. W. McCall, "Diffusion in Paraffin Hydrocarbons," en, *The Journal of Physical Chemistry*, vol. 62, no. 9, pp. 1102–1107, Sep. 1958, ISSN: 0022-3654, 1541-5740. DOI: 10.1021/j150567a020.
- [42] P. T. Callaghan, C. D. Eccles, and Y. Xia, "NMR microscopy of dynamic displacements: K-space and q-space imaging," *Journal of Physics E: Scientific Instruments*, vol. 21, no. 8, pp. 820–822, Aug. 1988, ISSN: 0022-3735. DOI: 10.1088/0022-3735/21/8/017.
- [43] P. Callaghan, D. MacGowan, K. Packer, and F. Zelaya, "High-resolution q-space imaging in porous structures," en, *Journal of Magnetic Resonance (1969)*, vol. 90, no. 1, pp. 177–182, Oct. 1990, ISSN: 00222364. DOI: 10.1016/0022-2364(90)90376-K.

- [44] V. J. Wedeen, P. Hagmann, W.-Y. I. Tseng, T. G. Reese, and R. M. Weiskoff, "Mapping complex tissue architecture with diffusion spectrum magnetic resonance imaging," en, *Magnetic Resonance in Medicine*, vol. 54, no. 6, pp. 1377–1386, Dec. 2005, ISSN: 0740-3194, 1522-2594. DOI: 10.1002/mrm.20642.
- [45] P. Mitra and B. Halperin, "Effects of Finite Gradient-Pulse Widths in Pulsed-Field-Gradient Diffusion Measurements," en, *Journal of Magnetic Resonance, Series A*, vol. 113, no. 1, pp. 94–101, Mar. 1995, ISSN: 10641858. DOI: 10.1006/jmra.1995.1060.
- [46] F. B. Laun, T. A. Kuder, A. Wetscherek, B. Stieltjes, and W. Semmler, "NMR-based diffusion pore imaging," en, *Physical Review E*, vol. 86, no. 2, p. 021 906, Aug. 2012, ISSN: 1539-3755, 1550-2376. DOI: 10.1103/PhysRevE.86.021906.
- [47] C. Liu, R. Bammer, B. Acar, and M. E. Moseley, "Characterizing non-gaussian diffusion by using generalized diffusion tensors," en, *Magnetic Resonance in Medicine*, vol. 51, no. 5, pp. 924–937, May 2004, ISSN: 0740-3194, 1522-2594. DOI: 10.1002/mrm.20071.
- [48] D. K. Jones PhD, Ed., *Diffusion MRI*, en. Oxford University Press, Sep. 2012, vol. 1, ISBN: 978-0-19-536977-9. DOI: 10.1093/med/9780195369779.001.0001.
- [49] D. S. Grebenkov, "From the microstructure to diffusion MRI, and back," 2015, Publisher: Citeseer.
- [50] J. H. Jensen, J. A. Helpert, A. Ramani, H. Lu, and K. Kaczynski, "Diffusional kurtosis imaging: The quantification of non-gaussian water diffusion by means of magnetic resonance imaging," en, *Magnetic Resonance in Medicine*, vol. 53, no. 6, pp. 1432–1440, Jun. 2005, ISSN: 0740-3194, 1522-2594. DOI: 10.1002/mrm.20508.
- [51] J. L. Paulsen, E. Özarslan, M. E. Komlosh, P. J. Basser, and Y.-Q. Song, "Detecting compartmental non-Gaussian diffusion with symmetrized double-PFG MRI," en, *NMR in Biomedicine*, vol. 28, no. 11, pp. 1550–1556, Nov. 2015, ISSN: 0952-3480, 1099-1492. DOI: 10.1002/nbm.3363.
- [52] D. E. Woessner, "Effects of Diffusion in Nuclear Magnetic Resonance Spin-Echo Experiments," en, *The Journal of Chemical Physics*, vol. 34, no. 6, pp. 2057–2061, Jun. 1961, ISSN: 0021-9606, 1089-7690. DOI: 10.1063/1.1731821.
- [53] D. E. Woessner, "N.M.R. SPIN-ECHO SELF-DIFFUSION MEASUREMENTS ON FLUIDS UNDERGOING RESTRICTED DIFFUSION," en, *The Journal of Physical Chemistry*, vol. 67, no. 6, pp. 1365–1367, Jun. 1963, ISSN: 0022-3654, 1541-5740. DOI: 10.1021/j100800a509.
- [54] D. G. Cory, "Measurement of translational displacement probabilities by NMR: An indicator of compartmentation," en, *Magnetic Resonance in Medicine*, vol. 14, no. 3, pp. 435–444, Jun. 1990, ISSN: 07403194, 15222594. DOI: 10.1002/mrm.1910140303.

- [55] P. T. Callaghan, A. Coy, D. MacGowan, K. J. Packer, and F. O. Zelaya, "Diffraction-like effects in NMR diffusion studies of fluids in porous solids," en, *Nature*, vol. 351, no. 6326, pp. 467–469, Jun. 1991, ISSN: 0028-0836, 1476-4687. DOI: 10.1038/351467a0.
- [56] A. Caprihan, L. Wang, and E. Fukushima, "A Multiple-Narrow-Pulse Approximation for Restricted Diffusion in a Time-Varying Field Gradient," en, *Journal of Magnetic Resonance, Series A*, vol. 118, no. 1, pp. 94–102, Jan. 1996, ISSN: 10641858. DOI: 10.1006/jmra.1996.0013.
- [57] P. T. Callaghan, "A Simple Matrix Formalism for Spin Echo Analysis of Restricted Diffusion under Generalized Gradient Waveforms," en, *Journal of Magnetic Resonance*, vol. 129, no. 1, pp. 74–84, Nov. 1997, ISSN: 10907807. DOI: 10.1006/jmre.1997.1233.
- [58] S. Codd and P. Callaghan, "Spin Echo Analysis of Restricted Diffusion under Generalized Gradient Waveforms: Planar, Cylindrical, and Spherical Pores with Wall Relaxivity," en, *Journal of Magnetic Resonance*, vol. 137, no. 2, pp. 358–372, Apr. 1999, ISSN: 10907807. DOI: 10.1006/jmre.1998.1679.
- [59] E. Özarslan, N. Shemesh, and P. J. Basser, "A general framework to quantify the effect of restricted diffusion on the NMR signal with applications to double pulsed field gradient NMR experiments," en, *The Journal of Chemical Physics*, vol. 130, no. 10, p. 104702, Mar. 2009, ISSN: 0021-9606, 1089-7690. DOI: 10.1063/1.3082078.
- [60] C. Yolcu, M. Memiç, K. Şimşek, C.-F. Westin, and E. Özarslan, "NMR signal for particles diffusing under potentials: From path integrals and numerical methods to a model of diffusion anisotropy," en, *Physical Review E*, vol. 93, no. 5, p. 052602, May 2016, ISSN: 2470-0045, 2470-0053. DOI: 10.1103/PhysRevE.93.052602.
- [61] E. Özarslan, C.-F. Westin, and T. H. Mareci, "Characterizing magnetic resonance signal decay due to gaussian diffusion: The path integral approach and a convenient computational method: CHARACTERIZING MR SIGNAL DECAY DUE TO GAUSSIAN DIFFUSION," en, *Concepts in Magnetic Resonance Part A*, vol. 44, no. 4, pp. 203–213, Jul. 2015, ISSN: 15466086. DOI: 10.1002/cmr.a.21354.
- [62] G. E. Uhlenbeck and L. S. Ornstein, "On the Theory of the Brownian Motion," en, *Physical Review*, vol. 36, no. 5, pp. 823–841, Sep. 1930, ISSN: 0031-899X. DOI: 10.1103/PhysRev.36.823.
- [63] M. Smoluchowski, "Einige Beispiele Brown'scher Molekularbewegung unter Einfluss äusserer Kräfte," vol. ser A, p. 418, 1913.
- [64] M. Zucchelli, M. Afzali, C. Yolcu, C.-F. Westin, G. Menegaz, and E. Ozarslan, "The confinement tensor model improves characterization of diffusion-weighted magnetic resonance data with varied timing parameters," in *2016 IEEE 13th International Symposium on Biomedical Imaging (ISBI)*, Prague, Czech Republic: IEEE, Apr. 2016, pp. 1093–1096, ISBN: 978-1-4799-2349-6. DOI: 10.1109/ISBI.2016.7493456.

- [65] E. Özarslan, C. Yölcü, M. Herberthson, C.-F. Westin, and H. Knutsson, "Effective Potential for Magnetic Resonance Measurements of Restricted Diffusion," *Frontiers in Physics*, vol. 5, p. 68, Dec. 2017, ISSN: 2296-424X. DOI: 10.3389/fphy.2017.00068.
- [66] G. A. Brosamler, "Laws of the iterated logarithm for Brownian motions on compact manifolds," en, *Zeitschrift für Wahrscheinlichkeitstheorie und Verwandte Gebiete*, vol. 65, no. 1, pp. 99–114, 1983, ISSN: 0044-3719, 1432-2064. DOI: 10.1007/BF00534997.
- [67] J. Mattiello, P. Basser, and D. LeBihan, "Analytical Expressions for the b Matrix in NMR Diffusion Imaging and Spectroscopy," en, *Journal of Magnetic Resonance, Series A*, vol. 108, no. 2, pp. 131–141, Jun. 1994, ISSN: 10641858. DOI: 10.1006/jmra.1994.1103.
- [68] J. Sjölund, F. Szczepankiewicz, M. Nilsson, D. Topgaard, C.-F. Westin, and H. Knutsson, "Constrained optimization of gradient waveforms for generalized diffusion encoding," en, *Journal of Magnetic Resonance*, vol. 261, pp. 157–168, Dec. 2015, ISSN: 10907807. DOI: 10.1016/j.jmr.2015.10.012.
- [69] S. Mori and P. C. M. Van Zijl, "Diffusion Weighting by the Trace of the Diffusion Tensor within a Single Scan," en, *Magnetic Resonance in Medicine*, vol. 33, no. 1, pp. 41–52, Jan. 1995, ISSN: 07403194, 15222594. DOI: 10.1002/mrm.1910330107.
- [70] P. T. Callaghan and Y. Xia, "Velocity and diffusion imaging in dynamic NMR microscopy," en, *Journal of Magnetic Resonance (1969)*, vol. 91, no. 2, pp. 326–352, Feb. 1991, ISSN: 00222364. DOI: 10.1016/0022-2364(91)90196-Z.
- [71] N. Shemesh and Y. Cohen, "Microscopic and compartment shape anisotropies in gray and white matter revealed by angular bipolar double-PFG MR: D-PFG Reveals Microstructures in Gray Matter," en, *Magnetic Resonance in Medicine*, vol. 65, no. 5, pp. 1216–1227, May 2011, ISSN: 07403194. DOI: 10.1002/mrm.22738.
- [72] M. Nilsson, J. Lätt, D. Van Westen, S. Brockstedt, S. Lasič, F. Ståhlberg, and D. Topgaard, "Noninvasive mapping of water diffusional exchange in the human brain using filter-exchange imaging: Filtered-Exchange Imaging in the Human Brain," en, *Magnetic Resonance in Medicine*, vol. 69, no. 6, pp. 1572–1580, Jun. 2013, ISSN: 07403194. DOI: 10.1002/mrm.24395.
- [73] A. V. Avram, E. Özarslan, J. E. Sarlls, and P. J. Basser, "In vivo detection of microscopic anisotropy using quadruple pulsed-field gradient (qPFG) diffusion MRI on a clinical scanner," en, *NeuroImage*, vol. 64, pp. 229–239, Jan. 2013, ISSN: 10538119. DOI: 10.1016/j.neuroimage.2012.08.048.
- [74] D. A. Yablonskiy, G. L. Bretthorst, and J. J. Ackerman, "Statistical model for diffusion attenuated MR signal," en, *Magnetic Resonance in Medicine*, vol. 50, no. 4, pp. 664–669, Oct. 2003, ISSN: 0740-3194, 1522-2594. DOI: 10.1002/mrm.10578.
- [75] D. A. Yablonskiy and A. L. Sukstanskii, "Theoretical models of the diffusion weighted MR signal," en, *NMR in Biomedicine*, vol. 23, no. 7, pp. 661–681, Jun. 2010, ISSN: 09523480. DOI: 10.1002/nbm.1520.

- [76] K. N. Magdoom, S. Pajevic, G. Dario, and P. J. Basser, "A new framework for MR diffusion tensor distribution," en, *Scientific Reports*, vol. 11, no. 1, p. 2766, Feb. 2021, ISSN: 2045-2322. DOI: 10.1038/s41598-021-81264-x.
- [77] K. N. Magdoom, A. V. Avram, J. E. Sarlls, G. Dario, and P. J. Basser, "A novel framework for in-vivo diffusion tensor distribution MRI of the human brain," en, *NeuroImage*, vol. 271, p. 120 003, May 2023, ISSN: 10538119. DOI: 10.1016/j.neuroimage.2023.120003.
- [78] K. P. Whittall and A. L. MacKay, "Quantitative interpretation of NMR relaxation data," en, *Journal of Magnetic Resonance (1969)*, vol. 84, no. 1, pp. 134–152, Aug. 1989, ISSN: 00222364. DOI: 10.1016/0022-2364(89)90011-5.
- [79] M. Hürlimann and L. Venkataramanan, "Quantitative Measurement of Two-Dimensional Distribution Functions of Diffusion and Relaxation in Grossly Inhomogeneous Fields," en, *Journal of Magnetic Resonance*, vol. 157, no. 1, pp. 31–42, Jul. 2002, ISSN: 10907807. DOI: 10.1006/jmre.2002.2567.
- [80] P. Galvosas and P. T. Callaghan, "Multi-dimensional inverse Laplace spectroscopy in the NMR of porous media," en, *Comptes Rendus Physique*, vol. 11, no. 2, pp. 172–180, Mar. 2010, ISSN: 16310705. DOI: 10.1016/j.crhy.2010.06.014.
- [81] S. Nørhøj Jespersen, "White matter biomarkers from diffusion MRI," en, *Journal of Magnetic Resonance*, vol. 291, pp. 127–140, Jun. 2018, ISSN: 10907807. DOI: 10.1016/j.jmr.2018.03.001.
- [82] E. C. Wong, R. W. Cox, and A. W. Song, "Optimized isotropic diffusion weighting," en, *Magnetic Resonance in Medicine*, vol. 34, no. 2, pp. 139–143, Aug. 1995, ISSN: 07403194, 15222594. DOI: 10.1002/mrm.1910340202.
- [83] H. Lundell, M. Nilsson, T. B. Dyrby, G. J. M. Parker, P. L. H. Cristinacce, F.-L. Zhou, D. Topgaard, and S. Lasič, "Multidimensional diffusion MRI with spectrally modulated gradients reveals unprecedented microstructural detail," en, *Scientific Reports*, vol. 9, no. 1, p. 9026, Dec. 2019, ISSN: 2045-2322. DOI: 10.1038/s41598-019-45235-7.
- [84] D. Boito, C. Yolcu, and E. Özarslan, "Multidimensional Diffusion MRI Methods With Confined Subdomains," *Frontiers in Physics*, vol. 10, p. 830 274, Mar. 2022, ISSN: 2296-424X. DOI: 10.3389/fphy.2022.830274.
- [85] J. Wishart, "The Generalised Product Moment Distribution in Samples from a Normal Multivariate Population," *Biometrika*, vol. 20A, no. 1/2, p. 32, Jul. 1928, ISSN: 00063444. DOI: 10.2307/2331939.
- [86] R. J. Muirhead, *Aspects of multivariate statistical theory* (Wiley series in probability and statistics). Hoboken, N.J: Wiley-Interscience, 2005, ISBN: 978-0-471-76985-9.
- [87] F. Szczepankiewicz, S. Lasič, D. Van Westen, P. C. Sundgren, E. Englund, C.-F. Westin, F. Ståhlberg, J. Lätt, D. Topgaard, and M. Nilsson, "Quantification of microscopic diffusion anisotropy disentangles effects of orientation dispersion from microstructure: Applications in healthy volunteers and in brain tumors," en, *NeuroImage*, vol. 104, pp. 241–252, Jan. 2015, ISSN: 10538119. DOI: 10.1016/j.neuroimage.2014.09.057.

- [88] S. Shakya, N. Batool, E. Özarslan, and H. Knutsson, "Multi-Fiber Reconstruction Using Probabilistic Mixture Models for Diffusion MRI Examinations of the Brain," in *Modeling, Analysis, and Visualization of Anisotropy*, T. Schultz, E. Özarslan, and I. Hotz, Eds., Series Title: Mathematics and Visualization, Cham: Springer International Publishing, 2017, pp. 283–308, ISBN: 978-3-319-61357-4 978-3-319-61358-1. DOI: 10.1007/978-3-319-61358-1_12.
- [89] M. Herberthson, D. Boito, T. D. Haije, A. Feragen, C.-F. Westin, and E. Özarslan, "Q-space trajectory imaging with positivity constraints (QTI+)," en, *NeuroImage*, vol. 238, p. 118198, Sep. 2021, ISSN: 10538119. DOI: 10.1016/j.neuroimage.2021.118198.
- [90] D. Boito, M. Herberthson, T. Dela Haije, and E. Özarslan, "Applying positivity constraints to q-space trajectory imaging: The QTI+ implementation," en, *SoftwareX*, vol. 18, p. 101030, Jun. 2022, ISSN: 23527110. DOI: 10.1016/j.softx.2022.101030.
- [91] M. Moakher, "Fourth-order cartesian tensors: Old and new facts, notions and applications," en, *The Quarterly Journal of Mechanics and Applied Mathematics*, vol. 61, no. 2, pp. 181–203, Jan. 2008, ISSN: 0033-5614, 1464-3855. DOI: 10.1093/qjmam/hbm027.
- [92] S. C. Cowin, "PROPERTIES OF THE ANISOTROPIC ELASTICITY TENSOR," en, *The Quarterly Journal of Mechanics and Applied Mathematics*, vol. 42, no. 2, pp. 249–266, 1989, ISSN: 0033-5614, 1464-3855. DOI: 10.1093/qjmam/42.2.249.
- [93] P. Basser and S. Pajevic, "A normal distribution for tensor-valued random variables: Applications to diffusion tensor MRI," en, *IEEE Transactions on Medical Imaging*, vol. 22, no. 7, pp. 785–794, Jul. 2003, ISSN: 0278-0062. DOI: 10.1109/TMI.2003.815059.
- [94] Y. Cheng and D. G. Cory, "Multiple Scattering by NMR," en, *Journal of the American Chemical Society*, vol. 121, no. 34, pp. 7935–7936, Sep. 1999, ISSN: 0002-7863, 1520-5126. DOI: 10.1021/ja9843324.
- [95] E. Özarslan, "Compartment shape anisotropy (CSA) revealed by double pulsed field gradient MR," en, *Journal of Magnetic Resonance*, vol. 199, no. 1, pp. 56–67, Jul. 2009, ISSN: 10907807. DOI: 10.1016/j.jmr.2009.04.002.
- [96] M. Lawrenz, M. A. Koch, and J. Finsterbusch, "A tensor model and measures of microscopic anisotropy for double-wave-vector diffusion-weighting experiments with long mixing times," en, *Journal of Magnetic Resonance*, vol. 202, no. 1, pp. 43–56, Jan. 2010, ISSN: 10907807. DOI: 10.1016/j.jmr.2009.09.015.
- [97] S. N. Jespersen, H. Lundell, C. K. SØnderby, and T. B. Dyrby, "Orientationally invariant metrics of apparent compartment eccentricity from double pulsed field gradient diffusion experiments: ORIENTATIONALLY INVARIANT DOUBLE PFG DIFFUSION," en, *NMR in Biomedicine*, vol. 26, no. 12, pp. 1647–1662, Dec. 2013, ISSN: 09523480. DOI: 10.1002/nbm.2999.

- [98] A. Reymbaut, P. Mezzani, J. P. Almeida Martins, and D. Topgaard, "Accuracy and precision of statistical descriptors obtained from multidimensional diffusion signal inversion algorithms," en, *NMR in Biomedicine*, vol. 33, no. 12, Dec. 2020, ISSN: 0952-3480, 1099-1492. DOI: 10.1002/nbm.4267.
- [99] L. Kerkelä, F. Nery, R. Callaghan, F. Zhou, N. G. Gyori, F. Szczepankiewicz, M. Palombo, G. J. Parker, H. Zhang, M. G. Hall, and C. A. Clark, "Comparative analysis of signal models for microscopic fractional anisotropy estimation using q-space trajectory encoding," en, *NeuroImage*, vol. 242, p. 118 445, Nov. 2021, ISSN: 10538119. DOI: 10.1016/j.neuroimage.2021.118445.
- [100] A. Ianuş, S. N. Jespersen, T. Serradas Duarte, D. C. Alexander, I. Drobnjak, and N. Shemesh, "Accurate estimation of microscopic diffusion anisotropy and its time dependence in the mouse brain," en, *NeuroImage*, vol. 183, pp. 934–949, Dec. 2018, ISSN: 10538119. DOI: 10.1016/j.neuroimage.2018.08.034.
- [101] M. Holz, S. R. Heil, and A. Sacco, "Temperature-dependent self-diffusion coefficients of water and six selected molecular liquids for calibration in accurate 1H NMR PFG measurements," *Physical Chemistry Chemical Physics*, vol. 2, no. 20, pp. 4740–4742, 2000, ISSN: 14639076, 14639084. DOI: 10.1039/b005319h.
- [102] S. P. Boyd and L. Vandenberghe, *Convex optimization*. Cambridge, UK ; New York: Cambridge University Press, 2004, ISBN: 978-0-521-83378-3.
- [103] C. L. Lawson and R. J. Hanson, *Solving least squares problems* (Classics in applied mathematics 15). Philadelphia: SIAM, 1995, ISBN: 978-0-89871-356-5.
- [104] J. G. McWhirter and E. R. Pike, "On the numerical inversion of the Laplace transform and similar Fredholm integral equations of the first kind," *Journal of Physics A: Mathematical and General*, vol. 11, no. 9, pp. 1729–1745, Sep. 1978, ISSN: 0305-4470, 1361-6447. DOI: 10.1088/0305-4470/11/9/007.
- [105] M. Prange and Y.-Q. Song, "Quantifying uncertainty in NMR spectra using Monte Carlo inversion," en, *Journal of Magnetic Resonance*, vol. 196, no. 1, pp. 54–60, Jan. 2009, ISSN: 10907807. DOI: 10.1016/j.jmr.2008.10.008.
- [106] B. Jian and B. Vemuri, "A Unified Computational Framework for Deconvolution to Reconstruct Multiple Fibers From Diffusion Weighted MRI," *IEEE Transactions on Medical Imaging*, vol. 26, no. 11, pp. 1464–1471, Nov. 2007, ISSN: 0278-0062. DOI: 10.1109/TMI.2007.907552.
- [107] A. Daducci, E. J. Canales-Rodríguez, H. Zhang, T. B. Dyrby, D. C. Alexander, and J.-P. Thiran, "Accelerated Microstructure Imaging via Convex Optimization (AMICO) from diffusion MRI data," en, *NeuroImage*, vol. 105, pp. 32–44, Jan. 2015, ISSN: 10538119. DOI: 10.1016/j.neuroimage.2014.10.026.
- [108] P. Berman, O. Levi, Y. Parmet, M. Saunders, and Z. Wiesman, "Laplace inversion of low-resolution NMR relaxometry data using sparse representation methods," en, *Concepts in Magnetic Resonance Part A*, vol. 42, no. 3, pp. 72–88, May 2013, ISSN: 1546-6086, 1552-5023. DOI: 10.1002/cmra.21263.

- [109] A. Reci, A. Sederman, and L. Gladden, "Obtaining sparse distributions in 2D inverse problems," en, *Journal of Magnetic Resonance*, vol. 281, pp. 188–198, Aug. 2017, ISSN: 10907807. DOI: 10.1016/j.jmr.2017.05.010.
- [110] D. Benjamini and P. J. Basser, "Use of marginal distributions constrained optimization (MADCO) for accelerated 2D MRI relaxometry and diffusometry," en, *Journal of Magnetic Resonance*, vol. 271, pp. 40–45, Oct. 2016, ISSN: 10907807. DOI: 10.1016/j.jmr.2016.08.004.
- [111] A. N. Tikhonov and V. Arsenin, "Solutions of ill-posed problems," (*No Title*), 1977.
- [112] J. P. De Almeida Martins and D. Topgaard, "Multidimensional correlation of nuclear relaxation rates and diffusion tensors for model-free investigations of heterogeneous anisotropic porous materials," en, *Scientific Reports*, vol. 8, no. 1, p. 2488, Feb. 2018, ISSN: 2045-2322. DOI: 10.1038/s41598-018-19826-9.
- [113] J. P. De Almeida Martins, C. M. W. Tax, F. Szczepankiewicz, D. K. Jones, C.-F. Westin, and D. Topgaard, "Transferring principles of solid-state and Laplace NMR to the field of in vivo brain MRI," en, *Magnetic Resonance*, vol. 1, no. 1, pp. 27–43, Feb. 2020, ISSN: 2699-0016. DOI: 10.5194/mr-1-27-2020.
- [114] K. Levenberg, "A method for the solution of certain non-linear problems in least squares," en, *Quarterly of Applied Mathematics*, vol. 2, no. 2, pp. 164–168, 1944, ISSN: 0033-569X, 1552-4485. DOI: 10.1090/qam/10666.
- [115] D. W. Marquardt, "An Algorithm for Least-Squares Estimation of Nonlinear Parameters," en, *Journal of the Society for Industrial and Applied Mathematics*, vol. 11, no. 2, pp. 431–441, Jun. 1963, ISSN: 0368-4245, 2168-3484. DOI: 10.1137/0111030.
- [116] J. J. Moré, "The Levenberg-Marquardt algorithm: Implementation and theory," in *Numerical Analysis*, G. A. Watson, Ed., vol. 630, Series Title: Lecture Notes in Mathematics, Berlin, Heidelberg: Springer Berlin Heidelberg, 1978, pp. 105–116, ISBN: 978-3-540-08538-6 978-3-540-35972-2. DOI: 10.1007/BFb0067700.
- [117] C. Guan Koay, "Least Squares Approaches to Diffusion Tensor Estimation," in *Diffusion MRI*, D. K. Jones PhD, Ed., Oxford University Press, Nov. 2010, pp. 272–284, ISBN: 978-0-19-536977-9. DOI: 10.1093/med/9780195369779.003.0016.
- [118] R. Salvador, A. Peña, D. K. Menon, T. A. Carpenter, J. D. Pickard, and E. T. Bullmore, "Formal characterization and extension of the linearized diffusion tensor model: Linearized Diffusion Tensor Model," en, *Human Brain Mapping*, vol. 24, no. 2, pp. 144–155, Feb. 2005, ISSN: 10659471. DOI: 10.1002/hbm.20076.
- [119] J. Veraart, J. Sijbers, S. Sunaert, A. Leemans, and B. Jeurissen, "Weighted linear least squares estimation of diffusion MRI parameters: Strengths, limitations, and pitfalls," en, *NeuroImage*, vol. 81, pp. 335–346, Nov. 2013, ISSN: 10538119. DOI: 10.1016/j.neuroimage.2013.05.028.

- [120] E. Garyfallidis, M. Brett, B. Amirbekian, A. Rokem, S. Van Der Walt, M. Descoteaux, I. Nimmo-Smith, and Dipy Contributors, "Dipy, a library for the analysis of diffusion MRI data," *Frontiers in Neuroinformatics*, vol. 8, Feb. 2014, ISSN: 1662-5196. DOI: 10.3389/fninf.2014.00008.
- [121] J. P. De Almeida Martins, M. Nilsson, B. Lampinen, M. Palombo, P. T. While, C.-F. Westin, and F. Szczepankiewicz, "Neural networks for parameter estimation in microstructural MRI: Application to a diffusion-relaxation model of white matter," en, *NeuroImage*, vol. 244, p. 118601, Dec. 2021, ISSN: 10538119. DOI: 10.1016/j.neuroimage.2021.118601.
- [122] S. Barbieri, O. J. Gurney-Champion, R. Klaassen, and H. C. Thoeny, "Deep learning how to fit an intravoxel incoherent motion model to diffusion-weighted MRI," en, *Magnetic Resonance in Medicine*, vol. 83, no. 1, pp. 312–321, Jan. 2020, ISSN: 0740-3194, 1522-2594. DOI: 10.1002/mrm.27910.
- [123] M. Palombo, A. Ianus, M. Guerreri, D. Nunes, D. C. Alexander, N. Shemesh, and H. Zhang, "SANDI: A compartment-based model for non-invasive apparent soma and neurite imaging by diffusion MRI," en, *NeuroImage*, vol. 215, p. 116835, Jul. 2020, ISSN: 10538119. DOI: 10.1016/j.neuroimage.2020.116835.
- [124] I. O. Jelescu, J. Veraart, E. Fieremans, and D. S. Novikov, "Degeneracy in model parameter estimation for multi-compartmental diffusion in neuronal tissue: Degeneracy in Model Parameter Estimation of Diffusion in Neural Tissue," en, *NMR in Biomedicine*, vol. 29, no. 1, pp. 33–47, Jan. 2016, ISSN: 09523480. DOI: 10.1002/nbm.3450.
- [125] M. Reisert, E. Kellner, B. Dhital, J. Hennig, and V. G. Kiselev, "Disentangling micro from mesostructure by diffusion MRI: A Bayesian approach," en, *NeuroImage*, vol. 147, pp. 964–975, Feb. 2017, ISSN: 10538119. DOI: 10.1016/j.neuroimage.2016.09.058.
- [126] V. Golkov, A. Dosovitskiy, J. I. Sperl, M. I. Menzel, M. Czisch, P. Samann, T. Brox, and D. Cremers, "Q-Space Deep Learning: Twelve-Fold Shorter and Model-Free Diffusion MRI Scans," *IEEE Transactions on Medical Imaging*, vol. 35, no. 5, pp. 1344–1351, May 2016, ISSN: 0278-0062, 1558-254X. DOI: 10.1109/TMI.2016.2551324.
- [127] Q. Tian, B. Bilgic, Q. Fan, C. Liao, C. Ngamsombat, Y. Hu, T. Witzel, K. Setsompop, J. R. Polimeni, and S. Y. Huang, "DeepDTI: High-fidelity six-direction diffusion tensor imaging using deep learning," en, *NeuroImage*, vol. 219, p. 117017, Oct. 2020, ISSN: 10538119. DOI: 10.1016/j.neuroimage.2020.117017.
- [128] D.-A. Clevert, T. Unterthiner, and S. Hochreiter, "Fast and Accurate Deep Network Learning by Exponential Linear Units (ELUs)," 2015, Publisher: arXiv Version Number: 5. DOI: 10.48550/ARXIV.1511.07289.
- [129] N. Srivastava, G. Hinton, A. Krizhevsky, I. Sutskever, and R. Salakhutdinov, "Dropout: A simple way to prevent neural networks from overfitting," *Journal of Machine Learning Research*, vol. 15, no. 1, pp. 1929–1958, Jan. 2014, Number of pages: 30 Publisher: JMLR.org tex.issue_date: January 2014, ISSN: 1532-4435.

- [130] Y. Gal and Z. Ghahramani, "Dropout as a Bayesian Approximation: Representing Model Uncertainty in Deep Learning," 2015, Publisher: arXiv Version Number: 6. DOI: 10.48550/ARXIV.1506.02142.
- [131] S. M. Smith, M. Jenkinson, H. Johansen-Berg, D. Rueckert, T. E. Nichols, C. E. Mackay, K. E. Watkins, O. Ciccarelli, M. Z. Cader, P. M. Matthews, and T. E. Behrens, "Tract-based spatial statistics: Voxelwise analysis of multi-subject diffusion data," en, *NeuroImage*, vol. 31, no. 4, pp. 1487–1505, Jul. 2006, ISSN: 10538119. DOI: 10.1016/j.neuroimage.2006.02.024.
- [132] K.-C. Toh, M. J. Todd, and R. H. Tütüncü, "SDPT3—a MATLAB software package for semidefinite programming, version 1.3," *Optimization methods and software*, vol. 11, no. 1-4, pp. 545–581, 1999, Publisher: Taylor & Francis, ISSN: 1055-6788.
- [133] B. Lampinen, F. Szczepankiewicz, J. Mårtensson, D. van Westen, P. C. Sundgren, and M. Nilsson, "Neurite density imaging versus imaging of microscopic anisotropy in diffusion MRI: A model comparison using spherical tensor encoding," en, *NeuroImage*, vol. 147, pp. 517–531, Feb. 2017, ISSN: 10538119. DOI: 10.1016/j.neuroimage.2016.11.053.
- [134] T. Dela Haije, E. Özarslan, and A. Feragen, "Enforcing necessary non-negativity constraints for common diffusion MRI models using sum of squares programming," en, *NeuroImage*, vol. 209, p. 116 405, Apr. 2020, ISSN: 10538119. DOI: 10.1016/j.neuroimage.2019.116405.
- [135] M. Nilsson, F. Szczepankiewicz, J. Brabec, M. Taylor, C.-F. Westin, A. Golby, D. Van Westen, and P. C. Sundgren, "Tensor-valued diffusion MRI in under 3 minutes: An initial survey of microscopic anisotropy and tissue heterogeneity in intracranial tumors," en, *Magnetic Resonance in Medicine*, vol. 83, no. 2, pp. 608–620, Feb. 2020, ISSN: 0740-3194, 1522-2594. DOI: 10.1002/mrm.27959.
- [136] J. Veraart, W. Van Hecke, and J. Sijbers, "Constrained maximum likelihood estimation of the diffusion kurtosis tensor using a Rician noise model: Constrained Maximum Likelihood Estimation of the DKT," en, *Magnetic Resonance in Medicine*, vol. 66, no. 3, pp. 678–686, Sep. 2011, ISSN: 07403194. DOI: 10.1002/mrm.22835.
- [137] T. Greenhalgh, M. Sivan, B. Delaney, R. Evans, and R. Milne, "Long covid—an update for primary care," en, *BMJ*, e072117, Sep. 2022, ISSN: 1756-1833. DOI: 10.1136/bmj-2022-072117.
- [138] R. S. Peter, A. Nieters, H.-G. Kräusslich, S. O. Brockmann, S. Göpel, G. Kinde, U. Merle, J. M. Steinacker, D. Rothenbacher, and W. V. Kern, "Post-acute sequelae of covid-19 six to 12 months after infection: Population based study," en, *BMJ*, e071050, Oct. 2022, ISSN: 1756-1833. DOI: 10.1136/bmj-2022-071050.
- [139] M. Taquet, J. R. Geddes, M. Husain, S. Luciano, and P. J. Harrison, "6-month neurological and psychiatric outcomes in 236 379 survivors of COVID-19: A retrospective cohort study using electronic health records," en, *The Lancet Psychiatry*, vol. 8, no. 5, pp. 416–427, May 2021, ISSN: 22150366. DOI: 10.1016/S2215-0366(21)00084-5.

- [140] C. Wahlgren, G. Forsberg, A. Divanoglou, Å. Östholm Balkhed, K. Niward, S. Berg, and R. Levi, "Two-year follow-up of patients with post-COVID-19 condition in Sweden: A prospective cohort study," en, *The Lancet Regional Health - Europe*, p. 100595, Feb. 2023, ISSN: 26667762. DOI: 10.1016/j.lanepe.2023.100595.
- [141] G. Douaud, S. Lee, F. Alfaro-Almagro, C. Arthofer, C. Wang, P. McCarthy, F. Lange, J. L. R. Andersson, L. Griffanti, E. Duff, S. Jbabdi, B. Taschler, P. Keating, A. M. Winkler, R. Collins, P. M. Matthews, N. Allen, K. L. Miller, T. E. Nichols, and S. M. Smith, "SARS-CoV-2 is associated with changes in brain structure in UK Biobank," en, *Nature*, vol. 604, no. 7907, pp. 697–707, Apr. 2022, ISSN: 0028-0836, 1476-4687. DOI: 10.1038/s41586-022-04569-5.
- [142] S. Huang, Z. Zhou, D. Yang, W. Zhao, M. Zeng, X. Xie, Y. Du, Y. Jiang, X. Zhou, W. Yang, H. Guo, H. Sun, P. Liu, J. Liu, H. Luo, and J. Liu, "Persistent white matter changes in recovered COVID-19 patients at the 1-year follow-up," en, *Brain*, vol. 145, no. 5, pp. 1830–1838, Jun. 2022, ISSN: 0006-8950, 1460-2156. DOI: 10.1093/brain/awab435.
- [143] Y. Du, W. Zhao, S. Huang, Y. Huang, Y. Chen, H. Zhang, H. Guo, and J. Liu, "Two-year follow-up of brain structural changes in patients who recovered from COVID-19: A prospective study," en, *Psychiatry Research*, vol. 319, p. 114969, Jan. 2023, ISSN: 01651781. DOI: 10.1016/j.psychres.2022.114969.
- [144] L. Hellgren, U. Birberg Thornberg, K. Samuelsson, R. Levi, A. Divanoglou, and I. Blystad, "Brain MRI and neuropsychological findings at long-term follow-up after COVID-19 hospitalisation: An observational cohort study," en, *BMJ Open*, vol. 11, no. 10, e055164, Oct. 2021, ISSN: 2044-6055, 2044-6055. DOI: 10.1136/bmjopen-2021-055164.
- [145] P. J. Winklewski, A. Sabisz, P. Naumczyk, K. Jodzio, E. Szurowska, and A. Szarmach, "Understanding the Physiopathology Behind Axial and Radial Diffusivity Changes—What Do We Know?" *Frontiers in Neurology*, vol. 9, p. 92, Feb. 2018, ISSN: 1664-2295. DOI: 10.3389/fneur.2018.00092.
- [146] T. M. de Swiet and P. P. Mitra, "Possible Systematic Errors in Single-Shot Measurements of the Trace of the Diffusion Tensor," en, *Journal of Magnetic Resonance, Series B*, vol. 111, no. 1, pp. 15–22, Apr. 1996, ISSN: 10641866. DOI: 10.1006/jmrb.1996.0055.
- [147] R. N. Henriques, S. N. Jespersen, and N. Shemesh, "Correlation tensor magnetic resonance imaging," en, *NeuroImage*, vol. 211, p. 116605, May 2020, ISSN: 10538119. DOI: 10.1016/j.neuroimage.2020.116605.
- [148] R. N. Henriques, S. N. Jespersen, and N. Shemesh, "Evidence for microscopic kurtosis in neural tissue revealed by correlation tensor MRI," en, *Magnetic Resonance in Medicine*, vol. 86, no. 6, pp. 3111–3130, Dec. 2021, ISSN: 0740-3194, 1522-2594. DOI: 10.1002/mrm.28938.
- [149] L. Novello, R. N. Henriques, A. Ianuș, T. Feiweier, N. Shemesh, and J. Jovicich, "In vivo Correlation Tensor MRI reveals microscopic kurtosis in the human brain on a clinical 3T scanner," en, *NeuroImage*, vol. 254, p. 119137, Jul. 2022, ISSN: 10538119. DOI: 10.1016/j.neuroimage.2022.119137.

- [150] H.-H. Lee, A. Papaioannou, S.-L. Kim, D. S. Novikov, and E. Fieremans, "A time-dependent diffusion MRI signature of axon caliber variations and beading," en, *Communications Biology*, vol. 3, no. 1, p. 354, Jul. 2020, ISSN: 2399-3642. DOI: 10.1038/s42003-020-1050-x.
- [151] E. Fieremans, L. M. Burcaw, H.-H. Lee, G. Lemberskiy, J. Veraart, and D. S. Novikov, "In vivo observation and biophysical interpretation of time-dependent diffusion in human white matter," en, *NeuroImage*, vol. 129, pp. 414–427, Apr. 2016, ISSN: 10538119. DOI: 10.1016/j.neuroimage.2016.01.018.
- [152] F. Szczepankiewicz, S. Lasic, M. Nilsson, H. Lundell, C.-F. Westin, and D. Topgaard, "Is spherical diffusion encoding rotation invariant? An investigation of diffusion timedependence in the healthy brain," 2019.
- [153] D. S. Novikov, E. Fieremans, S. N. Jespersen, and V. G. Kiselev, "Quantifying brain microstructure with diffusion MRI: Theory and parameter estimation," en, *NMR in Biomedicine*, vol. 32, no. 4, Apr. 2019, ISSN: 0952-3480, 1099-1492. DOI: 10.1002/nbm.3998.
- [154] D. S. Novikov, "The present and the future of microstructure MRI: From a paradigm shift to normal science," en, *Journal of Neuroscience Methods*, vol. 351, p. 108947, Mar. 2021, ISSN: 01650270. DOI: 10.1016/j.jneumeth.2020.108947.
- [155] K. Kamiya, K. Kamagata, K. Ogaki, T. Hatano, T. Ogawa, H. Takeshige-Amano, S. Murata, C. Andica, K. Murata, T. Feiweier, M. Hori, N. Hattori, and S. Aoki, "Brain White-Matter Degeneration Due to Aging and Parkinson Disease as Revealed by Double Diffusion Encoding," *Frontiers in Neuroscience*, vol. 14, p. 584510, Oct. 2020, ISSN: 1662-453X. DOI: 10.3389/fnins.2020.584510.
- [156] G. Douaud, S. Jbabdi, T. E. Behrens, R. A. Menke, A. Gass, A. U. Monsch, A. Rao, B. Whitcher, G. Kindlmann, P. M. Matthews, and S. Smith, "DTI measures in crossing-fibre areas: Increased diffusion anisotropy reveals early white matter alteration in MCI and mild Alzheimer's disease," en, *NeuroImage*, vol. 55, no. 3, pp. 880–890, Apr. 2011, ISSN: 10538119. DOI: 10.1016/j.neuroimage.2010.12.008.
- [157] M. Lawrenz, S. Brassen, and J. Finsterbusch, "Microscopic diffusion anisotropy in the human brain: Age-related changes," en, *NeuroImage*, vol. 141, pp. 313–325, Nov. 2016, ISSN: 10538119. DOI: 10.1016/j.neuroimage.2016.07.031.
- [158] F. Szczepankiewicz, J. Sjölund, F. Ståhlberg, J. Lätt, and M. Nilsson, "Tensor-valued diffusion encoding for diffusional variance decomposition (DIVIDE): Technical feasibility in clinical MRI systems," en, *PLOS ONE*, vol. 14, no. 3, X. Chen, Ed., e0214238, Mar. 2019, ISSN: 1932-6203. DOI: 10.1371/journal.pone.0214238.
- [159] D. Boito, M. Herberthson, T. Dela Haije, and E. Özarslan, "Enforcing positivity constraints in q-space trajectory imaging (QTI) allows for reduced scan time," in *Proc Intl Soc Magn Reson Med*, vol. 29, 2021, p. 0404.

- [160] D. Boito, M. Herberthson, T. Dela Haije, I. Blystad, and E. Özarslan, “Diffusivity-limited q-space trajectory imaging,” en, *Magnetic Resonance Letters*, vol. 3, no. 2, pp. 187–196, May 2023, ISSN: 27725162. DOI: 10.1016/j.mrl.2022.12.003.

Q-space trajectory imaging with positivity constraints (QTI+)

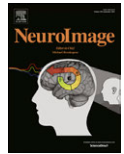
Magnus Herberthson
Deneb Boito
Tom Dela Haije
Aasa Feragen
Carl-Fredrik Westin
Evren Özarslan

Neuroimage, 2021, 238, 118198.

© 2021

Published by Elsevier Inc.

Reprinted with permission (CC BY-NC-ND 4.0)



Q-space trajectory imaging with positivity constraints (QTI+)

Magnus Herberthson^a, Deneb Boito^{b,c}, Tom Dela Haije^d, Aasa Feragen^e, Carl-Fredrik Westin^f, Evren Özarslan^{b,c,*}^a Department of Mathematics, Linköping University, Linköping, Sweden^b Department of Biomedical Engineering, Linköping University, Linköping, Sweden^c Center for Medical Image Science and Visualization, Linköping University, Linköping, Sweden^d Department of Computer Science, University of Copenhagen, Copenhagen, Denmark^e Department of Applied Mathematics and Computer Science, Technical University of Denmark, Lyngby, Denmark^f Laboratory for Mathematics in Imaging, Department of Radiology, Brigham and Women's Hospital, Harvard Medical School, Boston, MA, USA

ARTICLE INFO

Keywords:

Diffusion

MRI

Constrained

Positive definite

QTI

Multidimensional

mddMRI

Covariance

Microscopic anisotropy

ABSTRACT

Q-space trajectory imaging (QTI) enables the estimation of useful scalar measures indicative of the local tissue structure. This is accomplished by employing generalized gradient waveforms for diffusion sensitization alongside a diffusion tensor distribution (DTD) model. The first two moments of the underlying DTD are made available by acquisitions at low diffusion sensitivity (b-values). Here, we show that three independent conditions have to be fulfilled by the mean and covariance tensors associated with distributions of symmetric positive semidefinite tensors. We introduce an estimation framework utilizing semi-definite programming (SDP) to guarantee that these conditions are met. Applying the framework on simulated signal profiles for diffusion tensors distributed according to non-central Wishart distributions demonstrates the improved noise resilience of QTI+ over the commonly employed estimation methods. Our findings on a human brain data set also reveal pronounced improvements, especially so for acquisition protocols featuring few number of volumes. Our method's robustness to noise is expected to not only improve the accuracy of the estimates, but also enable a meaningful interpretation of contrast in the derived scalar maps. The technique's performance on shorter acquisitions could make it feasible in routine clinical practice.

1. Introduction

Determining the local structure of neural tissue using diffusion MRI has already made an impact in neuroscience and radiology. Diffusion MRI's sensitivity to tissue microstructure is exploited and interpreted through models that provide a simplified picture of the complex tissue makeup. The parameters of an adequate model reflect the key characteristics of the tissue that influence the stochastic movement of the water molecules. Measuring the diffusional process and estimating such model parameters from the acquired data are the two essential components of structure determination via diffusion MRI.

In q-space trajectory imaging (QTI) (Westin et al., 2016), diffusion sensitization is achieved via general time-dependent gradient waveforms while the tissue is envisioned to have numerous non-exchanging compartments. Diffusion is characterized by a diffusion tensor within each of these compartments. Consequently, the voxel is represented by a diffusion tensor distribution (DTD) (Jian et al., 2007). QTI exploits the sensitivity of the diffusion MRI signal to the statistical moments of

the parameters characterizing the microscopic domain (Özarslan et al., 2011). By doing so, QTI provides a simple means of relating the signal obtained via general gradient waveforms to the DTD, which is key for introducing meaningful MRI 'biomarkers' in QTI. Under the assumptions of the DTD picture, the effect of all measurement parameters is captured by a positive-semidefinite tensor, referred to as the b-tensor (Mattiello et al., 1994), and denoted by \mathbf{B}_{ij} in this work. The level of diffusion sensitization is usually quantified by the trace of this tensor, denoted by b .

Common clinical MRI examinations of the neural tissue probe the low-b regime of the MR signal attenuation. As shown by Westin et al. (2016), the data in this regime reveal the mean and covariance tensors of the underlying DTD. The former is a 3×3 symmetric positive semidefinite matrix, while the covariance tensor has the symmetries of the fourth order elasticity tensor in mechanics (Basser and Pajevic, 2003). Once estimated, these two tensors are employed in computing several scalar measures that characterize macroscopic and microscopic anisotropies, orientational coherence and size variance of the

* Corresponding author.

E-mail addresses: magnus.herberthson@liu.se (M. Herberthson), deneb.boito@liu.se (D. Boito), haije@di.ku.dk (T.D. Haije), afhar@dtu.dk (A. Feragen), westin@bwh.harvard.edu (C.-F. Westin), evren.ozarslan@liu.se (E. Özarslan).<https://doi.org/10.1016/j.neuroimage.2021.118198>

Received 9 January 2021; Received in revised form 2 May 2021; Accepted 20 May 2021

Available online 21 May 2021.

1053-8119/© 2021 Published by Elsevier Inc. This is an open access article under the CC BY-NC-ND license (<http://creativecommons.org/licenses/by-nc-nd/4.0/>)

subdomains making up the tissue. Thus, a key step in obtaining reliable estimates of these quantities involves accurate estimation of the mean and covariance tensors from the data. In this study, we investigate possible improvements in the estimates of the QTI-derived parameters when several necessary nonnegativity conditions are enforced.

Improvements due to constrained optimization have been reported for diffusion MRI models developed for traditional pulsed field gradient measurements of Stejskal and Tanner (1965). For example, diffusion tensor imaging (DTI) (Basser et al., 1994a; 1994b) has benefited from estimation schemes (Koay, 2010; Koay et al., 2006; Lenglet et al., 2006; Pennec et al., 2006; Wang et al., 2004) that ensure that the diffusion tensor is positive semidefinite—a condition that follows from the physics of diffusion. The estimation problems for models that go beyond DTI (Jensen et al., 2005; Özarslan and Mareci, 2003; Tournier et al., 2007) have also been studied via methods that enforce relevant constraints (Barmpoutis et al., 2012; 2009; Chen et al., 2013; Ghosh et al., 2014; Qi et al., 2010; Veraart et al., 2011).

In a recent work, Dela Haije et al. (2020) considered three such prominent models, namely, spherical deconvolution (Tournier et al., 2004), diffusion kurtosis imaging (Jensen et al., 2005; Liu et al., 2004), and mean apparent propagator MRI (Özarslan et al., 2013) and formulated several sum-of-squares (SoS) constraints arising from the nonnegativity of the relevant distribution functions yielding remarkable improvements in the model estimates over earlier methods. Enforcing them in the estimation via semidefinite programming (SDP) guaranteed the fulfillment of such constraints in contrast to earlier methods that either did not account for them or imposed them “softly,” i.e., did not ensure strict adherence to the relevant constraints. “Softly” imposed constraints were also initially considered for QTI in (Jeurissen et al., 2019), highlighting the interest and need for more sophisticated fitting approaches to be used with this method.

To investigate the effects of constrained optimization for the QTI technique, we devised an estimation framework that guarantees the fulfillment of three conditions that mean and covariance tensors of DTDs have to respect. Following the naming convention in Dela Haije et al. (2020), we refer to our method as QTI+. After introducing our notation and providing an overview of the QTI model, we introduce the constraints to be imposed. Several methods for estimating the mean and covariance tensors as well as a test for checking the fulfillment of one of the constraints are introduced. Simulated signals for non-central Wishart distributed DTDs (Shakya et al., 2017) are employed to compare the performance of commonly-employed methods with ours. We also provide analyses on tensor-valued diffusion encoded brain data (Szczypankiewicz et al., 2019) and assess the performance of our framework on data sets with few number of acquisitions.

2. Background

Our notation

There is a multitude of notations for tensors. Here, we describe the notations and conventions we employ. In this study, there is no need to make a distinction between contra- and covariant tensors. Thus, all indices are written as subscripts.

Scalars are denoted with italic characters, while matrices and second order tensors are denoted with boldface characters. Blackboard bold (double struck) characters are used for fourth-order tensors. For example, \mathbb{A}_{ijkl} is a fourth order tensor whose $ijkl$ th component is A_{ijkl} . Fourth-order tensors considered in this work can also be represented by 6×6 matrices. To make the distinction clear, we employ the following convention:

- Latin letters i, j, k, ℓ range from 1 to 3.
- Early Greek letters α, β , and γ range from 1 to 6.

Thus, \mathbb{A}_{ijkl} and $\mathbb{A}_{\alpha\beta}$ are the fourth order and second order representations of the same tensor. When used with double struck and boldface

characters, the indices are retained just to inform about the order of the tensor, which is the number of indices and the range of those indices; they do not refer to a particular component of the tensor.

We employ the Einstein summation convention, which is usually described as “all repeated indices are summed over.” E.g., $A_{ij} = \sum_{i=1}^3 A_{ij}$ is the trace of the matrix \mathbf{A}_{ij} , while $C_{ik} = A_{ij} B_{jk} = \sum_{j=1}^3 A_{ij} B_{jk}$ is the ik th component of the product of matrices \mathbf{A}_{ij} and \mathbf{B}_{ij} .

QTI

In this work, we are interested in the statistical properties of a distribution of diffusivity tensors \mathbf{D}_{ij} , represented by a family of samples $\{\mathbf{D}_{ij}^{(n)}\}$. Here, since it represents a diffusivity, which is proportional to second moment of displacements, each second order tensor $\mathbf{D}_{ij}^{(n)}$ is symmetric and positive semidefinite. With $\langle \cdot \rangle$ indicating mean (expectation) value, we would like to estimate the mean diffusivity tensor¹

$$\hat{\mathbf{D}}_{ij} = \langle \mathbf{D}_{ij} \rangle$$

and the covariance, which in this case becomes the fourth order (covariance) tensor \mathbf{C} , defined as

$$C_{ijkl} = \langle \mathbf{D}_{ij} - \hat{\mathbf{D}}_{ij} \rangle \otimes \langle \mathbf{D}_{kl} - \hat{\mathbf{D}}_{kl} \rangle.$$

This tensor has the so called minor ($C_{ijkl} = C_{jikl}$, $C_{ijkl} = C_{ijlk}$) and major ($C_{ijkl} = C_{klij}$) symmetries, which result in C_{ijkl} having 21 independent components. It is (as usual) possible to express C_{ijkl} in terms of the (second) moment tensor $\mathbb{M}_{ijkl} = \langle \mathbf{D}_{ij} \otimes \mathbf{D}_{kl} \rangle$ through the relationship

$$C_{ijkl} = \mathbb{M}_{ijkl} - \hat{\mathbf{D}}_{ij} \otimes \hat{\mathbf{D}}_{kl}.$$

\mathbb{M}_{ijkl} has the same symmetries and degrees of freedom as C_{ijkl} .

The QTI signal's dependence on the b-matrix \mathbf{B}_{ij} is given by (Westin et al., 2016)

$$S(\mathbf{B}_{ij}) = S_0 \exp \left(-\mathbf{B}_{ij} \hat{\mathbf{D}}_{ij} + \frac{1}{2} \mathbf{B}_{ij} \mathbf{B}_{kl} C_{ijkl} \right), \quad (1)$$

where S_0 is the signal with no diffusional attenuation, i.e., when $\mathbf{B}_{ij} = \mathbf{0}$. Thus, given a family of measurement tensors $\{\mathbf{B}_{ij}^{(n)}\}_{n=1}^N$ and the corresponding signal values S_1, S_2, \dots, S_N with $S_n = S(\mathbf{B}_{ij}^{(n)})$, the task, given the model (1), is to produce estimates of S_0 , $\hat{\mathbf{D}}_{ij}$ and C_{ijkl} .

The Voigt notation

The diffusivity tensors \mathbf{D}_{ij} in three-dimensional space are symmetric second order tensors. The set of all symmetric second order tensors forms a vector space V of dimension six, and this space is equipped with a natural scalar product: $\langle \mathbf{A}_{ij}, \mathbf{B}_{ij} \rangle = A_{ij} B_{ij}$. Hence one can introduce an orthonormal basis $\{\mathbf{e}_{ij}^{(\beta)}\}_{\beta=1}^6$ and express any tensor in V as

$$\mathbf{A}_{ij} = \sum_{\beta=1}^6 a_{\beta} \mathbf{e}_{ij}^{(\beta)}.$$

These six coordinates a_{β} are customarily put into a vector with six elements, and this is referred to as the Voigt notation. See Appendix A for our choice for the basis.

This approach yields various representations of the covariance tensor C_{ijkl} as well. Because of the symmetries of C_{ijkl} , this tensor can be regarded as a symmetric mapping $V \rightarrow V$, and in turn (given an orthonormal basis for V) represented as a symmetric 6×6 matrix, which is consistent with C_{ijkl} having 21 degrees of freedom. This matrix will be denoted by $\mathbf{C}_{\alpha\beta}$ where $1 \leq \alpha, \beta \leq 6$ as described above.

We can proceed in a similar manner. The set of symmetric mappings $V \rightarrow V$ constitute a vector space of dimensions 21 and, again, given an orthonormal-basis for this space, any tensor \mathbf{C} (with the appropriate symmetries) can be represented by a vector with 21 elements.

¹ The mean is defined in the traditional sense. For a family of N tensors, $\hat{\mathbf{D}}_{ij} = \frac{1}{N} \sum_{n=1}^N \mathbf{D}_{ij}^{(n)}$.

3. Theory

As mentioned in the previous section, given a family of measurements tensors $\{\mathbf{B}_{ij}^{(n)}\}_{n=1}^N$, the set of corresponding signal values $\{S_n\}_{n=1}^N$ and the model (1), the task is to produce estimates of $S_0, \hat{\mathbf{D}}_{ij}$ and $\mathbf{C}_{ijk\ell}$. Assuming approximately Gaussian noise, this is achieved by finding the $S_0, \hat{\mathbf{D}}_{ij}$ and $\mathbf{C}_{ijk\ell}$, which minimize the ‘error,’ i.e.,

$$\arg\min_{S_0, \hat{\mathbf{D}}_{ij}, \mathbf{C}_{ijk\ell}} \sum_{n=1}^N \left| S_n - S_0 e^{-\mathbf{B}_{ij}^{(n)} \hat{\mathbf{D}}_{ij} + \frac{1}{2} \mathbf{B}_{ij}^{(n)} \mathbf{B}_{kl}^{(n)} \mathbf{C}_{ijk\ell}} \right|^2. \quad (2)$$

Here we make two remarks:

1. Even if there is a global minimum, it is not easy to specify in advance a minimizing routine, which is guaranteed to find the minimum.
2. If a minimum is found, the obtained estimates of $\hat{\mathbf{D}}_{ij}$ and $\mathbf{C}_{ijk\ell}$ may be unacceptable.

We start by addressing the second issue in the following subsection.

3.1. Positivity conditions

There are a number of positivity conditions one can impose on the estimates, which have to be met in order for their interpretation to be physically reasonable. Here, we will give three such conditions, which are independent in the sense that any two of them do not imply the other. See Appendix B.

The first condition is on $\hat{\mathbf{D}}_{ij}$, namely, it should represent a diffusivity and thus $\hat{\mathbf{D}}_{ij}$ (in addition to being symmetric) is positive semi-definite. We express this condition as $\hat{\mathbf{D}}_{ij} \geq 0$.

The second condition is similar. From the fact that $\mathbf{C}_{ijk\ell}$ represents a covariance (so that $\mathbf{C}_{ijkl} \mathbf{A}_{ij} \mathbf{A}_{kl} \geq 0$ for all symmetric matrices \mathbf{A}_{ij}), it is necessary that when cast as a 6×6 matrix $\mathbf{C}_{a\beta}$, this matrix should also be positive semi-definite, i.e., $\mathbf{C}_{a\beta} \geq 0$.

The third condition is on $\mathbb{M}_{ijk\ell}$, i.e., concerns $\langle \mathbf{D}_{ij} \otimes \mathbf{D}_{kl} \rangle$. Since $\mathbb{M}_{ijk\ell}$ is the mean of tensor products of diffusion tensors, each of which is positive semi-definite, this property is carried over to $\mathbb{M}_{ijk\ell}$. The conclusion is that for any vector $\mathbf{u}_i \in \mathbb{R}^3$, the symmetric second order tensor, whose ij th component is $M_{ijk\ell} u_k u_\ell$, should be positive semi-definite. In other words, for any pair of vectors \mathbf{v}_i and \mathbf{u}_i , we must have $M_{ijk\ell} v_i v_j u_k u_\ell \geq 0$.

We shall refer to these three conditions as ‘(d)’, ‘(c)’, and ‘(m)’ where the letters indicate the tensor on which the conditions are imposed. To summarize, our conditions are, then,

- (d) $\hat{\mathbf{D}}_{ij} \geq 0$,
- (c) $\mathbf{C}_{a\beta} \geq 0$, and
- (m) for all \mathbf{v}_i and \mathbf{u}_i , $M_{ijk\ell} v_i v_j u_k u_\ell \geq 0$.

Let us also remark that the condition $S_0 \geq 0$ is obviously also required, but that it need not be imposed explicitly (this can be inferred from the fact that all $S_n \geq 0$).

3.2. Linearizing the equation and the least squares solution

As mentioned above, it is not trivial to ensure that a global minimum to (2) is found. However, there is a related problem for which a global minimum is guaranteed to be found. Namely, by taking the logarithm of (1), the model is linearized as

$$\ln(\mathbf{B}_{ij}) = \ln S_0 - \mathbf{B}_{ij} \hat{\mathbf{D}}_{ij} + \frac{1}{2} \mathbf{B}_{ij} \mathbf{B}_{kl} \mathbf{C}_{ijk\ell}. \quad (3)$$

Due to the heteroscedasticity caused by taking the logarithm of the signal, the minimization problem arising from (3) is the weighted problem (Basser et al., 1994a; Bevington and Robinson, 2003)

$$\arg\min_{S_0, \hat{\mathbf{D}}_{ij}, \mathbf{C}_{ijk\ell}} \sum_{n=1}^N S_n^2 \left| \ln(S_n) - \ln(S_0) + \mathbf{B}_{ij}^{(n)} \hat{\mathbf{D}}_{ij} - \frac{1}{2} \mathbf{B}_{ij}^{(n)} \mathbf{B}_{kl}^{(n)} \mathbf{C}_{ijk\ell} \right|^2. \quad (4)$$

which is an approximation to (2); see Appendix C. Using the Voigt notation, the unknowns determining $\ln(S_0), \hat{\mathbf{D}}_{ij}$ and $\mathbf{C}_{ijk\ell}$ can be stacked into a vector \mathbf{x} with $1 + 6 + 21 = 28$ components, i.e., $\mathbf{x} = (x_1, \dots, x_{28})^\top$. The components of \mathbf{x} could be determined through²

$$\begin{aligned} \ln(S_0) &= x_1 \\ \hat{\mathbf{D}}_{ij} &\doteq \frac{1}{\sqrt{2}} \begin{pmatrix} \sqrt{2}x_2 & x_5 & x_6 \\ x_5 & \sqrt{2}x_3 & x_7 \\ x_6 & x_7 & \sqrt{2}x_4 \end{pmatrix} \\ \mathbf{C}_{a\beta} &\doteq \frac{1}{\sqrt{2}} \begin{pmatrix} \sqrt{2}x_8 & x_{11} & x_{12} & x_{17} & x_{18} & x_{14} \\ x_{11} & \sqrt{2}x_9 & x_{13} & x_{19} & x_{15} & x_{20} \\ x_{12} & x_{13} & \sqrt{2}x_{10} & x_{16} & x_{21} & x_{22} \\ x_{17} & x_{19} & x_{16} & \sqrt{2}x_{23} & x_{26} & x_{27} \\ x_{18} & x_{15} & x_{21} & x_{26} & \sqrt{2}x_{24} & x_{28} \\ x_{14} & x_{20} & x_{22} & x_{27} & x_{28} & \sqrt{2}x_{25} \end{pmatrix}, \end{aligned}$$

and Eq. (4) can be formulated as the weighted linear least squares (WLLS) problem

$$\mathbf{A}\mathbf{x} = \mathbf{y} \quad (5)$$

where the vector $\mathbf{y} = (S_1 \ln(S_1), \dots, S_N \ln(S_N))^\top$ contains the weighted signals and the $N \times 28$ matrix \mathbf{A} is formed by the signal values S_n and the measurement tensors $\mathbf{B}_{ij}^{(n)}$.

Without further restrictions, the minimizing vector \mathbf{x} can easily be found by standard linear regression routines. However, we also give two other formulations, which are equivalent to (5) in the unconstrained case, but differ when it comes to imposing the positivity constraints (d), (c), and (m).

3.3. Quadratic programming (QP) for the linearized problem

First, we note that since the least squares solution minimizes $\|\mathbf{A}\mathbf{x} - \mathbf{y}\|^2$, i.e.,

$$\mathbf{x}^\top \mathbf{A}^\top \mathbf{A} \mathbf{x} - 2\mathbf{y}^\top \mathbf{A} \mathbf{x} + \mathbf{y}^\top \mathbf{y} \quad (6)$$

this can also be solved using quadratic programming (Nocedal and Wright, 2006). Note that if \mathbf{A} has full rank, $\mathbf{Q} = \mathbf{A}^\top \mathbf{A}$ is positive definite. Through the substitution $\mathbf{c} = -2\mathbf{A}^\top \mathbf{y}$, the (least squares) solution to (5) can also be found as the solution to

$$\arg\min_{\mathbf{x}} \mathbf{x}^\top \mathbf{Q} \mathbf{x} + \mathbf{c}^\top \mathbf{x}. \quad (7)$$

Here, we ignored the constant factor $\mathbf{y}^\top \mathbf{y}$ as we are interested in the minimizing argument.

3.4. Semidefinite programming (SDP) for the linearized problem

Eq. (7) can be further reformulated. First, we note that the minimizing argument \mathbf{x} can be found by minimizing an auxiliary variable t under the condition $t \geq \mathbf{x}^\top \mathbf{Q} \mathbf{x} + \mathbf{c}^\top \mathbf{x}$, i.e., we are interested in

$$\arg\min_{t, \mathbf{x}} t, \text{ subject to } t - \mathbf{x}^\top \mathbf{Q} \mathbf{x} - \mathbf{c}^\top \mathbf{x} \geq 0. \quad (8)$$

With \mathbf{P} being a square matrix such that $\mathbf{P}^\top \mathbf{P} = \mathbf{Q}$, and with \mathbf{I} being the identity matrix of the same size as \mathbf{Q} , this can be formulated as

$$\arg\min_{t, \mathbf{x}} t, \text{ subject to } \begin{pmatrix} \mathbf{I} & \mathbf{P}\mathbf{x} \\ \mathbf{x}^\top \mathbf{P}^\top & t - \mathbf{c}^\top \mathbf{x} \end{pmatrix} \succeq 0 \quad (9)$$

which shows that we can employ SDP as well to solve this problem (see Appendix D).

² Here, “ \doteq ” is used to indicate that the following matrix is just one representation of the tensor in a particular basis.

3.5. Imposing positivity conditions: Nonlinear least squares with (d) and (c) constraints (NLLS(dc))

Comparing the original problem (2), and the various linearized versions (4), (7), and (8), they all differ when it comes to imposing the positivity constraints (d), (c), and (m).

For Eq. (2), it is possible to impose conditions (d) and (c), by utilizing the Cholesky decomposition, i.e., the fact that any symmetric positive semi-definite matrix \mathbf{A} can be written $\mathbf{A} = \mathbf{L}\mathbf{L}^T$, where \mathbf{L} is a lower triangular matrix with positive diagonal entries.

To this end, we cast $\mathbf{C}_{ijk\ell}$ in its 6×6 matrix form $\mathbf{C}_{a\beta}$. We also introduce a fourth order tensor $\mathbb{B}'_{ijk\ell}$ whose $ijk\ell$ th component is $B_{ij}B_{k\ell}$ and its 6×6 matrix form is $\mathbf{B}'_{a\beta}$. We can use the ansatz

$$\begin{aligned}\hat{\mathbf{D}}_{ij} &= \mathbf{L}_{ik}\mathbf{L}_{jk} \text{ and} \\ \mathbf{C}_{a\beta} &= \mathbf{A}_{a\gamma}\mathbf{A}_{\beta\gamma}\end{aligned}\quad (10)$$

where both \mathbf{L}_{ij} and $\mathbf{A}_{a\beta}$ are lower triangular matrices with positive diagonal entries. The problem (2), then, becomes

$$\arg\min_{S_0, \mathbf{L}_{ij}, \mathbf{A}_{a\beta}} \sum_{n=1}^N \left\| S_n - S_0 e^{-\mathbf{B}_{ij}^{(n)} \mathbf{L}_{ik} \mathbf{L}_{jk} + \frac{1}{2} \mathbf{B}'_{a\beta} \mathbf{A}_{a\gamma} \mathbf{A}_{\beta\gamma}} \right\|^2, \quad (11)$$

which guarantees that (d) and (c) (but not necessarily (m)) are satisfied.

3.6. Imposing positivity conditions: SDP with (d) and (c) constraints (SDP(dc))

The estimation schemes based on the linearized version of the model (weighted linear, quadratic programming, and semidefinite programming) described above, which all produce global minima, differ when it comes to imposing the positivity constraints. In particular, the semidefinite programming (SDP) framework is particularly well-suited for imposing (d) and (c). With $\mathbf{x} = (x_1, \dots, x_{28})^T$ as before, the conditions (d) and (c), namely that $\hat{\mathbf{D}}_{ij}$ and $\mathbf{C}_{a\beta}$ are nonnegative, then fit directly into the SDP framework, i.e., we can impose (d) and (c) by solving

$$\arg\min_{t, \mathbf{x}} t, \text{ subject to } \begin{pmatrix} \mathbf{I} & \mathbf{P}\mathbf{x} & 0 & 0 \\ \mathbf{x}^T \mathbf{P}^T & t - \mathbf{c}^T \mathbf{x} & 0 & 0 \\ 0 & 0 & \hat{\mathbf{D}}_{ij} & 0 \\ 0 & 0 & 0 & \mathbf{C}_{a\beta} \end{pmatrix} \geq 0. \quad (12)$$

Again, condition (m) is not imposed, which is mostly because $\mathbb{M}_{ijk\ell}$ depends quadratically on $\langle \mathbf{D}_{ij} \rangle$.

3.7. An SDP scheme for checking if condition (m) is fulfilled ((m)-check)

Addressing (11) or (12), we get (initial) estimates of $S_0, \langle \mathbf{D}_{ij} \rangle, \mathbf{C}_{ijk\ell}$ and $\mathbb{M}_{ijk\ell}$, where the constraints (d) and (c) are imposed. To determine whether condition (m) needs to be imposed, we first check whether it is violated or not. Hence, we pose the question: for a given estimate of $\mathbb{M}_{ijk\ell}$, is it true that

$$\text{for all } v_i, u_i, \quad \mathbb{M}_{ijk\ell} v_i v_j u_k u_\ell \geq 0? \quad (13)$$

Again, this can be investigated with SDP by addressing a feasibility problem. As explained in Appendix E, it is possible from $\mathbb{M}_{ijk\ell}$ to construct a 9×9 matrix \mathbf{M} where each entry is a first order polynomial in the parameters $\ell_1, \ell_2, \dots, \ell_9$, and check (using SDP) whether there are feasible solutions to the problem

$$\min_{\ell} 0, \text{ subject to } \mathbf{M}(\ell) \geq 0. \quad (14)$$

Here we have put the parameters ℓ_i into a vector: $\ell = (\ell_1, \ell_2, \dots, \ell_9)^T$. This expression differs from the earlier adaptations of the SDP method in that we are only interested in finding out whether a solution fulfilling all the constraints exists. Thus, the function to be minimized is unimportant, and is taken to be 0 by choice. If the SDP routine finds a vector ℓ , condition (m), i.e., (13) is satisfied.

3.8. Imposing positivity conditions: SDP with (c) and (m) constraints (SDP(dcm))

In the case when condition (m) is violated, it is imposed in the following way. From the estimate at hand, we fix S_0 and $\hat{\mathbf{D}}_{ij}$, i.e., $x_8, x_1, x_2, \dots, x_7$,⁴ so that $\mathbb{M}_{ijk\ell}$ is linear in the remaining variables x_8, \dots, x_{28} . These are then re-estimated to ensure that both (c) and (m) are satisfied. Again, this can be accomplished with SDP, and we refer the reader to Appendix F for the formulation. In short, with x_1, \dots, x_7 fixed, we set $\tilde{\mathbf{x}} = (x_8, \dots, x_{28})^T$ and $\tilde{\ell} = (\ell_1, \ell_2, \dots, \ell_9)^T$ and can assert (c) and (m) by solving

$$\min_{t, \tilde{\mathbf{x}}, \tilde{\ell}} t, \text{ subject to } \begin{pmatrix} \mathbf{I} & \tilde{\mathbf{x}} & 0 & 0 \\ \tilde{\mathbf{x}}^T & t - \tilde{\ell}^T \tilde{\mathbf{x}} & 0 & 0 \\ 0 & 0 & \mathbf{C}_{a\beta} & 0 \\ 0 & 0 & 0 & \mathbf{M}(\tilde{\ell}) \end{pmatrix} \geq 0. \quad (15)$$

Note that we refer to this scheme as “SDP(dcm)” as it relies on a previous estimate of $\hat{\mathbf{D}}_{ij}$, which is positive semidefinite. Thus, the end result is guaranteed to fulfill all three conditions (d), (c), and (m).

3.9. Rank deficient estimation

Normally, it is assumed that the matrix \mathbf{A} in the (weighted) least squares problem (5) is of full rank, which in our case is $1 + 6 + 21 = 28$. This is achieved by having a sufficiently rich family of measurement tensors $\{\mathbf{B}_{ij}^{(n)}\}_{n=1}^N$, which ‘spans the parameter space.’ However, for practical reasons there is a trade-off since there is also a desire to keep the measurement protocol short.

Acquisition protocols could feature measurements having \mathbf{B}_{ij} tensors with quite general features (e.g., non-axisymmetric or anisotropic rank-3 tensors), which could offer some benefits (Herberthson et al., 2019). However, in the current practice, it is quite common to use measurement tensors which fall into one of the following three classes: (i) LTE (linear tensor encoding) where each measurement tensor is the outer product of some vector with itself, implying the eigenvalues of each such $\mathbf{B}_{ij}^{(n)}$ being $\{\lambda^{(n)}, 0, 0\}$ for some $\lambda^{(n)} > 0$. (ii) PTE (planar tensor encoding), where each such measurement tensor $\mathbf{B}_{ij}^{(n)}$ has eigenvalues $\{\lambda^{(n)}, \lambda^{(n)}, 0\}$, $\lambda^{(n)} > 0$. (iii) STE (spherical tensor encoding) where each such measurement tensor is proportional to the identity matrix.

For protocols that use measurements of only type (i) and (iii), i.e., LTE and STE, this will lead to a rank deficient matrix \mathbf{A} , with (maximum) rank $1 + 6 + 16 = 23$. The reason for this is that with measurement tensors of type (i), i.e., LTE, the measurements are only sensitive to the completely symmetric part of $\mathbf{C}_{ijk\ell}$, and the space of such tensors has dimension 15. Furthermore, since all isotropic (STE) measurement tensors, i.e., tensors of type (iii), are proportional to each other, they will only be capable of measuring one more dimension in the parameter space.

This raises two questions. First, how does this affect the estimates and the routines to find these? The observation is that the solution is non-unique and also that derived matrices like $\mathbf{Q} = \mathbf{A}^T \mathbf{A}$ become singular (positive semidefinite but not positive definite). There are various ways to handle this challenge; the most common with degenerate least squares problem is perhaps to pick the solution vector with minimal norm. This can be achieved by employing a pseudoinverse or using a so called subspace reduction. When integrated into the WLLS method, we refer to the technique as “WLLS(ss).”

The second question is: how are the presented results affected by the rank deficiency of the design matrix? Indeed, because of this degeneracy, many $\mathbf{C}_{ijk\ell}$ tensors are equivalent in terms of their ability to represent the data. However, as shown in Appendix G, all scalar measures to be used in this work are insensitive to this degeneracy, the exception

⁴ This may seem like a restriction. In our experience, however, the estimates of x_1, x_2, \dots, x_7 are relatively ‘stable’ as compared to x_8, \dots, x_{28} .

³ We do not have strict equivalence, see Appendix E

being the Frobenius norm involving the covariance tensor $C_{ijk\ell}$ in the case of rank deficient estimation.

4. Methods

4.1. Implementation

In this section, we describe our strategy incorporating the techniques described above into a unified framework. The framework contains the following steps:

1. SDP(dc): See Section 3.6 and Eq. (12). The result of this step could be taken as the final result. However, it can also be treated as an initial estimate and fed into Step 2, for which heteroscedasticity is not an issue. It can also be fed into Step 3 (and 4 if necessary) for imposing condition (m).
2. NLLS(dc): See Section 3.5 and Eq. (11). This step employs the original (nonlinear) model, which should in general reduce the residues (in the nonlinear form of the model) obtained via SDP(dc). In rare cases when NLLS(dc) fails to produce an improvement over SDP(dc), which can occur when the modified Cholesky decomposition leads to poor initial estimates, the SDP(dc) outcome is retained. The result of this step could be used as the final result. However, if condition (m) is to be imposed, further analysis is necessary.
3. (m)-check: See Section 3.7 and Eq. (14). If the voxel satisfies condition (m), no further step is necessary. If not, the next step is employed.
4. SDP(dcm): See Section 3.8 and Eq. (15).

All the fitting routines were implemented in Matlab (The Mathworks Inc, Natick, Massachusetts). For SDP we used CVX, a package for specifying and solving convex programs in Matlab (Grant and Boyd, 2008; 2014). In steps 1, 3, and 4 CVX calls the solver MOSEK version 9.1.9 (MOSEK ApS, Denmark). For the non-linear fit in step 2 we used the Matlab routine *lsqcurvefit*. For the standard QTI analysis, the multidimensional dMRI toolbox, provided at <https://github.com/markus-nilsson/mddmri> was employed. The estimation methods were also independently implemented in Mathematica (Wolfram Research Inc., Champaign, IL, USA) to check for consistency.

4.2. Simulations

We performed simulations to assess the impact of adding different constraints to the estimation of S_0 , $\hat{\mathbf{D}}_{ij}$ and $C_{ijk\ell}$. We considered an independent method for the generation of the diffusion signals to be fitted with both the available and proposed methods. For this task, we chose the non-central Wishart distribution whose mean and covariance tensors can be derived analytically. As discussed elsewhere (Herberthson et al., 2019; Jian et al., 2009; 2007), the diffusion MR signal is the Laplace transform of the underlying DTD. For the case of non-central Wishart distributions, the result is provided by Mayerhofer (2013). Given some measurement tensor \mathbf{B}_{ij} , the signal for a non-central Wishart distribution with the non-centrality matrix⁵ Ω_{ij} , the scale parameter (degrees of freedom) p , and scale matrix Σ_{ij} is given by⁶ (Shakya et al., 2017)

$$S(\mathbf{B}) = S_0 |\mathbf{I} + \Sigma \mathbf{B}|^{-p} \exp(-\text{Tr}[\mathbf{B}(\mathbf{I} + \Sigma \mathbf{B})^{-1} \Omega]) \quad (16)$$

where “ $|\cdot|$ ” indicates matrix determinant and we dropped the subscripts for brevity. We employed this expression for the signal to find $\hat{\mathbf{D}}_{ij}$ and $C_{ijk\ell}$ in the model (1), the result being

$$\hat{\mathbf{D}}_{ij} = p \Sigma_{ij} + \Omega_{ij} \quad (17)$$

⁵ Here we are following the notation of Letac and Massam (1998). In this work, which emphasizes the relation to gamma distributions, the Wishart distribution is written $\gamma_{p,\Sigma}$. It is related to the more common notation $W_p(p, \Sigma)$ by $\gamma_{p,\Sigma} = W_p(2p, \Sigma/2)$.

⁶ We note and correct an error in the order of Σ and \mathbf{B} matrices in (Shakya et al., 2017).

Table 1

The five protocols considered in this study. The protocol p217 contains thirteen non-diffusion weighted images while the others have one such image.

Protocol	Encoding	b-values [ms/m ²]	Samples per shell
p217	LTE	0.1, 0.7, 1.4, 2.0	10,10,16,46
p217	PTE	0.1, 0.7, 1.4, 2.0	10,10,16,46
p217	STE	0.1, 0.7, 1.4, 2.0	10,10,10,10
p81	LTE	0.1, 0.7, 1.4, 2.0	6,6,10,21
p81	STE	0.1, 0.7, 1.4, 2.0	6,6,10,15
p56	LTE	0.1, 1.4, 2.0	4,10,15
p56	STE	0.1, 1.4, 2.0	6,10,10
p56s	LTE	0.1, 1.0, 2.0	4,10,15
p56s	STE	0.1, 1.0, 2.0	6,10,10
p39	LTE	0.1, 1.4, 2.0	4,10,15
p39	STE	0.1, 1.4, 2.0	3,3,3

$$C_{ijk\ell} = \frac{p}{2} (\Sigma_{i\ell} \Sigma_{jk} + \Sigma_{ik} \Sigma_{j\ell}) + \frac{1}{2} (\Sigma_{jk} \Omega_{i\ell} + \Sigma_{i\ell} \Omega_{jk} + \Sigma_{j\ell} \Omega_{ik} + \Sigma_{ik} \Omega_{j\ell}). \quad (18)$$

The derivation of the above expressions is provided in Appendix H. The non-central Wishart distribution simulated here has higher order cumulants, which is what we expect to have in neural tissue as well. However, we provide the expressions for the first two cumulants, which are to be estimated using the model.

In our simulations, we took $0.7 \mu\text{m}^2/\text{ms}$ for $\frac{1}{2} \text{Tr}(\hat{\mathbf{D}}_{ij})$, and set $\Sigma_{ij} = \hat{\mathbf{D}}_{ij}/(5p)$. We performed two simulations, first having isotropic $\hat{\mathbf{D}}_{ij}$ with $p = 2$, while in the other we took $p = 4$ and the eigenvalues of $\hat{\mathbf{D}}_{ij}$ to be 0.6, 0.2, and $1.3 \mu\text{m}^2/\text{ms}$. Note that p determines the asymptotic behavior of the signal decay curve; see (16). For $p = 2$, one obtains a signal decay consistent with Debye-Porod law, which is the expected decay for diffusion in porous media measured via Stejskal-Tanner pulse sequence featuring narrow pulses (Sen et al., 1995). For wide pulses, such slow decay is replaced by a steeper one (Özarslan et al., 2018). Fig. 1 shows the joint distributions of Mean Diffusivity (MD) and Fractional Anisotropy (FA) for the tensor distributions whose averages are the anisotropic and isotropic $\hat{\mathbf{D}}_{ij}$ considered in the simulations.

Two sets of measurement tensors \mathbf{B}_{ij} were used to generate the signal for the simulations. The shorter protocol having 56 measurements is referred to as p56s. This protocol combines \mathbf{B}_{ij} tensors of rank 1 and 3, i.e., linear (LTE) and spherical (STE) encodings, and one measurement without diffusion encoding. A longer protocol, referred to as p217, consisting of 217 measurements was also considered. This longer protocol combines encoding tensors of rank 1, 2, and 3 as well as 13 measurements without diffusion weighting. The two protocols are summarized in Table 1. The protocol p56s can be found at http://github.com/filip-szczepankiewicz/fwf_seq_resources/tree/master/GE. The longer protocol p217 is a subset of the one described in Szczepankiewicz et al. (2019) and available at https://github.com/filip-szczepankiewicz/Szczepankiewicz_DIB_2019. In particular, the repeated STE measurements were removed from the full protocol in Szczepankiewicz et al. (2019). Note that the shorter protocol p56s leads to rank-deficient design matrices while the matrices associated with the long protocol p217 are not rank-deficient.

Noisy Gaussian and Rician distributed signals were synthesized by adding Gaussian noise to the real and to the real and imaginary parts of the analytical signals obtained from (16), respectively. The standard deviations of the Gaussian noise were taken to be $\sigma = [0, 0.020, 0.056, 0.092, 0.128, 0.164, 0.200]$, which correspond to SNR⁷ values of $\text{SNR} = 1/\sigma = [\infty, 50, 18, 11, 8, 6, 5]$ for the non-diffusion weighted sig-

⁷ Our definition of the SNR is the same as that in other studies on noise in MRI (Gudbjartsson and Patz, 1995; Koay et al., 2009).

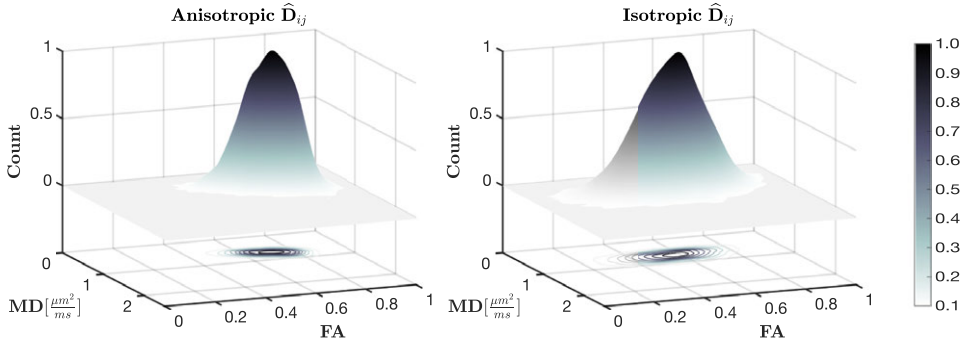


Fig. 1. Joint distribution of MD and FA values of the diffusion tensors in the simulated DTDs. Left: DTD with anisotropic mean. Right: DTD with isotropic mean.

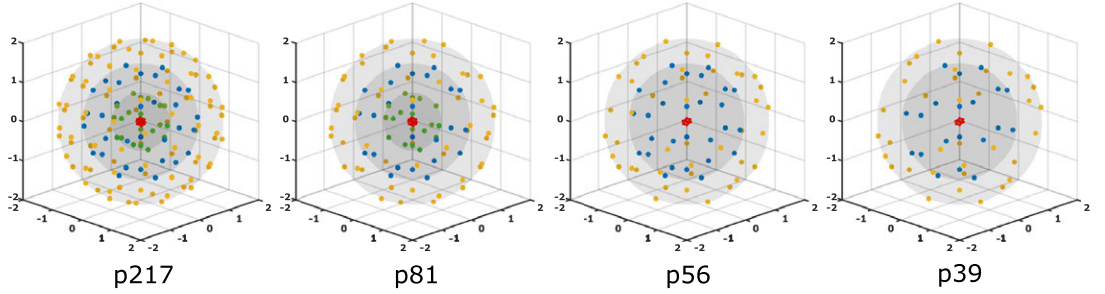


Fig. 2. The four protocols considered in this study for the analysis of the experimental data. From left to right: p217, p81, p56, and p39 refer to the protocols having 217, 81, 56, and 39 volumes, respectively. The colored dots show the initial direction of each diffusion gradient waveform. Red, green, blue, and yellow dots indicate such directions for samples at b -values of 0.1, 0.7, 1.4, and 2.0 $\text{ms}/\mu\text{m}^2$, respectively. (For interpretation of the references to colour in this figure legend, the reader is referred to the web version of this article.)

nal, where this signal was taken to be $S_0 = 1$. For each standard deviation, 1000 noisy signals were generated and then fitted using the various QTI and QTI+ estimation schemes. We compared the results produced by the different methods using metrics derived from $\hat{\mathbf{D}}_{ij}$ and \mathbf{C}_{ijkl} . These metrics involved both a direct measure of the distance between the analytical and the estimated tensors, given by the Frobenius norm of the difference between the reference and estimated tensors normalized with the Frobenius norm of the reference tensors, $\|\Delta\hat{\mathbf{D}}_{ij}\|/\|\hat{\mathbf{D}}_{ij}\|$ and $\|\Delta\mathbf{C}_{ijkl}\|/\|\mathbf{C}_{ijkl}\|$, and invariants obtained from the estimated $\hat{\mathbf{D}}_{ij}$ (fractional anisotropy (FA), mean diffusivity (MD), and macroscopic anisotropy (C_M)) as well as those that utilize additional information from the covariance tensor (microscopic anisotropy (C_μ), size variance (C_{MD}), and microscopic orientation coherence (C_c)).

4.3. Experimental data

Four subsets of the data set publicly available at https://github.com/filip-szczepankiewicz/Szczepankiewicz_DIB_2019 and described in Szczepankiewicz et al. (2019) were used to test the proposed framework. One subset was formed with the 217 samples previously described in Table 1, i.e., protocol p217. Further subsets containing 39, 56, and 81 measurements produced the protocols p39, p56, and p81, respectively. These are also summarized in Table 1. The samples in p56 and p81 were chosen with the purpose of mimicking the protocols found at http://github.com/filip-szczepankiewicz/fwf_seq_resources/tree/master/GE. Having to pick samples out of an existing dataset, we randomly selected the measurements from the ones available with the goal of keeping reasonably spread measurement directions

while making sure that the design matrix will have rank 23. Fig. 2 shows the sample distributions for p217, p81, p56, and p39.

On these four datasets, we fitted the QTI model using Eqs. (5) (with and without subspace implementation), (12), (11), and (15). For each fit we then checked where the conditions (d), (c), and (m) were violated. Conditions (d) and (c) were considered satisfied if the eigenvalues of the estimated $\hat{\mathbf{D}}_{ij}$ and $\mathbf{C}_{\alpha\beta}$ were non-negative. However, we consider that a simple check done on the raw eigenvalues of the two tensors might mistake a violation of the two conditions with numerical errors arising from limited tolerances in the employed fitting routines. For example, a tensor having eigenvalues 2, 1, and -10^{-8} can still be considered nonnegative if the proximity of the negative eigenvalue to 0 is smaller than numerical tolerance. To overcome this ambiguity, we introduced a metric we refer to as “negativity index,” which in essence is a normalized and dimensionless indicator of the positivity violations. For any symmetric matrix, we calculate the eigenvalues $\lambda_1, \dots, \lambda_N$ and form the quotient

$$\text{NI} = \frac{\sum_{i, \lambda_i < 0} \lambda_i^2}{\sum_i \lambda_i^2} \quad (19)$$

i.e., the sum in the numerator is only taken over the negative eigenvalues. Note that this measure is insensitive to scalings of the underlying matrix. When NI is below 5×10^{-4} , the nonnegativity condition (d) or (c) is deemed to be fulfilled. To check whether condition (m) is fulfilled, we employed the scheme described in Appendix E.

4.4. Synthetic data

Additional simulations, inspired by those performed in Dela Haije et al. (2020), were performed to further assess the relevance of enforcing positivity constraints for the estimation of the parameters. The S_0 , \hat{D}_{ij} , and C_{ijkl} estimated by applying SDP(dcm) on the dataset with 217 measurements were used to create a synthetic dataset according to equation (1). As explained in Dela Haije et al. (2020), such dataset can be seen as the output of an ideal preprocessing pipeline which removes any bias and artifacts in the data. Moreover, assuming that the signal reconstruction provided by the investigated model is representative of the acquired data, this dataset can effectively be seen as a collection of signals produced by many different plausible tissue specimens. Therefore, it can act as ground truth for validation purposes.

Gaussian and Rician noise with standard deviation $\sigma = 0.04$, corresponding to $\text{SNR} = 1/\sigma = 25$ on an S_0 value estimated from a region of interest containing white and gray matter voxels, was added to the dataset. The noisy datasets were then subsampled to 56 measurements. The parameters were estimated through both WLLS(ss) and SDP(dcm) applied on the noisy synthetic datasets with 217 and 56 measurements.

5. Results

5.1. Simulations

The results of our simulations are illustrated in Fig. 3 for the isotropic \hat{D}_{ij} and Fig. 4 for the anisotropic \hat{D}_{ij} . The analytical results are depicted via dotted lines, which can be regarded as the ground truth in cases when QTI offers an accurate representation of the analytical signal. For a comparison of the QTI model in general compared to other methods for estimating statistical descriptors, we refer to (Reymbaut et al., 2020)⁸. Here, it is observed that the QTI model allows for, and indeed may produce, negative estimates of manifestly non-negative quantities. If the model in (1) is insufficient in describing the signal, i.e., when the higher order cumulants influence the signal within the range of employed diffusion weightings, we expect a deviation of the noiseless ($\text{SNR}=\infty$) estimates from the dotted lines. Each solid circle shows the mean value of the estimates, different colors representing different estimation methods. The standard deviations are depicted via error bars. No appreciable difference was observed between the fits obtained on the noisy Rician and Gaussian distributed signals, therefore only the results on the Rician noise are shown.

From Figs. 3 and 4, it is clear that the QTI+ estimates obtained via SDP(dc), NLLS(dc), and SDP(dcm) methods are more robust to noise. In general, this refers to smaller deviations of the mean of the presented metrics, and substantially reduced standard deviations (error bars). This is particularly evident for the derived scalar measures. The Frobenius norms exhibit more noise sensitivity, which is likely because the Frobenius norm captures the tensors in their entirety while the other parameters are sensitive only to certain features of the tensors. Therefore, larger deviations appear, as expected, in the Frobenius norms of the difference between the reference and estimated tensors. This suffices to explain as well why most of the metrics derived from the WLLS(ss) fit are acceptable for SNRs down to ≈ 20 despite complications due to the rank deficiency of the design matrix for the shorter protocol.

Concerning the QTI+ estimation methods, we note that the results produced with SDP(dc), NLLS(dc), and SDP(dcm) are not drastically different. Especially when comparing NLLS(dc) and SDP(dcm), the difference is very subtle. This is partly because the violations of condition (m) are not frequent⁹ and perhaps also because satisfying condition (m) does not have a very strong influence on the estimated metrics.

⁸ Note, however, that the work of Reymbaut et al. (2020) focuses on DTDs of axisymmetric diffusion tensors.

⁹ The numbers of signal profiles that violated condition (m) after the NLLS(dc) fitting and were subsequently fed into the SDP(dcm) routine were highest for

Looking at specific metrics, we note that FA increases with noise when \hat{D}_{ij} is isotropic. Interestingly, constrained estimation tends to reduce FA in simulations featuring anisotropic \hat{D}_{ij} tensors. This could be explained considering that in absence of constraints, smaller eigenvalues would spread in the negative direction, thus incorrectly increasing the spread of the eigenvalues of \hat{D}_{ij} hence the FA value, while when constraints are applied, the small eigenvalues can only grow in the positive direction, leading to a reduction in anisotropy. The same trends are evident in the C_C results as expected.

Microscopic anisotropy is perhaps the most interesting scalar measure that has prompted much interest in the development of alternative diffusion encoding methods (Cheng and Cory, 1999; Cory et al., 1990; Ianus et al., 2017; Lawrenz et al., 2010; Özarslan, 2009) that eventually led to the introduction of QTI. Note that having isotropic \hat{D}_{ij} does not imply 0 microscopic anisotropy because a non-central Wishart distributed set of tensors represent an ensemble of anisotropic subdomains even if their mean is isotropic. Our simulations suggest that the microscopic anisotropy index ($C_\mu = \mu\text{FA}^2$) is also quite susceptible to noise when traditional QTI methods are employed. The estimates benefit greatly from constrained estimation methods.

The noise sensitivity issue is more serious for indices of size variance (C_{MD}) and coherence (C_C). In fact, the estimates are simply unreliable under noisy conditions when no constraint is employed. QTI+ estimates of these indices could make them suitable for comparative analyses.

Effects of employing shorter acquisition protocols can be assessed by comparing the two panels of Figs. 3 and 4. Remarkably, employing the shorter protocol leads to a very considerable loss of quality for unconstrained QTI estimates of C_μ for example. As far as the constrained QTI+ estimators are concerned, the influence of the protocol has a relatively minor effect. This observation is important as it suggests that QTI+ could facilitate the employment of the method in clinical investigations where the acquisition time is a critically important limitation.

5.2. Experimental data

In Fig. 5, we illustrate the extent of the violations of the three positivity conditions. For both the long protocol p217 (left) and shorter protocol p56 (right), condition (c) is violated almost everywhere within the brain parenchyma when WLLS methods are employed. Condition (d) seems to be violated mostly in the very anisotropic and coherently organized regions like in the corpus callosum. As expected, these violations do not prevail when the QTI+ methods are employed. The rank deficiency of the design matrix associated with the shorter protocol seems to have the biggest impact on condition (m). Without the formulation in the subspace, this issue manifests as violation of (m) in almost all voxels. WLLS(ss) reduces the extent of such violations considerably. Interestingly, the SDP(dc) method provides further improvement although the condition (m) is not enforced. SDP(dcm) fulfills all three conditions as expected.

Fig. 6 illustrates the maps of the scalars obtained through various estimation methods for the dataset comprising 56 volumes. Despite the apparent similarity of the maps, some differences are visible, particularly in anisotropy measures (FA, C_M , C_μ , μFA). Namely, the maps derived through constrained estimation methods shown in the last three rows appear to be smoother than those obtained via unconstrained estimation. As none of the analyses employs information from neighboring voxels, we think this is an important finding, which corroborates the noise resilience associated with the constrained estimation methods evident in the simulations. Appreciable changes are also evident in the C_C maps by way of a reduction in the apparent coherence values in CSF.

Fig. 7 shows the scalar maps obtained by fitting the considered protocols, respectively, with WLLS(ss) and SDP(dcm). Looking at both pan-

the simulations of the p56s protocol with anisotropic \hat{D}_{ij} . These numbers were, respectively, 0, 12, 92, 200, 307, 358, out of the 1000 noisy samples for each (non-zero) noise level.

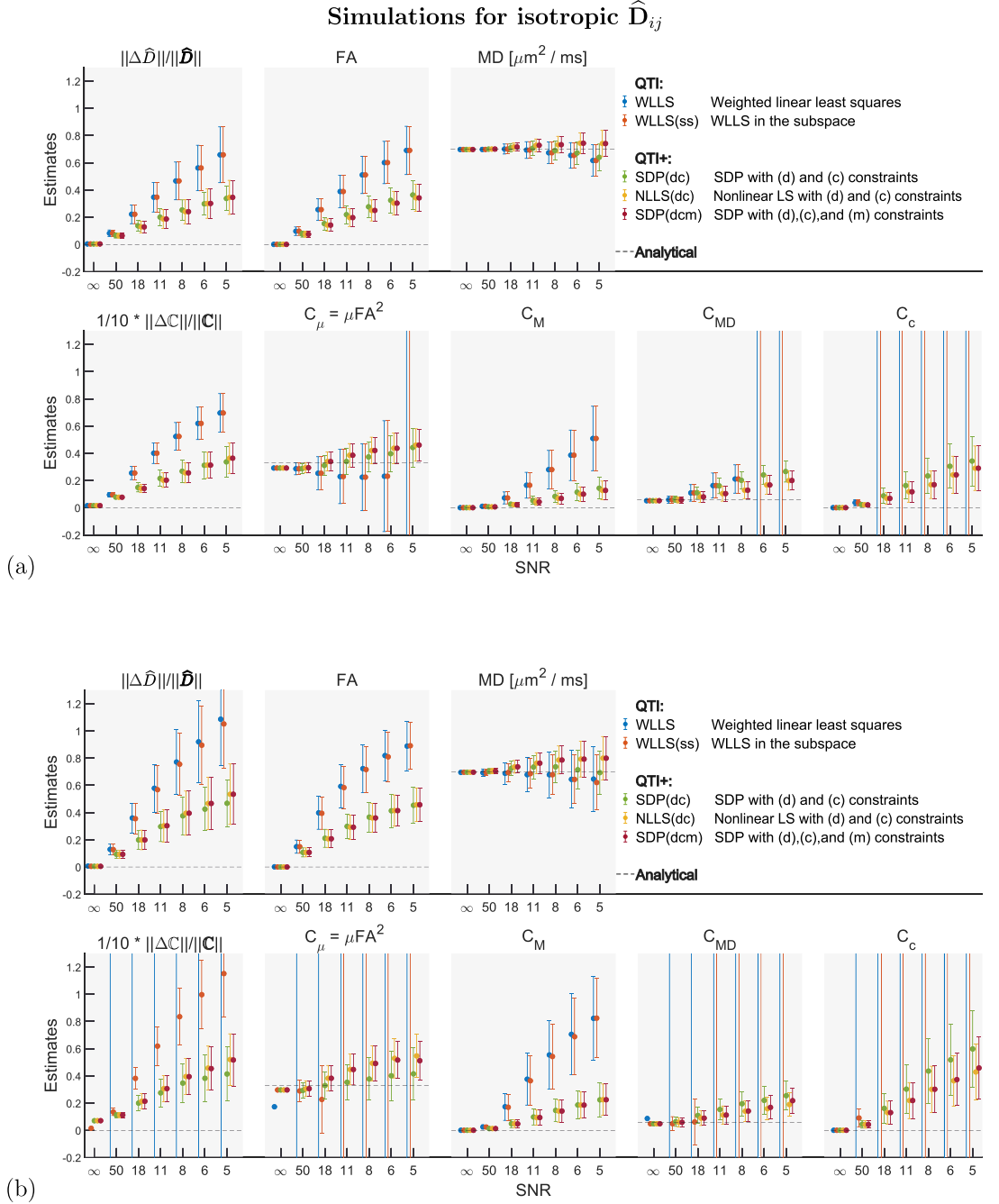


Fig. 3. Simulations for isotropic \hat{D}_{ij} , and Rician distributed noisy signals. Frobenius norms (indicated by $\|\cdot\|$) and the estimated measures under varying noise levels for the estimation methods considered. C stands for C_{ijk} while \hat{D} stands for \hat{D}_{ij} . (a) protocol p217. (b) protocol p56s.

Simulations for anisotropic \hat{D}_{ij}

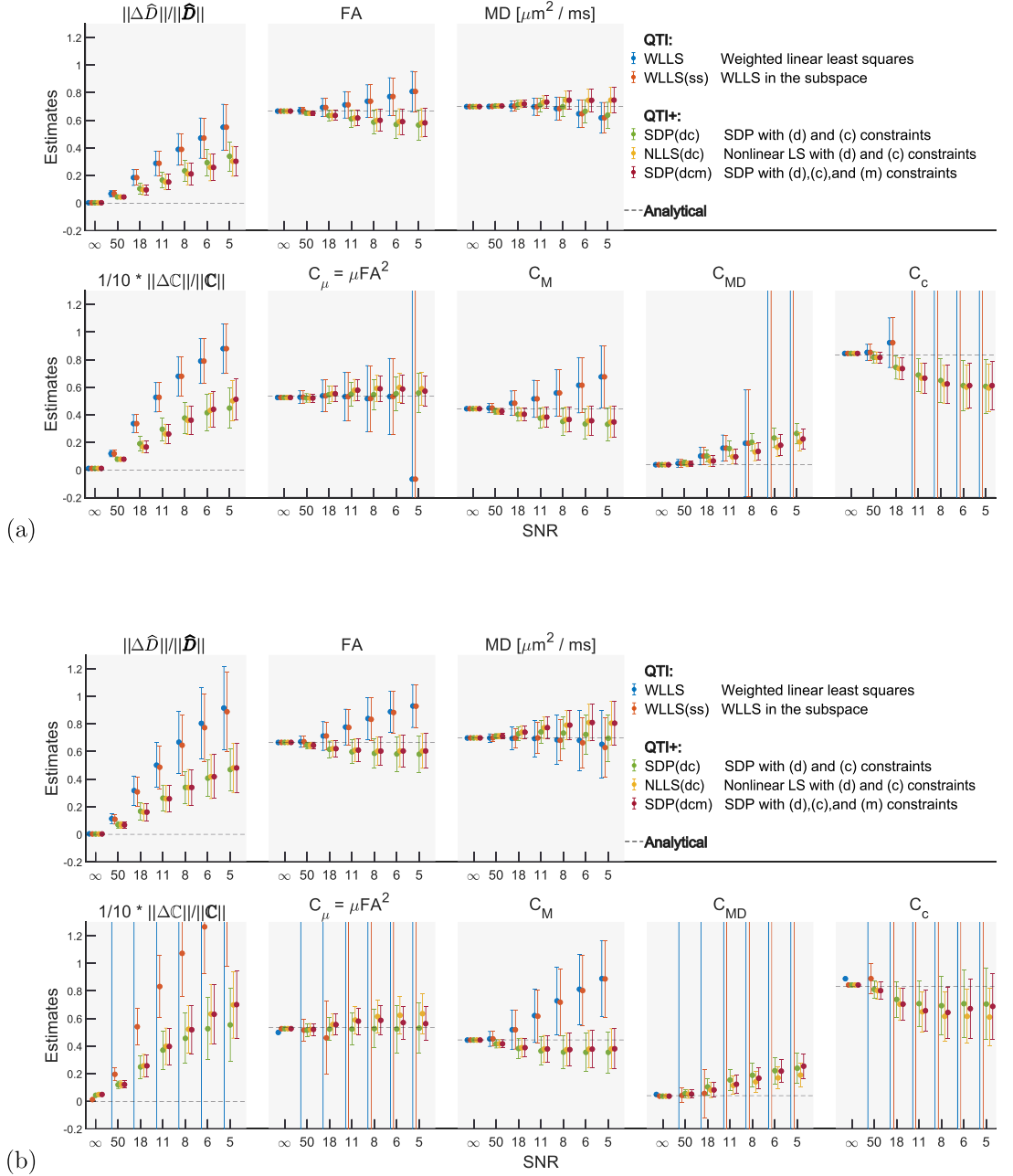


Fig. 4. Simulations for anisotropic \hat{D}_{ij} , and Rician distributed noisy signals. Frobenius norms (indicated by $\|\cdot\|$) and the estimated measures under varying noise levels for the estimation methods considered. C stands for C_{ijk} while \hat{D} stands for \hat{D}_{ij} . (a) protocol p217. (b) protocol p56s.

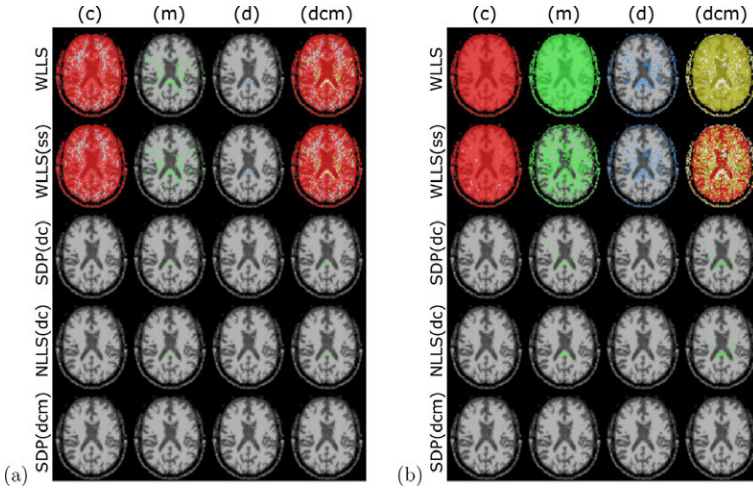


Fig. 5. The violations of the three constraints are color encoded and depicted on brain images. Red, green, and blue indicate violation of conditions (c), (m), and (d) respectively. The last column indicates the constraints together where yellow indicates violations of (c) and (m), magenta (c) and (d), and cyan (d) and (m). All three conditions are violated in white pixels. (a) protocol p217. (b) protocol p56. (For interpretation of the references to colour in this figure legend, the reader is referred to the web version of this article.)

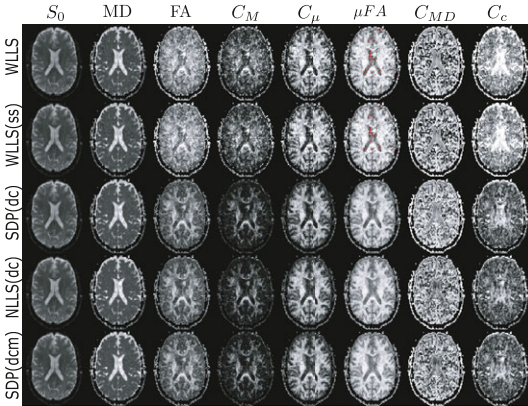


Fig. 6. Maps estimated through various methods from data involving 56 volumes. Red voxels on the μ FA maps indicate imaginary values. Despite the voxel-by-voxel analysis, the QTI+ maps (last three rows) are visibly smoother than the QTI maps employing weighted linear estimations (first two rows).

els, one observes that the non-diffusion weighted (S_0) and mean diffusivity (MD) maps are not severely affected by the downsampling. The anisotropy maps (fractional anisotropy FA, macroscopic anisotropy C_M , and microscopic anisotropy $C_\mu = \mu\text{FA}^2$) obtained via both methods are acceptable for the 81-measurement protocol. At sparser samplings, the improvement obtained by enforcing constraints becomes clear. Such improvement is evident also when looking at the bar plots indicating the mean absolute deviations of the scalar maps from their ground truth values, which are taken to be the maps computed on the p217 protocol. The results obtained by employing SDP(dcm) show consistent lower deviations from the respective ground truths compared to those obtained via WLLS(ss). The bar plots also reveal that the coherence (C_c) and size variance (C_{MD}) estimates have very large absolute deviations for unconstrained estimation. A further examination of the pixel values revealed that this can be attributed in part to a small number of voxels that yield

values way outside their expected range ([0, 1]). This issue is remedied by the QTI+ framework.

Figs. 8 and 9 show details for the FA and μ FA maps computed on all considered protocols by employing WLLS(ss) and SDP(dcm), respectively. Looking at the (a) panels, the benefits of applying constraints are already evident. Again, we stress how the maps obtained with SDP(dcm) appear overall smoother even though the method is performed on a voxel-by-voxel basis without incorporating any intervoxel information. Panels (b) in these figures show the difference between the maps estimated with the p217 protocol, taken here as reference, and its subsets p81, p56, and p39. It is quite interesting to note that reducing the number of measurements from 56 to 39 does not drastically change the results. The histograms in panels (c) illustrate how reducing the number of available samples introduces a bias towards higher values in the anisotropy measures. We also note that constraining the fit strongly reduces the number of voxels presenting values outside the expected range ([0,1] for FA and μ FA). With respect to this, applying constraints (d), (c), and (m) seems to be insufficient to guarantee the condition $\mu\text{FA} \leq 1$. We found that when μFA is greater than 1 in the results produced by SDP(dcm), the values are still very close to 1. Although one can be tempted to attribute this error to numerics, a more reasonable explanation is that μFA is formed from the estimates of \hat{D}_{ij} and C_{ijkl} , which are in a sense independent, and there is no guarantee that μFA should in fact not be greater than 1. Moreover, QTI+ only ensures some necessary constraints, but not all. Having μFA values strictly lower or equal to 1 could be added as a constraint, but from our findings this would have a very marginal effect¹⁰.

5.3. Synthetic data

Fig. 10 shows the results obtained by fitting the synthetic brain datasets with both the WLLS(ss) and SDP(dcm) routines. The performance of the two methods was quantified through the Fobienius norms of the difference between the estimated and ground truth C_{ijkl} tensors, $\|\Delta C\|$, and differences between the estimated and ground truth metrics, ΔFA , $\Delta\mu\text{FA}$, ΔC_c , counted for all voxels (≈ 84000) in the dataset.

¹⁰ Out of the ≈ 84000 considered voxels, only 42, 30, 14, and 21 had μFA values > 1 for the SDP(dcm) fits performed on the 217, 81, 56, and 39 measurements datasets, respectively.

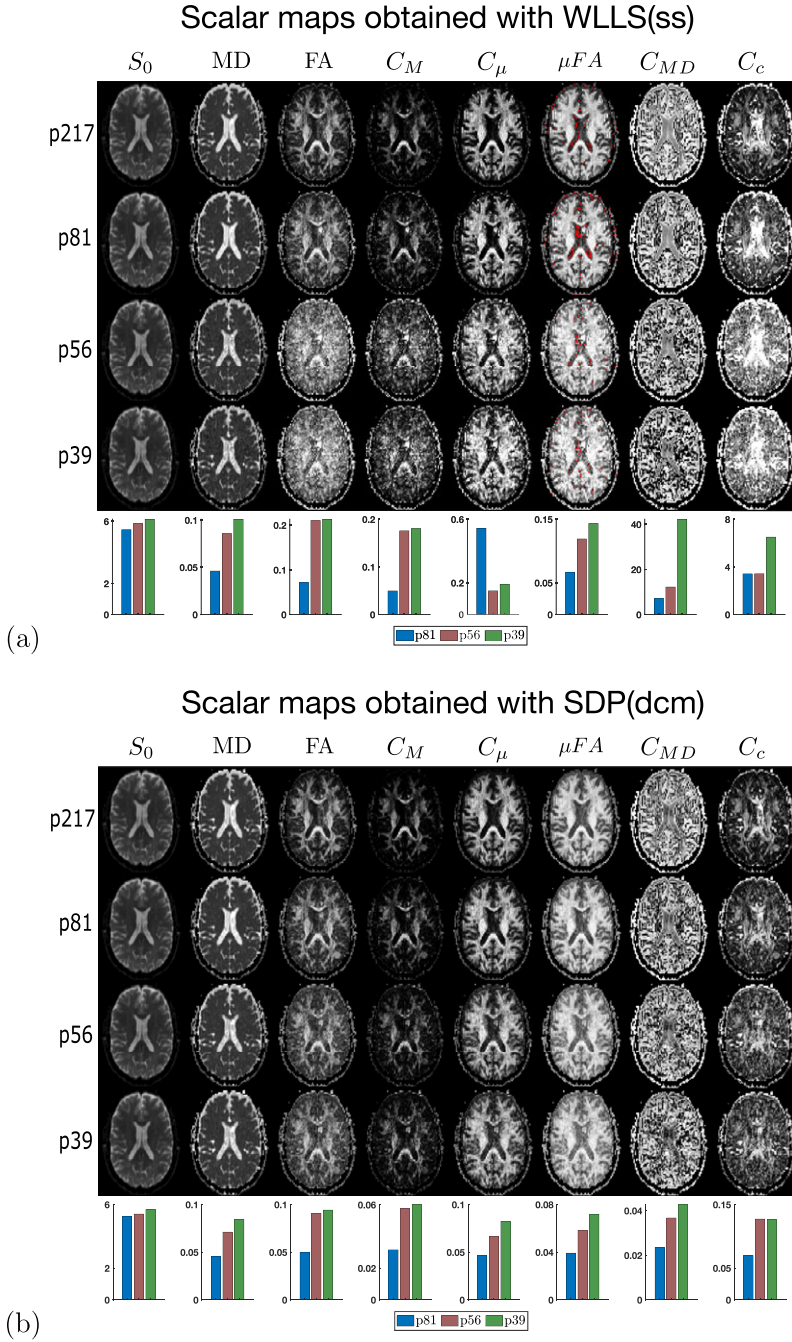


Fig. 7. Scalar maps obtained by employing WLLS(ss) and SDP(dcm) estimation schemes on p217, p81, p56, and p39 protocols. Red pixels on the μFA maps indicate complex values. The bars on the last rows of panels (a) and (b) show the mean absolute deviation of the respective parameters due to downsampling the p217 protocol. Here, S_0 has arbitrary units while MD is expressed in $\mu m^2/ms$. (a) WLLS(ss), (b) SDP(dcm).

Method comparison on FA estimation

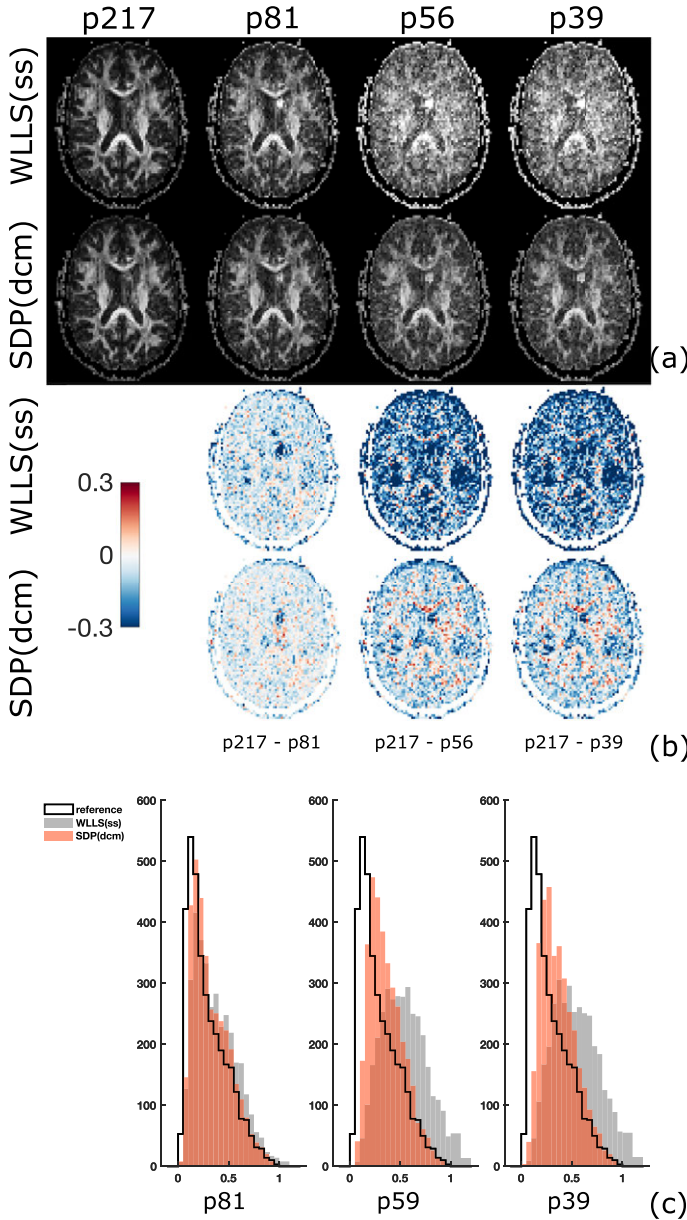


Fig. 8. (a) FA maps obtained by fitting the QTI model with WLLS(ss) and SDP(dcm) on the four protocols. The fits performed with both methods on the p217 protocol are used as reference. (b) Difference between the reference FA maps and those estimated with both methods on the three down-sampled protocols. (c) Histograms showing the distribution of FA values for the three protocols.

Looking globally at the results in panels (a) and (b), there seems to be no relevant difference between the fitting results obtained in the data corrupted with either Gaussian or Rician noise. There is moreover not a marked difference between the performance of QTI and QTI+ on the 217-measurement protocols, with QTI+ providing slightly better results. The difference in performance between WLLS(ss) and

SDP(dcm) is instead highlighted in the plots showing the results on the 56-measurement protocol. There, the distance between the estimated and reference metrics is almost centered about zero for QTI+, while the parameter values produced with QTI exhibit a more pronounced tendency towards being over-estimated.

Method comparison on μ FA estimation

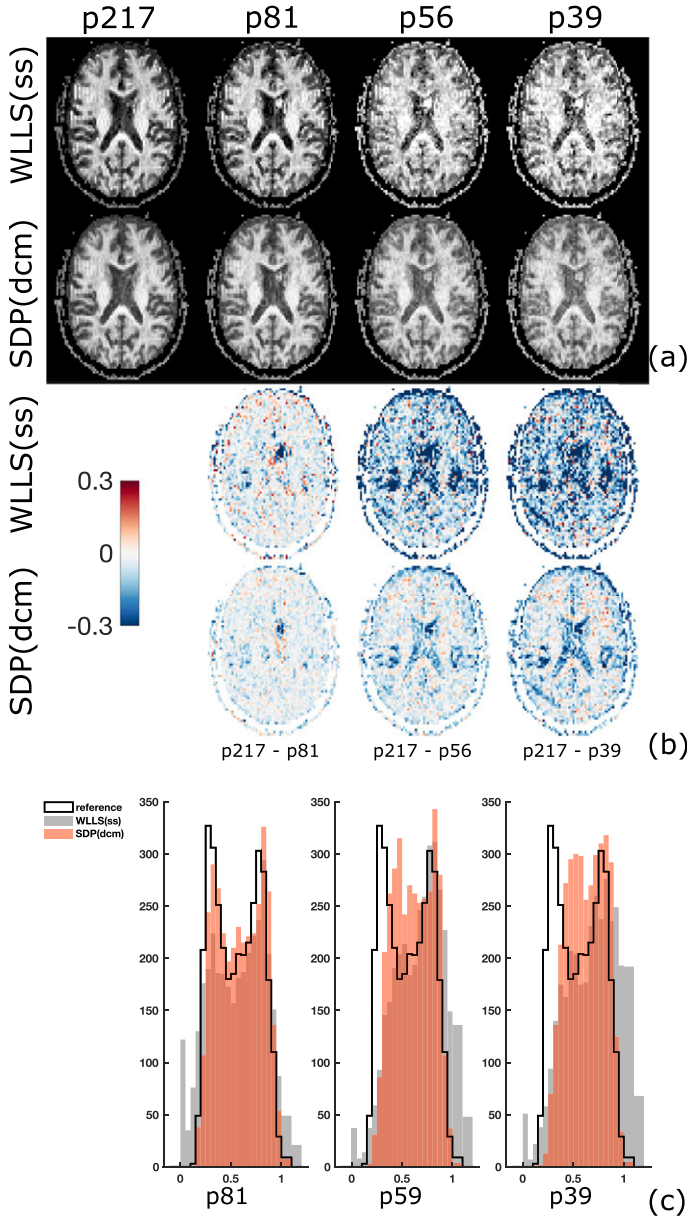


Fig. 9. (a) μ FA maps obtained by fitting the QTI model with WLLS(ss) and SDP(dcm) on the four protocols. The fits performed with both methods on the p217 protocol are used as reference. (b) Difference between the reference μ FA maps and those estimated with both methods on the three downsampled protocols. (c) Histograms showing the distribution of μ FA values for the three protocols.

5.4. Run times

One of the appealing features of QTI is the computational speed at which the estimation can be performed via standard linear regression routines; it takes only a few seconds to fit the model to an entire dataset.

This is definitely not the case for non-linear fitting routines, but also for the softwares currently available for semidefinite programming. As mentioned in the implementation section, we rely on an external package to solve the SDP problems. In our experience, calling this package on a voxel-by-voxel basis is inefficient, leading to prolonged computational

Comparison of QTI and QTI+ on synthetic data

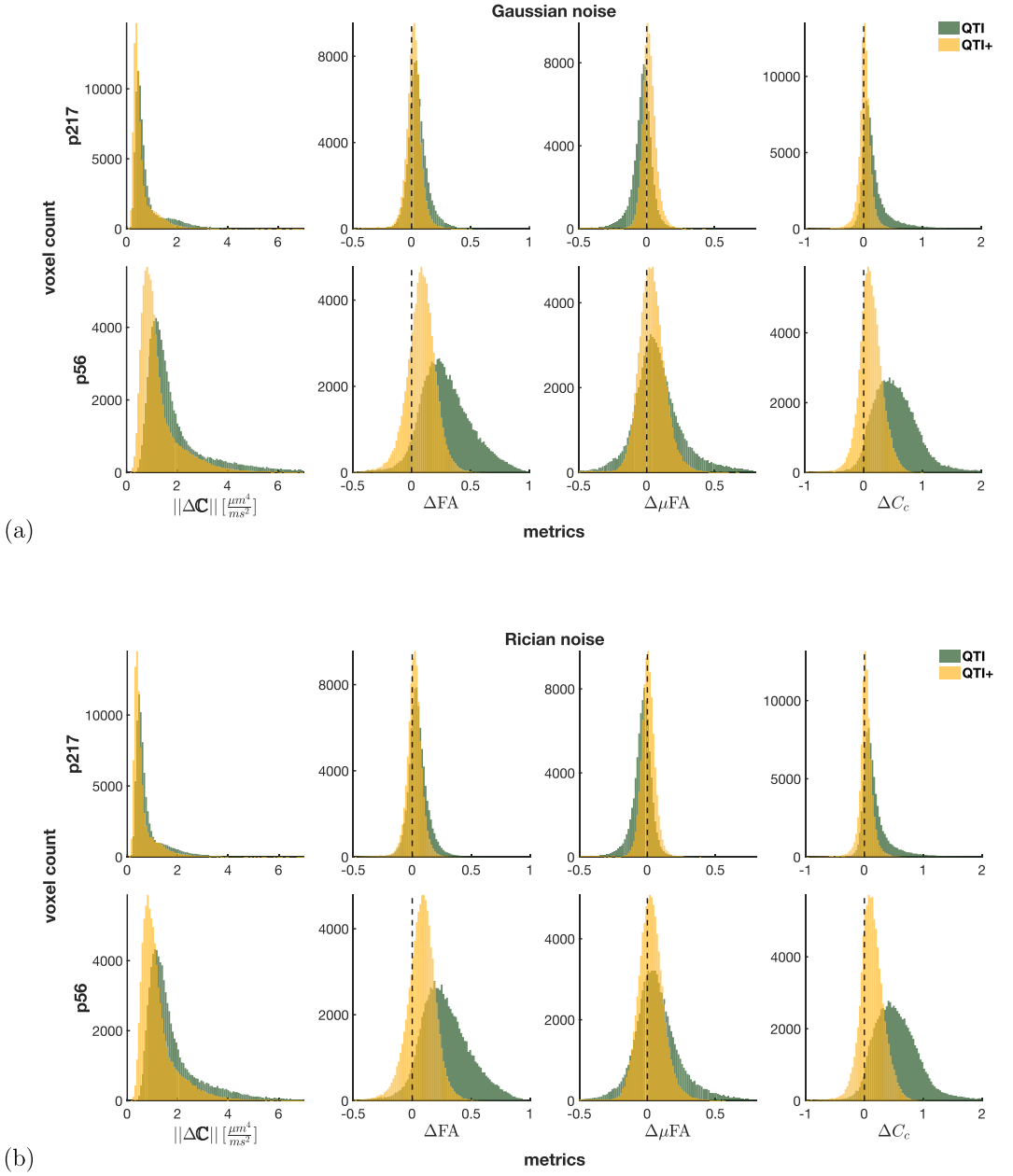


Fig. 10. Comparison of QTI and QTI+ on synthetic data. Frobenius norm of the difference between the ground truth and estimated $C_{ij\mu}$ (indicated by $\|\Delta C\|$) and differences between the estimated and ground truth metrics. Positive and negative values in the difference plots indicate parameters over- and under-estimated, respectively. (a) Gaussian noise. (b) Rician noise.

Table 2
Run times for the protocols with 217 and 56 volumes.

Protocol	Fitting Routine	Run Times
p217	SDP(dc), single voxel	43 min
p217	SDP(dc), multi voxel	6 min
p217	NLLS(dc), single voxel	11 min
p217	m-check + SDP(dcm), single voxel	37 min
p217	m-check + SDP(dcm), multi voxel	5 min
p217	SDP(dcm), multi voxel	14 min
p217	WLLS(ss)	4 s
p217	WLLS	2 s
p56	SDP(dc), single voxel	50 min
p56	SDP(dc), multi voxel	10 min
p56	NLLS(dc), single voxel	15 min
p56	m-check + SDP(dcm), single voxel	38 min
p56	m-check + SDP(dcm), multi voxel	10 min
p56	SDP(dcm), multi voxel	14 min
p56	WLLS(ss)	2 s
p56	WLLS	5 s

times. A better approach involves performing the operations on a batch of voxels each time the function is called. In this case, steps 1, 3, and 4 can be performed by, for example, solving the problems on 50 voxels at a time. This provided relevant speed up when compared to performing the analysis one voxel at a time, as shown in Table 2. The table shows the run times for the different routines using different strategies on the experimental dataset (≈ 84000 voxels) with, respectively, 217 and 56 measurements. The clock times were recorded on a workstation featuring a 12-core Intel Core i9-7920X CPU. The “multi voxel” implementation concerned sending 50 voxels at a time to the SDP solver.

Performing the fit on a multivoxel basis is perhaps intuitive for SDP(dc), but maybe not so much for the (m)-check and eventual SDP(dcm) steps, given the conditional step involved in the process. In the worst case scenario, one would in fact have to run the (m)-check on all batches of voxels, and then SDP(dcm) on all those batches. Even though this would still be faster than doing this process voxel-by-voxel, a faster option could be to skip the check on the (m) condition and directly perform SDP(dcm) on a multivoxel basis. However, since already after SDP(dc) (and NLLS(dc)) most of the (m) violations are resolved, and since the (m)-check appears to be faster than SDP(dcm), we find that the fastest option is to perform both the (m)-check and SDP(dcm) on a multivoxel basis.

It is well-known that non-linear fitting is typically more time-consuming than linear regression. One aspect to be considered is that having a good starting point, provided here by SDP(dc), helps in speeding up the non-linear fitting of the NLLS(dc) routine. However, we would like to remind the reader that NLLS(dc) is not a necessary step to perform in QTI+ as satisfactory results can be obtained using SDP(dc) and SDP(dcm). If truly pressed with time, one could also rely on the results produced with SDP(dc) only, as violations of the (m) condition are both infrequent and not extremely influential on the estimates.

6. Discussion

Since the inception of the DTD model (De Swiet and Mitra, 1996; Jian et al., 2007), the challenge of obtaining the underlying DTD from the MR signal has been addressed in different ways. One approach is to assume a parametric distribution, which can naturally ensure that all tensors in the DTD are positive-semidefinite. Indeed, Jian et al. (2007) have assumed a mixture of Wishart distributions for the DTD and even provided the analytical signal for diffusion encoding via arbitrary b-tensors; that relationship can be obtained by setting $\Omega = 0$ in (16). The Wishart distribution is the multidimensional generalization of the gamma distribution, which has been employed to represent the distribution of diffusivities for diffusion in polymer solutions (Röding et al., 2012). This approach has been adopted by Lasič et al. (2014) for representing the distribution of diffusivities along all directions combined. When employed

on tensor-encoded data, this approach yields visually appealing results for some of the parameters considered in this work (Szczepankiewicz et al., 2015; 2016). However, the validity of the gamma distribution is not guaranteed in all voxels, and the consequences of not fulfilling this assumption have not been understood. Moreover, this method relies on an accurate estimation of the orientationally-averaged signal, which can be challenging especially when the number of samples is limited (Afzali et al., 2020). Most recently, Magdoo et al. (2021) have introduced an alternative method, which employs a new pulsed field gradient sequence. The DTD is taken to be a tensor-valued normal distribution with non-positive-definite tensors suppressed. Due to the lack of an analytical form of the signal for this distribution, the signal is approximated using a large number of samples drawn from a given normal distribution. The mean and covariance are subsequently estimated using a least squares optimization.

Rather than employing an assumption regarding the underlying distribution like in the works mentioned above, we have employed the framework in Westin et al. (2016), which allows the estimation of the mean and covariance tensors only. It should be noted that this is not meant to represent the signal in the entire “b-space,” but only its behavior at low b-values, which are probed in typical clinical acquisitions. Here, we considered imposing three constraints on the estimated mean and covariance tensors. Strictly speaking, each and every diffusion tensor in the underlying DTD has to be positive-semidefinite. However, imposing such a strong condition without attempting to solve an extremely ill-posed problem that involves the reconstruction of the actual DTD (Jian et al., 2007; Topgaard, 2019) is likely to be infeasible under noisy conditions or with limited number of diffusion encodings. Interestingly, non-negativity of each microscopic diffusion tensor implied the (m) condition, which seemed to have a minor effect in our analyses. Much of the improvement is already obtained through imposing condition (d) together with the (c) condition, which follow from the nonnegativity of the covariance tensors¹¹; these conditions are valid even when the distribution is over a more general space—not necessarily the space of positive semidefinite tensors.

Satisfactory performance obtained by imposing only the conditions (d) and (c) have implications also when one decides on which estimation method to use. Our findings suggest that the (m) condition is relevant for a small portion of the voxels. Moreover, imposing the (d) and (c) conditions in the linearized version of the problem already provides a substantial portion of the overall gain. Thus, the SDP(dc) routine can be employed with relative confidence, which makes the overall estimation computationally inexpensive compared to the full framework that includes the subsequent NLLS(dc), (m) check and SDP(dcm) methods.

Our work could be extended to include higher order terms in the expansion in Eq. 1. However, the next order term introduces 56 new unknowns (Westin et al., 2016), which demands longer acquisition protocols, which make them challenging for clinical studies.

Another matter that we did not address here concerns the limitations of the DTD model. The latter assumes that diffusion is described fully by a diffusion tensor and the effect of the waveforms on the signal are captured by the b-matrix. As discussed elsewhere (Özarslan et al., 2015; Yolcu et al., 2016), this would be valid for large compartments or at very short measurement times. To address this problem, one can consider the distribution of confinement tensors (Afzali et al., 2015; Yolcu et al., 2016; Zucchelli et al., 2016), which are shown to have the correct time dependence in small compartments making it the effective model for many scenarios of interest (Boito et al., 2020; Liu and Özarslan, 2019; Özarslan et al., 2017). One manifestation of this problem concerns acquisitions with isotropic b-matrices (Avram et al., 2018; Mori and van Zijl, 1995; Wong et al., 1995). In this case, the DTD model predicts the same signal for all measurements at each b-value, thus suppressing the

¹¹ Here, we remark that the diffusion tensor is the covariance matrix of net displacements.

potentially relevant information due to the non-Gaussianity of the diffusion process (Jespersen et al., 2019; de Swiet and Mitra, 1996). Similarly, the DTD model ignores the higher order cumulants of the diffusion process within each compartment; this challenge has been studied in recent works (Henriques et al., 2020; Paulsen et al., 2015). We note that the estimation methods introduced here may be instrumental in developing constrained fitting techniques for models aiming to overcome the limitations of the DTD picture.

The protocols obtained by downsampling a long protocol were not optimized as the waveforms were selected from a preexisting set. This poses an additional limitation for the downsampled protocols. However, our constrained estimation framework yielded acceptable image quality even for the shortest protocol comprising only 39 acquisitions. Thus, QTI+ could be more robust to imperfections in the experimental design as well; such imperfections are encountered, for example, due to gradient nonlinearities. More generally, a typical data set is likely to exhibit various artifacts such as Gibbs-ringing, subject motion, and frequency drift. In this case, unconstrained fitting will likely yield violations of the mathematically-necessary conditions. Employing a constrained estimation framework like QTI+ is thus expected to help alleviate the effects of artifacts. Similarly, studies have shown that identifying and discarding outliers is an effective approach for dealing with some of the confounding factors (Chang et al., 2012; Maximov et al., 2011; Tax et al., 2015; Zwiers, 2010). We would like to stress that we do not envision QTI+ to be a replacement for techniques developed to address such effects. Rather it could be part of a series of algorithms (Maximov et al., 2019) that collectively provide accurate maps of the desired parameters.

In recent years, the sensitivity of QTI-accessible quantities like μ FA on various cerebral diseases including schizophrenia (Westin et al., 2016), brain tumors (Szczepankiewicz et al., 2016), epilepsy (Lampinen et al., 2020), multiple sclerosis (Andersen et al., 2020), and Parkinson's disease (Kamiya et al., 2020) have been investigated. Having reliable estimates of those quantities is of paramount importance for such studies, which could benefit particularly from the robustness of QTI+ to SNR. In fact, in the brain the signal without diffusion weighting does have some (typically T_2 -weighted) contrast, which may be amplified in the presence of pathologies. This contrast will lead to a spatially-dependent SNR, which ultimately affects the estimated parameters. Hardware-related effects such as spatially-varying sensitivity of the receiver coil are expected to contribute to this challenge. Our findings indicate that computing the sought after parameters via QTI+ could substantially reduce the SNR dependence of the findings, improving the accuracy and specificity of the estimated parameters.

Another important challenge in the translation of advanced imaging techniques into the clinical realm involves the limitations concerning the acquisition length. Recent works have attempted to address this issue by employing parsimonious data acquisition schemes (Nilsson et al., 2020). Our study demonstrates that sophisticated post-processing methods could be employed to achieve the same goal.

From a signal processing point of view, it is quite intriguing that the constrained estimation framework produces smoother maps and improved resilience to noise although the estimation is performed for each voxel independently, i.e., without employing any information from the adjacent voxels. Thus, the constrained methods do not yield a loss of image resolution, which is typically the case for routine smoothing methods. Moreover, the constraints have a very solid foundation pertaining to the mathematical properties of the estimated quantities. Consequently, the constrained estimation schemes like the ones we introduced here, do not involve any parameters that are to be decided in an *ad hoc* manner.

7. Conclusion

In conclusion, we introduced QTI+, a new estimation framework for q-space trajectory imaging that respects three positivity conditions arising from the mathematical properties of the quantities estimated. We demonstrated that QTI+ leads to notable improvements in the accuracy

and precision of the measured parameters. Although data smoothing is not employed, our framework is exceptionally robust to SNR, which has important ramifications for the interpretability of the derived parameters. The benefits of QTI+ are more conspicuous when shorter acquisition protocols with fewer number of diffusion-weighted volumes are available. Thus, our technique is expected to improve the feasibility as well as reliability, hence the diagnostic utility, of diffusion MRI measurements with generalized diffusion encoding.

Data and Code Availability Statement

In this work we use software and data that are available for academic purposes.

Credit authorship contribution statement

Magnus Herberthson: Methodology, Validation, Software, Formal analysis, Investigation, Writing - review & editing, Writing - Original Draft, Data Curation. **Deneb Boito:** Software, Validation, Investigation, Writing - review & editing, Formal Analysis, Data Curation, Visualization, Writing - Original Draft. **Tom Dela Haije:** Conceptualization, Methodology, Software, Validation, Formal Analysis, Writing - Review & Editing, Funding Acquisition. **Aasa Feragen:** Supervision, Funding acquisition, Project Administration, Writing - Review & Editing. **Carl-Fredrik Westin:** Funding acquisition, Project Administration, Writing - Review & Editing. **Evren Özarslan:** Conceptualization, Methodology, Validation, Formal analysis, Writing - review & editing, Supervision, Project administration, Funding acquisition, Writing - Original Draft.

Acknowledgements

This project was financially supported by Linköping University (LiU) Center for Industrial Information Technology (CENIIT), LiU Cancer, VINNOVA/ITEA3 17021 IMPACT, Analytic Imaging Diagnostic Arena (AIDA), the Swedish Foundation for Strategic Research (RMX18-0056), and the Swedish Research Council 2016-04482.

Tom Dela Haije and Aasa Feragen were supported by the Center for Stochastic Geometry and Advanced Bioimaging and by a block stipendium, both funded by the Villum Foundation (Denmark).

Appendix A. Convention for the Voigt notation

It is customary to use the Voigt notation so that the matrix

$$\mathbf{A}_{ij} = \begin{pmatrix} x_1 & x_4 & x_5 \\ x_4 & x_2 & x_6 \\ x_5 & x_6 & x_3 \end{pmatrix}$$

is represented by the vector

$$\mathbf{v}_i = \begin{pmatrix} a_1 \\ a_2 \\ a_3 \\ a_4 \\ a_5 \\ a_6 \end{pmatrix} = \begin{pmatrix} x_1 \\ x_2 \\ x_3 \\ \sqrt{2}x_4 \\ \sqrt{2}x_5 \\ \sqrt{2}x_6 \end{pmatrix}.$$

Here, $\mathbf{A}_{ij} = \sum_{\beta=1}^6 a_{\beta} \mathbf{e}_{ij}^{(\beta)}$, i.e., the coordinates a_1, a_2, \dots, a_6 express the matrix \mathbf{A}_{ij} in the (orthonormal) basis $\{\mathbf{e}_{ij}^{(1)}, \mathbf{e}_{ij}^{(2)}, \dots, \mathbf{e}_{ij}^{(6)}\}$. With the representation above, these basis matrices are

$$\begin{pmatrix} 1 & 0 & 0 \\ 0 & 0 & 0 \\ 0 & 0 & 0 \end{pmatrix}, \begin{pmatrix} 0 & 0 & 0 \\ 0 & 1 & 0 \\ 0 & 0 & 0 \end{pmatrix}, \begin{pmatrix} 0 & 0 & 0 \\ 0 & 0 & 0 \\ 0 & 0 & 1 \end{pmatrix}, \begin{pmatrix} 0 & \frac{1}{\sqrt{2}} & 0 \\ \frac{1}{\sqrt{2}} & 0 & 0 \\ 0 & 0 & 0 \end{pmatrix},$$

$$\begin{pmatrix} 0 & 0 & \frac{1}{\sqrt{2}} \\ 0 & 0 & 0 \\ \frac{1}{\sqrt{2}} & 0 & 0 \end{pmatrix} \begin{pmatrix} 0 & 0 & 0 \\ 0 & 0 & \frac{1}{\sqrt{2}} \\ 0 & \frac{1}{\sqrt{2}} & 0 \end{pmatrix}.$$

Appendix B. Independence of (d), (c), and (m)

Here, we take independence to mean that there are examples of tensors \mathbf{D}_{ij} , $\mathbf{C}_{ijk\ell}$, $\mathbb{M}_{ijk\ell}$, where two given constraints are satisfied but not the third.¹² To see that the conditions (d), (c), and (m) are independent in the above sense, we give the following examples.

(d) & (c) \nRightarrow (m): Let $\langle \mathbf{D}_{ij} \rangle = \mathbf{0}_{ij}$ and define \mathbf{E}_{ij} through $\mathbf{E}_{ij} = \begin{pmatrix} 0 & 1 & 0 \\ 1 & 0 & 0 \\ 0 & 0 & 0 \end{pmatrix}$. Take $\mathbf{C}_{ijk\ell} = \mathbf{E}_{ij} \otimes \mathbf{E}_{k\ell}$, which implies that also $\mathbb{M}_{ijk\ell} = \mathbf{E}_{ij} \otimes \mathbf{E}_{k\ell}$. By construction, $\mathbf{C}_{ijk\ell}$ is positive semi-definite as a symmetric mapping $V \rightarrow V$, but the choice $\mathbf{v}_i = (1, 1, 0)^T$, $\mathbf{u}_i = (1, -1, 0)^T$ gives an example where $\mathbb{M}_{ijk\ell} u_i u_j v_k v_\ell = -4 < 0$.

(d) & (m) \nRightarrow (c): Again, take $\langle \mathbf{D}_{ij} \rangle = \mathbf{0}_{ij}$ and define \mathbf{C} by

$$\mathbf{C}_{ijk\ell} = \begin{pmatrix} 1 & 0 & 0 \\ 0 & 1 & 0 \\ 0 & 0 & 1 \end{pmatrix} \otimes \begin{pmatrix} 1 & 0 & 0 \\ 0 & 1 & 0 \\ 0 & 0 & 1 \end{pmatrix} - \begin{pmatrix} 0 & 1 & 0 \\ 1 & 0 & 0 \\ 0 & 0 & 0 \end{pmatrix} \otimes \begin{pmatrix} 0 & 1 & 0 \\ 1 & 0 & 0 \\ 0 & 0 & 0 \end{pmatrix}$$

Then (c) is violated but on the other hand, for any vector $\mathbf{v}_i = (x, y, z)^T$

$$\mathbf{M}'_{ij} = \mathbb{M}_{ijk\ell} v_k v_\ell = \begin{pmatrix} x^2 + y^2 + z^2 & -2xy & 0 \\ -2xy & x^2 + y^2 + z^2 & 0 \\ 0 & 0 & x^2 + y^2 + z^2 \end{pmatrix}.$$

This matrix has eigenvalues $x^2 + y^2 + z^2$, $(x - y)^2 + z^2$ and $(x + y)^2 + z^2$, which means that \mathbf{M}'_{ij} is positive semi-definite for any vector \mathbf{v}_i . Hence (m) is satisfied.

(c) & (m) \nRightarrow (d): This is immediate since if $\mathbb{M}_{ijk\ell}$ is constructed as $\mathbb{M}_{ijk\ell} = \mathbf{C}_{ijk\ell} + \langle \mathbf{D}_{ij} \rangle \otimes \langle \mathbf{D}_{k\ell} \rangle$, then $\mathbb{M}_{ijk\ell}$ is unaffected by the replacement $\langle \mathbf{D}_{ij} \rangle \rightarrow -\langle \mathbf{D}_{ij} \rangle$, and by choosing an example with $\langle \mathbf{D}_{ij} \rangle \neq \mathbf{0}$, both $\langle \mathbf{D}_{ij} \rangle$ and $-\langle \mathbf{D}_{ij} \rangle$ cannot be positive semi-definite.

Appendix C. Heteroscedasticity compensation of the log-linearized problem.

In this appendix we motivate, very briefly the weighting of the linearized problem (4), i.e., the insertion of the weights S_n^2 . With

$$\Delta_n = S_0 e^{-B_{ij}^{(n)} \hat{D}_{ij} + \frac{1}{2} B_{ij}^{(n)} B_{k\ell}^{(n)} C_{ijk\ell}} - S_n, \quad n = 1, 2, \dots, N$$

a solution to (2) minimizes $\sum_{n=1}^N |\Delta_n|^2$. By adding S_n to both sides and taking logarithms, we get

$$\ln(S_n + \Delta_n) = \ln(S_0) - B_{ij}^{(n)} \hat{D}_{ij} + \frac{1}{2} B_{ij}^{(n)} B_{k\ell}^{(n)} C_{ijk\ell}.$$

If Δ_n is small compared to S_n , we get $\ln(S_n + \Delta_n) = \ln(S_n) + \ln(1 + \frac{\Delta_n}{S_n}) \approx \ln(S_n) + \frac{\Delta_n}{S_n}$. As a result, a straightforward least squares implementation will (approximately) minimize $\sum_{n=1}^N |\frac{\Delta_n}{S_n}|^2$. This is compensated for by multiplying the linearized equation for the n th measurement with the corresponding signal values S_n .

Appendix D. Equivalence of QP and SDP for the unconstrained linearized equation

Here we show that (7) is equivalent to (9), namely, we first see that to find an \mathbf{x} which minimizes $\mathbf{x}^T \mathbf{Q} \mathbf{x} + \mathbf{c}^T \mathbf{x}$, where $\mathbf{Q} > 0$, is equivalent to solving the problem

$$\underset{\mathbf{x}}{\operatorname{argmin}} t, \text{ subject to } t - \mathbf{x}^T \mathbf{Q} \mathbf{x} - \mathbf{c}^T \mathbf{x} \geq 0$$

¹² Not all possible constraints are independent in this sense. For instance, a possible constraint is that \mathbb{M} viewed as a symmetric mapping $V \rightarrow V$ is positive semi-definite. If (d) and (c) are satisfied, then this is automatically true.

because minimizing t in the inequality $t \geq \mathbf{x}^T \mathbf{Q} \mathbf{x} + \mathbf{c}^T \mathbf{x}$ leads us to find the minimum value of $\mathbf{x}^T \mathbf{Q} \mathbf{x} + \mathbf{c}^T \mathbf{x}$. Next, suppose \mathbf{P} is a square matrix with $\mathbf{P}^T \mathbf{P} = \mathbf{Q}$. Then, $\begin{pmatrix} \mathbf{I} & \mathbf{P} \mathbf{x} \\ \mathbf{x}^T \mathbf{P}^T & t - \mathbf{c}^T \mathbf{x} \end{pmatrix} \geq 0$ is equivalent to the statement

$$\forall \mathbf{v}, a, \quad \begin{pmatrix} \mathbf{I} & \mathbf{P} \mathbf{x} \\ \mathbf{x}^T \mathbf{P}^T & t - \mathbf{c}^T \mathbf{x} \end{pmatrix} \begin{pmatrix} \mathbf{v} \\ a \end{pmatrix} \geq 0.$$

But the expression on the left hand side can be written (using $\mathbf{P}^T \mathbf{P} = \mathbf{Q}$) as

$$(\mathbf{v} + a \mathbf{P} \mathbf{x})^T (\mathbf{v} + a \mathbf{P} \mathbf{x}) + a^2 (t - \mathbf{x}^T \mathbf{Q} \mathbf{x} - \mathbf{c}^T \mathbf{x}). \quad (\text{D.1})$$

But if this is nonnegative for all \mathbf{v} and a , then (by choosing $\mathbf{v} = -a \mathbf{P} \mathbf{x}$) so is $t - \mathbf{x}^T \mathbf{Q} \mathbf{x} - \mathbf{c}^T \mathbf{x}$. Conversely, if $t - \mathbf{x}^T \mathbf{Q} \mathbf{x} - \mathbf{c}^T \mathbf{x} \geq 0$, then so is the expression in (D.1).

Appendix E. Checking condition (m) using SDP

Here, we describe our scheme for checking condition (m), i.e.,

For all $\mathbf{v}_i, \mathbf{u}_i$, $\mathbb{M}_{ijk\ell} v_i v_j u_k u_\ell \geq 0$?

By putting $\mathbf{v}_i = (x, y, z)^T$ and $\mathbf{u}_i = (r, s, t)^T$, the contraction $\mathbb{M}_{ijk\ell} v_i v_j u_k u_\ell$ becomes a fourth order homogeneous polynomial p in the six variables x, y, z, r, s, t . Condition (m) can then be formulated as

$$p(x, y, z, r, s, t) \geq 0 \text{ for all } x, y, z, r, s, t? \quad (\text{E.1})$$

Because of the symmetries of $\mathbb{M}_{ijk\ell}$ and the form of the contraction with \mathbf{v}_i and \mathbf{u}_i , it is possible to represent p in the following way. We start by forming the vector $\mathbf{V} = (xr, xs, xt, yr, ys, yt, zr, zs, zt)^T$. Then, for any symmetric 9×9 matrix \mathbf{M} , it is clear that also $\mathbf{V}^T \mathbf{M} \mathbf{V}$ is a fourth order homogeneous polynomial in x, y, z, r, s, t , and it is not difficult to see that any \mathbb{M} can be represented by such a matrix \mathbf{M} . In fact, this representation is not unique, and by solving the equation $\mathbf{V}^T \mathbf{M} \mathbf{V} = 0$, one finds the solution space to be a nine-dimensional subspace (in the space of symmetric 9×9 matrices):

$$\mathbf{V}^T \begin{pmatrix} 0 & 0 & 0 & 0 & l_1 & l_2 & 0 & l_4 & l_6 \\ 0 & 0 & 0 & -l_1 & 0 & l_3 & -l_4 & 0 & l_7 \\ 0 & 0 & 0 & -l_2 & -l_3 & 0 & -l_6 & -l_7 & 0 \\ 0 & -l_1 & -l_2 & 0 & 0 & 0 & 0 & l_5 & l_8 \\ l_1 & 0 & -l_3 & 0 & 0 & 0 & -l_5 & 0 & l_9 \\ l_2 & l_3 & 0 & 0 & 0 & 0 & -l_8 & -l_9 & 0 \\ 0 & -l_4 & -l_6 & 0 & -l_5 & -l_8 & 0 & 0 & 0 \\ l_4 & 0 & -l_7 & l_5 & 0 & -l_9 & 0 & 0 & 0 \\ l_6 & l_7 & 0 & l_8 & l_9 & 0 & 0 & 0 & 0 \end{pmatrix} \mathbf{V} = 0, \quad l_1, \dots, l_9 \in \mathbb{R}.$$

We indicate this freedom by writing

$$p(x, y, z, r, s, t) = \mathbf{V}^T \mathbf{M}(\boldsymbol{\ell}) \mathbf{V}$$

where $\boldsymbol{\ell} = (\ell_1, \dots, \ell_9)$. Now if, for some value of the parameter vector $\boldsymbol{\ell}$, the matrix $\mathbf{M}(\boldsymbol{\ell})$ is positive semi-definite, then it is clear that (E.1) (and hence also (m)) holds. This is exactly the feasibility problem (14). By diagonalizing $\mathbf{M}(\boldsymbol{\ell})$ (if it is nonnegative) one sees that p is expressed as a sum of squared (SoS) polynomials, i.e.,

$$p(x, y, z, r, s, t) = \sum_{i=1}^9 \alpha_i p_i^2(x, y, z, r, s, t)$$

where $\{\alpha_i\}_{i=1}^9$ are the (non-negative) eigenvalues of $\mathbf{M}(\boldsymbol{\ell})$ and each p_i is a linear combination of the entries of the vector \mathbf{V} . This is thus an example of the rich theory of SoS polynomials (Berg et al., 1976; Lasserre, 2007). We should remark that it is not strictly necessary that $\mathbf{M}(\boldsymbol{\ell})$ is positive semi-definite for (E.1) to hold, which means that the condition $\mathbf{M}(\boldsymbol{\ell}) \geq 0$ is slightly stronger, as there are non-negative polynomials which are not SoS. In practice, however, this drawback is compensated for by the computational convenience offered by SDP. Also, there are results which show that the set of SoS polynomials are, in a certain sense (Lasserre, 2007), dense in the set of non-negative polynomials.

Appendix F. Imposing condition (m) using SDP

By choosing the independent variables x_1, x_2, \dots, x_{28} to encode for $S_0, \hat{\mathbf{D}}_{ij}$ and C_{ijkl} as explained in Section 3, the tensor $\mathbb{M}_{ijkl} = C_{ijkl} + \hat{\mathbf{D}}_{ij} \otimes \hat{\mathbf{D}}_{kl}$ becomes linear in x_8, \dots, x_{28} but quadratic in x_2, \dots, x_7 . For this reason, we have adopted the strategy that if (m) is violated (in an estimate where (d) and (c) are imposed), we fix the estimates of x_1, \dots, x_7 , (i.e., $\ln(S_0)$ and $\hat{\mathbf{D}}_{ij}$) and re-estimate x_8, \dots, x_{28} using SDP while imposing both (c) and (m).

We shall return to the (un-constricted) scenario formulated as a quadratic programming problem. We seek

$$\arg\min_{\mathbf{x}} \mathbf{x}^T \mathbf{Q} \mathbf{x} + \mathbf{c}^T \mathbf{x} \quad (\text{F.1})$$

where $\mathbf{x} = (x_1, \dots, x_{28})^T$ and \mathbf{Q} is a symmetric matrix of size 28×28 . Next, we decompose $\mathbf{x} = (\tilde{\mathbf{x}}^T, \tilde{\mathbf{x}}'^T)^T$, where $\tilde{\mathbf{x}} = (x_1, \dots, x_7)^T$ is fixed, while $\tilde{\mathbf{x}}' = (x_8, \dots, x_{28})^T$ contains our remaining free parameters. To match this, we decompose \mathbf{Q} and \mathbf{c} into block matrices in the following fashion:

$$\mathbf{Q} = \begin{pmatrix} \mathbf{Q}_{11} & \mathbf{Q}_{12} \\ \mathbf{Q}_{21} & \mathbf{Q}_{22} \end{pmatrix}, \text{ and } \mathbf{c} = \begin{pmatrix} \mathbf{c}_1 \\ \mathbf{c}_2 \end{pmatrix}$$

where the sizes of \mathbf{Q}_{11} , \mathbf{Q}_{12} , \mathbf{Q}_{21} , \mathbf{Q}_{22} are 7×7 , 7×21 , 21×7 , and 21×21 , respectively, and $\mathbf{c}_1, \mathbf{c}_2$ are vectors with 7 and 21 elements. Then $\mathbf{x}^T \mathbf{Q} \mathbf{x} + \mathbf{c}^T \mathbf{x}$ becomes

$$(\tilde{\mathbf{x}}^T, \tilde{\mathbf{x}}'^T) \begin{pmatrix} \mathbf{Q}_{11} & \mathbf{Q}_{12} \\ \mathbf{Q}_{21} & \mathbf{Q}_{22} \end{pmatrix} \begin{pmatrix} \tilde{\mathbf{x}} \\ \tilde{\mathbf{x}}' \end{pmatrix} + (\mathbf{c}_1^T \quad \mathbf{c}_2^T) \begin{pmatrix} \tilde{\mathbf{x}} \\ \tilde{\mathbf{x}}' \end{pmatrix}$$

which simplifies to

$$\tilde{\mathbf{x}}^T \tilde{\mathbf{Q}} \tilde{\mathbf{x}} + \tilde{\mathbf{c}}^T \tilde{\mathbf{x}} + \mathbf{c}_0 \quad (\text{F.2})$$

where

$$\tilde{\mathbf{Q}} = \mathbf{Q}_{22}$$

$$\tilde{\mathbf{c}}^T = 2\tilde{\mathbf{x}}\mathbf{Q}_{12} + \mathbf{c}_2^T \text{ and}$$

$$\mathbf{c}_0 = \tilde{\mathbf{x}}^T \mathbf{Q}_{11} \tilde{\mathbf{x}} + \mathbf{c}_1^T \tilde{\mathbf{x}}.$$

With $\tilde{\mathbf{P}}$ such that $\tilde{\mathbf{P}}^T \tilde{\mathbf{P}} = \tilde{\mathbf{Q}}$ (and remembering that \mathbf{c}_0 is just a constant that does not affect the minimizing argument $\tilde{\mathbf{x}}$), (F.2) is if the form which admits a SDP formulation. Disregarding \mathbf{c}_0 , this is found in the upper left blocks of the matrix in (15). Since all the variables x_8, \dots, x_{28} are still free, and since they form $\mathbf{C}_{\alpha\beta}$, the positivity condition (c) remains the same: $\mathbf{C}_{\alpha\beta} \geq 0$. Finally, with $\hat{\mathbf{D}}_{ij}$ fixed, and since $\mathbb{M}_{ijkl} = C_{ijkl} + \hat{\mathbf{D}}_{ij} \otimes \hat{\mathbf{D}}_{kl}$, all entries of the components \mathbb{M}_{ijkl} will be first order polynomials in x_8, \dots, x_{28} and hence can be cast into a 9×9 symmetric matrix \mathbf{M} as described in Appendix E. By adding the freedom in terms of the parameters $\ell_1, \ell_2, \dots, \ell_9$ as also described in the previous section, we get the matrix $\mathbf{M}(\ell)$, (which could also be written $\mathbf{M}(\ell, \tilde{\mathbf{x}})$) and by this formulation, both conditions (c) and (m) will be imposed simultaneously in the formulation (15).

Appendix G. Scalar measures in the rank deficient case

As mentioned in Section 3, protocols that use measurements of only type (i) and (iii), i.e., LTE and STE, will produce matrices \mathbf{A} , which are rank deficient. In this case, the (maximum) rank will be 23 instead of 28, and as a result, there is a (five parameter worth) family of covariance tensors C_{ijkl} compatible with the (fit of the) measurements. Here, we will describe this freedom and also indicate why the scalars measures FA, MD, C_M , C_μ , μFA , C_{MD} , and C_c are unaffected by this non-uniqueness in the estimates of C_{ijkl} .

First we note that for measurements of type (i), i.e., of type LTE, such a measurement picks up only the content of the completely symmetric part $C_{(ijkl)}$ of C_{ijkl} . Namely, since any measurement tensor \mathbf{B}_{ij} of type (i) is symmetric, positive semi-definite and has rank

one, we can write $\mathbf{B}_{ij} = v_i v_j$ for some vector v_i . It is then clear that $C_{ijkl} \mathbf{B}_{ij} \mathbf{B}_{kl} = C_{ijkl} v_i v_j v_k v_l = C_{(ijkl)} v_i v_j v_k v_l$ since $v_i v_j v_k v_l$ itself is completely symmetric. As a result, the difference $\mathbb{K}_{ijkl} = C_{ijkl} - C_{(ijkl)}$ satisfies $\mathbb{K}_{ijkl} v_i v_j v_k v_l = 0$ for all vectors v_i . Moreover, since C_{ijkl} has 21 independent components while $C_{(ijkl)}$ has 15, this means that \mathbb{K}_{ijkl} has six degrees of freedom.

Next, we express the tensor \mathbb{K}_{ijkl} as a 6×6 matrix using the Voigt notation, yielding

$$\mathbf{K}_{\alpha\beta} = \begin{pmatrix} 0 & a+d-w & 0 & w-d & 0 & e \\ a+d-w & 0 & w-a & 0 & 0 & c \\ w-d & w-a & 0 & 0 & b & 0 \\ 0 & 0 & b & -a-d+w & -\frac{e}{\sqrt{2}} & -\frac{c}{\sqrt{2}} \\ 0 & c & 0 & -\frac{e}{\sqrt{2}} & d-w & -\frac{b}{\sqrt{2}} \\ e & 0 & 0 & -\frac{c}{\sqrt{2}} & -\frac{b}{\sqrt{2}} & a-w \end{pmatrix},$$

where a, b, c, d, e , and w are the six free parameters. Because $\mathbf{K}_{\alpha\beta}$ is symmetric, the corresponding fourth order tensor \mathbb{K}_{ijkl} has the correct symmetries. Moreover, for any vector $v_i = (x, y, z)^T$, the tensor $v_i v_j^T$ can be expressed as $\mathbf{V}_a = (x^2, y^2, z^2, \sqrt{2}xy, \sqrt{2}xz, \sqrt{2}yz)^T$ through the Voigt notation. Using this, it can be verified that $\mathbf{K}_{\alpha\beta} \mathbf{V}_a \mathbf{V}_b = 0$ and hence $\mathbb{K}_{ijkl} v_i v_j v_k v_l = 0$ for all vectors v_i .

To proceed, we now refer to (Westin et al., 2016), in which the definitions of the scalars can be found. The key observation is then that all the scalar measures involves C_{ijkl} (or, equivalently, $\mathbf{C}_{\alpha\beta}$) in such a way that inner products are taken with linear combinations of the fourth order tensors $\mathbb{E}_{ijkl}^{\text{iso}}$ and $\mathbb{E}_{ijkl}^{\text{bulk}}$, whose 6×6 representations are given by

$$\mathbf{E}_{\alpha\beta}^{\text{bulk}} = \frac{1}{9} \begin{pmatrix} 1 & 1 & 1 & 0 & 0 & 0 \\ 1 & 1 & 1 & 0 & 0 & 0 \\ 1 & 1 & 1 & 0 & 0 & 0 \\ 0 & 0 & 0 & 0 & 0 & 0 \\ 0 & 0 & 0 & 0 & 0 & 0 \\ 0 & 0 & 0 & 0 & 0 & 0 \end{pmatrix} \text{ and } \mathbf{E}_{\alpha\beta}^{\text{iso}} = \frac{1}{3} \begin{pmatrix} 1 & 0 & 0 & 0 & 0 & 0 \\ 0 & 1 & 0 & 0 & 0 & 0 \\ 0 & 0 & 1 & 0 & 0 & 0 \\ 0 & 0 & 0 & 1 & 0 & 0 \\ 0 & 0 & 0 & 0 & 1 & 0 \\ 0 & 0 & 0 & 0 & 0 & 1 \end{pmatrix},$$

where in particular $\mathbb{E}_{ijkl}^{\text{bulk}}$ is related to measurements of type (iii), i.e., STE. The contributions from \mathbb{K}_{ijkl} to such inner products are

$$K_{ijkl} E_{ijkl}^{\text{bulk}} = \frac{2w}{9},$$

$$K_{ijkl} E_{ijkl}^{\text{iso}} = -\frac{w}{3} = -\frac{3}{2} K_{ijkl} E_{ijkl}^{\text{bulk}}.$$

This implies that the set of scalar measures considered here are sensitive to \mathbb{K}_{ijkl} only through w , which can be obtained via an STE measurement in addition to a proper set of LTE acquisitions that enable the estimation of $C_{(ijkl)}$.

Appendix H. The mean and covariance of the Wishart distribution

Deriving the first two moments of the non-central Wishart distribution directly from the probability distribution function is a bit involved. However, using (16), we can find these by matching this expression to our model (1). In essence, we want to find $\hat{\mathbf{D}}_{ij}$ and C_{ijkl} so that

$$[\mathbf{I} + \mathbf{\Sigma B}]^{-p} \exp(-\text{Tr}[\mathbf{B}(\mathbf{I} + \mathbf{\Sigma B})^{-1} \mathbf{\Omega}]) = e^{-B_0 \hat{D}_{ij} + \frac{1}{2} B_{ij} B_{kl} C_{ijkl}} + O((B_{ij})^3).$$

By taking logarithms and introducing a scale parameter x , we demand that for each fixed (symmetric, positive semi-definite) \mathbf{B}_{ij} , it holds that

$$-p \ln [\mathbf{I} + x \mathbf{\Sigma B}] - \text{Tr}[x \mathbf{B}(\mathbf{I} + x \mathbf{\Sigma B})^{-1} \mathbf{\Omega}]$$

$$= -x B_{ij} \hat{D}_{ij} + \frac{x^2}{2} B_{ij} B_{kl} C_{ijk\ell} + O(x^3). \quad (\text{H.1})$$

It follows from the definition of the (3×3) determinant that

$$|\mathbf{I} + x\mathbf{\Sigma B}| = 1 + x\text{Tr}[\mathbf{\Sigma B}] + \frac{x^2}{2} (\text{Tr}[\mathbf{\Sigma B}]^2 - \text{Tr}[(\mathbf{\Sigma B})^2]) + O(x^3)$$

and

$$\ln |\mathbf{I} + x\mathbf{\Sigma B}| = x\text{Tr}[\mathbf{\Sigma B}] - \frac{x^2}{2} \text{Tr}[(\mathbf{\Sigma B})^2] + O(x^3)$$

so that

$$-p \ln |\mathbf{I} + x\mathbf{\Sigma B}| = -px \Sigma_{ij} B_{ji} + p \frac{x^2}{2} \Sigma_{ij} B_{jk} \Sigma_{k\ell} B_{\ell i} + O(x^3). \quad (\text{H.2})$$

Next, since $(\mathbf{I} + x\mathbf{\Sigma B})^{-1} = \mathbf{I} - x\mathbf{\Sigma B} + O(x^2)$,

$$-\text{Tr}[\mathbf{x B}(\mathbf{I} + x\mathbf{\Sigma B})^{-1} \mathbf{\Omega}] = -x B_{ik} (x - x \Sigma_{km} B_{mn}) \Omega_{ni} + O(x^2). \quad (\text{H.3})$$

Inserting (H.2) and (H.3) into (H.1) and identifying terms w.r.t. x , we find that, for each symmetric \mathbf{B}_{ij} ,

$$(\hat{D}_{ij} - p \Sigma_{ij} - \Omega_{ij}) B_{ij} = 0 \quad (\text{H.4})$$

$$(C_{ijk\ell} - p \Sigma_{i\ell} \Sigma_{jk} - 2 \Sigma_{jk} \Omega_{\ell i}) B_{ij} B_{k\ell} = 0. \quad (\text{H.5})$$

Note that the first equation does not imply that $\hat{D}_{ij} = p \Sigma_{ij} + \Omega_{ij}$ unless we take the symmetry of \hat{D}_{ij} into account since $A_{ij} B_{ij} = 0$ for any anti-symmetric matrix A_{ij} (\mathbf{B}_{ij} being symmetric). On the other hand, with \hat{D}_{ij} symmetric, it is necessary that $\hat{D}_{ij} = p \Sigma_{ij} + \Omega_{ij}$, since if for a symmetric matrix A_{ij} , $A_{ij} B_{ij} = 0$ for all symmetric positive definite matrices \mathbf{B}_{ij} , then $A_{ij} = 0$. For (H.5), the terms $\Sigma_{i\ell} \Sigma_{jk}$ and $\Sigma_{jk} \Omega_{\ell i}$ do not have the symmetries of $C_{ijk\ell}$. On the other hand, using the symmetry of \mathbf{B}_{ij} , one can check that, for all \mathbf{B}_{ij} , $\Sigma_{i\ell} \Sigma_{jk} B_{ij} B_{k\ell} = \frac{1}{2} (\Sigma_{i\ell} \Sigma_{jk} + \Sigma_{jk} \Sigma_{i\ell}) B_{ij} B_{k\ell}$ and $2 \Sigma_{jk} \Omega_{\ell i} B_{ij} B_{k\ell} = \frac{1}{2} (\Sigma_{jk} \Omega_{i\ell} + \Sigma_{i\ell} \Omega_{jk} + \Sigma_{j\ell} \Omega_{ik} + \Sigma_{ik} \Omega_{j\ell}) B_{ij} B_{k\ell}$, so that we can replace (H.5) by

$$A_{ijkl} B_{ij} B_{kl} = 0$$

for all symmetric positive semidefinite matrices \mathbf{B}_{ij} , where $A_{ijkl} = C_{ijk\ell} - \frac{p}{2} (\Sigma_{i\ell} \Sigma_{jk} + \Sigma_{jk} \Sigma_{i\ell}) - \frac{1}{2} (\Sigma_{jk} \Omega_{i\ell} + \Sigma_{i\ell} \Omega_{jk} + \Sigma_{j\ell} \Omega_{ik} + \Sigma_{ik} \Omega_{j\ell})$ has the same symmetries as $C_{ijk\ell}$. But this forces A_{ijkl} to be zero since we know (c.f. the discussion in (3.9)) that with general measurement tensors \mathbf{B}_{ij} , we can produce tensors with components $B_{ij} B_{kl}$, which together determine A_{ijkl} above. This proves (18).

References

- Afzali, M., Knutsson, H., Özarslan, E., Jones, D.K., 2020. Computing the orientational-average of diffusion-weighted MRI signals: a comparison of different techniques. *bioRxiv* (10.1101/2020.11.18.388272).
- Afzali, M., Yölcü, C., Özarslan, E., 2015. Characterizing Diffusion Anisotropy for Molecules under the Influence of a Parabolic Potential: A Plausible Alternative to Dti. In: *Proc Intl Soc Mag Reson Med*, Vol. 23, p. 2795.
- Andersen, K.W., Lasic, S., Lundell, H., Nilsson, M., Topgaard, D., Sellebjerg, F., Szczepankiewicz, F., Siebner, H.R., Blinkenberg, M., Dyrbjerg, T.B., 2020. Distinguishing white-matter damage from physiological fibre orientation dispersion in multiple sclerosis. *Brain Commun.* 2 (2), fcaa077. doi:10.1093/braincomms/fcaa077.
- Avram, A.V., Sarlls, J.E., Hutchinson, E., Basser, P.J., 2018. Efficient experimental designs for isotropic generalized diffusion tensor MRI (IGDTI). *Magn. Reson. Med.* 79 (1), 180–194. doi:10.1002/mrm.26656.
- Barmpoutis, A., Ho, J., Vemuri, B.C., 2012. Approximating symmetric positive semidefinite tensors of even order. *SIAM J. Imaging Sci.* 5 (1), 434–464. doi:10.1137/100801664.
- Barmpoutis, A., Hwang, M.S., Howland, D., Forder, J.R., Vemuri, B.C., 2009. Regularized positive-definite fourth order tensor field estimation from DW-MRI. *Neuroimage* 45 (1). doi:10.1016/j.neuroimage.2008.10.056. S153–S162.
- Basser, P.J., Mattiello, J., LeBihan, D., 1994. Estimation of the effective self-diffusion tensor from the NMR spin echo. *J. Magn. Reson. B* 103 (3), 247–254.

- Basser, P.J., Mattiello, J., LeBihan, D., 1994. MR Diffusion tensor spectroscopy and imaging. *Biophys. J.* 66 (1), 259–267.
- Basser, P.J., Pajevic, S., 2003. A normal distribution for tensor-valued random variables: applications to diffusion tensor MRI. *IEEE Trans. Med. Imaging* 22 (7), 785–794. doi:10.1109/TMI.2003.815059.
- Berg, C., Christensen, J.P.R., Ressel, P., 1976. Positive definite functions on abelian semi-groups. *Math. Ann.* 223, 253–274.
- Bevington, P.R., Robinson, D.K., 2003. Data reduction and error analysis for the physical sciences, 3rd McGraw-Hill.
- Boito, D., Yölcü, C., Özarslan, E., 2020. Compartment-specific Diffusivity: A New Dimension in Multidimensional Diffusion MRI? In: *Proc Intl Soc Mag Reson Med*, Vol. 28, p. 4442.
- Chang, L.C., Walker, L., Pierpaoli, C., 2012. Informed “restore”: a method for robust estimation of diffusion tensor from low redundancy datasets in the presence of physiological noise artifacts. *Magn. Reson. Med.* 68 (5), 1654–1663. doi:10.1002/mrm.24173.
- Chen, Y., Dai, Y., Han, D., Sun, W., 2013. Positive semidefinite generalized diffusion tensor imaging via quadratic semidefinite programming. *SIAM J. Imaging Sci.* 6 (3), 1531–1552. doi:10.1137/110843526.
- Cheng, Y., Cory, D.G., 1999. Multiple scattering by NMR. *J. Am. Chem. Soc.* 121, 7935–7936.
- Cory, D.G., Garroway, A.N., Miller, J.B., 1990. Applications of spin transport as a probe of local geometry. *Polym Preprints* 31, 149.
- De Swiet, T.M., Mitra, P.P., 1996. Possible Systematic Errors in Single-Shot Measurements of the Trace of the Diffusion Tensor. *J. Magn. Reson. B* 111, 15–22.
- Dela Haije, T., Özarslan, E., Feren, A., 2020. Enforcing necessary non-negativity constraints for common diffusion MRI models using sum of squares programming. *Neuroimage* 209, 116405.
- Ghosh, A., Milne, T., Deriche, R., 2014. Constrained diffusion kurtosis imaging using ternary quartics & MLE. *Magn. Reson. Med.* 71 (4), 1581–1591. doi:10.1002/mrm.24781.
- Grant, M., Boyd, S., 2008. Graph Implementations for Nonsmooth Convex Programs. In: Blondel, V., Boyd, S., Kimura, H. (Eds.), *Recent Advances in Learning and Control*. Springer-Verlag Limited, pp. 95–110. *Lecture Notes in Control and Information Sciences*; <http://stanford.edu/~boyd/graph.dcp.html>
- Grant, M., Boyd, S., 2014. CVX: Matlab software for disciplined convex programming, version 2.1. <http://cvxr.com/cvx>.
- Gudbjartsson, H., Patz, S., 1995. The rician distribution of noisy MRI data. *Magn. Reson. Med.* 34 (6), 910–914.
- Henriques, R.N., Jespersen, S.N., Shemesh, N., 2020. Correlation tensor magnetic resonance imaging. *Neuroimage* 211, 116605. doi:10.1016/j.neuroimage.2020.116605.
- Herberthson, M., Yölcü, C., Knutsson, H., Westin, C.F., Özarslan, E., 2019. Orientationally-averaged diffusion-attenuated magnetic resonance factor for locally-anisotropic diffusion. *Sci. Rep.* 9 (1), 4899. doi:10.1038/s41598-019-41317-8.
- Ianus, A., Shemesh, N., Alexander, D.C., Drobniak, I., 2017. Measuring Microscopic Anisotropy with Diffusion Magnetic Resonance: From Material Science to Biomedical Imaging. In: Schultz, T., Özarslan, E., Hotz, I. (Eds.), *Modeling, Analysis, and Visualization of Anisotropy*. Springer International Publishing: Mathematics and Visualization, pp. 229–255.
- Jensen, J.H., Helper, J.A., Ramani, A., Lu, H., Kaczynski, K., 2005. Diffusional kurtosis imaging: the quantification of non-gaussian water diffusion by means of magnetic resonance imaging. *Magn. Reson. Med.* 53, 1432–1440.
- Jespersen, S.N., Olesen, J.L., Ianus, A., Shemesh, N., 2019. Effects of nongaussian diffusion on “isotropic diffusion” measurements: an ex-vivo microimaging and simulation study. *J. Magn. Reson.* 300, 84–94. doi:10.1016/j.jmr.2019.01.007.
- Jeurissen, B., Westin, C.F., Sijbers, J., Szczepankiewicz, F., 2019. Improved precision and accuracy in q-space trajectory imaging by model-based super-resolution reconstruction. *Proc Intl Soc Mag Reson Med.* 27.
- Jian, B., Vemuri, B., Özarslan, E., 2009. A Mixture of Wisharts (MOW) Model for Multi-fiber Reconstruction. In: Laidlaw, D., Weickert, J. (Eds.), *Visualization and Processing of Tensor Fields*. Springer-Verlag, pp. 39–55.
- Jian, B., Vemuri, B.C., Özarslan, E., Carney, P.R., Mareci, T.H., 2007. A novel tensor distribution model for the diffusion-weighted MR signal. *Neuroimage* 37 (1), 164–176. doi:10.1016/j.neuroimage.2007.03.074.
- Kamiya, K., Kamagata, K., Ogaki, K., Hatano, T., Ogawa, T., Takeshige-Amano, H., Murata, S., Andica, C., Murata, K., Feiwel, T., et al., 2020. Brain white-matter degeneration due to aging and parkinson disease as revealed by double diffusion encoding. *Front. Neurosci.* 14, 584510.
- Koay, C.G., 2010. Least Squares Approaches to Diffusion Tensor Estimation. In: Jones P.D., D.K. (Ed.), *Diffusion MRI*. Oxford University Press, pp. 272–284.
- Koay, C.G., Chang, L.C., Carew, J.D., Pierpaoli, C., Basser, P.J., 2006. A unifying theoretical and algorithmic framework for least squares methods of estimation in diffusion tensor imaging. *J. Magn. Reson.* 182 (1), 115–125. doi:10.1016/j.jmr.2006.06.020.
- Koay, C.G., Özarslan, E., Basser, P.J., 2009. A signal transformation framework for breaking the noise floor and its applications in MRI. *J. Magn. Reson.* 197 (2), 108–119. doi:10.1016/j.jmr.2008.11.015.
- Lampinen, B., Zampeli, A., Björkman-Burtscher, I.M., Szczepankiewicz, F., Källén, K., Compagno Strandberg, M., Nilsson, M., 2020. Tensor-valued diffusion MRI differentiates cortex and white matter in malformations of cortical development associated with epilepsy. *Epilepsia* doi:10.1111/epi.16605.
- Lasic, S., Szczepankiewicz, F., Eriksson, S., Nilsson, M., Topgaard, D., 2014. Microanisotropy imaging: quantification of microscopic diffusion anisotropy and orientational order parameter by diffusion MRI with magic-angle spinning of the q-vector. *Front. Phys.* 2, 11.
- Lasserre, J.B., 2007. A sum of squares approximation of nonnegative polynomials. *SIAM Rev.* 49, 651–669.

- Lawrenz, M., Koch, M.A., Finsterbusch, J., 2010. A tensor model and measures of microscopic anisotropy for double-wave-vector diffusion-weighting experiments with long mixing times. *J. Magn. Reson.* 202 (1), 43–56. doi:10.1016/j.jmr.2009.09.015.
- Lenglet, C., Rousson, M., Deriche, R., Faugeras, O., 2006. Statistics on the manifold of multivariate normal distributions: theory and application to diffusion tensor MRI processing. *J. Math. Imaging Vis.* 25 (3), 423–444. doi:10.1007/s10851-006-6897-z.
- Letac, G., Massam, H., 1998. Quadratic and inverse regressions for wishart distributions. *Ann. Stat.* 26 (2), 573–595.
- Liu, C., Bammer, R., Acar, B., Moseley, M.E., 2004. Characterizing non-gaussian diffusion by using generalized diffusion tensors. *Magn. Reson. Med.* 51 (5), 924–937. doi:10.1002/mrm.20071.
- Liu, C., Özarslan, E., 2019. Multimodal integration of diffusion MRI for better characterization of tissue biology. *NMR Biomed.* 32 (4), e3939. doi:10.1002/nbm.3939.
- Magdoo, K.N., Pajević, S., Dario, G., Basser, P.J., 2021. A new framework for MR diffusion tensor distribution. *Sci. Rep.* 11 (1), 2766. doi:10.1038/s41598-021-81264-x.
- Mattiello, J., Basser, P.J., LeBihan, D., 1994. Analytical expressions for the b-matrix in NMR diffusion imaging and spectroscopy. *J. Magn. Reson.* A 108 (2), 131–141.
- Maximov, I.I., Alnaes, D., Westlye, L.T., 2019. Towards an optimised processing pipeline for diffusion magnetic resonance imaging data: effects of artefact corrections on diffusion metrics and their age associations in UK biobank. *Hum. Brain Mapp.* 40 (14), 4146–4162. doi:10.1002/hbm.24691.
- Maximov, I.I., Grinberg, F., Shah, N.J., 2011. Robust tensor estimation in diffusion tensor imaging. *J. Magn. Reson.* 213 (1), 136–144. doi:10.1016/j.jmr.2011.09.035.
- Mayerhofer, E., 2013. On the existence of non-central wishart distributions. *J. Multivariate Anal.* 114, 448–456.
- Mori, S., van Zijl, P.C., 1995. Diffusion weighting by the trace of the diffusion tensor within a single scan. *Magn. Reson. Med.* 33 (1), 41–52.
- Nilsson, M., Szczepankiewicz, F., Brabec, J., Taylor, M., Westin, C.F., Golby, A., van Westen, D., Sundgren, P.C., 2020. Tensor-valued diffusion MRI in under 3 minutes: an initial survey of microscopic anisotropy and tissue heterogeneity in intracranial tumors. *Magn. Reson. Med.* 83 (2), 608–620. doi:10.1002/mrm.27959.
- Nocedal, J., Wright, S.J., 2006. Numerical optimization, 2nd Springer-Verlag, Berlin.
- Özarslan, E., 2009. Compartment shape anisotropy (CSA) revealed by double pulsed field gradient MR. *J. Magn. Reson.* 199 (1), 56–67. doi:10.1016/j.jmr.2009.04.002.
- Özarslan, E., Koay, C.G., Shepherd, T.M., Komlosh, M.E., İrfanoglu, M.O., Pierpaoli, C., Basser, P.J., 2013. Mean apparent propagator (MAP) MRI: a novel diffusion imaging method for mapping tissue microstructure. *Neuroimage* 78, 16–32. doi:10.1016/j.neuroimage.2013.04.016.
- Özarslan, E., Mareci, T.H., 2003. Generalized diffusion tensor imaging and analytical relationships between diffusion tensor imaging and high angular resolution diffusion imaging. *Magn. Reson. Med.* 50 (5), 955–965. doi:10.1002/mrm.10596.
- Özarslan, E., Shemesh, N., Koay, C.G., Cohen, Y., Basser, P.J., 2011. Nuclear magnetic resonance characterization of general compartment size distributions. *New J. Phys.* 13, 15010. doi:10.1088/1367-2630/13/1/015010.
- Özarslan, E., Westin, C.F., Mareci, T.H., 2015. Characterizing magnetic resonance signal decay due to gaussian diffusion: the path integral approach and a convenient computational method. *Concepts Magn. Reson. Part A* 44, 203–213.
- Özarslan, E., Yölcü, C., Herberthson, M., Knutsson, H., Westin, C.F., 2018. Influence of the size and curvedness of neural projections on the orientationally averaged diffusion MR signal. *Front. Phys.* 6, 17.
- Özarslan, E., Yölcü, C., Herberthson, M., Westin, C.F., Knutsson, H., 2017. Effective potential for magnetic resonance measurements of restricted diffusion. *Front. Phys.* 5, 68.
- Paulsen, J.L., Özarslan, E., Komlosh, M.E., Basser, P.J., Song, Y.Q., 2015. Detecting compartmental non-gaussian diffusion with symmetrized double-PFG MRI. *NMR Biomed.* 28 (11), 1550–1556. doi:10.1002/nbm.3363.
- Pennec, X., Fillard, P., Ayache, N., 2006. A riemannian framework for tensor computing. *Int. J. Comput. Vis.* 66 (1), 41–66.
- Qi, L., Yu, G., Wu, E.X., 2010. Higher order positive semidefinite diffusion tensor imaging. *SIAM J. Imaging Sci.* 3 (3), 416–433. doi:10.1137/090755138.
- Reymbault, A., Mezzani, P., de Almeida, M.J., Topgaard, D., 2020. Accuracy and precision of statistical descriptors obtained from multidimensional diffusion signal inversion algorithms. *NMR Biomed.* 33, e4267.
- Röding, M., Bernin, D., Jonasson, J., Särkkä, A., Topgaard, D., Rudemo, M., Nydén, M., 2012. The gamma distribution model for pulsed-field gradient NMR studies of molecular-weight distributions of polymers. *J. Magn. Reson.* 222, 105–111. doi:10.1016/j.jmr.2012.07.005.
- Sen, P.N., Hürlimann, M.D., de Swiet, T.M., 1995. Debye-porod law of diffraction for diffusion in porous media. *Phys. Rev. B* 51 (1), 601–604.
- Shakya, S., Batool, N., Özarslan, E., Knutsson, H., 2017. Multi-fiber Reconstruction Using Probabilistic Mixture Models for Diffusion MRI Examinations of the Brain. In: Schultz, T., Özarslan, E., Hotz, I. (Eds.), *Modeling, Analysis, and Visualization of Anisotropy*. Springer International Publishing, Cham, pp. 283–308.
- Stejskal, E.O., Tanner, J.E., 1965. Spin diffusion measurements: spin echoes in the presence of a time-dependent field gradient. *J. Chem. Phys.* 42 (1), 288–292.
- de Swiet, T.M., Mitra, P.P., 1996. Possible systematic errors in single-shot measurements of the trace of the diffusion tensor. *J. Magn. Reson. B* 111 (1), 15–22. doi:10.1006/jmr.1996.0055.
- Szczepankiewicz, F., Hoge, S., Westin, C.F., 2019. Linear, planar and spherical tensor-valued diffusion MRI data by free waveform encoding in healthy brain, water, oil and liquid crystals. *Data Brief* 25, 104208. doi:10.1016/j.dib.2019.104208.
- Szczepankiewicz, F., Lasić, S., van Westen, D., Sundgren, P.C., Englund, E., Westin, C.F., Ståhlberg, F., Lätt, J., Topgaard, D., Nilsson, M., 2015. Quantification of microscopic diffusion anisotropy disentangles effects of orientation dispersion from microstructure: applications in healthy volunteers and in brain tumors. *Neuroimage* 104, 241–252. doi:10.1016/j.neuroimage.2014.09.057.
- Szczepankiewicz, F., van Westen, D., Englund, E., Westin, C.F., Ståhlberg, F., Lätt, J., Sundgren, P.C., Nilsson, M., 2016. The link between diffusion MRI and tumor heterogeneity: mapping cell eccentricity and density by diffusional variance decomposition (DIVIDE). *Neuroimage* 142, 522–532. doi:10.1016/j.neuroimage.2016.07.038.
- Tax, C.M.W., Otte, W.M., Viergever, M.A., Dijkhuizen, R.M., Leemans, A., 2015. “REKINDLE”: Robust extraction of kurtosis indices with linear estimation. *Magn. Reson. Med.* 73 (2), 794–808. doi:10.1002/mrm.25165.
- Topgaard, D., 2019. Diffusion tensor distribution imaging. *NMR Biomed.* 32 (5), e4066. doi:10.1002/nbm.4066.
- Tournier, J.D., Calamante, F., Connelly, A., 2007. Robust determination of the fibre orientation distribution in diffusion MRI: non-negativity constrained super-resolved spherical deconvolution. *Neuroimage* 35 (4), 1459–1472. doi:10.1016/j.neuroimage.2007.02.016.
- Tournier, J.D., Calamante, F., Gadian, D.G., Connelly, A., 2004. Direct estimation of the fiber orientation density function from diffusion-weighted MRI data using spherical deconvolution. *Neuroimage* 23, 1176–1185.
- Veraart, J., Van Hecke, W., Sijbers, J., 2011. Constrained maximum likelihood estimation of the diffusion kurtosis tensor using a rician noise model. *Magn. Reson. Med.* 66 (3), 678–686. doi:10.1002/mrm.22835.
- Wang, Z., Vemuri, B.C., Chen, Y., Mareci, T.H., 2004. A constrained variational principle for tensor field restoration from complex-valued DWI. *IEEE Trans. on Medical Imaging* 23 (8), 930–939.
- Westin, C.F., Knutsson, H., Pasternak, O., Szczepankiewicz, F., Özarslan, E., van Westen, D., Mattisson, C., Bogren, M., O'Donnell, L.J., Kubicki, M., Topgaard, D., Nilsson, M., 2016. Q-Space trajectory imaging for multidimensional diffusion MRI of the human brain. *Neuroimage* 135, 345–362. doi:10.1016/j.neuroimage.2016.02.039.
- Wong, E.C., Cox, R.W., Song, A.W., 1995. Optimized isotropic diffusion weighting. *Magn. Reson. Med.* 34 (2), 139–143.
- Yölcü, C., Memiş, M., Şimşek, K., Westin, C.F., Özarslan, E., 2016. NMR Signal for particles diffusing under potentials: from path integrals and numerical methods to a model of diffusion anisotropy. *Phys. Rev. E* 93, 052602.
- Zucchelli, M., Afzali, M., Yölcü, C., Westin, C.F., Menegaz, G., Özarslan, E., 2016. The Confinement Tensor Model Improves Characterization of Diffusion-weighted Magnetic Resonance Data with Varied Timing Parameters. *Biomedical Imaging (ISBI), 2016 IEEE 13th International Symposium on*. IEEE, 1093–1096.
- Zwiers, M.P., 2010. Patching cardiac and head motion artefacts in diffusion-weighted images. *Neuroimage* 53 (2), 565–575. doi:10.1016/j.neuroimage.2010.06.014.

Diffusivity-limited q-space trajectory imaging

Deneb Boito

Magnus Herberthson

Tom Dela Haije

Ida Blystad

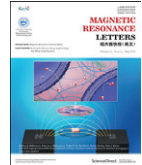
Evren Özarslan

Magnetic Resonance Letters, 2023, 3, 187-196.

© 2023 The Authors.

Published by Elsevier B.V. on behalf of KeAi Communications Co. Ltd.

Reprinted with permission (CC BY-NC-ND 4.0)



Research Article

Diffusivity-limited q-space trajectory imaging

Deneb Boito ^{a, b, *}, Magnus Herberthson ^c, Tom Dela Haije ^d, Ida Blystad ^{b, e},
Evren Özarslan ^{a, b, **}

^a Department of Biomedical Engineering, Campus US, Linköping University, Linköping, SE-581 83, Sweden

^b Center for Medical Image Science and Visualization, Linköping University, Linköping, SE-581 83, Sweden

^c Department of Mathematics, Linköping University, Linköping, SE-581 83, Sweden

^d Department of Computer Science, University of Copenhagen, Copenhagen, DK-2300, Denmark

^e Department of Radiology in Linköping and Department of Health, Medicine and Caring Sciences, Linköping University, Linköping, SE-581 83, Sweden

ARTICLE INFO

Article history:

Received 28 September 2022

Received in revised form 13 December 2022

Accepted 25 December 2022

Available online 6 January 2023

Keywords:

Diffusion

Diffusion MRI

q-space trajectory imaging

QTI

Microstructure

Microscopic anisotropy

QTI+

Constrained

ABSTRACT

Q-space trajectory imaging (QTI) allows non-invasive estimation of microstructural features of heterogeneous porous media via diffusion magnetic resonance imaging performed with generalised gradient waveforms. A recently proposed constrained estimation framework, called QTI+, improved QTI's resilience to noise and data sparsity, thus increasing the reliability of the method by enforcing relevant positivity constraints. In this work we consider expanding the set of constraints to be applied during the fitting of the QTI model. We show that the additional conditions, which introduce an upper bound on the diffusivity values, further improve the retrieved parameters on a publicly available human brain dataset as well as on data acquired from healthy volunteers using a scanner-ready protocol.

© 2023 The Authors. Publishing services by Elsevier B.V. on behalf of KeAi Communications Co. Ltd. This is an open access article under the CC BY-NC-ND license (<http://creativecommons.org/licenses/by-nc-nd/4.0/>).

1. Introduction

Diffusion magnetic resonance imaging (dMRI) is an imaging technique possessing exquisite inherent sensitivity to the random motion of water molecules, which can be exploited to determine local features of complex porous media. The random motion can be encoded into the MR signal by means of time-varying magnetic field gradients, and interpreted using (bio) physical models or signal representations. In Q-space trajectory imaging (QTI) [1], the medium is imagined as being composed of several non-exchanging gaussian compartments, each represented by a diffusion tensor [2]. As such, each voxel is represented using a diffusion tensor distribution (DTD) [3]. At low diffusion sensitivities achieved with general gradient waveforms, QTI gives access to the first statistical moments of the DTD via the cumulant expansion. These are quantified in a 3×3 symmetric positive semidefinite matrix denoting the average diffusion tensor, and a fourth order object denoting the covariance of the diffusion tensors — the two quantities that define a tensor-variate normal distribution [4]. From these two, it is possible to compute a series of metrics which are sensitive to different microstructural features of porous structures. Akin

* Corresponding author. Department of Biomedical Engineering, Campus US, Linköping University, Linköping, SE-581 83, Sweden.

** Corresponding author. Department of Biomedical Engineering, Campus US, Linköping University, Linköping, SE-581 83, Sweden.

E-mail addresses: deneb.boito@liu.se (D. Boito), evren.ozarslan@liu.se (E. Özarslan).

Peer review under responsibility of Innovation Academy for Precision Measurement Science and Technology (APM), CAS.

to what is done for characterizing size distributions [5], the goal in QTI is to estimate the statistical moments of the DTD from the collected data, and use these to interpret structural properties of complex media.

Herberthson et al. recently introduced a framework called QTI+ [6], which improved QTI's robustness to noise thus increasing its reliability. This was accomplished by imposing relevant positivity constraints as was done for other diffusion MR models [7]. It was shown that by performing the constrained estimation, it was possible to obtain more accurate parameter estimates which seemed to promote smoothness in the derived maps, despite each voxel being fitted independently [6]. Moreover, it was found that the constrained fit lowered the demand on the number of diffusion measurements to be acquired and considered for the estimation [8]. In addition to these encouraging findings, we encountered unrealistically high values of some of the scalar measures particularly in voxels with a large cerebrospinal fluid (CSF) content. To address this issue, in this work we formulate and apply complementary constraints which prohibit water diffusivity to exceed its theoretical physical value. Other works also considered imposing upper bounds while estimating metrics in other diffusion models, such as diffusion kurtosis imaging [9,10]. We thus incorporate the new constraints into the QTI+ framework, determine the extent of the violations of such conditions, and observe how imposing them influences the QTI metrics on human brain data obtained from a GE scanner.

2. Methods

2.1. Theory

2.1.1. Notation

The notation in this work is kept consistent with the one used in Ref. [6]. In short, italic characters are reserved for scalar quantities, boldface characters are used for matrices and second order tensors, and blackboard bold (double struck) characters denote fourth-order tensors. By choosing a basis in the 6-dimensional space of symmetric 3×3 matrices, all their mutual tensor products give 6×6 elements of the same type as the fourth order tensors occurring here. Hence these fourth order tensors can be represented as 6×6 matrices, and the tensor symmetries also imply that these 6×6 matrices are symmetric.

For the indexing, when expressed through Latin letters i, j, k , and l , they range from 1 to 3, while when expressed through the early Greek letters α, β , and γ , they range from 1 to 6. As an example, \mathbb{A}_{ijkl} and $\mathbf{A}_{\alpha\beta}$ are the fourth order and second order representations of the same tensor. When used with double struck and boldface characters, the indices do not refer to a particular component of the tensor but rather to the order of the elements. As explained in Ref. [6], the components of a tensor are addressed using ordinary capital letters, e.g., A_{ij} . The matrix products are expressed using the Einstein summation convention.

2.1.2. QTI

QTI [1] is a framework utilizing diffusion measurements with time varying magnetic field gradients and a diffusion tensor distribution [3] model, with stochastic variable \mathbf{D}_{ij} , for the medium microstructure. The DTD model assumes Gaussian diffusion within the subdomains making up the tissue. Consequently, all experimental parameters of each diffusion magnetic resonance experiment are captured by a measurement tensor, which we refer to in the text as \mathbf{B}_{ij} [11]. In the limit of small \mathbf{B}_{ij} , the MR signal in QTI is interpreted through the first two statistical cumulants of the DTD, namely the mean $\hat{\mathbf{D}}_{ij} = \langle \mathbf{D}_{ij} \rangle$ and fourth order covariance tensor $C_{ijkl} = \langle (\mathbf{D}_{ij} - \hat{\mathbf{D}}_{ij}) \otimes (\mathbf{D}_{kl} - \hat{\mathbf{D}}_{kl}) \rangle$. The MR signal, via cumulant expansion, can thus be written as [1]:

$$S(\mathbf{B}_{ij}) = S_0 \exp \left(-B_{ij} \hat{\mathbf{D}}_{ij} + \frac{1}{2} B_{ij} B_{kl} C_{ijkl} \right). \quad (1)$$

Given a family of measurements \mathbf{B}_{ij} , the parameters S_0 , $\hat{\mathbf{D}}_{ij}$, and C_{ijkl} can be estimated by solving the following problem:

$$\underset{S_0, \hat{\mathbf{D}}_{ij}, C_{ijkl}}{\operatorname{argmin}} \sum_{n=1}^N \left| S_n - S_0 e^{-B_{ij}^{(n)} \hat{\mathbf{D}}_{ij} + \frac{1}{2} B_{ij}^{(n)} B_{kl}^{(n)} C_{ijkl}} \right|^2 \quad (2)$$

which upon linearization by taking the logarithm becomes the weighted linear least squares problem:

$$\underset{S_0, \hat{\mathbf{D}}_{ij}, C_{ijkl}}{\operatorname{argmin}} \sum_{n=1}^N S_n^2 \left| \ln(S_n) - \ln(S_0) + B_{ij}^{(n)} \hat{\mathbf{D}}_{ij} - \frac{1}{2} B_{ij}^{(n)} B_{kl}^{(n)} C_{ijkl} \right|^2 \quad (3)$$

where the heteroskedasticity introduced by the logarithmic operation is accounted for by the factor S_n^2 . The problems defined in equations (2) and (3) can be solved by traditional non-linear and (weighted) linear least squares routines, respectively.

2.1.3. QTI+

In QTI+, the problems defined in equations (2) and (3) are solved while necessary positivity conditions are applied on the tensors to be estimated using non-linear and semidefinite programming (SDP) routines. The applied conditions were named

‘(d)’, ‘(c)’, and ‘(m)’, with the letters indicating which tensor the condition is imposed on. Here, ≥ 0 stands for positive semi-definite in the sense that all eigenvalues are non-negative:

$$(d) \hat{\mathbf{D}}_{ij} \geq 0,$$

$$(c) \mathbf{C}_{\alpha\beta} \geq 0, \text{ and}$$

$$(m) \text{ for all } \mathbf{v}_i \text{ and } \mathbf{u}_i, M_{ijkl} v_i v_j u_k u_l \geq 0$$

where M_{ijkl} are the elements of the fourth order tensor $\mathbb{M}_{ijkl} = \mathbf{C}_{ijkl} + \hat{\mathbf{D}}_{ij} \otimes \hat{\mathbf{D}}_{kl}$.

2.1.4. Diffusivity-limiting conditions

In this section, we describe additional conditions that could be imposed. In particular, the earlier conditions are expanded based on the observation that the maximum values of the diffusivities must be bounded from above. This maximum allowed value could be specified to be the bulk diffusivity D_0 for free diffusion occurring at a certain temperature. Mathematically, this translates into saying that $\hat{\mathbf{D}}_{ij} - D_0 \mathbf{I}_{ij}$ must be negative semidefinite for some bulk diffusivity D_0 . We refer to this condition as (d_{SL}) , where SL stands for ‘speed limit’:

$$(d_{SL}) \quad \hat{\mathbf{D}}_{ij} - D_0 \mathbf{I}_{ij} \leq 0$$

The same reasoning applied to the covariance tensor \mathbf{C}_{ijkl} results in several constraints. Below, the components \mathbf{C}_{ijkl} are expressed with respect to an orthonormal basis, and the coefficients $C_{\alpha\beta}$ with respect to a basis which is discussed in the appendix:

$$(c1_{SL}) \quad -D_0^2/4 \leq C_{\alpha\beta} \leq D_0^2/4 \text{ and } 0 \leq C_{\alpha\alpha} \leq D_0^2/4, \text{ if } 1 \leq \alpha, \beta \leq 3$$

$$(c2_{SL}) \quad 0 \leq \lambda_i \leq \frac{3}{4} D_0^2, i = 1, 2, 3, 4, 5, 6, \text{ where } \lambda_i \text{ are the eigenvalues of } \mathbf{C}_{\alpha\beta}$$

$$(\Gamma_{SL}^+) \quad \left(\mathbf{C}_{ijkl} + \frac{D_0^2}{4} \mathbf{I}_{ij} \mathbf{I}_{kl} \right) u_i u_j u_k u_l \geq 0$$

$$(\Gamma_{SL}^-) \quad \left(\mathbf{C}_{ijkl} - \frac{D_0^2}{4} \mathbf{I}_{ij} \mathbf{I}_{kl} \right) u_i u_j u_k u_l \leq 0$$

When applied on the tensor \mathbb{M}_{ijkl} , this constraint results in the condition

$$(m_{SL}) \quad \left(M_{ijkl} - D_0^2 \mathbf{I}_{ij} \mathbf{I}_{kl} \right) u_i u_j u_k u_l \leq 0$$

To apply these constraints, one is forced to determine the appropriate D_0 to be used as maximum allowed diffusivity. This value is mostly depending on the water temperature at the moment the experiment is performed. As there is no simple way of measuring this, the chosen threshold will most likely be an approximation of what the correct one should be. The discussion around possible choices of this value for human brain dMRI acquisition is found in later sections.

2.2. QTI \pm

The conditions derived in the previous sections can be applied alongside those enforced in QTI+ using semidefinite programming. Fig. 1 shows how both the positivity and diffusivity-limiting conditions are enforced in the newly created QTI \pm framework. In the nomenclature, the ‘-’ sign refers to the diffusivity-limiting conditions, while the ‘+’ sign refers to the non-negativity constraints.

In the SDP(dc \pm) step, conditions (d), (c), (d $_{SL}$), (c $_{SL}$), (c2 $_{SL}$), and (Γ_{SL}^-) are enforced. Note that condition (Γ_{SL}^+) does not need to be applied, as it is already implied by condition (c). The results obtained in this step can then be checked to verify whether they satisfy conditions (m) and (m $_{SL}$). As it was explained in QTI+ [6], these conditions can be checked with a semidefinite programming approach. If both are satisfied, then the results obtained in SDP(dc \pm) are the final result. If instead either “m” condition is violated, SDP(dcm \pm), which imposes conditions (c), (m), (c $_{SL}$), (Γ_{SL}^-) and (m $_{SL}$), is performed. In this step, the estimated values obtained for \mathbf{D}_{ij} in SDP(dc \pm), which are already guaranteed to satisfy conditions (d) and (d $_{SL}$), are fixed, so that \mathbb{M}_{ijkl} is linear in the variables to be estimated.

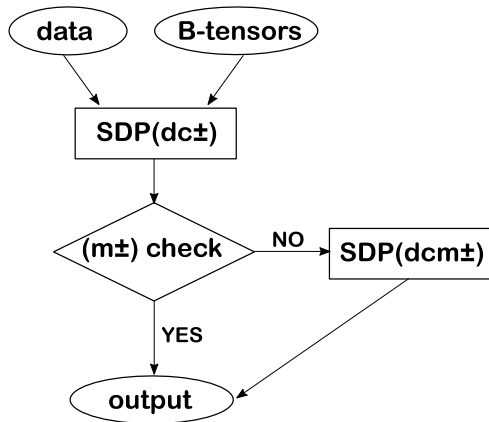


Fig. 1. QTI± framework. First, the data and b-tensors are input to the SDP(dc±) method. The produced estimates are checked for violations of both conditions (m) and (m_{SL}). If both are satisfied, the obtained parameters constitute the output of the framework. Otherwise, the estimates produced in SDP(dc±) are used as starting point in SDP(dcm±), which then produces the final estimates for the model parameters.

Note that while the framework depicted in Fig. 1 is what we find to provide the best solutions, it is not compulsory to execute all of its steps. For example, one option could be to take the output of SDP(dc±) as the final result. Another option is to skip the check on conditions (m) and (m_{SL}), and directly execute SDP(dcm±) after SDP(dc±). The results presented in later sections and the run times reported in Table 1 should provide the necessary information for the users to make an informed decision on which option to choose.

2.3. Implementation

The functions performing the constrained fit with both positivity and diffusivity-limiting conditions were implemented in Matlab as an extension to the *qtiplus* software available at <https://github.com/DenebBoito/qtiplus> and described in Ref. [12]. Two SDP optimizers, namely SDPT3 [13] and MOSEK (MOSEK ApS, Denmark), interfaced via CVX [14,15], were interchangeably used to fit the model to the data, and to check the violations of the (m) and (m_{SL}) conditions.

2.4. Violations of the conditions

A publicly available and thoroughly sampled human brain dataset, described in Ref. [16] and available at https://github.com/filip-szczepankiewicz/Szczepankiewicz_DIB_2019, was used to investigate where the diffusivity-limiting conditions are violated on model parameter estimates produced with the QTI+ (SDP(dcm+) method) framework. To simulate shorter acquisitions, this dataset was downsampled as described in Ref. [6], to produce datasets comprising, respectively, 217, 81, 56, and 39 diffusion measurements. We refer to these datasets as, respectively, p217, p81, p56, and p39. These datasets are available at https://github.com/filip-szczepankiewicz/Szczepankiewicz_DIB_2019/tree/master/DATA/brain/NII_Boito_SubSamples.

First, to verify the violations' dependence on the set maximum allowed bulk diffusivity D_0 , the diffusivity-limiting conditions were checked on model parameter estimates produced on the p81 datasets for 5 different D_0 values. These D_0 values were derived from the work of Holz et al. [17], for water temperatures in the range [36.5°C – 39.5°C].

Secondly, to assess whether the violations exhibit some dependence on the amount of available data, the conditions were checked on the p217, p81, p56, and p39 for the same maximum allowed bulk diffusivity $D_0 = 3.0750 \mu\text{m}^2/\text{ms}$.

Table 1
Run times for different estimation methods in the QTI+ and QTI± frameworks. The times were clocked while fitting one of the collected datasets (≈ 60000 voxels).

Method	Run time
SDP(dc+)	7 min
SDP(dc±)	22 min
SDP(dcm+)	9 min
SDP(dcm±)	50 min
m-check + SDP(dcm+)	7 min
m-check + SDP(dcm±)	48 min

2.5. Experimental data

Data from 8 healthy volunteers were collected with ethical approval from the Swedish Ethical Review Authority (Dnr 2019–06123) on a clinical GE Signa Architect 3T MR scanner using a q-space trajectory imaging diffusion protocol. The imaging parameters were: TE = 122 ms, TR = 3289 ms, field-of-view = $240 \times 240 \times 304 \text{ mm}^3$, matrix size = $80 \times 80 \times 39$, voxel size = $3 \times 3 \times 4 \text{ mm}^3$ with 4 mm spacing between slices. The QTI protocol consisted of 122 diffusion measurements organized as follows:

LTE: 6, 6, 16, and 30 directions at, respectively, $b = [0.1, 0.7, 1.4, 2.0] \mu\text{m}^2/\text{ms}$

PTE: 6, 10, and 15 directions at, respectively, $b = [0.1, 1.0, 2.0] \mu\text{m}^2/\text{ms}$

STE: 6, 6, 10, and 10 directions at, respectively, $b = [0.1, 0.7, 1.4, 2.0] \mu\text{m}^2/\text{ms}$

where LTE stands for linear tensor encoding, PTE for planar tensor encoding, STE for spherical tensor encoding, and b is the trace of the measurement tensor \mathbf{B}_{ij} . Prior to model fitting, the data were preprocessed for motion and eddy current corrections using the *eddy* tool from FSL [18] interfaced via *MRtrix3* [19] with default parameters.

3. Results

3.1. Violations of the conditions

Fig. 2 shows where the violations of conditions (d_{SL}), ($c1_{\text{SL}}$), ($c2_{\text{SL}}$), (Γ_{SL}^-), and (m_{SL}) occur. The voxels are color-coded based on which condition is violated in them: blue for the condition on \mathbf{D}_{ij} (d_{SL}), red for the conditions on \mathbf{C}_{ijkl} ($c1_{\text{SL}}$), ($c2_{\text{SL}}$) and (Γ_{SL}^-), and green for the condition on \mathbb{M}_{ijkl} (m_{SL}). The (dcm_{SL}) column shows the voxels in which at least one of the diffusivity limiting conditions is violated; the color there is based on an RGB colormap resulting from the sum of the first 5 columns.

The maps in panel a), obtained on the p81 protocol, highlight how the violations are independent of the maximum allowed diffusivity, for the considered values. The maps in panel b) show that the violations are consistent — in terms of occurring in regions where there is abundance of free water — for model parameters estimated from datasets comprising different numbers of diffusion measurements. From both panels, it is evident that the conditions on the maximum allowed diffusivity are violated almost exclusively in tissues containing large fractions of cerebrospinal fluid (CSF).

3.2. Imposing the conditions

Fig. 3 shows on the left the violations of the diffusivity limiting conditions on fits produced with the unconstrained routine (as implemented in <https://github.com/markus-nilsson/md-dmri>), QTI+, SDP(dc_{\pm}), and SDP(dcm_{\pm}). The resulting QTI stains (Mean Diffusivity (MD), Fractional Anisotropy (FA), microscopic Fractional Anisotropy (μFA), Size Variance (C_{MD}), and

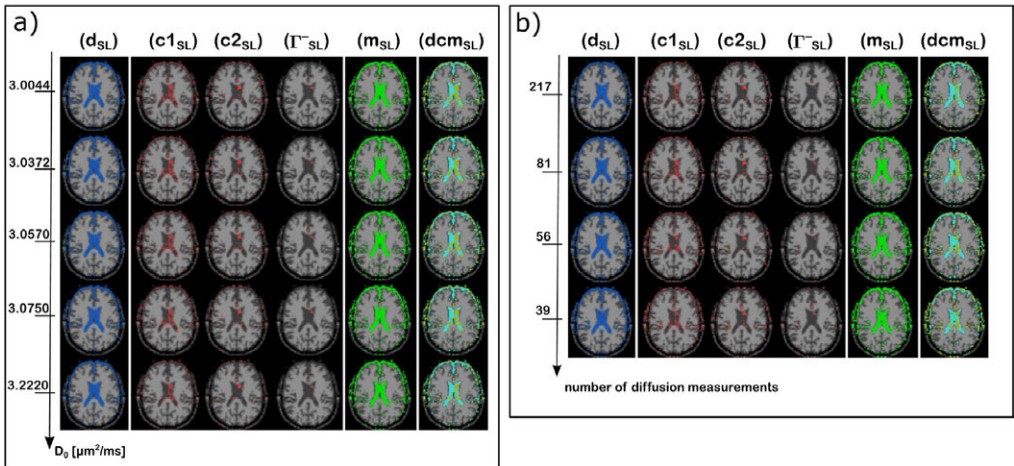


Fig. 2. Violations of the conditions for different choices of D_0 and protocol p81 (panel a), and the considered protocols and maximum allowed diffusivity $D_0 = 3.0750 \mu\text{m}^2/\text{ms}$ (panel b). Colors are used to indicate which of the conditions is violated in each voxel: blue for (d_{SL}), red for ($c1_{\text{SL}}$), ($c2_{\text{SL}}$) and (Γ_{SL}^-), and green for (m_{SL}). The (dcm_{SL}) column shows all the voxels in which at least one of the conditions is violated as a sum of the first 5 columns RGB values. The model parameters on which the conditions are checked are produced with QTI+ (SDP(dcm_{\pm})). Both panels highlight how, within the range of considered scenarios, the violations are largely independent of the set maximum allowed diffusivity, and number of diffusion measurements. Moreover, the violations are almost entirely limited to tissues containing a significant amount of CSF.

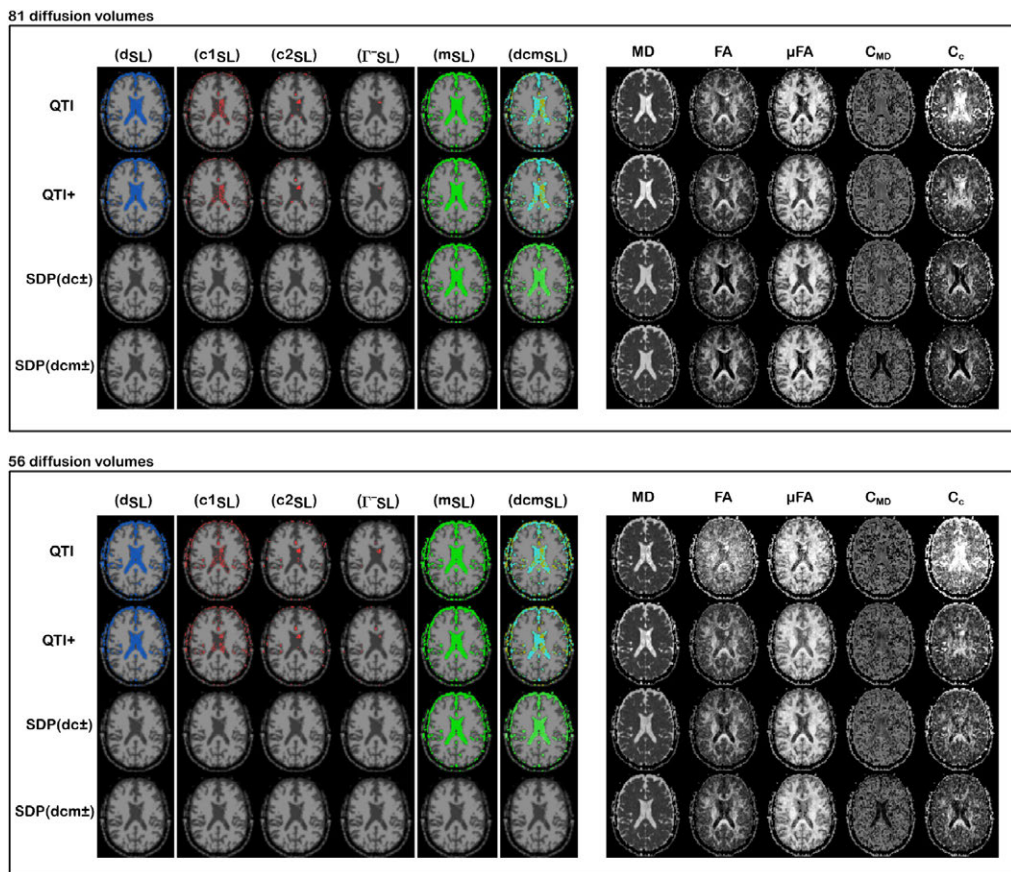


Fig. 3. Violations of the conditions (left) and scalar maps (right) obtained through the p81 (top) and p56 (bottom) protocols. The maximum allowed diffusivity was set to $D_0 = 3.0750 \mu\text{m}^2/\text{ms}$.

Orientation Coherence (C_c) are shown on the right. The model fitting was performed on the p81 (top panel) and p56 (bottom panel) protocols. The violation maps for SDP($dc\pm$) and SDP($dcm\pm$) highlight how imposing the constraints provides model estimates which satisfy the targeted conditions.

The maps located on the right side in the panels show how the constraints affect the stains derived in the QTI analysis. The conditions imposed in QTI+ provide generally smoother looking maps, while most of the changes introduced by the new constrained framework are most easily observable in the ventricles, where the theoretical value of FA, μFA , C_{MD} , and C_c should be 0, while the value of MD should have an upper limit set by the maximum allowed diffusivity D_0 . The fits produced with SDP($dc\pm$) already provide an improvement in several maps when compared with those produced in QTI+. In particular, it was possible to remove the flow artefact located in the frontal horn of the left ventricle. The results are further improved when all the diffusivity limiting conditions are applied in SDP($dcm\pm$). Observe for example how the μFA , C_{MD} , and C_c quantities are further pushed towards their expected value. Note however that on the fit produced on the p56 protocol, μFA seems to erroneously increase in value in the ventricles.

3.3. Experimental data

Fig. 4 shows the scalar maps obtained by fitting the data for two healthy subjects with QTI+, SDP($dc\pm$) and SDP($dcm\pm$). Similar to the results obtained on the p56 and p81 datasets, the QTI maps obtained with the extended list of constraints exhibit improved parameter estimation in tissue containing large fractions of CSF. This provides in general better delineation of different anatomical regions, most evidently in C_{MD} and C_c maps.

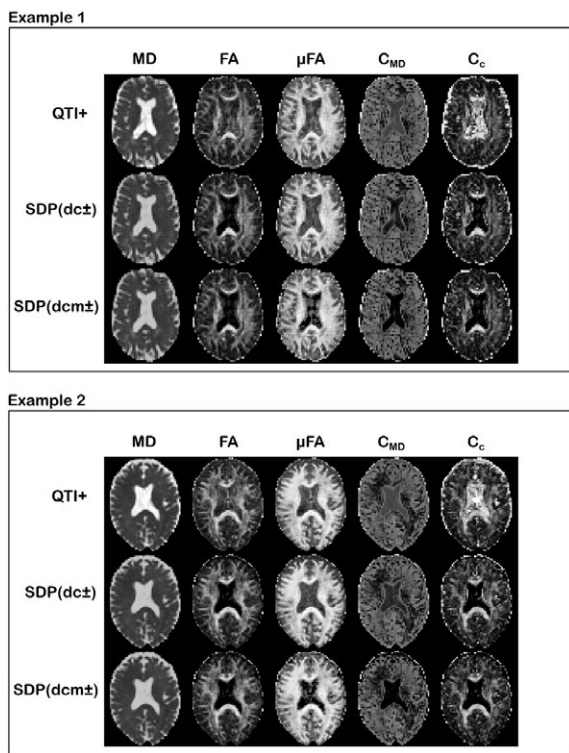


Fig. 4. Example results on two datasets collected on healthy volunteers using a protocol readily available on GE MR scanners. The maximum allowed diffusivity was set to $D_0 = 3.0750 \mu\text{m}^2/\text{ms}$.

3.4. Computational times

In Table 1 we report the run times for the different steps of the QTI± framework and representative steps of the QTI+ framework, for fittings performed on one of the collected datasets. The run times were recorded on a workstation featuring a 12-core Intel Core i9-7920X CPU. The considered voxels for the fit amounted to ≈ 60000 .

4. Discussion

The results displayed in Fig. 2 highlighted how the violations of the conditions are almost exclusively restricted to areas containing large fractions of CSF. This is perhaps to be expected since in these regions the diffusivity is approximately the same as the speed limit. The results in Fig. 2 panel a) also suggested that when the diffusivity limit is surpassed, it is most likely surpassed by a considerable margin. This consideration could help to relax strict demands on setting an accurate maximum allowed diffusivity to be used for constraining the fit.

Though regions containing *only* free water are typically of little interest for subsequent analysis, we would like to stress that the proposed constraints are relevant for voxels with partial voluming between free water and structures. We show examples of this in Fig. 5. After removing the voxels in which at least one of the eigenvalues of $\hat{\mathbf{D}}$ (estimated with QTI+) exceeds the speed limit, there remain voxels violating condition (m_{SL}). These voxels are most likely located at the interface between white-matter and grey-matter or CSF, i.e., where partial voluming is bound to occur due to the limited achievable spatial resolution. As condition (m_{SL}) is related to the speed limit for each compartment in the voxel's DTD, the violation can be explained by considering that the diffusivity limit is exceeded by the free water fraction in the voxel. In Fig. 5 panel b) we then show how different the QTI stains are in these voxels if estimated with QTI+ (SDP(dcm+)) or QTI± (SDP(dcm±)). While, as expected, the metrics computed from $\hat{\mathbf{D}}$ are essentially equal, there is a substantial discrepancy between the μ FA, C_{MD} , and C_c values produced with QTI+ and QTI±. Such discrepancy could play a major role when characterizing tissue heterogeneity via quantitative analysis. This would be especially relevant when analysing diseased tissues, such as brain tumors. The necrotic and oedematous tumor compartments typically contain large fractions of free water, which could bias the recovered

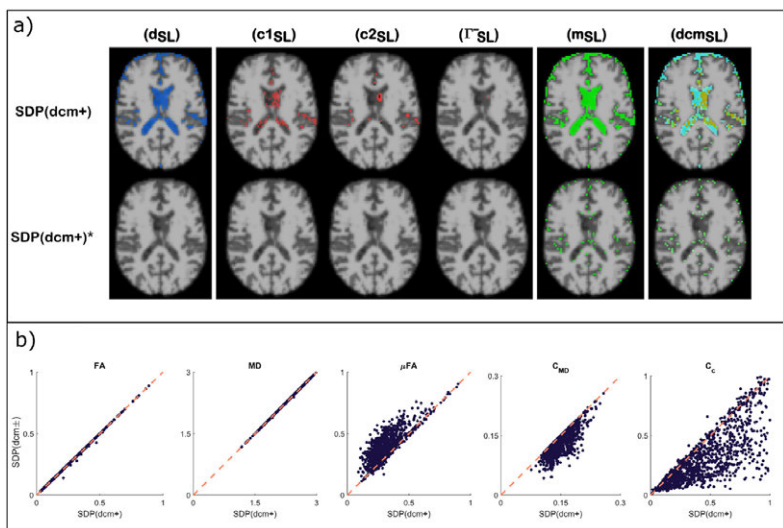


Fig. 5. a) Violations of the speed limit conditions for fits produced with $SDP(dcm+)$ on the p81 dataset. The second row, marked with $SDP(dcm+)^*$, shows the violations remaining after masking out the voxels in which the condition (d_{SL}) is not respected. Violations of condition (m_{SL}) can still be observed where partial voluming between different tissue types is occurring. The maximum allowed diffusivity was set to $D_0 = 3.0750 \mu m^2/ms$. b) Scatter plots comparing QTI stains computed from the fits produced employing QTI+ ($SDP(dcm+)$) and QTI± ($SDP(dcm\pm)$) on the voxels remaining after masking out those in which condition (d_{SL}) is not respected (a total of 1221 voxels across the all brain). The plots show that FA and MD have essentially equal values for the two fits, while μFA , C_{MD} and C_c may differ quite substantially.

metrics [20]. Therefore, methods accounting for possible artifacts arising from free water partial voluming should be considered for better *in vivo* assessment of tissue heterogeneity.

The results shown in Fig. 3 depicted the improvement introduced in the QTI stains when the diffusivity-limiting conditions are imposed. These results were consistent with those obtained on the datasets acquired during the study, thus demonstrating the validity of our findings across platforms. Note however that, as pointed out in section 3.2, some values of the constraint estimated μFA are pushed in the wrong direction. This is plausibly due to performing the fit on fewer data which are also already at the noise floor. Enforcing constraints under these conditions might produce biased estimates for parameters whose value is supposedly distributed around 0. As illustrated for example in Fig. 3 for the μFA values in the ventricles, this seems to manifest mostly on fits to datasets very sparsely sampled, such as p39 (results not shown) and p56. The effect is instead more contained on datasets comprising a higher number of data points, such as p217 (results not shown) and p81.

To be considered are also the run times reported in Table 1. The overall improvement in the parameters' estimation brought by performing constrained optimization comes at the cost of increasing the time it takes to estimate the model parameters. Future advances on the solvers' algorithmic side could help reduce the current processing time.

5. Conclusion

In this work we considered extending the list of conditions to be applied while fitting the QTI model, by adding constraints targeting the maximum allowed diffusivity. We showed that in regions where freely diffusing water is abundant these conditions are easily violated, with the violations plausibly due to contributions of different factors such as noise, CSF flow artifacts, and acquisition protocols not designed for data collection in these specific brain areas. Imposing the constraints helps the parameters derived from the QTI analysis to be directed towards their expected values, and generally provides stronger visual contrast between different brain tissues.

CRedit authorship contribution statement

Deneb Boito: Software, Validation, Investigation, Data curation, Writing – original draft, Writing – review & editing. **Magnus Herberthson:** Methodology, Formal analysis, Writing – original draft, Writing – review & editing. **Tom Dela Haije:** Methodology, Funding acquisition, Writing – review & editing. **Ida Blystad:** Supervision, Resources, Data curation, Writing – review & editing. **Evren Özarslan:** Conceptualization, Methodology, Formal analysis, Writing – review & editing, Supervision, Project administration, Funding acquisition, Writing – original draft.

Declaration of competing interest

Ö and MH are shareholders in Spin Nord AB. The remaining authors declare no conflict of interest.

Acknowledgement

This research was funded by Sweden's Innovation Agency (VINNOVA) ASSIST, Analytic Imaging Diagnostic Arena (AIDA), Swedish Foundation for Strategic Research (RMX18-0056), Linköping University Center for Industrial Information Technology (CENIIT), LiU Cancer Barncancerfonden, and a research grant (00028384) from VILLUM FONDEN.

Appendix. Derivation of the diffusivity-limiting conditions

In this appendix we discuss some of the inequalities presented in section 2.1.4.

Suppose that \mathbf{D}_{ij} is a stochastic variable which satisfies $0 \leq \mathbf{D}_{ij} \leq D_0 \mathbf{I}_{ij}$. For a non-zero vector u_j , which without loss of generalisation can be assumed to have unit length, from $M_{ijkl} = \langle D_{ij} D_{kl} \rangle$ it follows that $M_{ijkl} = \langle D_{ij} u_i u_j D_{kl} u_k u_l \rangle = \langle X^2 \rangle$, where $X = D_{ij} u_i u_j$, so that X takes values in $[0, D_0]$. This means that $\langle X^2 \rangle \leq D_0^2$, i.e., $M_{ijkl} u_i u_j u_k u_l \leq D_0^2 = D_{ij}^2 I_{ij} I_{kl} u_i u_j u_k u_l$ which is condition (m_{SL}).

It can also be shown that the variance of the stochastic variable X satisfies $V(X) \leq D_0^2/4$. To see this, we first note that the variance is independent of translations, i.e., we can assume that X takes values in $[-d_0, d_0]$, where $d_0 = D_0/2$. The problem

can then be formulated as follows: suppose $\text{supp}(p) \subset [-d_0, d_0]$, $p \geq 0$, $\int_{-d_0}^{d_0} p(x) dx = 1$, $\int_{-d_0}^{d_0} x p(x) dx = \mu$. What is the maximal value of

$$\int_{-d_0}^{d_0} (x - \mu)^2 p(x) dx = \int_{-d_0}^{d_0} x^2 p(x) dx - \mu^2?$$

Let g be the even part of p , $g(x) = (p(x) + p(-x))/2$. Then $\int_{-d_0}^{d_0} x g(x) dx = 0$ and

$$\int_{-d_0}^{d_0} (x - 0)^2 g(x) dx = \int_{-d_0}^{d_0} x^2 \frac{p(x) + p(-x)}{2} dx = \int_{-d_0}^{d_0} x^2 p(x) dx \geq \int_{-d_0}^{d_0} x^2 p(x) dx - \mu^2 = \int_{-d_0}^{d_0} (x - \mu)^2 p(x) dx.$$

Hence, we can assume that p is even (so that $\mu = 0$). Next, since $p \geq 0$,

$$\int_{-d_0}^{d_0} x^2 p(x) dx \leq d_0^2 \int_{-d_0}^{d_0} p(x) dx = d_0^2 = D_0^2/4,$$

and this value is obtained for $p(x) = \frac{1}{2} \delta(x + d_0) + \frac{1}{2} \delta(x - d_0)$. Since $C_{ijkl} u_i u_j u_k u_l$ is precisely $V(x)$, (and since $I_{ij} u_i u_j = 1$), condition (Γ_{SL}^-) follows.

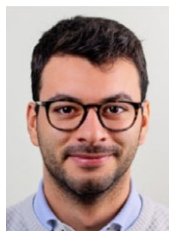
Conditions (c1_{SL}) and (c2_{SL}) can be proven by first considering that the coefficients $C_{\alpha\beta}$ are expressed with respect to an particular orthonormal set of basis matrices $\{A_1, A_2, A_3, A_4, A_5, A_6\}$ in the space of symmetric 3×3 matrices, with orthogonality taken with respect to the scalar product $\langle A, B \rangle = \text{tr}(AB)$. Namely, the three first matrices in the basis are $A_1 = \begin{pmatrix} 1 & 0 & 0 \\ 0 & 0 & 0 \\ 0 & 0 & 0 \end{pmatrix}$, $A_2 = \begin{pmatrix} 0 & 0 & 0 \\ 0 & 1 & 0 \\ 0 & 0 & 0 \end{pmatrix}$, $A_3 = \begin{pmatrix} 0 & 0 & 0 \\ 0 & 0 & 0 \\ 0 & 0 & 1 \end{pmatrix}$. Defining $X_1 = D_{ij}(A_1)_{ij}$, $X_2 = D_{ij}(A_2)_{ij}$, $X_3 = D_{ij}(A_3)_{ij}$, we get three stochastic variables taking values in $[0, D_0]$. Hence $0 \leq V(X_i) \leq D_0^2/4$, $i = 1, 2, 3$. For $1 \leq \alpha, \beta \leq 3$, $C_{\alpha\beta} = \text{Cov}(X_\alpha, X_\beta)$. Since $-\sqrt{V(X)V(Y)} \leq \text{Cov}(X, Y) \leq \sqrt{V(X)V(Y)}$, which results in condition (c1_{SL}).

Finally, note that if b_α is an eigenvector with eigenvalue λ to $C_{\alpha\beta}$, and if b_α has unit norm, then $C_{\alpha\beta} b_\alpha b_\beta = \lambda$. In terms of C_{ijkl} and the corresponding (eigen)matrix B_{ij} (with unit norm) this means that $C_{ijkl} B_{ij} B_{kl} = \lambda$. Define $Y = (D_{ij} - d_0 I_{ij}) B_{ij}$ with $d_0 = D_0/2$. Then $V(Y) = \langle (Y - \langle Y \rangle)(Y - \langle Y \rangle) \rangle = \langle ((D_{ij} - d_0 I_{ij}) B_{ij} - \langle (D_{ij} - d_0 I_{ij}) B_{ij} \rangle) ((D_{kl} - d_0 I_{kl}) B_{kl} - \langle (D_{kl} - d_0 I_{kl}) B_{kl} \rangle) \rangle = \langle (D_{ij} B_{ij} - \langle D_{ij} B_{ij} \rangle) (D_{kl} B_{kl} - \langle D_{kl} B_{kl} \rangle) \rangle = C_{ijkl} B_{ij} B_{kl}$. On the other hand,

$|Y| = |(D_{ij} - d_0 I_{ij}) B_{ij}| \leq \|(D_{ij} - d_0 I_{ij})\| \cdot \|B_{ij}\| = \|(D_{ij} - d_0 I_{ij})\|$. All the eigenvalues of $D_{ij} - d_0 I_{ij}$ lie in the range $[-d_0, d_0]$ and hence $\|(D_{ij} - d_0 I_{ij})\| \leq d_0 \|I_{ij}\| = \sqrt{3}d_0 = \sqrt{3}D_0/2$. By the earlier results, $V(Y) \leq 3D_0^2/4$, which proves condition (c2_{SL}).

References

- [1] C.F. Westin, H. Knutsson, O. Pasternak, F. Szczepankiewicz, E. Özarslan, D. van Westen, C. Mattisson, M. Bogren, L.J. O'Donnell, M. Kubicki, D. Topgaard, M. Nilsson, Q-space trajectory imaging for multidimensional diffusion MRI of the human brain, *Neuroimage* 135 (Jul 2016) 345–362.
- [2] T.M. de Swiet, P.P. Mitra, Possible systematic errors in single-shot measurements of the trace of the diffusion tensor, *J. Magn. Reson. B* 111 (Apr 1996) 15–22.
- [3] B. Jian, B.C. Vemuri, E. Özarslan, P.R. Carney, T.H. Mareci, A novel tensor distribution model for the diffusion-weighted MR signal, *Neuroimage* 37 (1) (2007) 164–176.
- [4] P.J. Basser, S. Pajevic, A normal distribution for tensor-valued random variables: applications to diffusion tensor MRI, *IEEE Trans. Med. Imag.* 22 (Jul 2003) 785–794.
- [5] E. Özarslan, N. Shemesh, C.G. Koay, Y. Cohen, P.J. Basser, Nuclear magnetic resonance characterization of general compartment size distributions, *New J. Phys.* 13 (2011), 15010.
- [6] M. Herberthson, D. Boito, T. Dela Haije, A. Feragen, C.-F. Westin, E. Özarslan, Q-space trajectory imaging with positivity constraints (QTI+), *Neuroimage* 238 (2021), 118198.
- [7] T. Dela Haije, E. Özarslan, A. Feragen, Enforcing necessary non-negativity constraints for common diffusion MRI models using sum of squares programming, *Neuroimage* 209 (2020), 116405.
- [8] D. Boito, M. Herberthson, T. Dela Haije, E. Özarslan, Enforcing positivity constraints in q-space trajectory imaging (QTI) allows for reduced scan time, in: *Proc Intl Soc Mag Reson Med*, vol. 29, 2021, 0404.
- [9] A. Ghosh, T. Milne, R. Deriche, Constrained diffusion kurtosis imaging using ternary quartics & MLE, *Magn. Reson. Med.* 71 (Apr. 2014) 1581–1591.
- [10] J. Veraart, W. Van Hecke, J. Sijbers, Constrained maximum likelihood estimation of the diffusion kurtosis tensor using a Rician noise model, *Magn. Reson. Med.* 66 (Sept. 2011) 678–686.
- [11] J. Mattiello, P.J. Basser, D. Le Bihan, The b matrix in diffusion tensor echo-planar imaging, *Magn. Reson. Med.* 37 (Feb 1997) 292–300.
- [12] D. Boito, M. Herberthson, T. Dela Haije, E. Özarslan, Applying positivity constraints to q-space trajectory imaging: the QTI+ implementation, *Software* 18 (2022), 101030.
- [13] K.C. Toh, M.J. Todd, R.H. Tütüncü, SDPT3 — a Matlab software package for semidefinite programming, version 1.3, *Optim. Methods Software* 11 (1–4) (1999) 545–581.
- [14] M. Grant, S. Boyd, CVX: Matlab Software for Disciplined Convex Programming, mar 2014 version 2.1, <http://cvxr.com/cvx>.
- [15] M. Grant, S. Boyd, Graph implementations for nonsmooth convex programs, in: V. Blondel, S. Boyd, H. Kimura (Eds.), *Recent Advances in Learning and Control*, Springer-Verlag Limited, 2008, pp. 95–110. Lecture Notes in Control and Information Sciences, http://stanford.edu/~boyd/graph_dcp.html.
- [16] F. Szczepankiewicz, S. Hoge, C.-F. Westin, Linear, planar and spherical tensor-valued diffusion MRI data by free waveform encoding in healthy brain, water, oil and liquid crystals, *Data Brief* 25 (Aug 2019) 104208.
- [17] M. Holz, S.R. Heil, A. Sacco, Temperature-dependent self-diffusion coefficients of water and six selected molecular liquids for calibration in accurate 1h nmr pfg measurements, *Phys. Chem. Chem. Phys.* 2 (2000) 4740–4742.
- [18] J.L. Andersson, S.N. Sotiropoulos, An integrated approach to correction for off-resonance effects and subject movement in diffusion MR imaging, *Neuroimage* 125 (Jan. 2016) 1063–1078.
- [19] J.-D. Tournier, R. Smith, D. Raffelt, R. Tabbara, T. Dhollander, M. Pietsch, D. Christiaens, B. Jeurissen, C.-H. Yeh, A. Connelly, MRtrix3: a fast, flexible and open software framework for medical image processing and visualisation, *Neuroimage* 202 (Nov. 2019) 116137.
- [20] L. Starck, F. Zaccagna, O. Pasternak, F.A. Gallagher, R. Grüner, F. Riemer, Effects of multi-shell free water correction on glioma characterization, *Diagnosics* 11 (12) (2021).



Deneb Boito received his B.S. degree in Biomedical Engineering from the University of Padua in 2015, and his M.Sc. degree in Biomedical Engineering from Linköping University in 2018. He is currently a Doctoral Student at Linköping University under the supervision of Dr. Evren Özarslan. He specializes in diffusion magnetic resonance imaging methods and data processing for characterizing the microstructure of the human brain.



Evren Özarslan received his bachelor's degree in Physics from the University of Illinois, Urbana-Champaign and his PhD from University of Florida where he also obtained a master's degree in Biomedical Engineering. He worked in Peter J. Basser's lab at the National Institutes of Health, first as a postdoctoral fellow, then as a scientist with the Center for Neuroscience and Regenerative Medicine. Evren subsequently accepted a position with the Department of Radiology, Brigham and Women's Hospital, where he was promoted to the rank of assistant professor at Harvard Medical School. In 2013, Evren moved to Istanbul where he was an assistant professor in the Department of Physics at Boğaziçi University. Since early 2016, he has been with the Department of Biomedical Engineering, Linköping University in Sweden. Evren's current research is on developing innovative magnetic resonance techniques with the aim of characterizing water dynamics within biological tissues as well as other porous media.

PAPER

III

MRI with generalized diffusion encoding reveals damaged white matter in patients previously hospitalized for COVID-19 and with persisting symptoms at follow-up

Deneb Boito
Anders Eklund
Anders Tisell
Richard Levi
Evren Özarslan
Ida Blystad

Brain Communications, 2023, 5

© 2023 The Authors.

Published by Oxford University Press on behalf of the Guarantors of Brain.

Reprinted with permission (CC BY 4.0)

BRAIN COMMUNICATIONS

MRI with generalized diffusion encoding reveals damaged white matter in patients previously hospitalized for COVID-19 and with persisting symptoms at follow-up

Deneb Boito,^{1,2} Anders Eklund,^{1,2,3} Anders Tisell,^{2,4,5} Richard Levi,^{2,5,6} Evren Özarslan^{1,2,*} and  Ida Blystad^{2,5,7,*}

* These authors contributed equally to this work.

There is mounting evidence of the long-term effects of COVID-19 on the central nervous system, with patients experiencing diverse symptoms, often suggesting brain involvement. Conventional brain MRI of these patients shows unspecific patterns, with no clear connection of the symptomatology to brain tissue abnormalities, whereas diffusion tensor studies and volumetric analyses detect measurable changes in the brain after COVID-19. Diffusion MRI exploits the random motion of water molecules to achieve unique sensitivity to structures at the microscopic level, and new sequences employing generalized diffusion encoding provide structural information which are sensitive to intravoxel features. In this observational study, a total of 32 persons were investigated: 16 patients previously hospitalized for COVID-19 with persisting symptoms of post-COVID condition (mean age 60 years: range 41–79, all male) at 7-month follow-up and 16 matched controls, not previously hospitalized for COVID-19, with no post-COVID symptoms (mean age 58 years, range 46–69, 11 males). Standard MRI and generalized diffusion encoding MRI were employed to examine the brain white matter of the subjects. To detect possible group differences, several tissue microstructure descriptors obtainable with the employed diffusion sequence, the fractional anisotropy, mean diffusivity, axial diffusivity, radial diffusivity, microscopic anisotropy, orientational coherence (C_c) and variance in compartment's size (C_{MD}) were analysed using the tract-based spatial statistics framework. The tract-based spatial statistics analysis showed widespread statistically significant differences ($P < 0.05$, corrected for multiple comparisons using the familywise error rate) in all the considered metrics in the white matter of the patients compared to the controls. Fractional anisotropy, microscopic anisotropy and C_c were lower in the patient group, while axial diffusivity, radial diffusivity, mean diffusivity and C_{MD} were higher. Significant changes in fractional anisotropy, microscopic anisotropy and C_{MD} affected approximately half of the analysed white matter voxels located across all brain lobes, while changes in C_c were mainly found in the occipital parts of the brain. Given the predominant alteration in microscopic anisotropy compared to C_c , the observed changes in diffusion anisotropy are mostly due to loss of local anisotropy, possibly connected to axonal damage, rather than white matter fibre coherence disruption. The increase in radial diffusivity is indicative of demyelination, while the changes in mean diffusivity and C_{MD} are compatible with vasogenic oedema. In summary, these widespread alterations of white matter microstructure are indicative of vasogenic oedema, demyelination and axonal damage. These changes might be a contributing factor to the diversity of central nervous system symptoms that many patients experience after COVID-19.

- 1 Department of Biomedical Engineering, Linköping University, S-58183 Linköping, Sweden
- 2 Centre for Medical Image Science and Visualization (CMIV), Linköping University, S-58183 Linköping, Sweden
- 3 Division of Statistics and Machine learning, Department of Computer and Information Science, Linköping University, S-58183 Linköping, Sweden
- 4 Department of Radiation Physics, Linköping University, S-58185 Linköping, Sweden

Received May 02, 2023. Revised August 25, 2023. Accepted October 26, 2023. Advance access publication October 22, 2023

© The Author(s) 2023. Published by Oxford University Press on behalf of the Guarantors of Brain.

This is an Open Access article distributed under the terms of the Creative Commons Attribution License (<https://creativecommons.org/licenses/by/4.0/>), which permits unrestricted reuse, distribution, and reproduction in any medium, provided the original work is properly cited.

- 5 Department of Health, Medicine and Caring Sciences, Linköping University, S58183 Linköping, Sweden
 6 Department of Rehabilitation Medicine in Linköping, Linköping University, S-58185 Linköping, Sweden
 7 Department of Radiology in Linköping, Linköping University, S-58185 Linköping, Sweden

Correspondence to: Ida Blystad
 Röntgenkliniken Universitetssjukhuset
 Linköping S-58185, Sweden
 E-mail: ida.blystad@liu.se

Keywords: MRI; Q-space trajectory imaging; microscopic fractional anisotropy; fractional anisotropy; COVID-19

Graphical Abstract

MRI with generalized diffusion encoding reveals damaged white matter in patients previously hospitalized for COVID-19 and with persisting symptoms at follow-up

Population

Healthy controls

- n=16 (11 males, 5 females)



Patients

- n=16, all males
- previously hospitalized for COVID-19
- persisting post-covid symptoms



diffusion Magnetic Resonance Imaging (dMRI) data

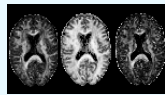
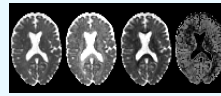
Group comparison based on
diffusion MRI metrics

mean diffusivity MD

axial diffusivity AD

radial diffusivity RD

variance in mean diffusivity C_{MD}



FA fractional anisotropy

μ FA microscopic fractional anisotropy

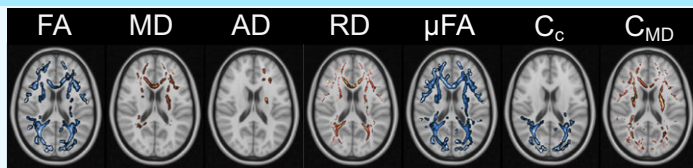
C_c orientation coherence

Brain microstructural alterations after COVID-19

controls > patients



controls < patients



These alterations are compatible with

vasogenic oedema
 demyelination
 axonal damage

Introduction

COVID-19 and the brain

Since the first wave of the COVID-19 pandemic, it has become clear that the infection caused by the corona virus may go with long-term sequelae, affecting a considerable percentage of the population on a long-term basis (5%,¹ 6.5–28.5%²). Symptoms are diverse and often suggest brain involvement, manifesting in problems such as fatigue, cognitive impairment, depression and anxiety.³ Persisting problems can linger for several years, affecting patients irrespective of the initial disease severity.⁴ Brain findings on MRI in the acute phase of the infection during the first pandemic were often associated with vascular changes, such as ischaemic and haemorrhagic events.^{5,6} At later follow-up, conventional clinical MRI shows unspecific patterns of structural changes,^{7,8} whereas diffusion tensor studies and volumetric analyses detect measurable changes in the brain after COVID-19.^{9–11} In this work, advanced diffusion MRI (dMRI) is used to quantitatively analyse the properties of brain tissue in 16 patients previously hospitalized for COVID-19 and with persisting symptoms after the infection at 7-month follow-up. The analysis is based on a comparison between this group and 16 controls with no post-COVID symptoms and who were not hospitalized for COVID-19.

dMRI and Q-space trajectory imaging

dMRI is an imaging technique with extreme sensitivity to tissue structure on the micrometre level. The structural properties of the tissue can be retrieved by measuring, typically with a pair of pulsed magnetic field gradients,¹² and modelling the random motion of water molecules.^{13–15} Barriers in the tissue guide the diffusion process, thus imprinting their presence and characteristics into the measurement. Models can then be applied to the measured diffusion signal to retrieve these features.

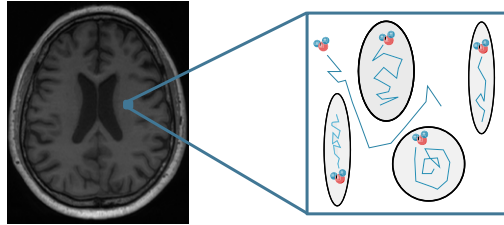
In neurological medical practice, dMRI has become a staple for fast detection of acute brain ischaemia and for studying brain connectivity.¹⁶ Diffusion MR images obtainable with standard clinical MR systems are however typically limited to 2–3 mm spatial resolution while being sensitive to structures at the microscopic level. This means that all the contributions from different micrometre-level features within a voxel conflate and are typically lost when only voxel-scale metrics, such as those obtainable with diffusion tensor imaging (DTI),¹⁷ are used.

Recent efforts directed towards resolving this limitation resulted in innovative dMRI encodings and methods. While standard dMRI acquisitions rely on single diffusion encoding (SDE), i.e. diffusion being measured along a single direction at a time, new protocols involving simultaneous diffusion measurements in multiple directions have been developed.^{18–23} This has allowed for retrieval of more specific features of the tissue microstructure which prompted interest towards bringing these methods into the clinic.

Q-space trajectory imaging (QTI)²⁴ is a diffusion imaging technique that utilizes diffusion data acquired with general time-varying magnetic field gradients,^{25,26} which allow time-efficient measurements of water displacement in multiple directions. The diffusion waveforms employed in QTI are typically referred to as linear tensor encoding (LTE), planar tensor encoding (PTE) and spherical tensor encoding (STE), for 1D, 2D and 3D diffusion measurements, respectively. For analysing the collected data, QTI employs a multi-compartment model for the tissue microstructure, where each voxel is envisioned as being composed of many diffusion tensors.²⁷ In a sense, this method alleviates the limitation of DTI where all intravoxel microscopic tensors are condensed into one, which represents their average. Figure 1A shows this idea of modelling each voxel as a collection of separate environments where water is freely diffusing within and in between them, exploiting dMRI's sensitivity to finer-than-voxel size features. Figure 1B shows two diffusion-weighted pulse sequences, one where conventional trapezoidal gradients are used to achieve diffusion sensitization and one where general time-varying magnetic field gradients are employed to achieve diffusion sensitization.

The QTI analysis provides several quantities akin to various 'stains' used in histology, which capture different aspects of the tissue microstructure. Figure 2A shows pictorially four such measures and how they change based on the characteristics of the intravoxel environment. Macroscopic anisotropy is typically quantified by fractional anisotropy (FA),²⁸ which measures the voxel-level degree of diffusion anisotropy and orientational coherence. FA is 0 when voxel-averaged diffusion is equally probable in all directions and 1 when diffusion occurs in only one direction. In terms of the multicompartment picture, this means that in order for FA to take the value 1, diffusion in all microenvironments needs to share the same preferred orientation. In the case where all microenvironments exhibit anisotropic diffusion but not along the same direction, FA will take a value lower than 1. Microscopic anisotropy (μ FA) captures the degree of anisotropy on a local level (i.e. for each microscopic environment), and it is thus insensitive to the relative orientation of the compartments. This metric then takes the value 0 when diffusion is isotropic in all microenvironments, while its value is close to 1 when the voxel comprises highly anisotropic microenvironments, irrespective of whether they share a common preferred orientation. The degree to which diffusion exhibits a global preferred orientation is captured by the orientational coherence (C_c) parameter. When diffusion is locally anisotropic but not globally, this parameter takes the value 0. When diffusion is instead both locally and globally anisotropic, its value is close to 1. The size variance (C_{MD}) parameter reflects the degree of variation in compartment size within each voxel. If compartments are all the same size, this parameter takes the value 0, whereas when compartments have different sizes, it takes a value closer to 1. Figure 2B shows an example of how these parameters look for one of the healthy subjects enrolled in this study.

A Diffusion MRI is sensitive to intravoxel structure



B Diffusion MRI pulse sequences

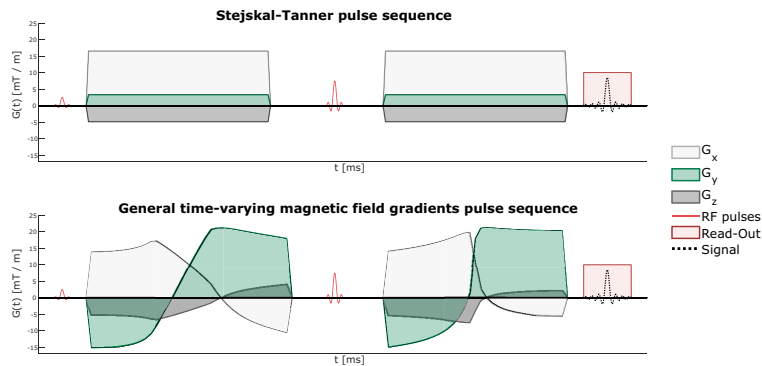


Figure 1 dMRI pulse sequences and sensitivity to intra-voxel features. **(A)** dMRI images achieve millimetre-scale spatial resolution while probing structures at the microscopic level, meaning that intra-voxel microstructural features are available. The analysis method employed here pictures the intra-voxel environment as being composed of several non-exchanging pores, each modelled with a diffusion tensor. **(B)** dMRI pulse sequences. *Top row:* conventional Stejskal–Tanner pulse sequence employing trapezoidal magnetic field gradients before and after the refocussing radiofrequency (RF) pulse to achieve diffusion sensitization. *Bottom row:* a pulse sequence utilizing time-varying magnetic field gradients for diffusion encoding. In both experiments, the relative intensities of the x, y and z components of the gradients determine the gradient direction at a given time.

Recent studies investigated the sensitivity of QTI-accessible metrics, like μFA and C_{MD} , on various cerebral diseases such as schizophrenia,²⁴ brain tumours,²⁹ epilepsy,³⁰ multiple sclerosis³¹ and Parkinson's disease.³² All these studies showed the potential for these metrics to characterize the disease more specifically, when compared to quantities obtainable with conventional dMRI methods such as DTI.

Aim

The aim of this study was to compare the brain white matter of patients previously hospitalized for COVID-19 and with subsequent persisting symptoms after the infection, with a matched healthy control group, using advanced dMRI. We hypothesized that the symptomatology reported by the patients at 7-month follow-up would be reflected by altered water diffusion patterns, due to microstructural changes in the brain tissue.

Most previous dMRI studies on brain-related effects of COVID-19 employed conventional dMRI quantities and methods (apparent diffusion coefficient³³ and DTI^{9,34,35}). In this work, the dMRI data were instead acquired using general time-varying magnetic field gradients and analysed using QTI. A second aim was therefore to assess the sensitivity of the diffusion metrics accessible via QTI to possible microstructural alterations and to determine whether the newly available quantities add relevant information when compared to DTI-derived metrics.

Materials and methods

Participants

Sixteen patients from the Linköping COVID-19 Study cohort^{7,36} previously hospitalized with a laboratory-confirmed (polymerase chain reaction) COVID-19 diagnosis during the

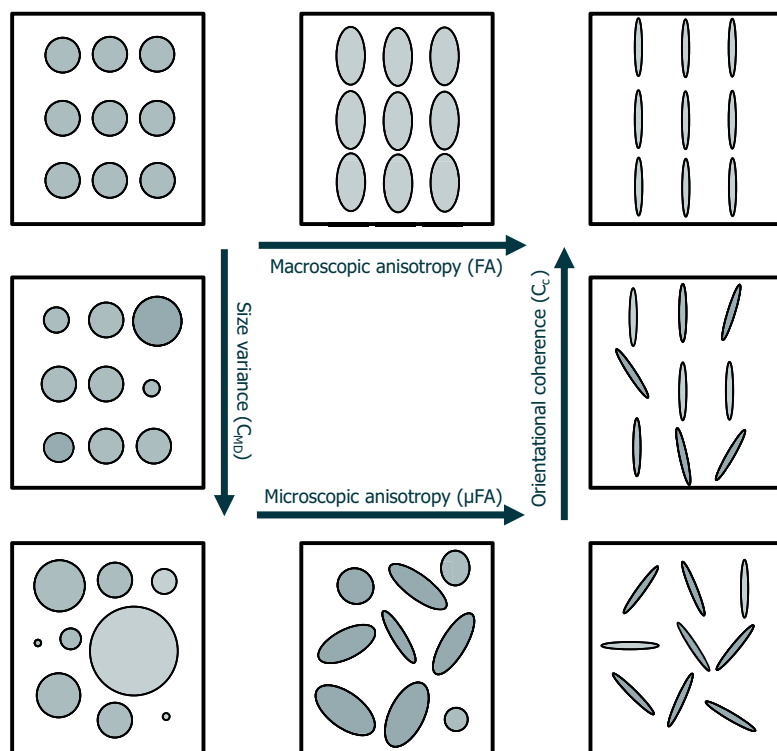
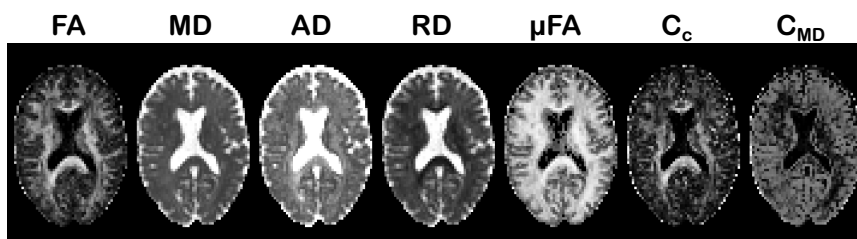
A Q-space trajectory Imaging (QTI) - indices**B Example maps of QTI-derived indices**

Figure 2 QTI indices. (A) Indices of tissue microstructure features retrieved with QTI. The arrows indicate the direction of increasing value for each metric [macroscopic anisotropy, quantified by FA, μ FA, size variance (C_{MD}) and orientational coherence (C_c)]. All metrics are bounded between 0 and 1. (B) Example maps of QTI-derived indices for one of the healthy volunteers included in the study.

first wave of the pandemic in the spring of 2020, and with persisting symptoms at the clinical evaluation during follow-up, were included for an extended MR examination. Premorbid level of function was assessed, and individuals with severe frailty and severe pre-existing comorbidities

were not included.⁷ Mean patient age was 60 years (41–79 years), and all were men. Eleven of these patients had been in ventilator care for a mean of 15 days (7–41 days). The MR scan was performed after outpatient follow-up on average 230 days after the admission to the hospital (204–256

Table 1 Description of participants

Participants	Patients	Healthy controls
Gender M/F	16/0	11/5
Age	60 (41–79 years)	58 (46–69 years)
Ventilator care	11	N/A
Time in ventilator	15 (7–41 days)	N/A
Time to follow-up	230 (204–256 days)	N/A
Fazekas 0	4	6
Fazekas 1	8	10
Fazekas 2	4	

Time is given in mean with range. Time to follow-up is from hospital admission. N/A, not applicable.

days). This is a subgroup of the cohort reported in Hellgren *et al.*⁷ An age-matched control group of 16 healthy individuals with no neurological disease, no symptoms of post-COVID condition and not previously hospitalized for COVID-19 was recruited [mean age 58 years (46–69 years), 11 men and 5 women]. The control group did not undergo infection status assessment (see Table 1 for details on demographics). Data were collected with ethical approval from the Swedish ethical review authority Dnr 2020-03029, 2015/13-31, and informed written consent was obtained from all participants.

Neuroimaging data acquisition

The 32 subjects were scanned with a 48-channel head coil on a clinical GE Signa Architect 3T MR scanner at Linköping University Hospital, using the clinical protocol described in Hellgren *et al.*,⁷ with the addition of the advanced diffusion sequence. Briefly, the clinical protocol included axial T₂-fluid-attenuated inversion recovery, axial T₂-fast spin echo (T₂-FSE), T₁-FSE, 3D T₁-gradient echo, axial diffusion weighted imaging and axial susceptibility-weighted imaging.

The diffusion MR images were collected using a QTI protocol comprising 122 measurements of which 6, 6, 16 and 30 LTE measurements at $b = 100, 700, 1400$ and 2000 s/mm^2 ; 6, 10 and 15 PTE measurements at $b = 100, 1000$ and 2000 s/mm^2 ; 6, 6, 10 and 10 STE measurements at $b = 100, 700, 1400$ and 2000 s/mm^2 ; and 1 measurement without diffusion weighting. The imaging parameters were echo time = 122 ms, repetition time = 3289 ms, field of view $240 \times 240 \times 156 \text{ mm}^3$, matrix size = $80 \times 80 \times 39$ and voxel size = $3 \times 3 \times 4 \text{ mm}^3$. Total QTI scan time was 6 and 45 s.

Data analyses

Subject-level preprocessing

After converting the collected DICOM images to NIFTI using 'dcm2nii',³⁷ the data were preprocessed for head motion and eddy current correction using the 'eddy' tool from 'FSL',³⁸ interfaced via 'Mrtrix3'.³⁹ Susceptibility distortion correction was not applied, since the diffusion data were only collected with a single phase-encoding direction. The QTI maps were then obtained using the QTI \pm framework,⁴⁰

which achieves robust estimates throughout the brain by enforcing a set of mathematical constraints.^{40,41}

Group comparisons

To detect possible group differences in terms of the microstructure metrics obtainable with QTI, the FA, μFA , C_c , mean diffusivity (MD), axial diffusivity (AD), radial diffusivity (RD) and C_{MD} maps were analysed using the tract-based spatial statistics (TBSS)⁴² framework. Briefly, the FA maps of all subjects were non-linearly co-registered using the FMRIB58_FA template image as target and subsequently affine aligned to the MNI152 space. The FA maps were then averaged, and the average FA map was used to derive a skeleton of voxels which should represent the white matter tracts common to all subjects. A threshold of 0.2 (selected according to the TBSS user recommendations and after visual inspection) was used to refine the mean FA skeleton. Each subject's FA map was then projected onto the skeleton prior to performing the statistical analysis. One-sided two-sample unpaired *t*-tests were employed to detect FA differences between the two groups, testing both directions ($\text{FA}^{\text{controls}} > \text{FA}^{\text{patients}}$ and $\text{FA}^{\text{controls}} < \text{FA}^{\text{patients}}$). This was performed using the 'randomise' function in FSL,⁴³ as recommended by the TBSS user guide. Five thousand permutations were used to build the null hypothesis, and the threshold-free cluster enhancement option was used as it often results in a higher statistical power compared to cluster extent thresholding.⁴⁴ Age and sex were included as covariates, to make sure that any group difference is not due to age or sex. The same procedure was then repeated for the other QTI-derived maps using the registration matrices and projection vectors obtained from the FA analysis to co-register the images and populate the skeleton, respectively.

Results

As reported in Hellgren *et al.*,⁷ the findings of the conventional images in the patient cohort were unspecific with white matter lesions and some abnormalities on susceptibility-weighted images. There were no clinically significant findings of the conventional images of the control group, only unspecific white matter lesions. The Fazekas scores are presented in Table 1.

TBSS results

The TBSS analysis showed widespread differences in all QTI-derived metrics in the white matter of the patients compared to the controls. Figure 3 shows exemplary results from the statistical analysis performed within the TBSS framework in different slices for a statistical significance level of $P < 0.05$, corrected for multiple comparisons using family-wise error rate (FWE). Figure 4 shows the TBSS results in different anatomical regions for $P < 0.05$, FWE-corrected for multiple comparisons. In these figures, the colour map is chosen to highlight results for $P < 0.0036$, where a Bonferroni

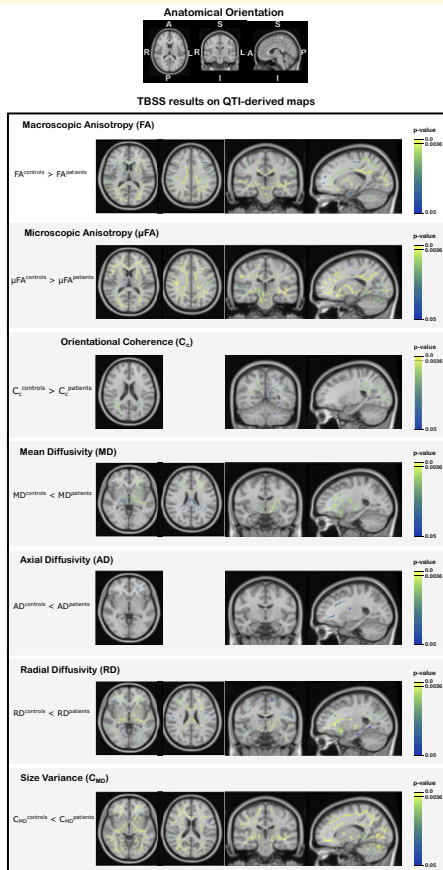


Figure 3 TBSS results on QTI-derived maps. TBSS results for the QTI-derived maps. Each row shows the results of the comparison between the mean value of each map for the two groups, with symbols '>' and '<' indicating the direction of the test. The voxels coloured in the blue–yellow colour scale depict the locations on the skeleton where statistically significant differences emerged ($P < 0.05$, FWE corrected). The $P < 0.0036$ represents the statistical threshold for significance when correcting the familywise error for multiple contrasts.

correction for testing over multiple contrasts (seven microstructure metrics tested for the mean of each group being either greater or lower than the other group's mean, leading to $P = 0.05/14 = 0.0036$) is applied.⁴⁵ The results of the TBSS analysis can also be explored in NeuroVault (<https://identifiers.org/neurovault.collection:13799>) where we share all the statistical maps.

In general, the two measures of diffusion anisotropy, FA and μ FA, were found to be lower in the patients' white

matter, while the MD and the variance in compartment size C_{MD} were found to be higher in the patient group. When looking at the axial and radial diffusivities (AD and RD), RD had higher values in the whole brain in the patient group, whereas differences in AD, with higher values for patients, were limited to the white matter of the left frontal lobe. The parameter describing the structural orientational coherence within the voxel, C_c , was found to be lower for the patient group.

Quantification of the inter-group difference for each QTI-derived metric over the skeleton voxels exhibiting statistical significance is presented in Fig. 5. The histograms show the distributions of differences between the metric's mean (indicated with \bar{x}) for the two groups. A positive value indicates that the mean for the healthy controls is higher compared to the patients, and vice versa. The results in percentage units show that all the metrics present quite pronounced differences (median values 8.5, 5.2, 11.7, -9.2, -7.3, -11.9 and -15.3%, for FA, μ FA, C_c , MD, AD, RD and C_{MD} , respectively). Figure 6 shows where these differences are localized in the brain. FA, μ FA, C_{MD} and RD presented the most widespread differences between the two groups, showing statistically significant differences ($P < 0.05$, FWE corrected) in, respectively, 44, 56, 47 and 36% of the analysed white matter voxels. MD, AD and C_c presented differences in, respectively, 17, 1 and 12% of the skeleton voxels. Changes in MD and AD were mostly localized in the frontal part of the brain, while differences in C_c were found occipitally.

Discussion

In this study, we found widespread changes in the white matter of the brain in patients previously hospitalized for COVID-19 with persisting symptoms at follow-up, compared to a matched healthy control group, as revealed by advanced dMRI. As seen in other neuroinflammatory and neurodegenerative conditions,^{46,47} patients show a decrease in anisotropy-related measurements and an increase in diffusivity-related metrics compared to the controls, indicating a general loss of tissue integrity at the microstructural level as well as diffuse oedema. As shown in the histograms in Fig. 5, the amount by which the metrics differ between the two groups can be quite pronounced. Displaying these differences in multiple axial slices highlights how some metrics (FA, μ FA, RD and C_{MD}) are widely affected, while others (MD, AD and C_c) exhibit more localized changes in the frontal and parietal lobes.

Focusing on voxel-level metrics (FA, MD, RD, AD), these changes were seemingly due to an increase in RD, while the AD was essentially unaltered. Other publications³³⁻³⁵ where dMRI was also employed to study COVID-19-induced alterations in the brain report similar trends. Though not specific to any biological tissue feature, these metrics have been correlated with different neuronal damaging processes. Increased values of RD were found to be related to

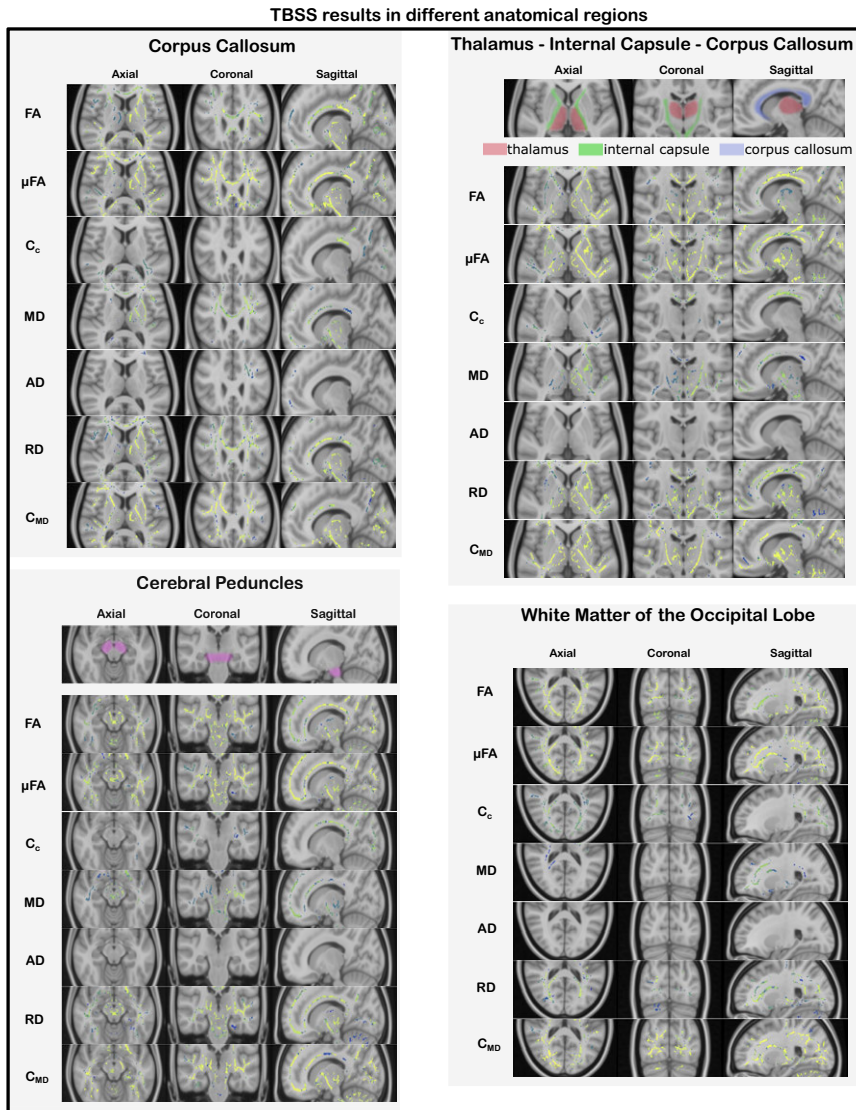
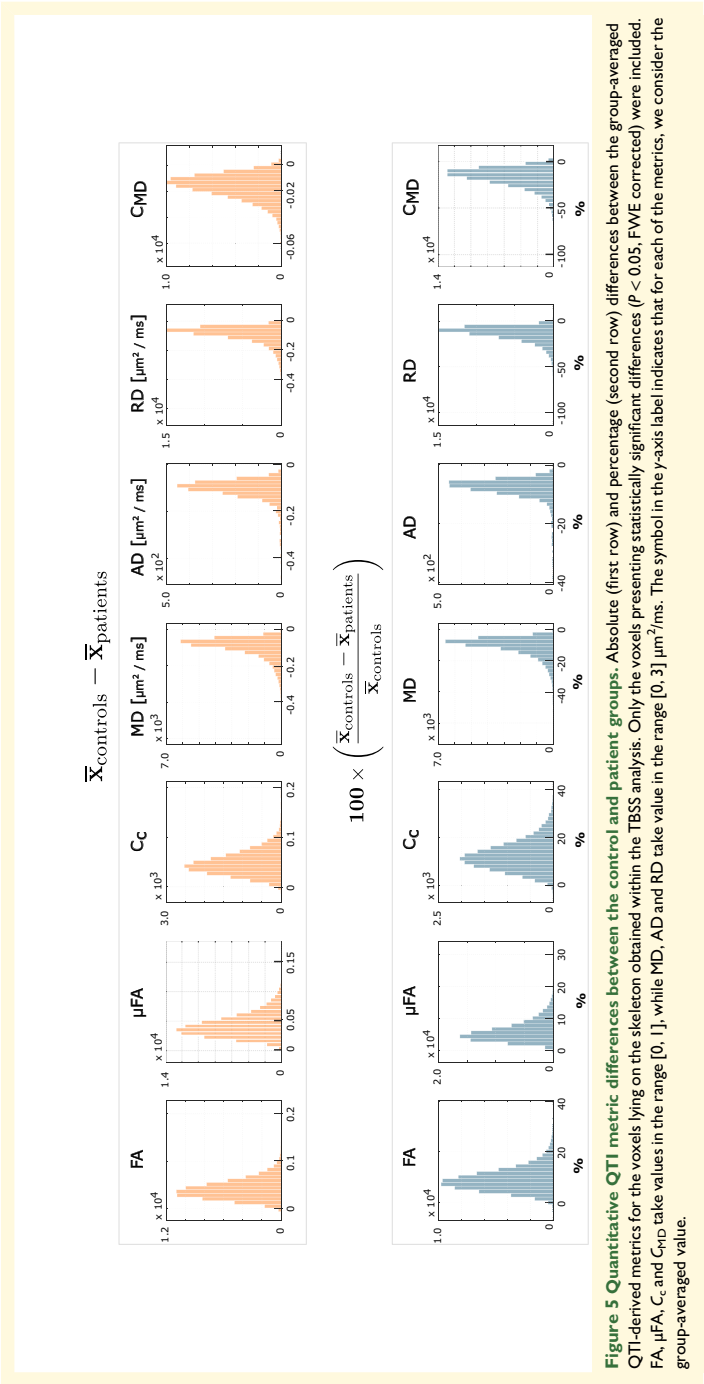


Figure 4 TBSS results in different anatomical areas. TBSS results for all the considered QTI-derived metrics in different brain regions and anatomical structures for the tests which resulted in statistically significant differences ($P < 0.05$, FWE corrected) between the two groups ($FA^{\text{controls}} > FA^{\text{patients}}$, $\mu FA^{\text{controls}} > \mu FA^{\text{patients}}$, $C_c^{\text{controls}} > C_c^{\text{patients}}$, $MD^{\text{controls}} < MD^{\text{patients}}$, $AD^{\text{controls}} < AD^{\text{patients}}$, $RD^{\text{controls}} < RD^{\text{patients}}$ and $C_{MD}^{\text{controls}} < C_{MD}^{\text{patients}}$). Changes were widespread, affecting all lobes of the brain.

demyelination, while alterations of AD were representative of axonal damage.⁴⁸ Our results would then suggest an underlying process of myelin damage, which is reasonable given that demyelination is an unspecific reaction when

damage occurs to the white matter. Demyelination can be a product of inflammatory or infectious processes in the CNS and has been reported in association with COVID-19.^{49,50}



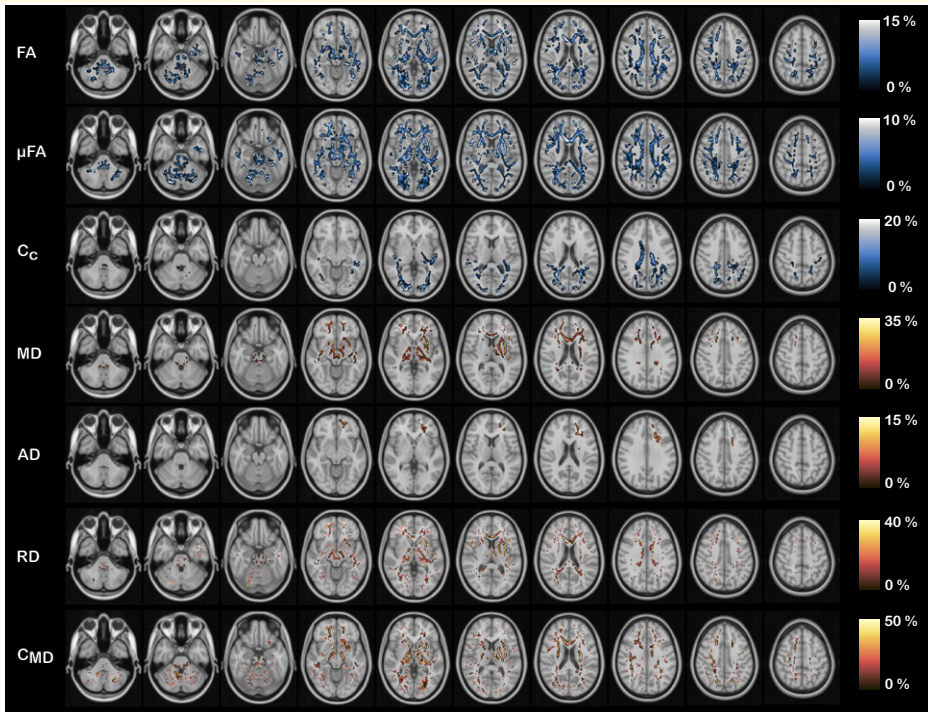


Figure 6 Visualization of the QTI metric differences in percentage across the brain. Visualization of the QTI metric differences in percentage between patients and controls across the brain. FA, μ FA, RD and C_{MD} present widespread differences. Changes in MD and AD are localized in the frontal part of the brain, while changes in C_c are localized in the dorsal part of the brain. The cold black-blue-white colours indicate a reduction in the metric, while the warm black-red-yellow colours indicate an increase in the metric. Only the voxels presenting statistically significant differences ($P < 0.05$, FWE corrected) were included.

Rau *et al.* employed the diffusion microstructure imaging methods for a three-compartment biophysical model [similar in spirit to the neurite orientation dispersion and density imaging (NODDI)⁵¹ model] for interpreting the dMRI data of COVID-19 patients with neurological symptoms.⁵² In their work, a volume fraction shift from the intra- and extra-axonal spaces to the free water compartment was reported and interpreted as being representative of vasogenic oedema. The reduction in FA and increase in MD and RD (as well as increase in C_{MD} , discussed later) found in our study could also fit with this explanation. However, it is important to stress that conventional dMRI data (as the one used in Rau *et al.*⁵²) has been shown to not contain enough information to allow for reliable estimation of such biophysical model parameters^{53,54}; thus, care should be taken when interpreting the results. Moreover, due to the unspecific nature of metrics such as FA and MD with respect to biological features, drawing conclusions on the exact physiological mechanisms underpinning these changes is problematic.

The major advantage deriving from combining the advanced diffusion acquisition sequence and analysis employed in this study is that it allows estimation of intra-voxel microstructural features, thus complementing the voxel-level information obtainable with standard dMRI protocols and methods. This is particularly relevant when competing intra-voxel effects lead to opposite directional changes in voxel-level metrics,⁵⁴⁻⁵⁶ thus limiting their sensitivity and interpretability. Conversely, separating each effect's contribution has already been shown to boost specificity when characterizing different brain diseases, such as brain tumours²⁹ and multiple sclerosis.³¹

Similarly to what was reported in those studies, the results obtained here suggest μ FA as a more sensitive (and specific) metric for detecting microstructural changes compared to FA. Conversely to FA, μ FA is a measure of diffusion anisotropy unconfounded by orientation dispersion, this latter being quantified by C_c . Therefore, having access to these two metrics (μ FA and C_c) not only allows for increased specificity to the exact mechanism underpinning changes in

diffusion patterns but may also highlight alterations in the microstructure which would not appear when FA alone is considered. Looking at the results in Figs 3–5, one can postulate that, given the predominant alterations in μ FA compared to C_c , the observed change in diffusion anisotropy is mostly due to loss of local anisotropy rather than white matter fibre coherence disruption. Since μ FA has been proposed as a measure reflecting axons rather than myelin,^{57,58} this suggests widespread axonal damage resulting from the severe COVID-19 infection. Therefore, considering the observed results on voxel and intra-voxel metrics, alterations in the microstructure seems to be due to damage to both myelin and axons. We stress that this argument would not have been possible if only the voxel-level metrics, as accessible with conventional DTI, were available.

In regions where C_c was found to be significantly different between the two groups, as for example in the parieto-occipital lobes and the dorsal parts of corpus callosum, changes to the microstructure could also be subject to additional interpretations including disruptions in tissue integrity in the form of loss of fibre coherence. In the neuropsychological evaluation,⁷ patients with white matter lesions in the brain MRI had a lower visuospatial index compared to those with normal MRI findings. The parietal lobes are important in the integration of sensory input, and the localized finding of changes in orientational coherence (C_c) in the dorsal part of the brain could be related to affected visuospatial performance.

The variance in compartments' size (C_{MD}) was among the metrics showing widespread change between the control and patient groups. C_{MD} has previously been connected to cell density,²⁹ where higher C_{MD} values stood for low cell density, and vice versa. Thus, the increase in C_{MD} observed in this cohort may be indicative of white matter damage in the form of cellular membrane disruption, cell swelling, cellular atrophy and necrosis.

Age-related effects on the considered QTI-derived metrics were also investigated. Consistent with other studies,^{32,56} we observed a decrease in FA and μ FA and an increase in MD with increasing age. C_c was also found to decrease with age while C_{MD} seems to not be affected by aging.

The Fazekas scores (see Table 1) are slightly higher in the patient group, but no study participant had a Grade 3, meaning that the white matter changes are generally minimal to moderate. The white matter hyperintensities reflect damaged white matter, which is in line with the findings of the diffusion analysis. Studies have shown that white matter lesions are common in the acute/subacute phase of the disease but also persist at follow-up after COVID-19.^{5,6,10} The white matter thus seems to be affected on the micro- as well as on the macrolevel.

Limitations

Several possible limitations need mentioning with respect to the adopted methodology for the data analysis. First, the accuracy and precision of the microstructural metrics as obtained via QTI were recently investigated.⁵⁹ It was found that when such metrics are retrieved via QTI, they tend to

be inaccurate in voxels presenting large variations in compartment size and/or high degree of orientation dispersion. While this should not severely affect the analysis of healthy white matter, care should be taken when considering, for example, oedematous fibrous tissue. Moreover, it was also recently reported that QTI metrics could be severely biased in noisy^{41,59} and under-sampled⁴¹ data. This issue was however recently addressed,^{40,41} and the estimation framework employed in this work should produce robust estimates with respect to these two issues.

Second, the adopted method assumes no diffusion time dependence; thus, contributions of restriction and exchange on the diffusion signal are not captured.⁶⁰ Recent studies^{61–63} have shown that such contributions, while subtle, may not be negligible in the human brain; thus, the metrics considered here may be biased by neglecting them. Therefore, in future studies, methods including restriction effects and time dependence^{64–66} and exchange⁶⁷ should be considered. Note that similar limitations apply to other studies employing DTI and NODDI.

Third, while TBSS is currently the most adopted method for comparing groups based on white matter diffusion metrics, concerns regarding the reliability of the different steps included in the framework have been raised.^{68,69} In particular, the results may depend on the selected target for the registration of all subjects to a common template, the performance of the registration algorithm and on the user's choices for different settings.⁶⁸ In this study, we adhered to the default and recommended settings as stated in the TBSS documentation (<https://fsl.fmrib.ox.ac.uk/fsl/fslwiki/TBSS/UserGuide>) since this should provide ground for comparison with other studies.⁶⁸ Moreover, while the results shown here were obtained by using the FMRIB58_FA template as target for the registration, we also repeated the analysis using one of the healthy controls' FA as template to check for results' dependency on this step. Indeed, the results do not match perfectly, since the derived skeletons differ. However, they showed the same trends with respect to direction of change for the different QTI-derived metrics and their localization in the brain. Nevertheless, for this and other studies employing the TBSS framework, we advocate for caution when interpreting the results for specific tracts or anatomical structures.

Additional limiting factors for the interpretation of the results obtained in this study arise from the rather small cohort and the cross-sectional design which omits the longitudinal perspective on the development of brain-associated changes after COVID-19. The infectious status of the control group was not investigated, which might be considered a limitation. However, the inclusion criterion for the patient group was a previous hospitalization for COVID-19 with persisting symptoms at follow-up. Hence, the controls were recruited and included regardless of their previous infectious state if they were in good health with no symptoms of a post-COVID condition nor a previous hospitalization due to COVID-19. The differences found between the two groups might therefore be contributed to the course of the disease, where the hospitalization for COVID with persisting

10. Huang S, Zhou Z, Yang D, *et al.* Persistent white matter changes in recovered COVID-19 patients at the 1-year follow-up. *Brain*. 2022; 145(5):1830-1838.
11. Du Y, Zhao W, Huang S, *et al.* Two-year follow-up of brain structural changes in patients who recovered from COVID-19: A prospective study. *Psychiatry Res*. 2023;319:114969.
12. Stejskal EO, Tanner JE. Spin diffusion measurements: Spin echoes in the presence of a time-dependent field gradient. *J Chem Phys*. 1965; 42(1):288-292.
13. Liu C, Özarslan E. Multimodal integration of diffusion MRI for better characterization of tissue biology. *NMR Biomed*. 2019;32(4).
14. Novikov DS, Kiselev VG, Jespersen SN. On modeling. *Magn Reson Med*. 2018;79(6):3172-3193.
15. Jelescu IO, Budde MD. Design and validation of diffusion MRI models of white matter. *Front Phys*. 2017;5:61.
16. Le Bihan D, Lima M. Diffusion magnetic resonance imaging: What water tells us about biological tissues. *PLoS Biol*. 2015;13(7): e1002203.
17. Basser PJ, Mattiello J, LeBihan D. MR diffusion tensor spectroscopy and imaging. *Biophys J*. 1994;66(1):259-267.
18. Cory DG, Garroway AN, Miller JB. Applications of spin transport as a probe of local geometry. *Polym Prepr*. 1990;31:149-150.
19. Mitra PP. Multiple wave-vector extensions of the NMR pulsed-field-gradient spin-echo diffusion measurement. *Phys Rev B*. 1995;51(21):15074-15078.
20. Mori S, Van Zijl PCM. Diffusion weighting by the trace of the diffusion tensor within a single scan. *Magn Reson Med*. 1995;33(1):41-52.
21. Eriksson S, Lasic S, Topgaard D. Isotropic diffusion weighting in PGSE NMR by magic-angle spinning of the q-vector. *J Magn Reson*. 2013;226:13-18.
22. Wong EC, Cox RW, Song AW. Optimized isotropic diffusion weighting. *Magn Reson Med*. 1995;34(2):139-143.
23. Özarslan E, Shemesh N, Basser PJ. A general framework to quantify the effect of restricted diffusion on the NMR signal with applications to double pulsed field gradient NMR experiments. *J Chem Phys*. 2009;130(10):104702.
24. Westin CF, Knutsson H, Pasternak O, *et al.* Q-space trajectory imaging for multidimensional diffusion MRI of the human brain. *NeuroImage*. 2016;135:345-362.
25. Westin CF, Szczepankiewicz F, Pasternak O, *et al.* Measurement tensors in diffusion MRI: Generalizing the concept of diffusion encoding. In: Golland P, Hata N, Barillot C, Hornegger J and Howe R, eds. *Medical image computing and computer-assisted intervention — MICCAI 2014*. Springer; 2014:209-216.
26. Caprihan A, Wang LZ, Fukushima E. A multiple-narrow-pulse approximation for restricted diffusion in a time-varying field gradient. *J Magn Reson A*. 1996;118(1):94-102.
27. Jian B, Vemuri BC, Özarslan E, Carney PR, Mareci TH. A novel tensor distribution model for the diffusion-weighted MR signal. *NeuroImage*. 2007;37(1):164-176.
28. Basser PJ, Pierpaoli C. Microstructural and physiological features of tissues elucidated by quantitative-diffusion-tensor MRI. *J Magn Reson*. 2011;213(2):560-570.
29. Szczepankiewicz F, van Westen D, Englund E, *et al.* The link between diffusion MRI and tumor heterogeneity: Mapping cell eccentricity and density by diffusional variance decomposition (DIVIDE). *NeuroImage*. 2016;142:522-532.
30. Lampinen B, Zampeli A, Björkman-Burtscher IM, *et al.* Tensor-valued diffusion MRI differentiates cortex and white matter in malformations of cortical development associated with epilepsy. *Epilepsia*. 2020;61(8):1701-1713.
31. Andersen KW, Lasić S, Lundell H, *et al.* Disentangling white-matter damage from physiological fibre orientation dispersion in multiple sclerosis. *Brain Commun*. 2020;2(2):fcaa077.
32. Kamiya K, Kamagata K, Ogaki K, *et al.* Brain white-matter degeneration due to aging and Parkinson disease as revealed by double diffusion encoding. *Front Neurosci*. 2020;14:584510.
33. Caroli A, Capelli S, Napolitano A, *et al.* Brain diffusion alterations in patients with COVID-19 pathology and neurological manifestations. *NeuroImage Clin*. 2023;37:103338.
34. Qin Y, Wu J, Chen T, *et al.* Long-term microstructure and cerebral blood flow changes in patients recovered from COVID-19 without neurological manifestations. *J Clin Invest*. 2021;131(8):e147329.
35. Paolini M, Palladini M, Mazza MG, *et al.* Brain correlates of subjective cognitive complaints in COVID-19 survivors: A multimodal magnetic resonance imaging study. *Eur Neuropsychopharmacol*. 2023;68:1-10.
36. Divanoglou A, Samuelsson K, Sjö Dahl ER, Andersson C, Levi R. Rehabilitation needs and mortality associated with the Covid-19 pandemic: A population-based study of all hospitalised and home-healthcare individuals in a Swedish healthcare region. *EclinicalMedicine*. 2021;36:100920.
37. Li X, Morgan PS, Ashburner J, Smith J, Rorden C. The first step for neuroimaging data analysis: DICOM to NIfTI conversion. *J Neurosci Methods*. 2016;264:47-56.
38. Andersson JLR, Sotiropoulos SN. An integrated approach to correction for off-resonance effects and subject movement in diffusion MR imaging. *NeuroImage*. 2016;125:1063-1078.
39. Tournier JD, Smith R, Raffelt D, *et al.* MRtrix3: A fast, flexible and open software framework for medical image processing and visualisation. *NeuroImage*. 2019;202:116137.
40. Boito D, Herberthson M, Dela Haije T, Blystad I, Özarslan E. Diffusivity-limited q-space trajectory imaging. *Magn Reson Lett*. 2023;3:187-196.
41. Herberthson M, Boito D, Haije TD, Fergen A, Westin CF, Özarslan E. Q-space trajectory imaging with positivity constraints (QTI+). *NeuroImage*. 2021;238:118198.
42. Smith SM, Jenkinson M, Johansen-Berg H, *et al.* Tract-based spatial statistics: Voxelwise analysis of multi-subject diffusion data. *NeuroImage*. 2006;31(4):1487-1505.
43. Winkler AM, Ridgway GR, Webster MA, Smith SM, Nichols TE. Permutation inference for the general linear model. *NeuroImage*. 2014;92:381-397.
44. Smith S, Nichols T. Threshold-free cluster enhancement: Addressing problems of smoothing, threshold dependence and localisation in cluster inference. *NeuroImage*. 2009;44(1):83-98.
45. Alberton BAV, Nichols TE, Gamba HR, Winkler AM. Multiple testing correction over contrasts for brain imaging. *NeuroImage*. 2020;216:116760.
46. Bao J, Tu H, Li Y, *et al.* Diffusion tensor imaging revealed microstructural changes in normal-appearing white matter regions in relapsing-remitting multiple sclerosis. *Front Neurosci*. 2022;16:837452.
47. Rektor I, Svátková A, Vojtěšek L, *et al.* White matter alterations in Parkinson's disease with normal cognition precede grey matter atrophy. *PLoS One*. 2018;13(1):e0187939.
48. Winkiewicz PJ, Sabisz A, Naumczyk P, Jodzio K, Szurawska E, Szarmach A. Understanding the physiopathology behind axial and radial diffusivity changes—What do we know? *Front Neurol*. 2018;9:92.
49. Ismail II, Salama S. Association of CNS demyelination and COVID-19 infection: An updated systematic review. *J Neurol*. 2022;269(2):541-576.
50. Shabani Z. Demyelination as a result of an immune response in patients with COVID-19. *Acta Neurol Belg*. 2021;121(4):859-866.
51. Zhang H, Schneider T, Wheeler-Kingshott CA, Alexander DC. NODDI: Practical in vivo neurite orientation dispersion and density imaging of the human brain. *NeuroImage*. 2012;61(4):1000-1016.
52. Rau A, Schroeter N, Blazhenets G, *et al.* Widespread white matter oedema in subacute COVID-19 patients with neurological symptoms. *Brain*. 2022;145(9):3203-3213.
53. Jelescu IO, Veraart J, Fieremans E, Novikov DS. Degeneracy in model parameter estimation for multi-compartmental diffusion in neuronal tissue: Degeneracy in model parameter estimation of diffusion in neural tissue. *NMR Biomed*. 2016;29(1):33-47.

54. Lampinen B, Szczepankiewicz F, Mårtensson J, van Westen D, Sundgren PC, Nilsson M. Neurite density imaging versus imaging of microscopic anisotropy in diffusion MRI: A model comparison using spherical tensor encoding. *NeuroImage*. 2017;147:517-531.
55. Douaud G, Jbabdi S, Behrens TEJ, et al. DTI measures in crossing-fibre areas: Increased diffusion anisotropy reveals early white matter alteration in MCI and mild Alzheimer's disease. *NeuroImage*. 2011; 55(3):880-890.
56. Lawrenz M, Brassen S, Finsterbusch J. Microscopic diffusion anisotropy in the human brain: Age-related changes. *NeuroImage*. 2016;141:313-325.
57. Beaulieu C. The basis of anisotropic water diffusion in the nervous system—A technical review. *NMR Biomed*. 2002;15(7-8):435-455.
58. Lampinen B, Szczepankiewicz F, Novén M, et al. Searching for the neurite density with diffusion MRI: Challenges for biophysical modeling. *Hum Brain Mapp*. 2019;40(8):2529-2545.
59. Reyembaut A, Mezzani P, de Almeida Martins JP, Topgaard D. Accuracy and precision of statistical descriptors obtained from multidimensional diffusion signal inversion algorithms. *NMR Biomed*. 2020;33(12).
60. Özarslan E, Westin CF, Mareci TH. Characterizing magnetic resonance signal decay due to Gaussian diffusion: The path integral approach and a convenient computational method: characterizing MR signal decay due to Gaussian diffusion. *Concepts Magn Reson Part A*. 2015;44(4):203-213.
61. Fieremans E, Burcaw LM, Lee HH, Lemberskiy G, Veraart J, Novikov DS. In vivo observation and biophysical interpretation of time-dependent diffusion in human white matter. *NeuroImage*. 2016;129:414-427.
62. Lee HH, Papaioannou A, Kim SL, Novikov DS, Fieremans E. A time-dependent diffusion MRI signature of axon caliber variations and beading. *Commun Biol*. 2020;3(1):354.
63. Novello L, Henriques RN, Ianuş A, Feiweier T, Shemesh N, Jovicich J. In vivo correlation tensor MRI reveals microscopic kurtosis in the human brain on a clinical 3T scanner. *NeuroImage*. 2022;254:119137.
64. Boito D, Yolcu C, Özarslan E. Multidimensional diffusion MRI methods with confined subdomains. *Front Phys*. 2022;10:830274.
65. Yolcu C, Memiç M, Şimşek K, Westin CF, Özarslan E. NMR signal for particles diffusing under potentials: From path integrals and numerical methods to a model of diffusion anisotropy. *Phys Rev E*. 2016;93(5):052602.
66. Henriques RN, Jespersen SN, Shemesh N. Correlation tensor magnetic resonance imaging. *NeuroImage*. 2020;211:116605.
67. Stanisz GJ, Wright GA, Henkelman RM, Szafer A. An analytical model of restricted diffusion in bovine optic nerve. *Magn Reson Med*. 1997;37(1):103-111.
68. Bach M, Laun FB, Leemans A, et al. Methodological considerations on tract-based spatial statistics (TBSS). *NeuroImage*. 2014;100:358-369.
69. Keihaninejad S, Ryan NS, Malone IB, et al. The importance of group-wise registration in tract based spatial statistics study of neurodegeneration: A simulation study in Alzheimer's disease. *PLoS One*. 2012;7(11):e45996.
70. Lee MH, Perl DP, Nair G, et al. Microvascular injury in the brains of patients with Covid-19. *N Engl J Med*. 2021;384(5):481-483.
71. da Graça Morais Martin M, Paes VR, Cardoso EF, et al. Postmortem brain 7T MRI with minimally invasive pathological correlation in deceased COVID-19 subjects. *Insights Imaging*. 2022;13(1):7.

Multidimensional diffusion MRI methods with confined subdomains

Deneb Boito
Cem Yolcu
Evren Özarslan

Frontiers in Physics, 2022, 10, 830274.

© 2022
Published by Frontiers Media S.A.
Reprinted with permission (CC BY 4.0)



Multidimensional Diffusion MRI Methods With Confined Subdomains

Deneb Boito^{1,2}, Cem Yolcu¹ and Evren Özarslan^{1,2*}

¹Department of Biomedical Engineering, Linköping University, Linköping, Sweden, ²Center for Medical Image Science and Visualization, Linköping University, Linköping, Sweden

OPEN ACCESS

Edited by:

Mustapha Bouhrara,
National Institute on Aging (NIH),
United States

Reviewed by:

Daniel Topgaard,
Lund University, Sweden
Silvia Capuani,
National Research Council (CNR), Italy

*Correspondence:

Evren Özarslan
evren.ozarslan@liu.se

Specialty section:

This article was submitted to
Medical Physics and Imaging,
a section of the journal
Frontiers in Physics

Received: 06 December 2021

Accepted: 31 January 2022

Published: 23 March 2022

Citation:

Boito D, Yolcu C and Özarslan E (2022)
Multidimensional Diffusion MRI
Methods With Confined Subdomains.
Front. Phys. 10:830274.
doi: 10.3389/fphy.2022.830274

Diffusion Magnetic Resonance Imaging (dMRI) is an imaging technique with exquisite sensitivity to the microstructural properties of heterogeneous media. The conventionally adopted acquisition schemes involving single pulsed field gradients encode the random motion of water molecules into the NMR signal, however typically conflating the effects of different sources contributing to the water motion. Time-varying magnetic field gradients have recently been considered for disentangling such effects during the data encoding phase, opening to the possibility of adding specificity to the recovered information about the medium's microstructure. Such data is typically represented via a diffusion tensor distribution (DTD) model, thus assuming the existence of several non-exchanging compartments in each of which diffusion is unrestricted. In this work, we consider a model that takes confinement into account and possesses a diffusion time-dependence closer to that of restricted diffusion, to replace the free diffusion assumption in multidimensional diffusion MRI methods. We first demonstrate how the confinement tensor model captures the relevant signal modulations impressed by water diffusing in both free and closed spaces, for data simulated with a clinically feasible protocol involving time-varying magnetic field gradients. Then, we provide the basis for incorporating this model into two multidimensional dMRI methods, and attempt to recover a confinement tensor distribution (CTD) on a human brain dataset.

Keywords: confinement, anisotropy, microstructure, restricted, tensor, distribution

1 INTRODUCTION

Diffusion Magnetic Resonance Imaging (dMRI) is a method used for investigating the microstructural organization of various heterogeneous media. This is achieved by sensitizing the MR signal to the random motion of water molecules inside the scanned substrate. To interpret and extract relevant information from the water motion, several models and signal representations have been developed.

At spatial resolutions achievable with current MR scanners, the scanned sample comprises several compartments within, outside, and possibly in between which diffusion is taking place. A general strategy for capturing this complexity without assuming any specific combination of compartments (see for example [1, 2] for reviews of multi-compartment models for brain white matter), considers modeling the medium as a collection of isolated pores, each represented by a diffusion tensor [3, 4]. This approach leads to a diffusion tensor distribution (DTD), which could also be represented parametrically via normal [5] and Wishart [4] distributions as well as other related distributions [6–8]. Advances in diffusion encoding schemes [9–13] provided ways of disentangling confounding signal contributions, thus possibly enabling the extraction of relevant information about the

medium's structure and composition via such modeling [14]. However, it is rather paradoxical to have free diffusion within isolated compartments, as the cellular membranes have a strong effect on diffusion, making them the primary determinant of diffusion anisotropy [15]. If this picture involving multiple isolated compartments is to be employed, it would be natural to represent the individual subdomains by accounting for confined diffusion within them [16].

A viable alternative to the diffusion tensor representation of individual subdomains utilizes confinement tensors [17] instead. In this case, the molecules are envisioned to be diffusing under the influence of an Hookean restoring force, i.e., according to the Ornstein-Uhlenbeck process [18]. Just like in restricted diffusion, the particle trajectories have limited extent, which has made the Ornstein-Uhlenbeck process a simple toy problem in earlier theoretical works on characterizing the influence of restricted diffusion on the NMR signal [19–21].

Following a series of developments [22, 23], the confinement tensor model has been noted to provide an alternative representation of diffusion anisotropy, very-well suited for studying heterogeneous media [17, 24, 25]. Furthermore, for NMR experiments involving long diffusion encoding pulses, the harmonic confinement becomes the effective model of restricted diffusion, giving rise to an approximately linear dependence of the effective stochastic force on the center-of-mass position of the particles during the application of the gradient pulses [26].

Similarly to the better-known diffusion tensor model, the model proposed by Yölcü et al. [17] captures the pore's geometry/anisotropy with a tensorial object, which can be visualized as an ellipsoid. However, the confinement tensor model offers an extra parameter to encode diffusivity. This parameter can either be a scalar bulk diffusivity, or another tensorial quantity. In either case, this represents the diffusivity when there is no impediment to the particles' motion, i.e., when the confinement value approaches 0. Therefore, the confinement tensor model can accommodate both restricted and unrestricted diffusion. In a recent study, the orientationally-averaged signal was studied for confined diffusion measured via single- and double diffusion encoding measurements demonstrating that certain features of the NMR signal [27, 28] that cannot be predicted by diffusion tensors are reproduced by the confinement tensor model [29].

These findings suggest the confinement tensor model as a plausible alternative for representing non-exchanging microscopic domains in multicompartment specimen models. In this work, we therefore propose to incorporate this model into the so-called multi-dimensional MRI methods [14]. In particular, we replace the diffusion with the confinement tensor in Diffusion Tensor Distribution Imaging (DTD) [4, 30], and illustrate that the moments of the DTD estimated using Q-space trajectory Imaging (QTI) [31] would have a different interpretation for confined diffusion. We start by assessing the capabilities of the confinement model in representing single pores on data simulated using a typical protocol involving general time-varying diffusion gradient fields [32], and then proceed with

first attempts at recovering distributions of confinement tensors in a human brain dataset.

2 BACKGROUND AND THEORY

2.1 Diffusion Under a Hookean Restoring Force

In a diffusion NMR experiment, diffusing molecules acquire a phase shift depending on their trajectory $\mathbf{x}(t)$ and on the time-varying magnetic field gradient $\mathbf{G}(t)$. The signal from all molecules can be expressed as

$$E = \left\langle e^{-i\gamma \int dt \mathbf{x}(t) \cdot \mathbf{G}(t)} \right\rangle, \quad (1)$$

where γ is the gyromagnetic ratio, and the averaging is performed over all particle trajectories.

For the case of diffusion under a Hookean restoring force, we shall denote by \mathbf{C} the confinement tensor, which, upon multiplication by the Boltzmann constant k_B and absolute temperature T , gives the tensorial force constant $\mathbf{f} = k_B T \mathbf{C}$ defining the Hookean potential V through $V(\mathbf{r}) = \frac{1}{2} \mathbf{r}^T \mathbf{f} \mathbf{r}$. Furthermore, we denote the possibly anisotropic free diffusion tensor by \mathbf{D} , and assume that \mathbf{D} and \mathbf{C} commute, i.e., they share the same eigendirections. Finally, we introduce $\mathbf{\Omega} = \mathbf{D}\mathbf{C}$ for brevity.

Statistical quantities, such as the signal, can be calculated using the path weight

$$\Pr[\mathbf{x}()] \propto \exp\left(-\frac{1}{4} \int dt \left(\frac{d\mathbf{x}}{dt} + \mathbf{\Omega}\mathbf{x}(t)\right)^T \mathbf{D}^{-1} \left(\frac{d\mathbf{x}}{dt} + \mathbf{\Omega}\mathbf{x}(t)\right)\right), \quad (2)$$

which represents the differential probability for a particle to follow the trajectory $\mathbf{x}()$. The NMR signal in (Eq. 1) can thus be evaluated, up to a constant, through the path integral

$$E \propto \int \mathcal{D}\mathbf{x}() \exp\left(-\int dt \left(\frac{1}{4} \left(\frac{d\mathbf{x}}{dt} + \mathbf{\Omega}\mathbf{x}(t)\right)^T \mathbf{D}^{-1} \left(\frac{d\mathbf{x}}{dt} + \mathbf{\Omega}\mathbf{x}(t)\right) + i\gamma \mathbf{x}(t) \cdot \mathbf{G}(t)\right)\right). \quad (3)$$

Thanks to stationarity, the time integration can be taken from $-\infty$ to ∞ , in which case employing the substitutions

$$\mathbf{x}(t) = \int \frac{d\omega}{2\pi} e^{i\omega t} \hat{\mathbf{x}}(\omega) \quad (4a)$$

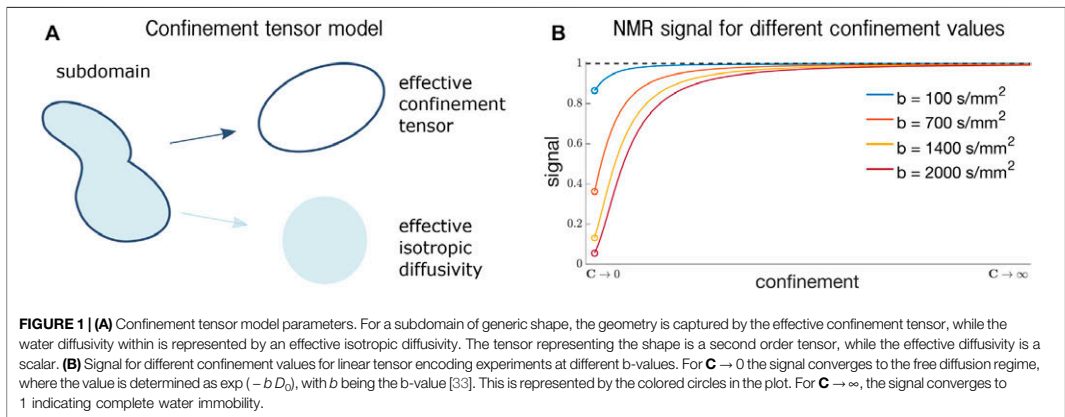
$$\mathbf{G}(t) = \int \frac{d\omega}{2\pi} e^{i\omega t} \hat{\mathbf{G}}(\omega) \quad (4b)$$

yields

$$E = \exp\left(-\int \frac{d\omega}{2\pi} \hat{\mathbf{G}}^\dagger(\omega) \mathbf{K}(\omega) \hat{\mathbf{G}}(\omega)\right) \quad (5)$$

with

$$\mathbf{K}(\omega) = 2\gamma^2 \mathbf{D}(\omega^2 \mathbf{I} + \mathbf{\Omega}^2)^{-1}. \quad (6)$$



Converting Eq. 5 to the time domain yields

$$E = \exp\left(-\frac{\gamma^2}{2} \int dt \int dt' \mathbf{G}^\top(t') \mathbf{D} \Omega^{-1} e^{-\Omega|t-t'|} \mathbf{G}(t)\right). \quad (7)$$

2.2 The Confinement Tensor Model

Figure 1A shows the parameters of the confinement tensor model [17] and how they represent a generic pore. The shape of the subdomain is captured by an effective confinement tensor \mathbf{C} with units of inverse squared length, like in the case of diffusion under a Hookean force as described above. On the other hand, the rate of water diffusivity is captured by a scalar effective isotropic diffusivity D_{eff} .

While the expression given in Eq. 7 is the natural way for defining the signal implied by the confinement tensor model, that is not optimal for the actual computation of the signal. To avoid potential numerical issues with the inversion of the Ω tensor within the integral, we find more advantageous to use the equivalent expression given by Yolcu et al. [17] for a gradient waveform applied between time points 0 and t_f

$$E = \exp\left(-D_{\text{eff}} \int_0^{t_f} dt |\mathbf{Q}(t)|^2\right) \exp\left(-\frac{D_{\text{eff}}}{2} \mathbf{Q}^\top(0) \Omega^{-1} \mathbf{Q}(0)\right) \quad (8)$$

with

$$\mathbf{Q}(t) = \gamma \int_t^{t_f} dt' e^{-\Omega(t'-t)} \mathbf{G}(t'). \quad (9)$$

Note that for $C \rightarrow 0$, the signal in Eq. 8 reduces to the NMR signal expression for isotropic free diffusion (the proof is provided in [17]), while for $C \rightarrow \infty$, the signal converges to 1, indicating particles' immobility. Both these scenarios are shown in Figure 1B, where the signal for confinement values in the range $[0, \infty)$ is shown.

2.3 md-dMRI With Confinement

The expressions derived thus far concern the MR signal for a single confinement tensor. Here, we instead consider the case

where a distribution of such tensors is collectively giving rise to the signal. In particular, we provide the signal expression for a confinement tensor distribution (CTD), which could be used for performing Confinement Tensor Distribution Imaging (CTDI), and discuss employing QTI for locally confined diffusion.

2.3.1 Confinement Tensor Distribution

The NMR signal expression for a distribution $\mathcal{P}(\mathbf{D})$ of diffusion tensors is given by [4]

$$S(\mathbf{b}) = S_0 \int \mathcal{P}(\mathbf{D}) e^{-\mathbf{b} : \mathbf{D}} d\mathbf{D}, \quad (10)$$

where \mathbf{b} is the measurement tensor [34], \mathbf{D} is the diffusion tensor, and $“:”$ indicates the generalized scalar product between tensors. A similar expression can be introduced to include the confinement tensor model. Due to the extra parameter D_{eff} , the considered distribution becomes the joint distribution of effective confinement tensors and effective diffusivities $\mathcal{P}(\mathbf{C}, D_{\text{eff}})$. The signal expression for an experiment determined by a general time varying magnetic field gradient $\mathbf{G}(t)$ is

$$S(\mathbf{G}(t)) = S_0 \int \mathcal{P}(\mathbf{C}, D_{\text{eff}}) E(\mathbf{G}(t), \mathbf{C}, D_{\text{eff}}) d\mathbf{C} dD_{\text{eff}}, \quad (11)$$

where $E(\mathbf{G}(t), \mathbf{C}, D_{\text{eff}})$ is as defined in Eq. 7 or Eq. 8. Eqs 10, 11 can be considered to be generalizations of the Laplace transforms of $\mathcal{P}(\mathbf{D})$ and $\mathcal{P}(\mathbf{C}, D_{\text{eff}})$, respectively. Recovering the $\mathcal{P}(\mathbf{D})$ (or $\mathcal{P}(\mathbf{C}, D_{\text{eff}})$) from a series of measurements, i.e., numerically inverting the Laplace transform, is well known to be an ill-posed problem [30, 35, 36].

2.3.2 QTI for Locally Confined Diffusion

The QTI technique exploits the sensitivity of the detected signal to the statistical moments of the structural parameters describing the specimen [37]. When the DTD model is employed for the latter, the high signal (low diffusion sensitivity) regime reveals the

first few moments of the diffusivities [31, 38]. For a DTD characterized by the distribution $P(\mathbf{D})$ the signal decay in (10) can be expressed by

$$E(\mathbf{b}) = \langle e^{-b_{kt} D_{kt}} \rangle, \quad (12)$$

where we employed the Einstein summation convention. At low diffusion sensitivity, the natural logarithm of the signal decay is approximated by the Maclaurin series of the above expression around $\mathbf{b} \approx \mathbf{0}$, yielding

$$\ln E(\mathbf{b}) \approx -b_{kt} \langle D_{kt} \rangle + \frac{1}{2} b_{kt} b_{mn} \langle D_{kt} D_{mn} \rangle_c, \quad (13)$$

where the last quantity is the second cumulant, i.e., $\langle D_{kt} D_{mn} \rangle_c = \langle D_{kt} D_{mn} \rangle - \langle D_{kt} \rangle \langle D_{mn} \rangle$. We remind that the components of the measurement tensor are given through [34, 39].

$$b_{kt} = \gamma^2 \int_0^{t_f} dt \int_0^t dt' \int_0^{t'} dt'' G_k(t') G_\ell(t''). \quad (14)$$

In the case of a CTD, the averaging takes the form of an integration over D_{eff} as well as \mathbf{C} ; see (Eq. 11). Applying the same procedure for the signal in frequency domain, (Eq. 5), yields

$$\begin{aligned} \ln E(\hat{\mathbf{G}}(\omega)) &\approx - \int \frac{d\omega}{2\pi} \hat{G}_k(\omega) \hat{G}_\ell(\omega) \langle K_{kt}(\omega) \rangle \\ &+ \frac{1}{2} \int \frac{d\omega'}{2\pi} \int \frac{d\omega''}{2\pi} \hat{G}_k(\omega) \hat{G}_\ell(\omega) \hat{G}_m(\omega') \hat{G}_n(\omega'') \\ &\langle K_{kt}(\omega) K_{mn}(\omega'') \rangle_c, \end{aligned} \quad (15)$$

while the same is given in the time-domain by

$$\begin{aligned} \ln E(\mathbf{G}(t)) &\approx - \int dt \int dt' G_k(t) G_\ell(t') \langle H_{kt}(t, t') \rangle \\ &+ \frac{1}{2} \int dt \int dt' \int dt'' \int dt''' G_k(t) G_\ell(t') \\ &G_m(t'') G_n(t''') \langle H_{kt}(t, t') H_{mn}(t'', t''') \rangle_c, \end{aligned} \quad (16)$$

where

$$H_{kt}(t, t') = \frac{\gamma^2}{2} \mathbf{C}^{-1} e^{-\mathbf{DC}|t-t'|} \quad (17)$$

since \mathbf{C} and \mathbf{D} commute.

Note that, the shape of the waveform $\mathbf{G}(t)$ is inextricably linked to the signal in the CTD case. Furthermore, the interpretations of the signal decay rate are substantially different for the CTD and DTD assumptions. Thus, when QTI is performed, one can quantify only apparent moments of a DTD while the same analysis employing the CTD model would provide a more meaningful description of the low diffusion sensitivity regime.

3 IMPLEMENTATION

The confinement tensor model was implemented in Matlab (The Mathworks Inc., Natick, Massachusetts) according to Eqs 8, 9.

Numerical integration was performed using the trapezoidal rule. The signal computation for a given confinement tensor and effective isotropic diffusivity was carried out in a reference frame in which $\mathbf{\Omega}$ is diagonal. This is achieved by rotating the measurement waveforms $\mathbf{G}(t)$ with the rotation matrix determined by the eigenvectors of $\mathbf{\Omega}$. This allows for computations to be carried out separately for each of the eigenvalues of $\mathbf{\Omega}$ thanks to the separability of the model [17]. This approach mitigates numerical issues that arise for small confinement values, in which case inverting $\mathbf{\Omega}$ may become problematic. Possible issues can be alleviated by considering a Taylor expansion for the second exponential factor in Eq. 8 to remove the dependency of that part of the signal on $\mathbf{\Omega}$. The derivation of the expression for computing the approximation of the signal using the Taylor expansion is provided in Appendix.

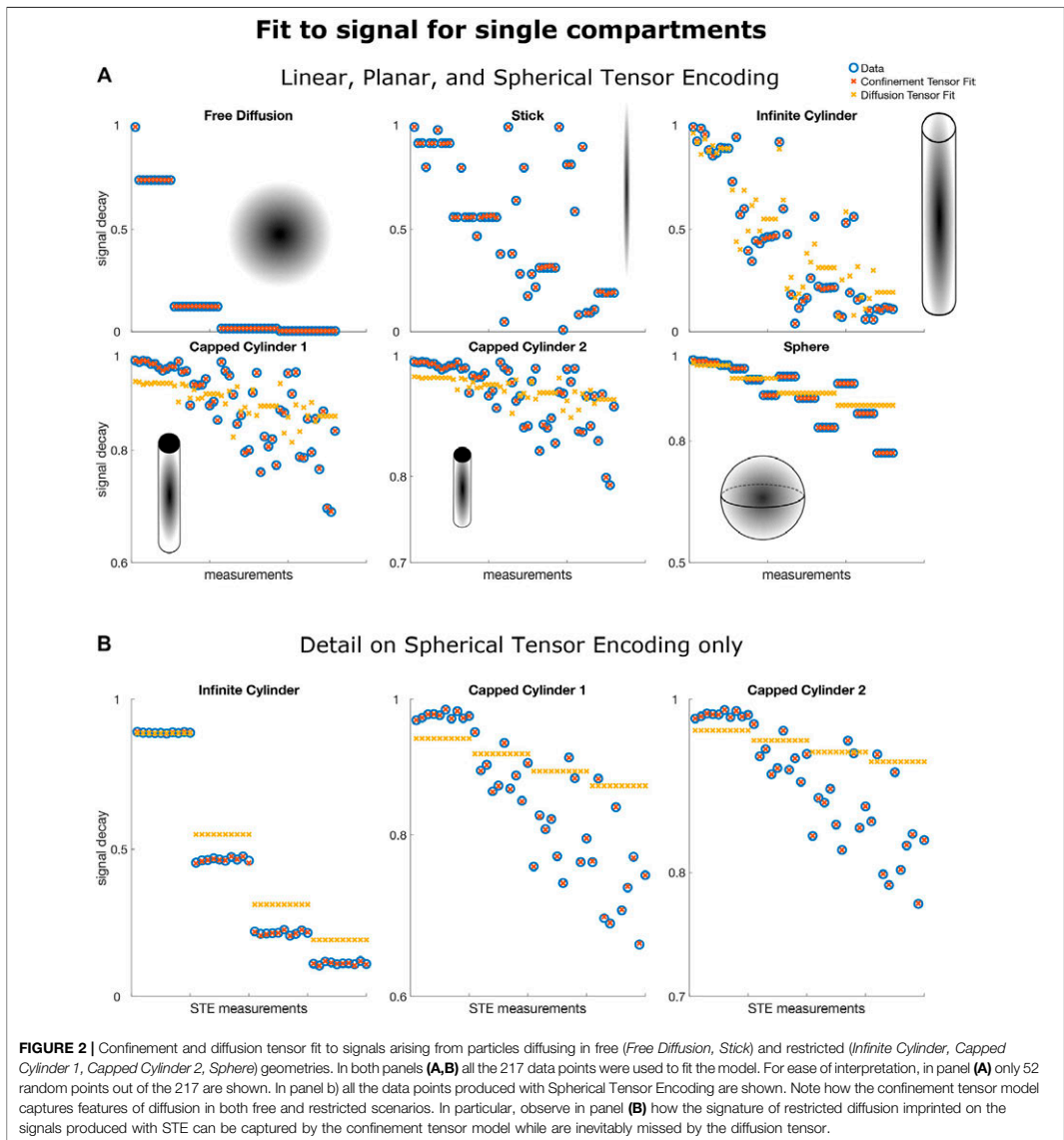
To fit the confinement model to the data, we used the Matlab function *lsqnonlin* with Levenberg-Marquardt as algorithm. The unknown estimated quantities consist of the signal without diffusion weighting S_0 , the effective diffusivity D_{eff} and the six unique components of the confinement tensor \mathbf{C} . During the fitting, the tensor $\mathbf{\Omega}$ is replaced by its Cholesky factorization to ensure the positive semidefiniteness of the estimated confinement tensor [40].

To estimate the joint distribution of confinement tensors and effective isotropic diffusivities, we adapted the existing technology implementing a Monte Carlo inversion of Eq. 10, as detailed in [36] and retrieved from <https://github.com/markus-nilsson/md-dmri>. As for the original implementation, we limit ourselves to the case of axisymmetric tensors. These can be represented using 4 parameters: the parallel and perpendicular confinement (C_{para} and C_{perp}) capture the pore's geometry, while the other two define the pore orientation through the azimuthal (ϕ) and polar (θ) angles. Altogether, each pore is represented by 5 parameters (C_{para} , C_{perp} , ϕ , θ , and D_{eff}). While performing the inversion, these parameters are searched within the limits $8 \leq \log_{10}(C_{\text{para}}/m^{-2})$, $\log_{10}(C_{\text{perp}}/m^{-2}) \leq 12$, $0.1 \leq (D_{\text{eff}}/\mu m^2 ms^{-1}) \leq 3$, $2, 0 \leq \phi \leq 2\pi$, $0 \leq \cos(\theta) \leq 1$. For each voxel, the recovered $\mathcal{P}(\mathbf{C}, D_{\text{eff}})$ can be visualized in 3D plots where C_{para} and C_{perp} vary along the x and y axes, while D_{eff} varies along the z axis, respectively. The pore direction is encoded using the RGB color scale. We adopted the convention of displaying the color according to the main diffusion direction, not according to the direction of maximum confinement.

4 RESULTS

4.1 Signal for Single Compartments

In this section we investigate the capabilities of the confinement tensor model in capturing features of both free and restricted diffusion in data where the diffusion sensitization is achieved with general time varying magnetic field gradients. We employ a protocol featuring 217 measurements comprising Linear, Planar, and Spherical Tensor Encoding (LTE, PTE, and STE respectively) [32]. We refer to this protocol as *tensor encoding*. Signals for diffusion taking place in closed and open geometries



were computed using this protocol. The pore shapes and the respective defining parameters were as follows:

- Free isotropic diffusion, $D_0 = 3 \mu\text{m}^2/\text{ms}$
- Stick compartment (uni-directional free diffusion), $D_0 = 2.5 \mu\text{m}^2/\text{ms}$
- Infinite cylinder, $r = 5 \mu\text{m}$, $D_0 = 3 \mu\text{m}^2/\text{ms}$
- Capped cylinder 1, $l = 12 \mu\text{m}$, $r = 2 \mu\text{m}$, $D_0 = 2 \mu\text{m}^2/\text{ms}$

- Capped cylinder 2, $l = 10 \mu\text{m}$, $r = 1.5 \mu\text{m}$, $D_0 = 2.5 \mu\text{m}^2/\text{ms}$,
- Sphere, $r = 5 \mu\text{m}$, $D_0 = 2 \mu\text{m}^2/\text{ms}$

where D_0 is the bulk diffusivity, r is the radius, and l is the length. The diffusion tensor model was used to generate the signals for the free diffusion and the stick compartments, while the method described in [12] was used to generate the signals for the cylinders and the sphere.

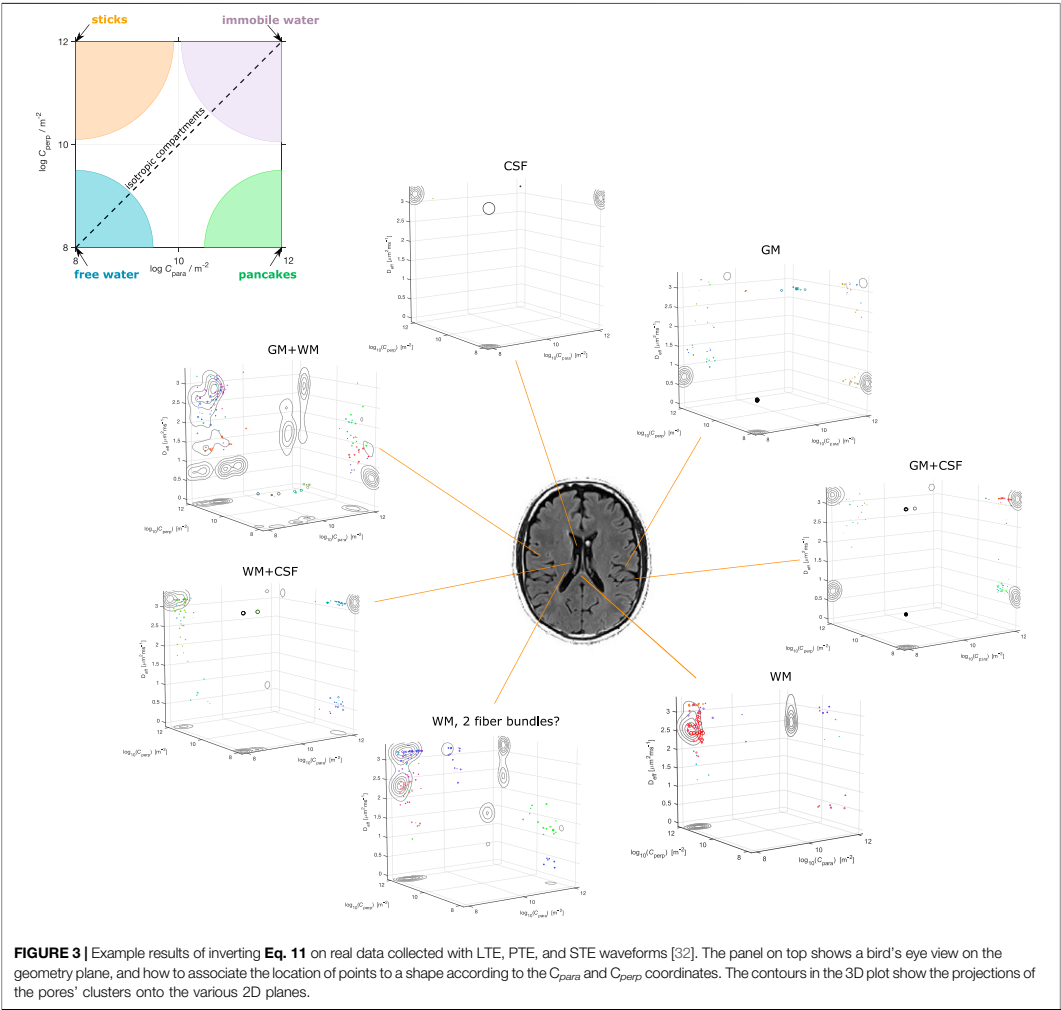


FIGURE 3 | Example results of inverting Eq. 11 on real data collected with LTE, PTE, and STE waveforms [32]. The panel on top shows a bird's eye view on the geometry plane, and how to associate the location of points to a shape according to the C_{pore} and C_{perp} coordinates. The contours in the 3D plot show the projections of the pores' clusters onto the various 2D planes.

Figure 2A shows the results obtained by fitting the confinement tensor model and the diffusion tensor to the simulated signals. Only a subset of the measurements is shown for easier visual inspection. For the considered protocol, the confinement tensor model seems to capture well the features of both free and restricted diffusion, suggesting that the model given in Eq. 8 has sufficient degrees of freedom and there is no need for employing a tensorial diffusivity. Note that as illustrated for the 1D problem of restricted diffusion between two parallel plates [26], in the ideal scenario involving only very long pulses and simple geometries, one would expect the measurement to be sensitive only to the product of squared confinement and diffusivity, in which case there is no need to employ an

effective diffusivity in the model. However, in practice there is such sensitivity, and the relationship between the parameters of the model (D_{eff} and C) and those of the geometry requires further investigations. What is remarkable however is that having only one additional parameter (D_{eff}) offers sufficient complexity to capture the information in the signal for the considered acquisition scenario. This is also evident in **Figure 2B**, which better illustrates how the assumption of free diffusion fails [3, 41] while the confinement tensor model fully captures the signal modulations due to restricted diffusion probed by STE measurements.

The recovered values of the effective diffusivity D_{eff} coincided with the bulk diffusivity D_0 for the stick and free water

compartments. For the compartments in which diffusion is fully restricted, the estimated values were lower than the nominal D_0 . Respectively, $1.65 \mu\text{m}^2/\text{ms}$ for Capped Cylinder 1, $2.0 \mu\text{m}^2/\text{ms}$ for Capped Cylinder 2, and $1.7 \mu\text{m}^2/\text{ms}$ for Sphere.

4.2 Signal for a Distribution of Compartments

Illustrative results obtainable with the Monte Carlo inversion method described in Section 3 were produced on a publicly available brain dataset [32] collected via the *tensor encoding* protocol used in the simulations. Figure 3 shows Monte Carlo inversion results on a few selected voxels on the bottom, and a bird's-eye view on the plane displaying the geometric information about the tensors in the distribution on the top. In this last, the colored areas indicate what shape each tensor would have for different values of C_{para} and C_{perp} . Pores with isotropic geometries are found along the diagonal where $C_{para} = C_{perp}$. Free isotropic diffusion is found for low $C_{para} = C_{perp}$, while confined isotropic diffusion is found for high $C_{para} = C_{perp}$. Stick-like pores are located at the $C_{para} \ll C_{perp}$ corner, while pancake-like pores are found at the $C_{para} \gg C_{perp}$ corner.

In the same spirit of what was shown in [42] for the DTD model, the 3D plots in Figure 3 show what the $\mathcal{P}(\mathbf{C}, D_{\text{eff}})$ for voxels containing either single or multiple types of brain tissues, as obtained from the data, could be. For example, voxels containing pure CSF would have a $\mathcal{P}(\mathbf{C}, D_{\text{eff}})$ of only free diffusion geometry with $D_{\text{eff}} \approx 3.1 \mu\text{m}^2/\text{ms}$. Pure white matter voxels would only contain collections of stick-like geometries (see the voxel from the Corpus Callosum), while, for the considered dataset, gray matter could contain isotropic free water at lower D_{eff} compared to free water. Voxels with mixed tissue types could build their $\mathcal{P}(\mathbf{C}, D_{\text{eff}})$ based on those from single tissues. Note how having separate components encoding for the pore geometry (\mathbf{C}) and the water diffusivity (D_{eff}) allows for clearly identifying scenarios where pores could have the same shape, but different water mobility. See for example the voxel “WM, 2 fiber bundles?”, where the distribution seems to suggest the presence of two differently oriented fiber bundles, which can be teased apart also by looking at their water diffusivity. The same specificity could not be achieved by only considering a distribution of diffusion tensors, where the information about the pore geometry is inextricably entangled to that of water diffusivity.

Note however that all what is presented and discussed in this section are simply initial conjectures, which may very well be the results of falling into the temptation of over-interpreting the outcomes of the DTD or CTD estimation. As shown by [36], inverting Eq. 10, and by extension Eq. 11, is already challenging even at infinite SNR. The situation worsens in real data where the validity of the solutions proves to be very sensitive to the presence of noise. Moreover, as we present and discuss later, the results, and their interpretation, strongly depend upon the adopted acquisition scheme. For example, we could expect to find sphere-like compartments in gray matter in data encoded with different diffusion times and higher diffusion sensitivity, possibly indicating that a relevant fraction of the signal is due to cell bodies. Moreover, while the considered protocol (and data)

should encode sufficient information for accurately recovering the pores' geometry, other waveforms could prove beneficial to study the time-dependence of the diffusion process, augmenting the reliability of the D_{eff} dimension.

5 DISCUSSION

The results in Figure 2 illustrate how well the confinement model captures the features of both free and restricted diffusion, for data simulated with a clinically-feasible protocol including typical time-varying magnetic field gradients. The signal's modulation due to restrictions is, under the considered experimental set-up, fully described by studying the problem of diffusion occurring in a potential landscape. This shows that the considered approach retains the right number of degrees of freedom to characterize diffusion processes within individual compartments. This finding is consistent with what was reported by Özarslan et al. [26] for experiments involving long duration pulses, and supports the idea of adopting the confinement tensor for representing isolated pores in multicompartment models.

Having a single model covering both restricted and unrestricted diffusion in different geometries could be advantageous when defining multi-compartmental models based on such shapes as building blocks. Biophysical models, such as the composite hindered and restricted model of diffusion (CHARMED) [43] and neurite orientation dispersion and density imaging (NODDI) [44] strive for modeling specifically the neural tissue, therefore are not suitable for different tissues and other heterogeneous media. The confinement tensor representation of each compartment could be integrated into such models and could provide a convenient means for accounting for restricted diffusion. On the other hand, the confinement tensor distribution model is far more general than such specific models as one would not need to make *a priori* assumptions on the specimen composition, apart from limiting its representation to numerous non-exchanging and possibly confined domains. The results in Figure 3 exemplified the specificity achievable by modeling a specimen with a joint distribution of confinement tensors-isotropic effective diffusivities. Other information about the water pools, such as T_1 and T_2 relaxations [42, 45], could be added to increase specificity to the tissue heterogeneity. Similarly to what was presented there, the confinement tensor model could also be considered for diffusion-relaxation studies [42, 46–49].

Note that on the specific dataset used in this work we did not observe striking modulation in the signal for isotropic measurements at constant b-value. This could be explained by the experiments not being sensitive to finite-sized anisotropic restrictions, i.e., axons could effectively be pictured as sticks. Under these conditions, the fit to signal for both the DTD and CTD would yield very close results. Having two fundamentally different models exhibiting good fits to the data suggests that the data is possibly not descriptive enough. Another factor contributing to equal performance could be found in both DTD and CTD being overly-parameterized, thus effectively having the capabilities to fit the data equally successfully. This should not however be interpreted as both models being acceptable and providing informative results. In addition,

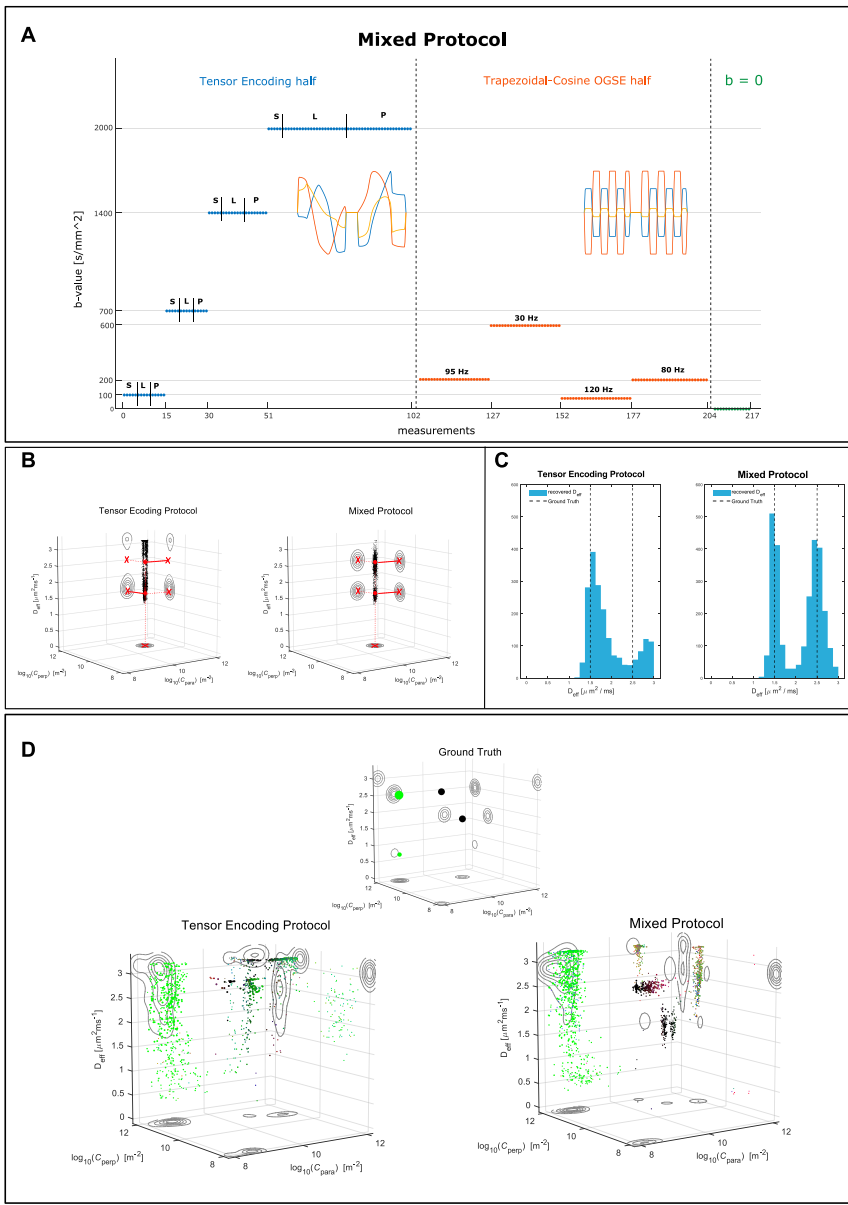


FIGURE 4 | (A) Layout of the *mixed* protocol. 102 measurements consist of LTE, PTE, and STE waveforms as defined in the *tensor encoding* protocol, but with their directions redistributed over the sphere to achieve more uniform directional sampling. Another 102 measurements consist of Trapezoidal Cosine Oscillating Gradient Spin Echo waveforms oscillating at 4 different frequencies. The last 13 measurements had null diffusion gradient strength. **(B)** Results of inverting Eq. 11 for a simple system consisting of two equally weighted water pools with identical geometries but different water diffusivities. Left, data encoded with the *tensor encoding* protocol. Right, data encoded with the *mixed* protocol. The red filled dots depict the ground truth values in the 3D plot, while the red crosses show the ground truth (Continued)

FIGURE 4 | values for the projections onto the various planes. **(C)** The distributions of D_{eff} obtained in **(B)**. **(D)** Results inverting Eq. 11 for a substrate comprising a free water compartment, a sphere compartment, a stick compartment, and an intra-axonal compartment, with the following weights in the distribution: 0.25, 0.25, 0.4, 0.1. The substrate ground truth is visualized in the small 3D plot on top. On the left, data encoded with the *tensor encoding* protocol. On the right, data encoded with the *mixed* protocol.

based on the results in Figure 2, we expect the CTD to provide meaningful information on data where restrictions have imprinted a clearer signature.

We would also care to iterate one more on the limitation of performing CTDI (or DTDI) using the technology implemented in <https://github.com/markus-nilsson/md-dmri>, due to the mathematically ill-posed problem that is being attempted. Different $\mathcal{P}(\mathbf{C}, D_{\text{eff}})$ in Eq. 11 will represent the signal equally well, thus possibly leading to wrong interpretations of the microstructural characteristics of the scanned specimen. A similar issue is referred to as the “degeneracy problem” [50] in recovering the brain microstructure. Multi-compartment models present flat fitting landscapes with multiple local minima located in different parts of the parameter space, each of which providing equally sound biological explanation for the signal. One approach to alleviate the problem involves including additional measurements, e.g. diffusion measurements having different temporal profiles, with the goal of disentangling the contribution of different parameters to the model interpretation [51].

When attempting at recovering the joint distribution of confinement tensors and isotropic effective diffusivities, we found from simulations that the pores’ geometry can be obtained relatively faithfully using the *tensor encoding* protocol only. However, determining the pore diffusivity relatively to the restriction size from data encoded exclusively in such manner seems to be more challenging. We provide examples of this in Figure 4. In Figure 4A we show a modified version of the *tensor encoding* protocol, where half of the waveforms are replaced with Trapezoidal-Cosine Oscillating Gradient Spin-Echo (TC-OGSE). We refer to this protocol as *mixed*. The goal is to achieve higher sensitivity to molecules’ diffusivity within restrictions by using waveforms with well defined encoding frequency, and by matching the frequency of such waveform to that of the diffusion process [52–54]. Retaining part of the original protocol should ensure accurate pore geometry estimation. In Figures 4B,C we show the results obtained for a simple scenario where the specimen consists of two pools of water in which molecules are diffusing at different rates. When the data are simulated with only LTE, PTE, and STE, it is possible to accurately recover the expected pore shapes but not the water diffusivity. Conversely, by introducing oscillating gradients, the diffusivity estimates, although still uncertain, converge to the correct values.

In Figure 4D we show the results on a more complex substrate consisting of a stick compartment, an extra-axonal compartment, a sphere compartment and a compartment with free diffusion. As for the simple scenario described above, the estimation of the pores’ diffusivity, in particular one of the sphere compartments, improves when the mixed protocol is used. This corroborates the idea of including measurements not only exploring different shapes of the

encoding tensors, but also probing different frequencies [53]. The results in Figure 4D also exemplify the uncertainty around inverting the Laplace transform, even for infinite SNR.

6 CONCLUSION

In this work we incorporated the confinement tensor model for individual subdomains of heterogeneous media into multidimensional diffusion MRI frameworks. We demonstrated how considering Brownian motion as taking place under the influence of a Hookean potential provides sufficient degrees of freedom to capture the signal modulations arising from water diffusing in restricted geometries. We argued that the confinement tensor distribution (CTD) model is a viable alternative to the diffusion tensor distribution model as CTD relies on the effective model of restricted diffusion, which makes it more consistent with the multicompartmental organization of complex tissue when examined via commonly performed diffusion MRI measurements. Despite its challenges, incorporating this model into multidimensional diffusion MRI methods could provide new insights regarding the structural composition of complex media.

DATA AVAILABILITY STATEMENT

Publicly available datasets were analyzed in this study. This data can be found here: https://github.com/filip-szczepankiewicz/Szczepankiewicz_DIB_2019.

AUTHOR CONTRIBUTIONS

DB: Methodology, Software, Validation, Formal analysis, Investigation, Writing—Original Draft, Visualization. CY: Methodology, Theory, Writing—Review and Editing. EÖ: Conceptualization, Methodology, Writing—Review and Editing, Supervision, Project administration, Funding acquisition.

FUNDING

This project was financially supported by Linköping University Center for Industrial Information Technology (CENIIT), Analytic Imaging Diagnostics Arena (AIDA), and Sweden’s Innovation Agency (VINNOVA) ASSIST.

ACKNOWLEDGMENTS

The authors thank Magnus Herberthson for stimulating discussions.

REFERENCES

- Panagiotaki E, Schneider T, Siow B, Hall MG, Lythgoe MF, Alexander DC. Compartment Models of the Diffusion MR Signal in Brain white Matter: A Taxonomy and Comparison. *NeuroImage* (2012) 59:2241–54. doi:10.1016/j.neuroimage.2011.09.081
- Jelescu IO, Budde MD. Design and Validation of Diffusion MRI Models of White Matter. *Front Phys* (2017) 5:61. doi:10.3389/fphys.2017.00061
- de Swiet TM, Mitra PP. Possible Systematic Errors in Single-Shot Measurements of the Trace of the Diffusion Tensor. *J Magn Reson Ser B* (1996) 111:15–22. doi:10.1006/jmr.1996.0055
- Jian B, Vemuri BC, Özarslan E, Carney PR, Mareci TH. A Novel Tensor Distribution Model for the Diffusion-Weighted MR Signal. *NeuroImage* (2007) 37:164–76. doi:10.1016/j.neuroimage.2007.03.074
- Basser PJ, Pajevic S. A normal Distribution for Tensor-Valued Random Variables: Applications to Diffusion Tensor MRI. *IEEE Trans Med Imaging* (2003) 22:785–94. doi:10.1109/TMI.2003.815059
- Magdoo KN, Pajevic S, Dario G, Basser PJ. A New Framework for MR Diffusion Tensor Distribution. *Sci Rep* (2021) 11:2766. doi:10.1038/s41598-021-81264-x
- Shakya S, Batool N, Özarslan E, Knutsson H. Multi-fiber Reconstruction Using Probabilistic Mixture Models for Diffusion MRI Examinations of the Brain. In: T Schultz, E Özarslan, I Hotz, editors. *Modeling, Analysis, and Visualization of Anisotropy*. Cham: Springer International Publishing (2017). 283–308. doi:10.1007/978-3-319-61358-1_12
- Herberthson M, Yölcü C, Knutsson H, Westin CF, Özarslan E. Orientationally-averaged Diffusion-Attenuated Magnetic Resonance Signal for Locally-Anisotropic Diffusion. *Sci Rep* (2019) 9:4899. doi:10.1038/s41598-019-41317-8
- Cory DG, Garroway AN, Miller JB. Applications of Spin Transport as a Probe of Local Geometry. *Abstr Pap Am Chem Soc* (1990) 199:105.
- Wong EC, Cox RW, Song AW. Optimized Isotropic Diffusion Weighting. *Magn Reson Med* (1995) 34:139–43. doi:10.1002/mrm.1910340202
- Caprihan A, Wang LZ, Fukushima E. A Multiple-Narrow-Pulse Approximation for Restricted Diffusion in a Time-Varying Field Gradient. *J Magn Reson Ser A* (1996) 118:94–102. doi:10.1006/jmra.1996.0013
- Özarslan E, Shemesh N, Basser PJ. A General Framework to Quantify the Effect of Restricted Diffusion on the NMR Signal with Applications to Double Pulsed Field Gradient NMR Experiments. *J Chem Phys* (2009) 130:104702. doi:10.1063/1.3082078
- Westin CF, Szczepankiewicz F, Pasternak O, Özarslan E, Topgaard D, Knutsson H, et al. Measurement Tensors in Diffusion MRI: Generalizing the Concept of Diffusion Encoding. In: P Golland, N Hata, C Barillot, J Hornegger, R Howe, editors. *Medical Image Computing and Computer-Assisted Intervention – MICCAI 2014*. Cham: Springer International Publishing (2014). p. 209–16. doi:10.1007/978-3-319-10443-0_27
- Topgaard D. Multidimensional Diffusion MRI. *J Magn Reson* (2017) 275: 98–113. doi:10.1016/j.jmr.2016.12.007
- Beaulieu C, Allen PS. Determinants of Anisotropic Water Diffusion in Nerves. *Magn Reson Med* (1994) 31:394–400. doi:10.1002/mrm.1910310408
- Woessner DE. N.M.R. Spin-echo Self-Diffusion Measurements on Fluids Undergoing Restricted Diffusion. *J Phys Chem* (1963) 67:1365–7. doi:10.1021/j100800a509
- Yölcü C, Memiş M, Şimşek K, Westin CF, Özarslan E. NMR Signal for Particles Diffusing under Potentials: From Path Integrals and Numerical Methods to a Model of Diffusion Anisotropy. *Phys Rev E* (2016) 93: 052602. doi:10.1103/PhysRevE.93.052602
- Uhlenbeck GE, Ornstein LS. On the Theory of the Brownian Motion. *Phys Rev* (1930) 36:823–41. doi:10.1103/physrev.36.823
- Stejskal EO. Use of Spin Echoes in a Pulsed Magnetic-Field Gradient to Study Anisotropic, Restricted Diffusion and Flow. *J Chem Phys* (1965) 43:3597–603. doi:10.1063/1.1696526
- Le Doussal P, Sen PN. Decay of Nuclear Magnetization by Diffusion in a Parabolic Magnetic Field: An Exactly Solvable Model. *Phys Rev B* (1992) 46: 3465–85. doi:10.1103/PhysRevB.46.3465
- Mitra P, Halperin B. Effects of Finite Gradient-Pulse Widths in Pulsed-Field-Gradient Diffusion Measurements. *J Magn Reson Ser A* (1995) 113:94–101. doi:10.1006/jmra.1995.1060
- Afzali M, Yölcü C, Özarslan E. Characterizing Diffusion Anisotropy for Molecules under the Influence of a Parabolic Potential: A Plausible Alternative to DTL. *Proc Intl Soc Mag Reson Med* (2015) 23:2795.
- Zucchelli M, Afzali M, Yölcü C, Westin CF, Menegaz G, Özarslan E. The Confinement Tensor Model Improves Characterization of Diffusion-Weighted Magnetic Resonance Data with Varied Timing Parameters. In: 2016 IEEE 13th International Symposium on Biomedical Imaging (ISBI), Prague, Czech Republic, April 13–16, 2016. IEEE (2016). 1093–6. doi:10.1109/isbi.2016.7493456
- Liu C, Özarslan E. Multimodal Integration of Diffusion MRI for Better Characterization of Tissue Biology. *NMR Biomed* (2019) 32:e3939. doi:10.1002/nbm.3939
- Afzali M, Pieciak T, Newman S, Garyfallidis E, Özarslan E, Cheng H, et al. The Sensitivity of Diffusion MRI to Microstructural Properties and Experimental Factors. *J Neurosci Methods* (2021) 347:108951. doi:10.1016/j.jneumeth.2020.108951
- Özarslan E, Yölcü C, Herberthson M, Westin CF, Knutsson H. Effective Potential for Magnetic Resonance Measurements of Restricted Diffusion. *Front Phys* (2017) 5:68. doi:10.3389/fphys.2017.00068
- Mitra PP. Multiple Wave-Vector Extensions of the NMR Pulsed-Field-Gradient Spin-echo Diffusion Measurement. *Phys Rev B* (1995) 51:15074–8. doi:10.1103/physrevb.51.15074
- Özarslan E, Basser PJ. Microscopic Anisotropy Revealed by NMR Double Pulsed Field Gradient Experiments with Arbitrary Timing Parameters. *J Chem Phys* (2008) 128:154511. doi:10.1063/1.2905765
- Yölcü C, Herberthson M, Westin CF, Özarslan E. Magnetic Resonance Assessment of Effective Confinement Anisotropy with Orientationally-Averaged Single and Double Diffusion Encoding. In: E Özarslan, T Schultz, E Zhang, A Fuster, editors. *Anisotropy across Fields and Scales*. Cham: Springer Nature (2021). 203–23. Mathematics and Visualization. doi:10.1007/978-3-030-56215-1_10
- Topgaard D. Diffusion Tensor Distribution Imaging. *NMR Biomed* (2019) 32: e4066. doi:10.1002/nbm.4066
- Westin CF, Knutsson H, Pasternak O, Szczepankiewicz F, Özarslan E, van Westen D, et al. Q-space Trajectory Imaging for Multidimensional Diffusion MRI of the Human Brain. *NeuroImage* (2016) 135:345–62. doi:10.1016/j.neuroimage.2016.02.039
- Szczepankiewicz F, Hoge S, Westin CF. Linear, Planar and Spherical Tensor-Valued Diffusion MRI Data by Free Waveform Encoding in Healthy Brain, Water, Oil and Liquid Crystals. *Data in Brief* (2019) 25:104208. doi:10.1016/j.dib.2019.104208
- LeBihan D, Breton E. Imagerie de diffusion *In Vivo* par résonance magnétique nucléaire. *C R Acad Sc* (1985) 15:1109–12.
- Mattiello J, Basser PJ, LeBihan D. Analytical Expressions for the B-Matrix in NMR Diffusion Imaging and Spectroscopy. *J Magn Reson A* (1994) 108: 131–41. doi:10.1006/jmra.1994.1103
- Galvosas P, Callaghan PT. Multi-dimensional Inverse Laplace Spectroscopy in the NMR of Porous media. *Comptes Rendus Physique* (2010) 11:172–80. doi:10.1016/j.crhy.2010.06.014
- Reymbaut A, Mezzani P, Almeida Martins JP, Topgaard D. Accuracy and Precision of Statistical Descriptors Obtained from Multidimensional Diffusion Signal Inversion Algorithms. *NMR Biomed* (2020) 33, e4267. doi:10.1002/nbm.4267
- Özarslan E, Shemesh N, Koay CG, Cohen Y, Basser PJ. Nuclear Magnetic Resonance Characterization of General Compartment Size Distributions. *New J Phys* (2011) 13:15010. doi:10.1088/1367-2630/13/1/015010
- Lasić S, Szczepankiewicz F, Eriksson S, Nilsson M, Topgaard D. Microanisotropy Imaging: Quantification of Microscopic Diffusion Anisotropy and Orientational Order Parameter by Diffusion MRI with Magic-Angle Spinning of the Q-Vector. *Front Phys* (2014) 2:11. doi:10.3389/fphys.2014.00011
- Özarslan E, Westin CF, Mareci TH. Characterizing Magnetic Resonance Signal Decay Due to Gaussian Diffusion: the Path Integral Approach and a Convenient Computational Method. *Concepts Magn Reson A* (2015) 44: 203–13. doi:10.1002/cmra.21354

40. Koay CG, Chang LC, Carew JD, Pierpaoli C, Basser PJ. A Unifying Theoretical and Algorithmic Framework for Least Squares Methods of Estimation in Diffusion Tensor Imaging. *J Magn Reson* (2006) 182:115–25. doi:10.1016/j.jmr.2006.06.020
41. Jespersen SN, Olesen JL, Ianuş A, Shemesh N. Effects of Nongaussian Diffusion on “Isotropic Diffusion” Measurements: An *Ex-Vivo* Microimaging and Simulation Study. *J Magn Reson* (2019) 300:84–94. doi:10.1016/j.jmr.2019.01.007
42. Topgaard D. Multiple Dimensions for Random Walks. *J Magn Reson* (2019) 306:150–4. doi:10.1016/j.jmr.2019.07.024
43. Assaf Y, Basser PJ. Composite Hindered and Restricted Model of Diffusion (Charmed) Mr Imaging of the Human Brain. *NeuroImage* (2005) 27:48–58. doi:10.1016/j.neuroimage.2005.03.042
44. Zhang H, Schneider T, Wheeler-Kingshott CA, Alexander DC. Noddi: Practical *In Vivo* Neurite Orientation Dispersion and Density Imaging of the Human Brain. *NeuroImage* (2012) 61:1000–16. doi:10.1016/j.neuroimage.2012.03.072
45. Callaghan PT, Arns CH, Galvosas P, Hunter MW, Qiao Y, Washburn KE. Recent Fourier and Laplace Perspectives for Multidimensional NMR in Porous media. *Magn Reson Imaging* (2007) 25:441–4. doi:10.1016/j.mri.2007.01.114
46. Benjamini D, Basser PJ. Multidimensional Correlation MRI. *NMR Biomed* (2020) 33. doi:10.1002/nbm.4226
47. Sator PJ, Palombo M, Miller KL, Westin CF, Laun F, Kim D, et al. Combined Diffusion-Relaxometry Microstructure Imaging: Current Status and Future Prospects. *Magn Reson Med* (2021) 86:2987–3011. doi:10.1002/mrm.28963
48. de Almeida Martins JP, Tax CMW, Reymbaut A, Szczepankiewicz F, Chamberland M, Jones DK, et al. Computing and Visualising Intra-voxel Orientation-specific Relaxation-Diffusion Features in the Human Brain. *Hum Brain Mapp* (2021) 42:310–28. doi:10.1002/hbm.25224
49. Martin J, Reymbaut A, Schmidt M, Doerfler A, Uder M, Laun FB, et al. Nonparametric D-R1-R2 Distribution MRI of the Living Human Brain. *Neuroimage* (2021) 245:118753. doi:10.1016/j.neuroimage.2021.118753
50. Jolescu IO, Veraart J, Fieremans E, Novikov DS. Degeneracy in Model Parameter Estimation for Multi-Compartmental Diffusion in Neuronal Tissue: Degeneracy in Model Parameter Estimation of Diffusion in Neural Tissue. *NMR Biomed* (2016) 29:33–47. doi:10.1002/nbm.3450
51. Coelho S, Pozo JM, Jespersen SN, Jones DK, Frangi AF. Resolving Degeneracy in Diffusion MRI Biophysical Model Parameter Estimation Using Double Diffusion Encoding. *Magn Reson Med* (2019) 82:395–410. doi:10.1002/mrm.27714
52. Stepišnik J. Time-dependent Self-Diffusion by NMR Spin-echo. *Physica B* (1993) 183:343–50.
53. Lundell H, Nilsson M, Dyrby TB, Parker GJM, Cristina PLH, Zhou FL, et al. Multidimensional Diffusion MRI with Spectrally Modulated Gradients Reveals Unprecedented Microstructural Detail. *Scientific Rep* (2019) 9:9026. doi:10.1038/s41598-019-45235-7
54. Drobnjak I, Cruz G, Alexander DC. Optimising Oscillating Waveform-Shape for Pore Size Sensitivity in Diffusion-Weighted MR. *Microporous Mesoporous Mater* (2013) 178:11–4. doi:10.1016/j.micromeso.2013.03.004

Conflict of Interest: EÖ is a shareholder of Spin Nord AB.

The remaining authors declare that the research was conducted in the absence of any commercial or financial relationships that could be construed as a potential conflict of interest.

Publisher's Note: All claims expressed in this article are solely those of the authors and do not necessarily represent those of their affiliated organizations, or those of the publisher, the editors and the reviewers. Any product that may be evaluated in this article, or claim that may be made by its manufacturer, is not guaranteed or endorsed by the publisher.

Copyright © 2022 Boito, Yolcu and Özarslan. This is an open-access article distributed under the terms of the Creative Commons Attribution License (CC BY). The use, distribution or reproduction in other forums is permitted, provided the original author(s) and the copyright owner(s) are credited and that the original publication in this journal is cited, in accordance with accepted academic practice. No use, distribution or reproduction is permitted which does not comply with these terms.

APPENDIX: NUMERICAL APPROXIMATION OF THE SIGNAL IN $C \rightarrow 0$ REGIME

The matrix inversion in the second exponential in equation (Eq. 8) can become numerically unstable for $C \rightarrow 0$. When working in the coordinate system determined by the eigenvectors of C , the matrix Ω is diagonal

$$\Omega = \begin{bmatrix} \lambda_1 & 0 & 0 \\ 0 & \lambda_2 & 0 \\ 0 & 0 & \lambda_3 \end{bmatrix}. \quad (18)$$

We take \vec{v}_1 , \vec{v}_2 , and \vec{v}_3 to be the eigenvectors of C , defining the new coordinate system for the experiment. The matrix R having \vec{v}_1 , \vec{v}_2 , and \vec{v}_3 as columns, can be used to determine the gradient waveforms used to collect the data in the new coordinate system through

$$G'(t) = [G'_1(t), G'_2(t), G'_3(t)]^T = R^T G(t). \quad (19)$$

Then, the signal contribution from the second exponential in Eq. 8 can be written as

$$\begin{aligned} & \exp\left(-\frac{D_{\text{eff}}}{2} [Q_1(0) \ Q_2(0) \ Q_3(0)] \begin{bmatrix} \lambda_1^{-1} & 0 & 0 \\ 0 & \lambda_2^{-1} & 0 \\ 0 & 0 & \lambda_3^{-1} \end{bmatrix} \begin{bmatrix} Q_1(0) \\ Q_2(0) \\ Q_3(0) \end{bmatrix}\right) \\ &= \exp\left(-\frac{D_{\text{eff}}}{2} Q_1^2(0) \lambda_1^{-1}\right) \exp\left(-\frac{D_{\text{eff}}}{2} Q_2^2(0) \lambda_2^{-1}\right) \exp\left(-\frac{D_{\text{eff}}}{2} Q_3^2(0) \lambda_3^{-1}\right) \end{aligned} \quad (20)$$

with

$$Q_i(0) = \gamma \int_0^{t_f} dt' e^{-\lambda_i t'} G'_i(t'), \quad i = 1, 2, 3. \quad (21)$$

In the case when the j th eigenvalue λ_j is small, so is $Q_j(0)$ due to the gradient echo condition, and the evaluation of the corresponding exponent on the right hand side of (Eq. 20) is numerically difficult. In this case, one can make use of the Taylor expansion of the exponential in (Eq. 21) yielding

$$\begin{aligned} & \exp\left(-\frac{D_{\text{eff}}}{2} Q_j^2(0) \lambda_j^{-1}\right) \\ & \approx \exp\left(-\frac{D_{\text{eff}}}{2} \left[\lambda_j \alpha_j^2 - \lambda_j^2 \alpha_j \beta_j + \lambda_j^3 \left(\frac{1}{4} \beta_j^2 + \frac{1}{3} \alpha_j \delta_j \right) \right] \right), \end{aligned} \quad (22)$$

where

$$\alpha_j = \gamma \int_0^{t_f} d\tau G'_j(\tau) \tau \quad (23a)$$

$$\beta_j = \gamma \int_0^{t_f} d\tau G'_j(\tau) \tau^2. \quad (23b)$$

$$\delta_j = \gamma \int_0^{t_f} d\tau G'_j(\tau) \tau^3. \quad (23c)$$

FACULTY OF SCIENCE AND ENGINEERING

Linköping Studies in Science and Technology, Dissertation No. 2362, 2023
Department of Biomedical Engineering

Linköping University
SE-581 83 Linköping, Sweden

www.liu.se

